CHARACTERIZATION OF FUNCTIONALIZED AND UNFUCTIONALIZED METAL OXIDE NANOPARTICLE INTERACTIONS WITH GAS MIXTURES ON POROUS SILICON

A Thesis
Presented to
The Academic Faculty

by

William Laminack

In Partial Fulfillment
of the Requirements for the Degree
Doctor of Philosophy in Physics

School of Physics
Georgia Institute of Technology
August 2015

CHARACTERIZATION OF FUNCTIONALIZED AND UNFUCTIONALIZED METAL OXIDE NANOPARTICLE INTERACTIONS WITH GAS MIXTURES ON POROUS SILICON

Approved by:

Professor James Gole, Advisor
School of Physics
Georgia Institute of Technology

Professor Philip First
School of Physics
Georgia Institute of Technology

Professor Alberto Fernandez-Nieves
School of Physics
Georgia Institute of Technology

Professor E. Kent Barefield
School of Chemistry
Georgia Institute of Technology

Professor Peter Hesketh
School of Mechanical Engineering
Georgia Institute of Technology

Date Approved: April, 17, 2015

To all my crazy roommates, this would have been done much sooner except for them

ACKNOWLEDGEMENTS

There are many people without whom, the work in this thesis wouldn't be completed. First of all, I would like to thank to my advisor Prof James Gole: all the challenging scientific discussions. The interesting idea of in-situ nitration of the metal oxides came from him. Without him and his tireless drive, I wouldn't be able to do this work. I admire his desire not to settle for the ordinary and to always try new avenues of research, and his hard work on reading this thesis. I would like to thank to Prof. Hesketh for valuable discussions about gas sensors and diffusion. I would like to thank Prof. Barefield for generously lending us a fumehood and also thank Prof. Fernandez-Nieves for graciously finding space in his lab for us after renovations moved us out of Dr. Barefield's fumehood.

I would also like to thank to all of my committee members: Prof. Hesketh, Prof. Fernandez-Nieves, Prof. First, and Prof. Barefield – for reading this thesis, making time for the thesis defense, and all their feedback.

I would like to thank Dr. Serdar Ozdemir who I worked under for all my undergraduate research, and who taught me the basic experimental setup. I also want to thank Caitlin Baker my lab mate for five years who helped with the multiple sensor setup. I would have to thank to the friendly cleanroom staff and encouraging cleanroom manager Gary Spinner.

I would like to thank Naveen Pouse, Christian Richter, Eddie Goude, and Patrick Pansuki and many other dedicated undergraduate students for their contributions during their undergraduate research studies. I would have to thank to all of my friends at School of Physics who have indirectly affected the success of this work. My roommates Eric Stribling, Josiah Laminack, Michael Bonner, Kelso Howington, and Richie Inza for many interesting hours.And finally I am thankful for my parents for their wonderful support and love.

TABLE OF CONTENTS

LIST OF TABLES

LIST OF FIGURES

CHAPTER I

INTRODUCTION

With the increased industrialization during the twentieth century, chemical processes have become more common. Combustion in factories, industrial chemical reactions, and the wide spread use of automobiles has brought a smorgasbord of environmental concerns which require the monitoring of individual gas levels. [1–4]

Improvements in gas sensors have been driven by four requirements: gas selectivity, low-level detection of gas concentration, stability, and response times. The first types of industrial gas sensors were palladium wires, which burned the analyte gas and measured the resistance change due to the heat of combustion. Though a functional technique, this method did not give good selectivity for different gases.

Electrochemical sensors, which measure electopotential changes, have also been studied for gas sensing. These sensors operate as a target gas oxidizes or reduces on the surface of electrodes [5]. These sensors gave better selectivity due to the tunable reduction potentials of various analyte gases. Later, metal oxide sensors became the standard sensor for industrial processes [6]. This marked a return to measuring resistance but more selectively than palladium wires, to meet the needs of targeting a wide range of gases. Some sensors could measure SO_2, produced in sulfuric acid production, others could detect NH_3 in industrial fertilizer processes, a few were designed to interact with PH_3 from pesticides, and a selection of sensors check the levels of CO, NO, or NO_2 from combustion of fossil fuel, such as in automobiles [7].

1.1 Today's Needs

Today, government regulation drives the gas sensor industry [8]. Examples of the importance of low-level detection are the requirements dictated by Occupational Safety and Health Administration (OSHA) regulations. For example, OSHA requires that the short-term

exposure to PH_3 be at 0.3 ppm levels. This low level of exposure means that sensors used to detect PH_3 must be both accurate and have a fast response time for workers safety.

Along with health and environmental concerns, other industries and agencies also require gas sensing. In the manufacture of illegal methamphetamines, PH_3 is produced [9]. The ability to detect sources of the PH_3 emissions is of great use to law enforcement, as they search for illegal production sites. As an example of gas detection in the health sector, a rapid increase of NO in the breath of a patient is an early warning sign of an asthmatic attack. NO is produced by the body to fight inflammation, an increase in NO indicates that the lungs are inflamed. However NO also reacts with the O_2 present in the breath. This chemical reaction produces NO_2. Being able to detect increasing NO quickly and cheaply and subsequently NO_2 can help prevent these attacks [10].

1.1.1 Sensor Characteristics

Historically advances in gas sensor technology have been driven by sensitivity, selectivity, stability, and response time; however, as other applications developed more detailed characterizations became desirable. The important attributes for determining the value of a sensor are listed below [5]:

1. Sensitivity is the change detected in the concentration of the analyte gas that the sensor can measure above the noise. A gas sensor with higher sensitivity can detect smaller changes in the gas concentration. The smallest concentration the sensor can detect accurately is defined as the limit of detection. Having a low limit of detection provides two benefits: first it allows for more accurate measurements and earlier detection of leaks or spills. Secondly, to decrease false signals from the sensor, the sensitivity should be well below the triggering value of the gas analyte, increasing the signal to noise ratio [11].

2. Selectivity is the sensitivity of the sensor to one gas over another gas. Most gas sensors operate to target one individual gas, and false positives, where other gases falsely trigger the sensor, are undesirable in these sensors. Indeed, very often, sensors must pick out one specific analyte from a gas mixture. Being able to isolate the sensor

response to one specific analyte is very difficult to do, so detecting the specific analyte is often achieved by processing the signals from an array of distinct sensors operating simultaneously with different levels of sensitivity for the gases of interest. This must be followed by mathematically solving for the required signal.

3. Response Time is the time required for the sensor to interact with a gas from the time the gas comes in contact with the sensor. Faster response time will allow distinguish the sensor response from baseline drift. Where baseline drift is defined as changes to the baseline over half and hour or longer time periods. Also, for toxic or flammable gases, it is desirable to reduce the response time as much as possible. In many sensors detection time is dominated by the rate of diffusion and the speed at which the gas diffuses to the sensor is rate limiting. Thus, the response time is often diffusion limited. The bottleneck for the response rate is how fast the gas gets to the sensing surface. If the material length scales, i.e. size of pores, are bigger than the mean free path, the distance a gas molecule moves before it encounters another gas molecule, Fickian diffusion occurs. However, porous materials with small length scales constrict airflow, since the gas collides with the pore walls of the material not with itself, and slow, Knudsen gas diffusion into the material occurs. This increases the response time.

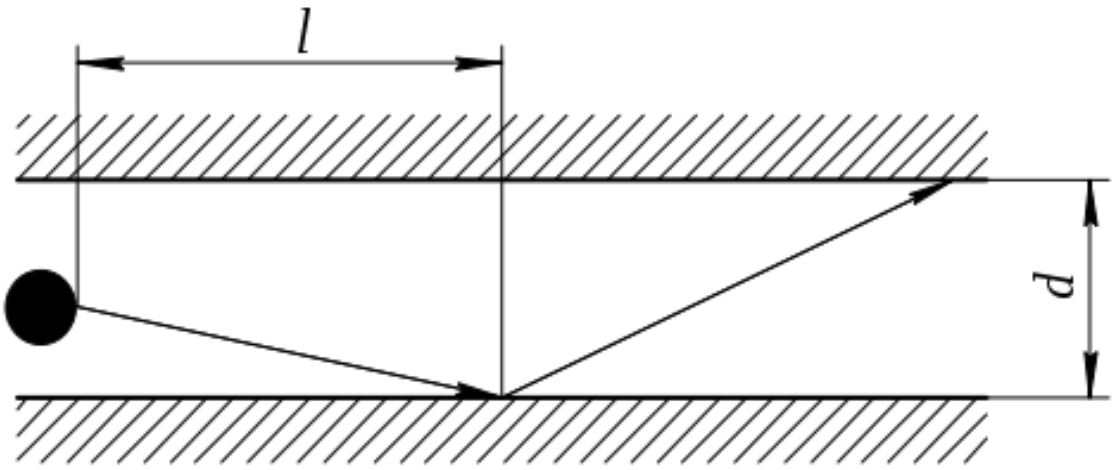

Figure 1.1: Picture of Knudsen diffusion. L is the mean path length of the gas and d is the diameter of the pore. Licensed under Creative Commons.

4. Recovery Time is the time after an exposure required for the sensor to return to within

90% of base line response. This characteristic is important when rapidly measuring the changing gases that might be encountered in a combustion environment. The recovery time depends on several factors. First how easily the gas desorbs off the surface. Second, how fast the gas diffuses out of the sensor area. Third, whether there is chemical bonding of the analyte gas to the sensor, which affects not just short term recovery time but also long term stability. This is because the chemical bonds formed are not reversible causing a long term degradation of the sensors

5. Long-term stability is a measure of a sensors measurement characteristics over time. Does the sensor quickly loose its sensitivity or does it remain fairly constant over long periods of operation? This metric is obviously harder to measure since it takes several months (or years) to test, however, it is very important for commercial applications [12].

6. Power consumption is the amount of power drawn by the sensor when in operation. This is especially important for remote sensing applications and handheld sensors. For extremely low-power consumption, renewable energy harvesters, making use of solar or thermal power to power the sensors, can be a valuable asset.

One last difficulty with the gas sensor that must be overcome is sensor poisoning. A problem emerges when instead of adsorbing reversibly onto the sensor surface a gas chemically bonds to the sensor surface or another deleterious gas attacks the surface . Chemical bonding poisons the active sites, thus slowly degrading the sensor and rendering it inactive [12].

Ruhland, et al., saw that SnO_2 sensors measuring NO_2, when heated to a high temperature (400 ^oC) experienced a poisoning effect. This poisoning effect was assumed to be caused when two NO_2 molecules interacted in close proximity to each other. At this high temperature, the NO_2 breaks down to $N_2O_4^{2-}$, which chemically bonds to the surface. The $N_2O_4^{2-}$ then reduces available bonding sites and decreases the majority charge carriers available to the SnO_2, thus reducing the sensor's conductivity and sensitivity [13].

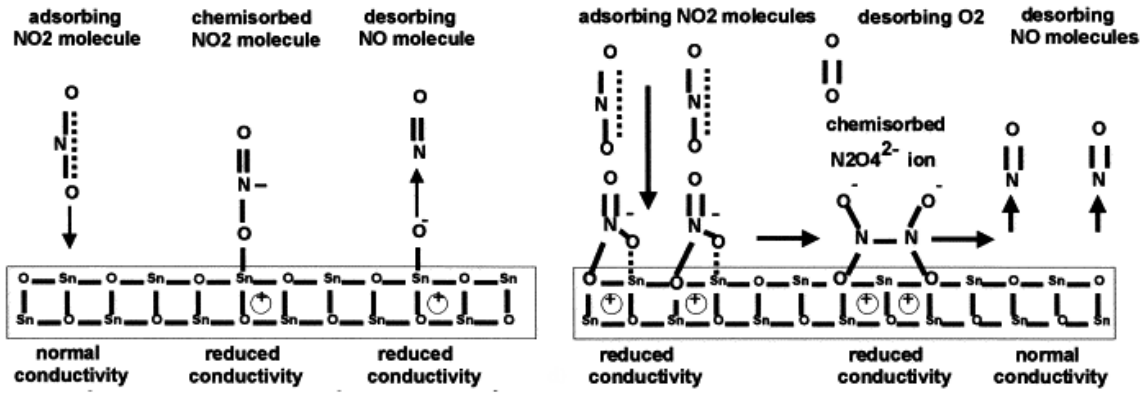

Figure 1.2: Methods of NO_2 poisoning on an SnO_2 surface at high temperature.

Yu, et al. [14] also found that their tin oxide nanobelts were being poisoned when detecting dimethylmethylphosphonate (DMMP), a nerve agent stimulant. The poisoning of the sensors was first thought to result from grain boundaries in the metal oxides; however, poisoning continued to occur in single-crystal nanobelts. The researchers determined that by creating a better electrical contact with the nanobelt, the poisoning stopped. It appears that the gas poisoning was actually a breakdown in the heterojunction between SnO_2 and the platinum contact to the nanobelt. This is important since the sensing material does not sense alone. The entire sensing system must be able to resist toxic analyte gases.

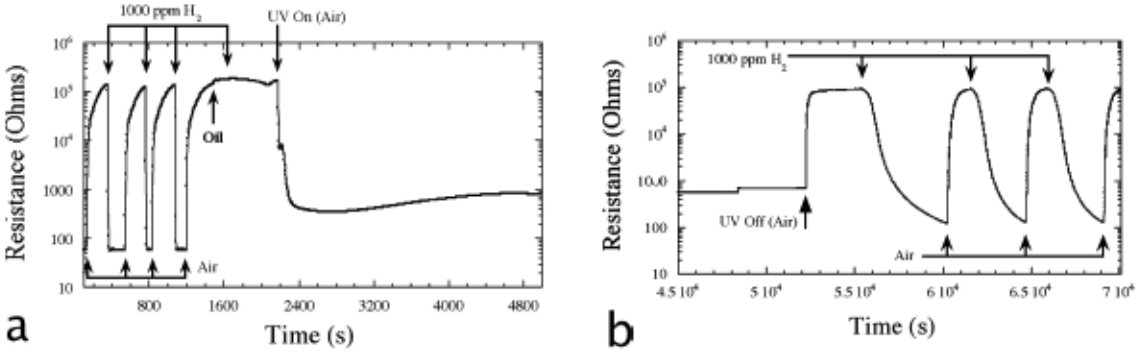

Figure 1.3: (a) A sensor running correctly to detect H_2 before oil contamination. Once oil was added no response to H_2 is observed. (b) After several hours of UV exposure the sensor has the same magnitude as the original response.

Mor et al. [15] suggested an interesting technique for reversing sensor poisoning. They created a hydrogen sensor out of a TiO_2 array, which had the ability to detect 1000

ppm of hydrogen. They then purposely covered the sensor with motor oil to simulate random air contaminants. The oil poisoned the sensor, degrading all response to the hydrogen. They then exposed the contaminated sensors to UV light. Since TiO_2 is photocatalytic, the TiO_2 then broke down the motor oil, allowing the sensors to return to their initial state before they were poisoned. The sensors require 10 h of UV exposure to return to the pre-poisoned state. This study suggests that TiO_2 nanoparticle photocatalysis could be used to clean a sensor of air contaminates. This is especially true since a normal sensor would not be rapidly exposed to so high a concentration of contaminants.

1.2 Gas Sensor Types

There is a wide variety of gas sensor types, including infrared spectroscopic, mass spectroscopic, mass sensitive, and solid state sensors. Spectroscopy measures the absorption levels of gas samples that absorb at various light frequencies. These systems have good selectivity; however, the limits of detection can be high, only 50,000 ppm for minor gas constituents due to the overlap of multiple gas spectral fingerprints. Mass spectroscopy is often used with infrared spectroscopy, this technique ionizes the gas and then determines the charge to mass ratio. This method is more used in stand-alone analysis due to the large size of spectrometers. Portable mass spectrometers are still suitcase sized, and to obtain good resolution a vacuum must be used to reduce noise, thus adding to weight requirements and operating expense. Mass sensitive devices such as cantilevers work by letting the analyte gas adsorb onto the surface of the sensor, resulting in an increase in the total mass [5]. The change is then measured via the mass or the resonance frequency shift of the sensing material. Solid state devices generally measure some electrical properties of the material and from that detect the gas. The most common type of solid state gas sensor available now is the metal oxide sensor. These sensors use the metal oxides of tungsten (WO_3), nickel (NiO), copper(Cu_xO), aluminum (Al_2O_3), titanium (TiO_2), or tin oxides (SnO_2). Zirconium is also used occasionally [16, 17]. The two methods that are cited in the literature for interface preparation usually use thin $<$ 1 micrometer films, though some examples use thick films doped with noble metals or various nanoshapes to effect grain boundaries [17–24]. These

metal oxides sensors are heated to specific high temperatures (that range from 100 up to 600 °C depending on the gas) during operation [17, 25–27].

1.2.1 Examples of Metal Oxides

In one study, a thin film of tungsten oxide was sputtered onto an aluminum substrate. This thin film sensor was then heated to between 100 to 250 °C. NO_2 introduced as the lone gas in nitrogen was then detected via changes in the films resistance allowing for detection down to the 100 ppb level at 150 °C.

Zirconia is mainly used as a solid electrolye in sensor applications. In a solid electrolyte material, the charge carriers are not electrons but are ions. This allows for zirconia to be used to detect O_2 levels in gases, which is especially useful in combustion applications involving automobile engines. Zirconia electrodes can also be paired with yttrium oxide to form a solid electrolyte sensor. In this sensor a membrane, that allows O_2^- ions to freely pass through, separates the zirconia and yttrium electrodes. As the ions rearrange due to the chemical potential the electrical potential also changes between the two electrolytes. This change in potential is measured and corresponds to gas concentrations [28]. By heating this sensor to 550-650 °C, the Yamazoe group was able to detect Cl_2 gas from 1-100 ppm. [29] In another study 50,000 ppm H_2 has also been detected in an N_2 background with a zirconium sensor held at 450 °C [30].

Nickel oxide films generally has a very rough shape providing significant surface area. At Ni vacancies on the surface, O atoms can react with the analyte gases causing an electron to jump into the NiO film. Some examples of NiO films include ultra thin NiO created by molecular beam epitaxy onto a silicon substrate, a time consuming process. The article shows that this technique allows for the reported sensing of H_2, NH_3, NO_2, SO_2, and CO, individually [31, 32]. For these sensors the film had to be heated to 300 °C for the detection of 100 ppm of these target gases via conductrimetrics. If NiO is heated to 450 °C, it can easily sense H_2, O_2, and CO_2 below 10,000 ppm concentration [31, 33].

The band structure of Cu_2O is often treated as a p-type semiconductor. The semiconductor has excellent conduction and junction properties allowing it to be used in diodes.

This results in the use of Cu_xO in conjunction with other metal oxides for sensing purposes [34]. A CuO nanoparticle on a sputtered thin film of SnO was found to decrease the response time to H_2S from 52 seconds down to 14. Chowdhuri, et al., theorized that the CuO had two purposes, first it acts as a catalyst for the reaction of CuO with H_2S allowing H_2 to be formed which easily reacts with the adsorbed O_2, and second it increases the surface area of the SnO_2 thus decreasing the response time [35]. One big advantage of this technique is that SnO_2/CuO mixtures can be screen-printed, decreasing costs. In another study ZnO heterojuctions of doped and undoped layers with CuO have been shown to detect CO and CO_2 [36, 37].

Porous anodic aluminum has good stability at room temperature for humidity sensing. Combining capacitance and resistance measurements, Naher, et al., were able to measure the range from 3% to 98% humidity [38]. H_2, O_2, and CO_2 detection to 90,000, 90,000, and 21,000 ppm respectively was reported by Seiyama, et al., using alumina thin films on silica at 450 ^oC [33].

Titanium oxide in addition to being a semiconductor also has photocatalytic properties and is used to create dye based solar cells. In the gas sensor realm Comini, et al., used TiO_2, produced by the sol gel technique, to detect 100 ppm of ethanol and methanol at 400 and 500 ^oC [39]. Titanium nanofiber networks (diameters between 200 to 500 nm) at 300 ^oC detected down to the 500 ppb level for NO_2 and could reach ppm levels of detection for CO, H_2, and CH_4, according to Kim, et al. [40]. Yates examined the chemisorption of NO to TiO_2 with UV light in a range of temperatures from 100 to 1500 ^oC [41]. Ferroni et al used nanosized TiO_2 films at 600 ^oC to detect NO to the 20 ppm level [42]. These thin films of TiO_2 have also detected 500 ppm of NH_3 when operating at 250 ^oC with small variances of temperature [43].

SnO_2 is one of the most common metal oxides studied for gas sensing purposes. It is stable and durable at high temperatures. SnO_2 has been used to measure H_2 at temperatures from 25 to 650 ^oC [31]. The only problem with this metal oxide is it's selectivity. Since tin oxide can be used to detect a wide range of gases at any given temperature, reconfiguring the response is important. In order to deal with this problem, creating various

shapes of the material has been tried. Single crystalline nanobelts of Sn have been found to detect CO, NO_2, and ethanol at 400 ^oC [39]. Nanowires have also had success in detecting CO in an oxygen background at 250 ^oC [44]. Other methods include doping with various metals like iron and nickel, these materials seem to decrease the SnO_2 grain size allowing for more interaction sites on the surface [22, 31, 45].

1.2.2 How Metal-Oxide Semiconductor Sensors Work.

The basic mechanism for metal oxide sensors was suggested in the 1960's. The metal oxides adsorb oxygen to their surface. Then the surface oxygen reacts with the analyte gas chemically, where the metal oxides catalyze a reaction causing the surface states to change. In order to facilitate the oxygen chemical reaction with the analyte gases the temperatures are raised to between 200 and 500 ^oC in order to ionize the oxygen atoms [1, 16, 46]. While O_2 is a reactive substance, in order chemically react with the analyte it must be broken down into O_2^-, O^-, or O^{2-} to facilitate an electrochemical reaction. These ionized reactants, when they adsorb onto the metal oxide surface, carry their charge with them. So when they react with the gas analytes, the charge is transferred away from the metal oxide and thus the reaction can be monitored. The temperatures determine whether it is molecular or atomic adsorption on the surface, defining what reactions will take place. Temperatures higher than 150 ^oC cause the O_2 molecules to break down into their atomic ions. In addition, the higher operational temperatures decrease the humidity fluctuations that affect the sensors reproducibility.

These chemical reactions affect the charge density and cause a band bending in the semiconductor. The oxygen by itself has a different Fermi level (E_f) then the metal oxides. In order to equilibrate the differing E_f's, the bands in the metal oxides bend to equilibrate with the oxygen. At higher temperatures, the O_2 molecules start to break down and form O^- on the surface. These molecules and atomic oxygen ions react with the various analyte gases [47]. If the gases are reducing (i.e. CO and NH_3), the reaction adds electrons into the surface of the metal oxide thus changing the resistance. If the gas instead oxidizes

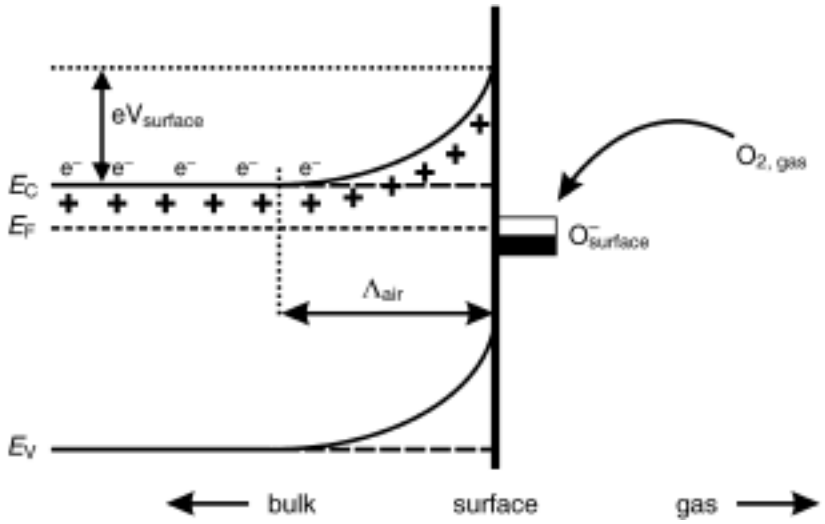

Figure 1.4: O_2 breaks down to O^- on the surface modifying the bands on the surface causing a depletion layer.

as does NO_2, then the reaction with the adsorbed oxygen removes electrons from the surface causing an opposite change in resistance. The response of the metal oxide depends on whether the majority charge carriers are holes or electrons. If the majority carriers are holes, then removing electrons increases conduction while adding electrons decreases the conduction. If the majority charge carriers are electrons, then adding more electrons increases the conductivity and decreasing the number of electrons lowers the conductivity.

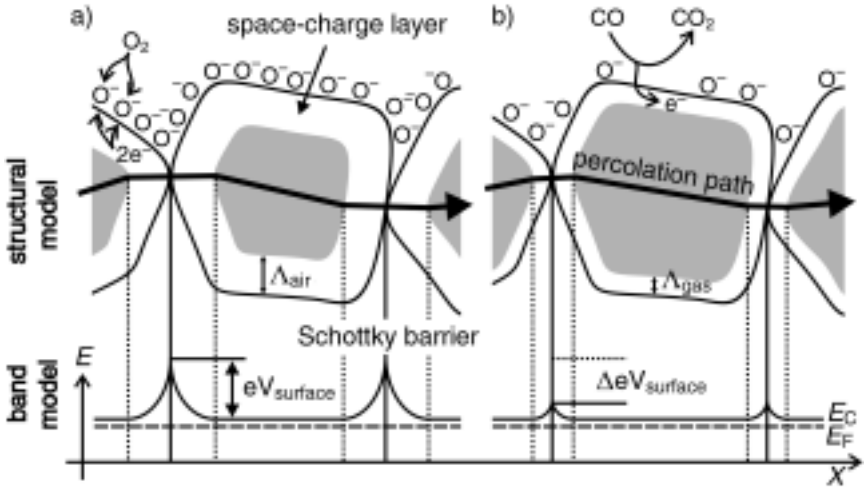

Figure 1.5: The left hand side shows the O- adsorbed on the surface of the metal creating the depletion layer on the oxides. The right side shows O- adsorbed on the sensor surface reacting with the analyte gases, in this case CO, modifying the surface and potential barrier across the sensor changing the resistance. Adapted from Reference [48]

1.3 Porous Silicon

The chemical etching of a silicon substrate creates porous silicon. There are a variety of methods to etch the silicon, the most common being metal assisted and electrochemical etches [49, 50]. Changing the parameters of the etching causes changes in the resulting physical characteristics of the resulting porous silicon. This allows for a large variety of possible pore sizes, depths, and densities. These are adjusted depending on the application desired.

Metal assisted etches are a recent development in porous silicon etching [49]. Small amounts of metal nanoparticles, normally from noble metals, are placed down on the silicon surface, and then the surface is exposed to a solution of oxidizers and HF. The metal oxides act as catalysis, and the silicon is etched underneath the metal. This promotes a very high aspect ratio for the etches; however, this comes at the expense of added materials and extra steps, versus other methods.

The most common and most studied method involves using electrochemical etches. In this method the silicon substrate is exposed to a chemical solution. An electrode is attached to the silicon, and another is placed in the chemical solution. Then an electric current is applied across the electrodes, which causes the silicon surface to roughen and eventually form pores via the removal of the silicon by electrochemical processes. Longer durations of etches generate a deeper pore structure. Higher current, to a point, creates a higher density of pores on the structure [50].

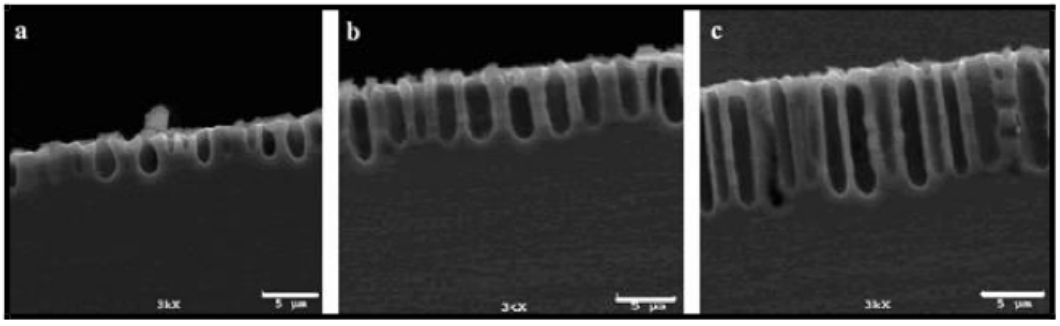

Figure 1.6: Etch depth as a function of etch times. The longer etches cause deeper pores. From Reference [51]

1.3.1 Applications of Porous Silicon

Porous silicon is used in several applications. Its large surface area makes it a good candidate for battery and ultra- capacitor electrodes, however there are problems as silicon does alloy with lithium. Porous silicon has been used to create high-current scalable batteries (it has a theoretical limit of 4140 mA h/g for lithium batteries, which is 11 times higher than the limit for graphite, the current anode in lithium batteries [52]. The use of porous silicon capacitors on a chip for power is a promising technology that is now being researched. Brunet and Kleimann found that they could reach capacitance levels of 700 nF/mm for their capacitor on a chip [53]. Porous silicon also has applications as a biomaterial. It is nontoxic and biodegradable [54–58]. The surface can be easily modified allowing for different growth rates that can be used to capture different cells. For the same reasons, it is also a good biosensor. Rossi, et al., used PS to measure plaque-forming units down to the 2 x 10^7 per mL by monitoring the change in fluorescence intensity of the PS [59].

Another property of PS is its photoluminescence. When nanoporous Si is illuminated by UV light, it releases energy in the viable light region. This effect has been studied for to use in optoelectronics [60], however the long lifetimes of the material limit the switching speed [61].

There are two theories on the origin of PS luminescence. The first theory is that porous silicon does not have the same band structure as normal silicon. The band structure of silicon is generally calculated by using single crystal bulk silicon without considering the surface. However due to the etching process the silicon becomes more amorphous with several different silicon crystals in each pore sidewall. This disorder creates previously impossible states for the electrons to occupy and removes other lower energy states which could release energy in the infrared [62, 63]. The main problem with this theory is that the spectrum of the PS should be thermally dependent, since the electron occupation depends on temperature, but the photoluminescense is not temperature dependent.

The second theory is that the luminescence results from a chemical phenomenon. Because the electrochemical etch breaks down the silicon through oxidation and fluoridation, the silicon can form oxide and oxyhydride and be in a different chemical state than the

original bulk silicon. It has been demonstrated that the etched silicon would be primarily a silicon oxyhydide hybrid polyatom surface coupled flourphore. Because of this the excitation would be more dependant on the functionalization of the surface. The functionalized silicon oxide groups rotate and vibrate, which allows energy states that accurately match the emitted electromagnetic radiation from PS. These emissions are not thermally dependent which agrees with experiment [64, 65].

1.3.2 Gole Research Group

The Gole group initially studied the effects of the chemical environment on the photoluminescence of porous silicon (PS) [66]. Various gases were found to interact with the PS surface and shift the emitted light frequency. Later in Gole's research conductometrics was found to be equally useful for measuring the response of the sensor interface to individual analytes [67]. As the Gole group had prior experience working with and creating metal oxide nanoparticles, specifically titanium and zirconium oxide [68,69], the research group thus experimented with decorating the porous silicon with these metal oxide particles and other electroless metal depositions such are gold, tin, nickel, and copper. Small amounts of metal oxides decorating the PS surface enhanced the response [70]. Substantially larger coatings degraded the sensitivity of the sensors. The correct depositions allowed the sensors to be tuned to a variety of individual gas responses enhancing the responses [71–77]. As an example tin oxide nanoparticles formed upon oxidation of electrolessly deposited tin allows for the room temperature detection of CO at much lower concentration levels than other PS systems [3, 78, 79].

Other groups have also experimented with using additives to the PS. PS has been used to detect NO_2, with Pd and SnO_2 treatments giving rise to 25s and 57s responses for NO_2 [80]. Rahimi, et al., have used a Pd coating on to porous poly silicon (PPS) and PS to detect hydrogen [81]. This Pd coating allows for a response to been seen with both the PPS and PS. This suggests the creation of a Schottky barrier which forces an induced dipole moment within the H_2 increasing a resistance change [82]. TiO_{2-x} has also been used for hydrogen detection by Arakelyan, et al. [83].

While electroless depositions are well studied as a method for adding metal oxides [84, 85], other methods include using an e-beam to deposit aluminum oxide [86]. An alternate method to make PS amenable to sensing is to sputter metal oxides onto the surface of the porous silicon. Tungsten oxide can be evaporated onto the porous silicon in a quartz tube heated to 100 ^{o}C. This forms an array of tungsten oxide nanorods with widths of 50 to 100 nm and lengths of around 20 micrometers. These nanorods then enhance the interaction of NO with the porous silicon. This allows the detection of 250 ppb of NO on the silicon surface at room temperature [87].

Though PS sensors doped with metal oxide particles offer the widest range of gas selectivity there are other options for using PS to detect gases. One method is the measurement of the capacitance of the PS, which has proved extremely useful for humidity measurements. The porous silicon used in these sensor studies had very small pore structures (on the order of 10 nm). Here, capillary effects are a very important consideration, leading to slower response times.

The hydrophobicity of the silicon surface is also an important consideration. It is more difficult for water to enter small silicon pores. The solution to this problem is to functionalize the silicon by oxidation or carbonization. This hydrophobicity also causes a strong hysteresis effect, While the water has a difficult time entering the pores, it has an equally difficult time exiting the pores causing the water to remain while the system is drying, lengthening the return to baseline [88–93].

Due to porous silicon's large surface area, optical measurements of the surface have also been used for sensing. Using an ellipsometer on the PS surface, it has been possible to measure acetone to the 49 ppm level [94]. However, an ellipsometer is not a practical tool for sensing, so alternative optical methods have been developed. A method, created by King, et al., was to remove the PS crystals, using an electropolishing technique, and then glue the crystals to the optical fiber with an epoxy. Using this technique they were easily able to measure down to the 100 ppm level [95]. Karacali, et al., refined this approach by simply attaching the light source directly to the wafer with epoxy. They have measured various different vapors repeatably with very small variations using this method although

at concentrations around 50,000ppm [96].

1.4 Basic Solid Gas Interactions

When a gas is adsorbed onto a solid, it either chemisorbs or physisorbs onto that solid. Chemisorbtion results when a gas reacts chemically with the surface, creating a strong ionic or covalent bond normally of the order .3 to 2 eV. However, there are chemisorption energies on the order of 10 eV. For example, oxygen chemisorbs strongly to copper with an energy of around 4 eV [97]. This type of adsorption is generally monolayered since the gas can only bond at the surface. This can be seen in the narrow valley of the chemisorption potential energy.

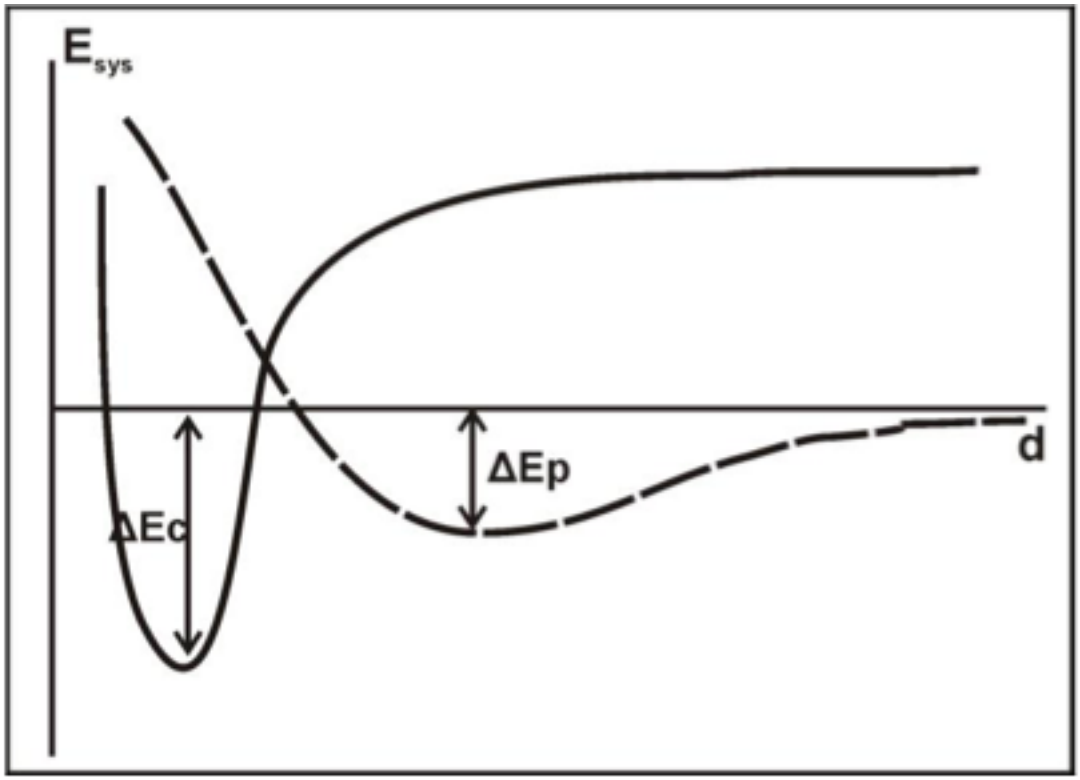

Figure 1.7: Potential shape of the chemisorption (solid line) and physisorption (dashed line). Note the broader but shallower potential well for the physisorption versus the chemisorption.

Physisorption generally has a much smaller interaction energy than chemisorption (on the order of 0.05 to 0.01 ev which is equivalent to roughly 500 to 100 kT) [98]. This interaction is due to van der Waals forces (dipole-dipole interactions). While the van der

Waals force attracts the gas to the solid the electrons of the gas begin to interact with the electron orbitals from the solid. Since electrons cannot occupy the same orbitals and there isn't enough energy to rearrange the surface, the gas is repulsed at short range. This leads to the shape of the physisorption potential, as seen in Figure 1.7. This wider potential energy well allows for a wider but weaker layer of adsorbed atoms then chemisorption [28, 99].

1.5 Gas-Semiconductor Interactions

1.5.1 Semiconductor Theory.

When an electrical potential is applied across a material, charges rearrange to minimize the potential inside the material. If the charges can move quickly through the material, then the material is classified as a conductor. If the electron mobility is very low, the material is classified as an insulator. If the electrical conductance of the material falls in-between these two extremes, the material is termed a semiconductor [100].

The conductance of the material is determined by the shape and position of the electronic band structure. These bands are a set of quantum states that electrons can occupy in the semiconductor. Since electrons have a half spin, they are defined as Fermions. Fermions cannot occupy the same quantum state, so the electrons fill up the available states two by two starting with the lowest energy levels until all the available electrons have been used. The highest energy level that the electrons reach at 0 K is called the Fermi energy. However thermal fluctuations at higher temperatures cause the electrons spread out more at the Fermi energy.

A similar concept is the Fermi level defined as the energy where the occupation of electrons is 50%, such that there is an equal chance of finding the state occupied as unoccupied. This definition is mathematically equivalent to the Fermi energy at 0 K and for simple band structures such as Figure 1.8, but this concept allows for the Fermi level, $E_{f,}$ to change with temperature in more complicated band diagrams. This concept is also called the total chemical potential.

It is often easier to look at the density of states of these electron bands. The more states available at an energy level the broader the density distribution of the band at that energy

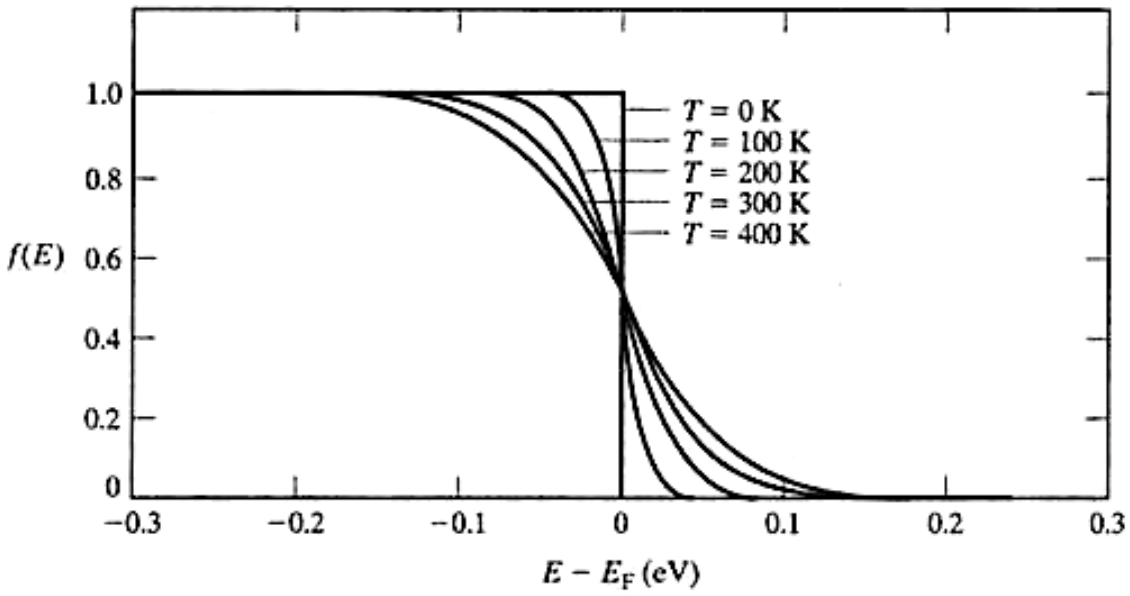

Figure 1.8: The Fermi distribution of electrons at various temperatures around E_f. for a metal. Notice the broadening of the distribution with increasing temperature.

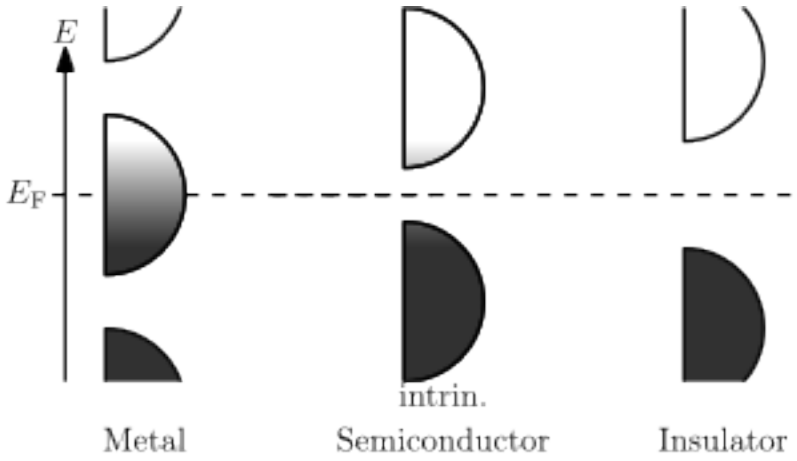

Figure 1.9: Density of states for various materials and their relation to the Fermi level. The metal has the Fermi level in a band of conduction states. The semiconductor has the Fermi level right in the middle of two bands with a small energy difference. The band with the lower energy is called the valence band and the higher energy band is called the conduction band. The insulator has the Fermi level in the middle of two well separated bands. Licensed under Creative Commons.

level. A material is a conductor when a conduction band is slightly filled with electrons, allowing space for the electrons to move up in energy and rearrange themselves easily. In other words, the E_f is located within the electron conduction band. If, on the other hand,

the band (valence band) is completely full and the next allowed band differs greatly in energy (on the order of 10 eV), the material is an insulator because the electrons do not have an easy way to surmount the energy gap and thus cannot rearrange the electrical charge. A semiconductor is a material where the valence band is full but the energy gap between the valence and conduction bands, (defined as the band gap), is small (on the order of 1.1 eV). In this case some electrons can be excited up to the conduction band, which then leaves holes in the previously filled valence band, allowing charge as holes to move in the valence band.

The conductivity is also determined by the electron mobility within the bands. Different bands have unique curves that describe the relationship between momentum space and energy space. The greater the curvature of these curves, the less energy is needed so as to add velocity to an electron. This effect is envisioned as changing the effective mass of the electron and it is manifest as if the mass of the electron has been changed. The effective mass and also the direction the electron moves can be increased or decreased and thus changed by the band structure. Since the bands are three-dimensional there can be a different effective mass for different directions. This makes the effective mass a tensor quanity. In practice the variations are minor so the tensor is simplified down to a single number. The formula for the effective mass tensor is

$$[M_{inert}^{-1}]_{ij} = \hbar^{-2} \frac{\partial^2 E}{\partial k_i \partial k_j} \tag{1.1}$$

where k is the wave vector and E is energy of the electron.

For the conduction band it is easy to describe the electrons moving in a fairly open band, but for the valence band with a large amount of electrons it is easier to look at the movement of empty states as the electrons rearrange. The empty states are called holes. For silicon the holes in the valence band have an average effective mass of 36% of a free electron. The effective mass of an electron in the conduction band of silicon is 26% that of a free electron. Since the electrons move faster than the holes in silicon, they have a higher mobility and can thus conduct more current, on average the electrons move more than three times faster than the holes in silicon.

1.5.2 Doping

If a semiconductor is in its pure elemental state it is called an intrinsic semiconductor. These semiconductors only have spontaneously-generated electron-hole pairs as the charge carriers (as seen in Figure 1.10). This depends on temperature as the conductivity increases with temperature; however, the number of charge carriers produced by thermo-fluctuations is very small and not conducive to significant conduction. In the intrinsic configuration, the Fermi energy is exactly in the middle of the band gap, $E_f=(E_v-E_c)/2$ where E_v is the highest energy of the valence band and E_c is the lowest energy of the conduction band.

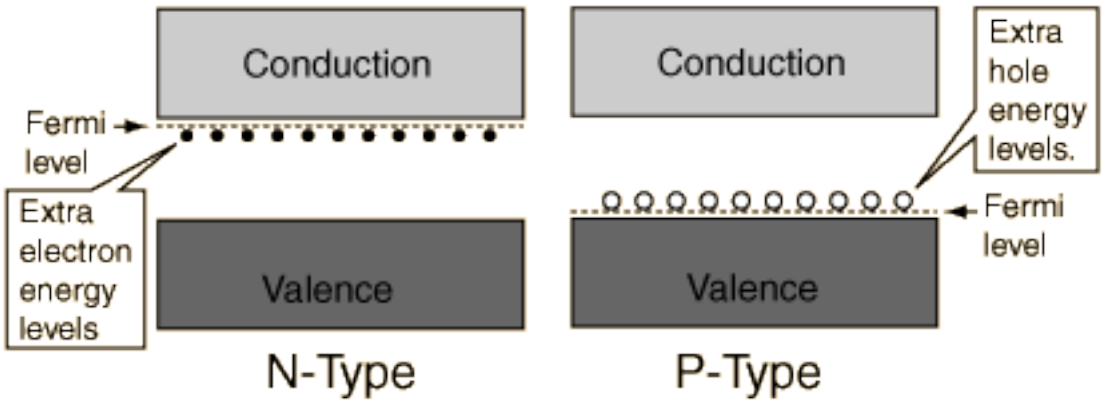

Figure 1.10: The left figure depicts the effect of n-type doping as a donor level is formed making available electrons to jump up to the conduction band. The right figure shows the effect of p-type doping as acceptor levels are formed, allowing holes to open up in the valence band.

Adding dopants to the semiconductor can increase the low conductivity in a semiconductor. Dopants are small trace amounts of a different material with a higher or lower valence than silicon that change the properties of this semiconductor. In semiconductors, dopants of higher valence can either add electrons to the conduction band by donating electrons from the donor levels or remove electrons from the valence band, creating holes which correspond to the charge carriers. Semiconductors thus modified are called extrinsic semiconductors. For silicon, boron is added to create holes and phosphorous/arsenic is added to donate additional electrons. These changes in the charge carrier density cause the Fermi level to shift at low temperatures (100 K). Adding electrons causes E_f to move closer to the conduction band; however as more electrons are excited up from the donor

levels to the conduction band, the electron distribution smears so that E_f decreases down to the intrinsic level. Similarly the acceptor atoms cause the E_f to start out near the valence band; however as the electrons jump up into the acceptor level and generate more holes, the distribution smears up towards the intrinsic level.

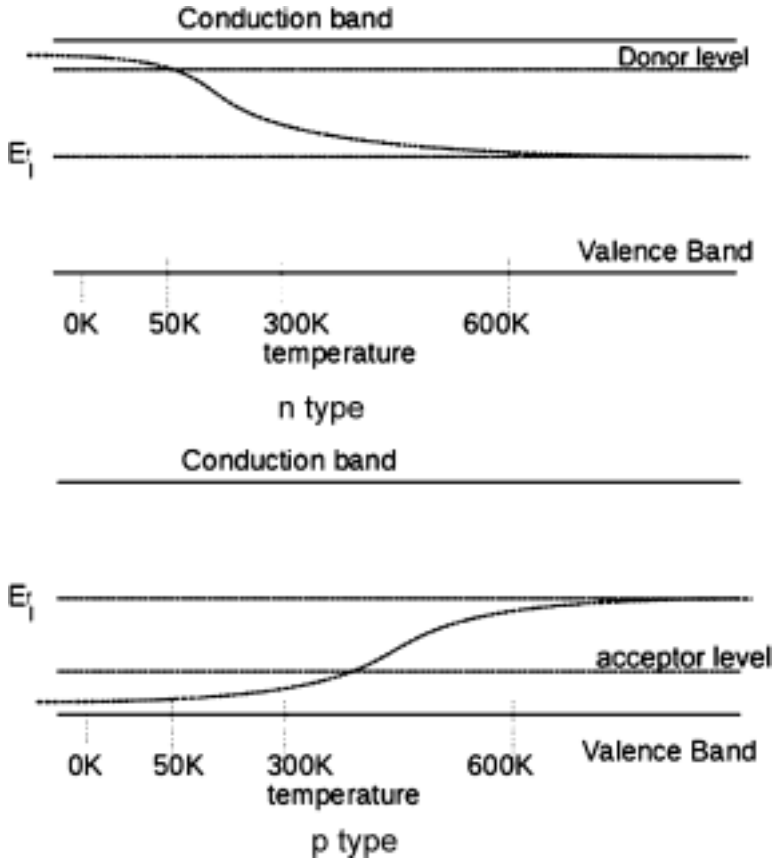

Figure 1.11: Effect of temperature with Fermi level for extrinsic semiconductors.

1.5.3 Band Bending

If any other material contacts a semiconductor, the E_f shifts so that the E_f of the two materials is equal [102, 103]. This charge shift causes band bending as the charges try to equalize the energy levels. This band bending causes a depletion layer to form in the semiconductor. The depth of the depletion layer is called the Debye length (L_d or D) [1]. The Debye length is dependent on the dielectric constant of the material, the temperature, the Boltzmann constant, the charge of the electron, and the charge density. The band bending has an important influence as it changes in conductivity. The potential barrier

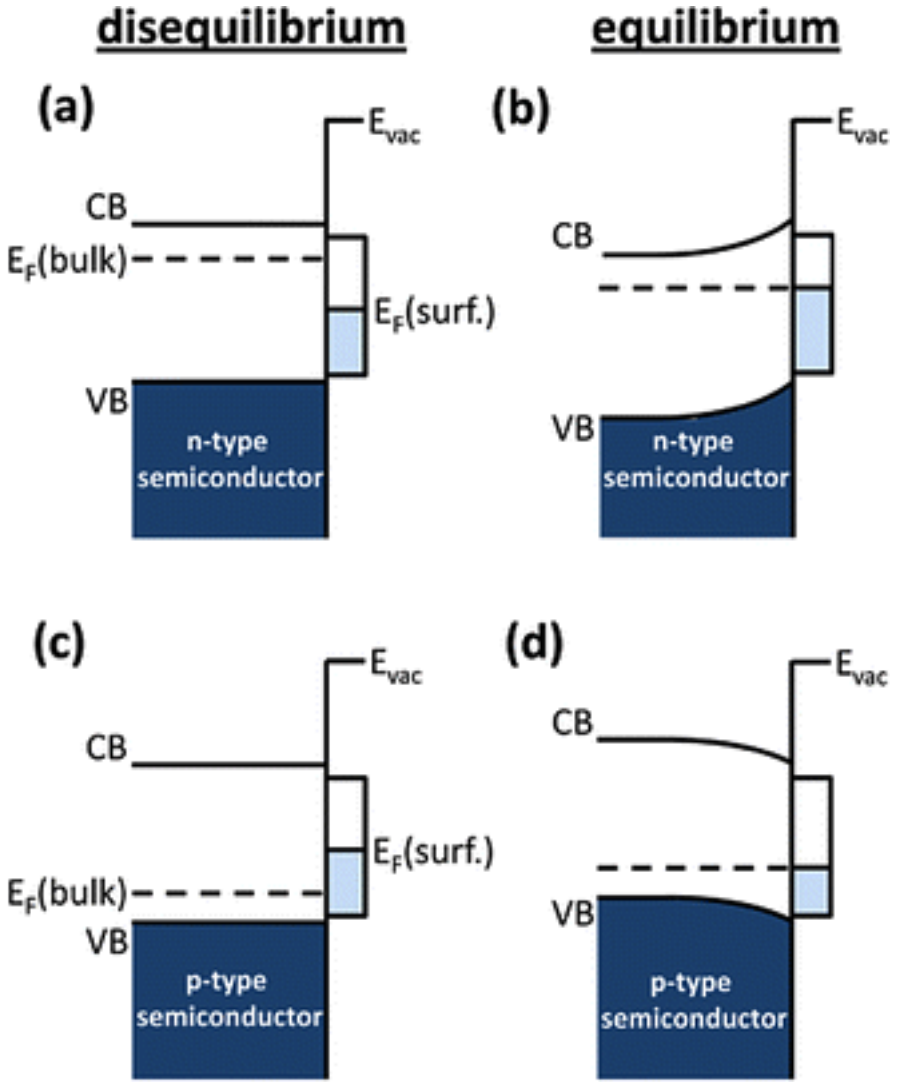

Figure 1.12: Examples of band bending for P and N-type semiconductors. The disequilibrium shows the bands and Fermi levels before the electrons rearrange to equalize the E_f in (a) and (c) and after, when the E_f is in equilibrium bending the bands in (b) and (d). Figure used from [101].

of the band junction is called V_s, and is related by an Arrhenius-type relationship to the conductivity of the material.

$$\sigma \propto e^{\frac{eV_s}{K_b T}} \tag{1.2}$$

Understanding gas semiconductor interactions is necessary to detecting gases using PS. When the analyte gas is adsorbed onto the surface of the semiconductor material, the change in the charge density in that region is due to an array of measurable properties of

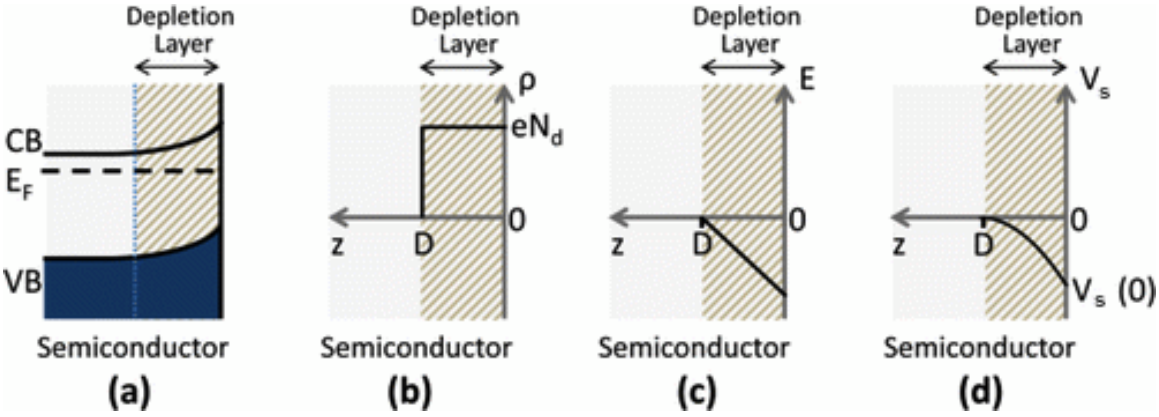

Figure 1.13: Band bending (a) shows the bands being bent, (b) shows the change in the charge density creating a depletion layer for a distance D, (c) shows the resulting electric field from the layer, and (d) shows the resulting voltage barrier V_s which affects the conduction. Adapted from reference [101]

the material such as conduction, capacitance, and light absorption. There is a limit to how much can be adsorbed onto a surface. Gas semiconductor interactions are best modeled by the Langmuir adsorption, which takes into account this asymptote [104, 105].

$$\Theta_a = \frac{K^a_{eq} P_A}{1 + K^a_{eq} P_A} \tag{1.3}$$

where P_A is the partial pressure of the analyte gas Θ_a is the coverage of the analyte gas and K^a is the adsorption constant of the gas with the surface. This relationship allows the gas to be more or less "sticky" with respect to the surface of the semiconductor.

1.6 Sensor Arrays

In the previous section an overview of sensors was given including metal oxide and semiconductor sensors. While there are numerous types of gas sensors, that can detect low levels of individual gases, the main problem is selectivity. In the previous discussion, the chemical/physical response between a sensor and a gas was described; however, most sensors do not distinguish between responses for various gases. The analytes will each interact with the sensor interface and, while each response might vary in magnitude, the signal cannot separate them. This difficulty is not as severe for the detection of a limited number of

analytes in high concentration using optical methods as the absorption spectrum is generally unique for each analyte gas. However for more solid state based materials, the sensor must be modified so it interacts with the anaylte gases differently, generally this is done by functionalizing the material or changing the temperature of the sensor allowing certain interactions to take place on the surface and discouraging other interactions [106].

One sensor is usually not selective enough to isolate the interaction of only one individual gas in a mixture of gases. In order to deal with the problem of selectivity, modified sensors are placed into an array. Here, each sensor has a variable response to each gas, and the signals from each sensor are to be cross-correlated to extract the make up of the anaylte gases. This allows for both higher selectivity and better sensitivity [107].

This method of slightly different materials being put together to construct a sensing array is used for a variety of different sensor types. Sensors that measure the resistances of polymer layers or a "thick" metal oxide films are common [104, 108], but these sensors generally have long response times due to slow diffusion through the film. Generally these are found in arrays of about twelve sensors. They are used to distinguish between different flavors in food such as beer and coffee. Another common example of a sensor array measures the current across an array of sixteen metal electrodes used to detect toxic vapors in cereal storage. Analysis using a MOSFET, made of various metals, generally requires a larger array than other sensor types (about twenty sensors); however, this number allows for a greater number of versatile measuring techniques and applications that include breath analysis or ammonia detection [104, 109].

1.6.1 Analysis

Analyzing sensor responses is difficult, but there are several different algorithms used in the multivariate analysis of responses. These algorithms are first divided into either statistically based algorithms or artificial neural networks. They are further sub-divided into those that use quantitative and those that use pattern analysis. Quantitative analysis is very useful for computing an exact number for the different gas concentrations. Meanwhile pattern analysis is useful to differentiate between various odors, for example for the detection

of various odors from food rotting in storage. For pattern analysis, the algorithms can be classified between unsupervised, supervised, and self-supervised. Supervised requires calibration measurements before starting the analysis [110]. Unsupervised pattern analysis simply classifies the odors into different groups [111]. Self supervised falls between those two extremes. There a small part of the data calibrated, for example the response to individual gases are labeled in the response but the more complicated response to multiple gases is not, forcing a computer to classify the response as best it can [112].

The most common statistical methods for multivariable analysis, due to their simplicity, are multiple linear regression(MLR) and partial least squares(PLS) [113, 114]. These methods assume that the response to all the gases is linear and that they are not interacting. These methods only work if the sensor response is linear, which is not always the case, especially at larger analyte concentrations. In order to deal with this problem, the sensor response can be linearized. One method of linearization is called transformation. In that method a nonlinear equation such as y=x/(1+x) is rewritten to a more linear form. In this case it would be 1/y=1/x+b which, with a change of variables becomes y*=x*+b. Only certain equations can be written this way, those that can be called intrinsically linear. As an example of a linear transformation, the resistance for a sensor can decrease as a response for certain gases. A decrease in resistance is the same as an increase in conduction. The conduction could be linearly increasing but since we are measuring resistance, which is the inverse of the response, the signal is nonlinear Dr=R/(1-C). While this equation is nonlinear we can rearrange the equation to Dc*R=1-C which is a linear equation, again thus allowing an MLR or PLS analysis to take place. [115]

If the function is not intrinsically linear, other methods can be used. One common method is to construct a nonlinear neural net [116]. Artificial neural nets are simply a set of nonlinear functions with variable weights on the functions. They also have feedback loops to the variable weights in order to adjust the response. This is especially useful for sensors that degrade over time.

One method useful in odor detection is Cluster analysis where responses are grouped together to reduce signal noise. One clustering method, the agglomeration method, looks at

the multivariable distance that each response is from all other closest neighbors [117, 118]. An alternate method, the divisive method begins the analysis by grouping all responses together and separating them out gradually into smaller groups [118, 119].

Principal component analysis (PCA) assumes that there will be a linear set of orthogonal relations between the sensor response and the gas mixture with various degrees of variance. In more practical terms one suggests that each response to a gas has a set amount of variation that can be isolated into a single axis. As an example, suppose we have an array of sensors A through E with a response A,B,C,D,E. The response to NH_3 in a sensor array ideally has a measurement 1,1,3,4,5 per ppm and NO has a response of 5,6,3,2,1.5 per ppm. However, the actual measured values will have a variance to them. The response from each individual sensor can vary independently by some amount. PCA simply takes a look at a large collection of the data and says, though taking the eigenvectors of covalent matrixes, this data has major trends in these directions (in multivariable space) a.k.a. the NH_3 in the 1,1,3,4,5 direction. Then since this trend in the data is a principle component, we fit the data along this direction, so everything moving in the 1,1,3,4,5 direction is considered a response to NH_3 in this example. This model handles the real fluctuations in the data very well, because PCA will group multiple sensors having similar responses together in thus reducing noise and increasing redundancy [120].

1.7 Doping Sensor Material

To create different elements in a sensor array, the sensing surfaces must be modified. When modifying the sensor, while still leaving the sensing mechanism intact, care must be taken. Very often this is accomplished by doping the sensing material with additives. For example tin oxide is often doped with other metals to enhance its sensing properties. When measuring CO levels, it can be doped with palladium, which increases the sensitivity five fold. With platinum the sensitivity increases to 4 to 10 times that of tin oxide [121]. Nickel has been added to tin oxide sensors to increase the sensitivity to liquefied petroleum gas by a factor of four [45]. The two major problems with these techniques, is that they either require a very high temperature to achieve modification of the metal oxides, (around 1400

°C) or they require expensive additives, such as palladium.

Another method of functionalizing the metal oxide is to add nitrogen or nitridate the oxide creating an oxynitride. Asahi, et al., increased interest in this method with their publication on visible light excited photocatalysis using $TiO_{2-x}N_x$. Doping with nitrogen lowers the band gap of the titanium oxide moving the adsorption range into the visible wavelength spectral region. Asahi sputtered N_2 onto TiO_2 and then annealed the material in an N_2 gas for 4 h at 550 °C. In another study Diwald used ion implantation to create a nitrogen doped TiO_2. [122] These authors sputtered N_2^+ ions mixed with Ar^+ into the TiO_2. The ion implantation is then annealed for 3-5 h at 900 K. This allows for a stable oxynitride to be formed [123].

One further example of nitridation passes NH_3 across the metal oxide. Irie managed to add nitrogen to titanium oxide by baking the TiO_2 in NH_3 at 500 to 600 °C for 3 h. However, this method did not lead to substantial doping and resulted in less than 1% conversion to $TiO_{2-x}N_x$ [124].

Sol-gel techniques are another method of generating nitrogen doped TiO_2. In the sol-gel method, the nanoparticles are created in a solution that is then allowed to gel into a solid. This method creates a very porous structure compared with alternate TiO_2 materials such as DeGussa P25. With the oxide formed and dispersed in solution, it is much easier to add dopants. Additives to the solution can thus change the chemistry of the resulting porous material much more easily [125].

Gole, et al., showed that treating a solution containing porous sol-gel generated TiO_2 nanoparticles allowed them to be easily modified into the oxynitrides. The resulting material was then washed, spun, and dried under vacuum. The material was subsequently baked at 200 °C for 45 to 60 min to remove any organic residue on the TiO_2. This method allowed for a more heavily doped material in the range of 1 to 20%. The resulting particles had a yellow tint and yielded excellent adsorption properties [126].

1.7.1 Sulfur Doping

While nitrogen doping is popular, other additives have been tried. Sulfur is another common additive. Tang and Li took TiO_2 nanotubes and put them into an oven heated to 380 °C for 12 h. Into this oven, a small amount of H_2S was flowed over the material. The resulting sulfur doped material had an increase in adsorption at longer wave lengths. This adsorption allowed for higher photocurrents thru the TiO_2. This effect is theorized to result from the band gap narrowing due to the mixing of the sulfur orbitals with the TiO_2 bands [127].

Sulfur can also be added to TiO_2 formed by sol gel methods. Yu, et al., added thiourea to P123 TiO_2 solution in order to dope it with sulfur. The solution were dried at 100 °C and then heated to 500 °C to remove a copolymer template. The resulting sulfur doped material adsorbs more in the visible range and displays antibacterial photocatalysis [128].

Another method for using sulfur with metal oxides, that the Gole group has developed, is using basic diethylsulfide (Et_2S), and acidic ethane and butane thiols (EtSH, BuSH)) to functionalize the surface of the metal oxide. The sulfur groups of S-$(CH_x)_y$ and S-H-$(CH_x)_y$modify the metal oxide and change it's Lewis acidity. The diethylsulfide decreases the Lewis acidity and the thiols increase the Lewis acidity. [129] The method of in-situ modification will describe in greater detail later in the thesis.

While the majority of the literature is on TiO_2 doping other metal oxides have been doped. For example, Bae, Seo, and Park created zinc oxide nanowires in a tube furnace. They heated zinc to 500 °C as Ar was flowed over the zinc for 2 h at 500 sccm. The zinc formed nanotube arrays on an Au particle substrate. In order to dope the zinc, sulfur was added to the tubes. This sulfur on the surface of the tubes was then modified as the photoluminescence from the wires increased the lower energy light emissions [130].

CHAPTER II

EXPERIMENTAL METHODS

2.1 Silicon Etch Theory

Silicon wafers are a cheap monocrystal material normally used for the creation of integrated circuits. Silicon crystals are grown using the Czochralski (CZ) process. These crystals are then diced into silicon wafers with various orientations, like (100) and (111). However for these experiments we used only (100) wafers.

Since these wafers are polished smooth, using the chemical mechanical polishing (CMP), for ease of fabrication, they do not have the surface area of a porous material in order to sense analyte material. In order to create a porous material some of the silicon in the wafer must be removed. This removal is called etching.

Because of this fact, the etching bulk silicon to create a porous silicon (PS) layer is the critical step for creating the gas sensors used in these experiments. An improper etch can ruin the sensor's response to the point of quenching it completely, so carefully understanding and controlling the etch process is crucial.

Porous silicon etches has three defining characteristics pore density, pore diameter, and pore depth. These characteristics are controlled by the etch technique and the doping levels of the bulk silicon wafer used to prepare the PS interface.

There are several methods to create PS. PS can be created via electroless etching, however, the PS created by this method, has the problem of being isotropic in all directions. Since the etch goes in all directions, the maximum depth of the pores is very small, on the order of 1-2 micrometers. Metal assisted etching is also popular. It results in an anisotropic etch and can easily give high pore width to depth ratios, however, the down side to metal assisted etching is the increased expense in time and materials [131].

Basic electrochemical etches offer a nice trade-off between the expense of metal assisted and the ease of electroless etches. These electrochemical wet etches are also the only style

that gives hybrid PS structure. Hybrid PS consists of micron sized pores with nanopores inside the surface of the micropores. The increased surface area of hybrid PS creates more reaction sites for an incoming analyte gas, enhancing the PS response to these analyte gases. Because of the need for hybrid etches, electrochemical etches are the only method used in this thesis to create PS.

In an electrochemical etch the main parameters are current density, etch time, and composition of the etch solution. Pore depth is generally controlled via the etch time while pore diameter and density is controlled by the current density and etch solution.

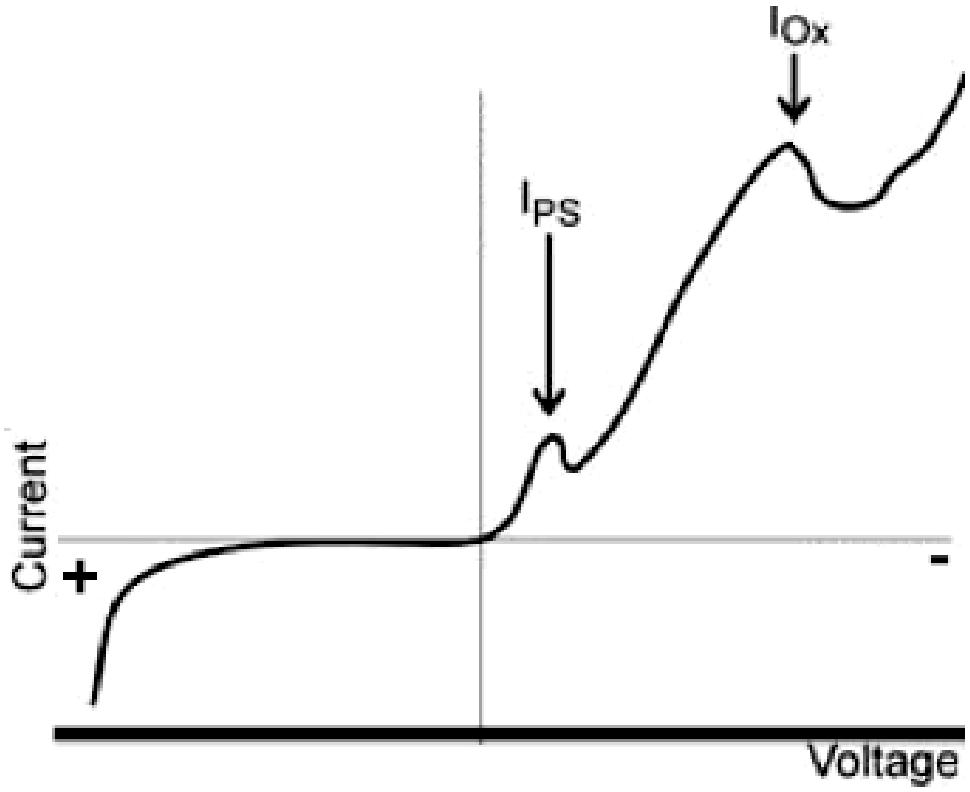

Figure 2.1: This is an IV sweep curve of a electrochemical etch. The voltage changes 0.25v per second and the current is measured. Current peaks in the curve correspond to electrochemical reactions, since these reactions require a charge transfer. The IPS corresponds to the current needed to etch porous silicon. I_{Ox} is the electropolishing current. Current is used to monitor and control the system as opposed to the voltage, since it is easier to measure the current at the surface of the wafer than the voltage.

The etch current helps control the pore size, which can be seen in the IV curve. A sample curve is shown in Figure 2.1. Peaks in the IV curve correspond to oxidation of the porous silicon. The lower voltage peak corresponds to the creation of PS, where small

amounts of the silicon are removed creating the pores. The higher voltage peak corresponds to electropolishing of the silicon wafer. Electropolishing is when the whole wafer is dissolved, smoothing out its surface.

While some PS etches use KOH to etch the silicon, the majority of PS etches use HF acid. The model proposed by Lehmann and Gosele to describes the silicon HF etching reaction is widely accepted in the community [132]. This model assumes that the silicon initially forms Si-H bonds on the surface. Si-F bond are created when a free F atom from HF interacts with a hole on the Si-H interface. This new bond polarizes the silicon atom weakening the Si-Si bonds. The F continues to replace the H till the silicon atom is attached only to F allowing the silicon atom to leave the bulk. This process can be seen in Figure 2.2. This is a simple model since other more complicated molecules can form on the surface; however, this model does highlight the importance of holes and current in etching silicon. Adding an oxidant doubles the current as the etch rate increases. [133, 134]

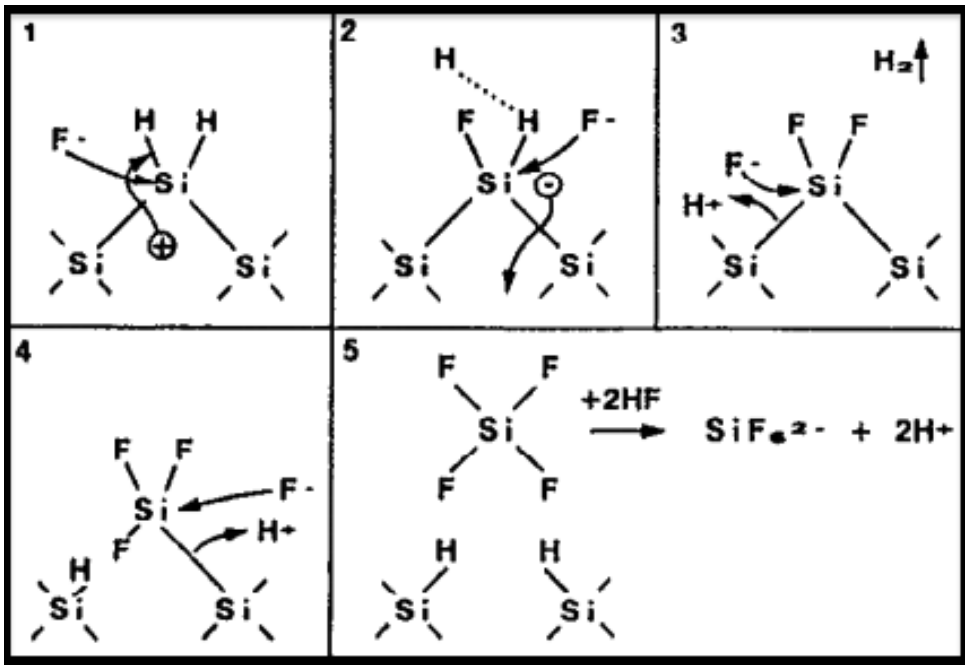

Figure 2.2: Steps taking in the etching of the silicon by the HF system. The holes allow the F to replace one of the surface H then this weakens the Si bond allowing for another F to replace the H. With those molecules attached the final two bonds to silicon go easily. This leaves a SiF_4 molecule away from the bulk. Adapted from [132]

The basic mechanisms for formation of porous silicon are as follows. The etch solution

begin to etch away the surface of a bulk silicon wafer. Initially a roughing of the silicon wafer surface happens where the electrical field effects is not prominent so the vertical (R_v) and the horizontal (R_h) etch rate are the same. Later in the etch the pores begin to form, the tip of the pore produces an easier hole injection allowing an anisotropical etch into the bulk material, so that R_v is much greater than R_h. This mechanisms are seen in Figure 2.3.

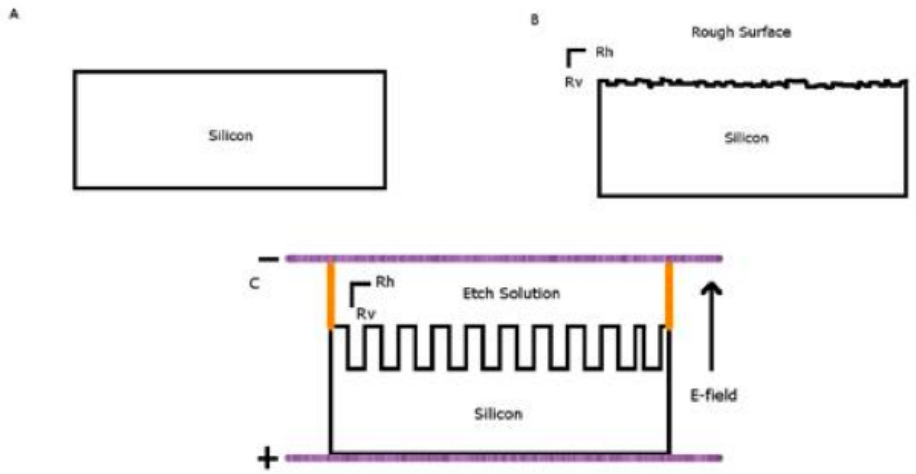

Figure 2.3: A) The flat prepared bulk silicon wafer before etching. B) The initial etching of the silicon were R_h is equal to the R_v. C) The etch, with the electric field in place, creating the anisotropic etch where R_h is much less than R_v.

2.1.1 Silicon Doping

While the silicon etch conditions are very important, the single most important variable is the dopant type and level of the wafer to be etched. There are two major types of wafers P-type and *n*-type. P-type wafers are doped with boron, a type III material, to remove electrons from the valence band thus generating holes. These holes are the majority charge carries and are positive, so the material is called P-type for positive. *n*-type wafers are doped with arsenic or phosphorus. These are type V material and add electrons to the conduction band. Since the majority carries are electrons with negative charge, they are labeled *n*-type for negative.

The various dopant atoms can be added in the CZ method and the amount added changes the resistance values. Since measuring the resistance is very easy vs. taking the dopant levels, all wafers are referred to their resistance value, in ohm cm. This resistance

value is measured using a 4-point probe.

Because the resistance can range from 0.001 ohm cm to 1000 ohm cm., the literature separates out the very heavily doped wafers as +. P+ and N+ type wafers are very heavily doped in the 0.01 to 0.001 ohm cm range.

2.1.2 P+ Etching

The etching PS depends on holes in the valence band to start the removal of silicon from the wafer. P+ wafers have a very high (1e18 to 1e19 dopant atoms per cm^3) number of accepter atoms, creating a large number of holes in the valence band. In theory a P+ silicon wafer, with an extremely high number of holes, would be easy to etch. However, the problem with the high number of dopants is that there are too many starting positions. Thus the PS etches but without enough initial anisotropy to create the nano or micro porous structures needed for the PS structures. As a result there is a limit to the dopant density which one can effectively use to produce etched PS. S. Lust and C. Levy Clement found that wafers with resistances of 0.1 to 0.2 ohm-cm (2e18 dopants per cm^3) {100} is the highest dopant level possible to get nanoporous silicon. 2-3 ohm-cm (1e16 dopants per cm^3) {100} resistivity were found to be the highest dopant level commenurate with the formation of nanopore coated microporous silicon [135]. We used 1-3 ohm-cm {100} wafers from Siltronic for our experiments, to fall with in this range.

In order to put the etch solution in contact with the P+ silicon wafer and to create a uniform current distribution, an etch cell is employed. The etch cell is made of high-density polyethylene (HDPE), chosen to make the cell because it is chemically inert. A platinum cathode is affixed to the wall closest to the wafer, as seen in Figure 2.5, to give a consistent current density across multiple etch sites on the wafer. A Viton gasket is placed on the polished surface of the wafer to surround the etch area. This allows the wafer some give as it is clamped onto the etch cell, insuring that the wafer does not crack. The gasket also creates a watertight seal maintaining the solution in the etch cell.

On the back of the wafer a steel disk wrapped in aluminum foil is added for two reasons. The first is to spread the pressure of the clamping across the wafer and the other is to make

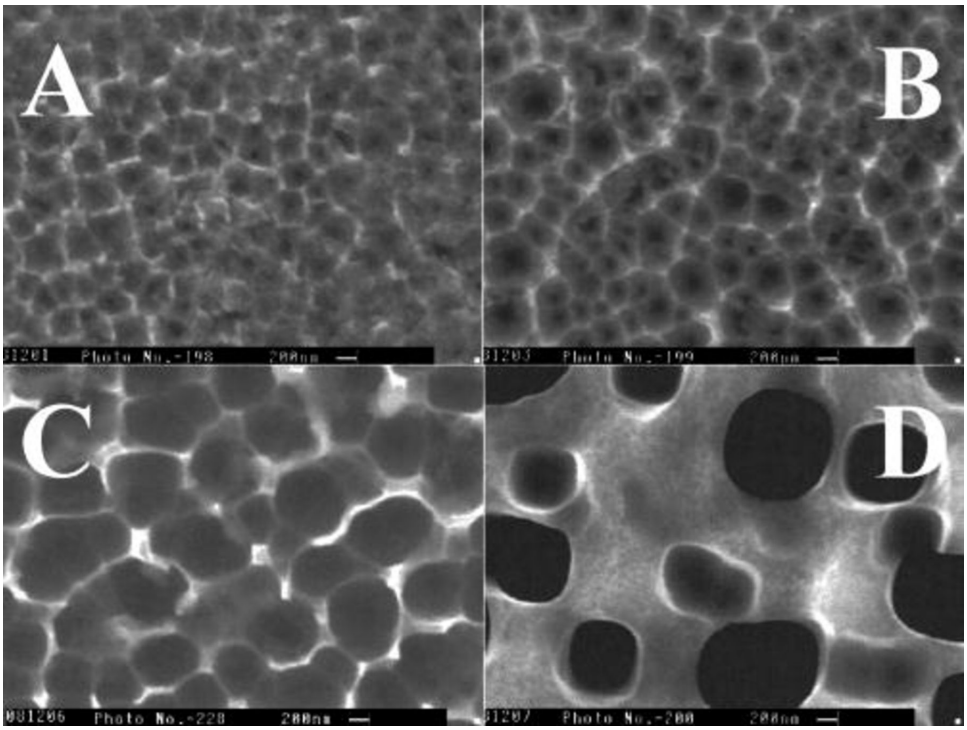

Figure 2.4: SEMs of the plane-view of p-type silicon with various resistivities, anodized in 4 M HF/DMSO (i=10 mA/cm^2, t=10min), without KOH treatment: (A) 0.1-0.2, (B) 1.2-2, (C) 2-3, and (D) 10-15 Ω cm. From reference [135]

a homogenous cathode electrode. The cell, gasket, wafer, and steel plate are then clamped together (with a C clamp) to form a watertight seal. The etch solution can then be added. Care should be taken to not over tighten the clamp and crack the wafer.

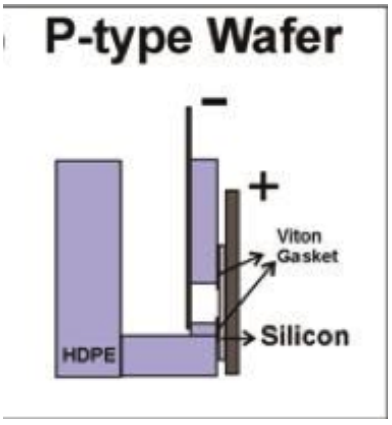

Figure 2.5: Diagram of the *p*-type etch cell. The platinum electrode epoxied to the cell insuring that the etches are easily reproducible.

Using DMF as the solvent and adding 4 M HF and 4.8 M H_2O (required because the HF

corresponds to a 50% by weight solution) creates the proper etch solution, The solutions are mixed in a plastic beaker. Then the solution is carefully pored into the etch cell. A Lab View program is used to control the power supply which provides the voltage to the etch cell. The etch current is then set at 10 mA/cm^2 for 10 min to create a PS layer. The average pore diameter of the resulting PS is 0. 7 micrometers with an average of 3 pores per micrometer^2. This creates a high fill volume.

In order to remove the nanoporous silicon top layer, the wafer was soaked in a 0.1 M KOH solution until this solution stops bubbling. The exact process of removal was not determined by Clement and Lust, nor why it only removed the top layer of nanoporous silicon and does not go deeper. A literature review has not enhanced our knowledge on this phenomena, but the removal of the nanoporous top layer is important for a smooth diffusion of the gas into the PS.

2.1.3 P Etching

P type etching is initially very similar to P+ etching. The same etch cell is used with the same setup. Because P-type silicon has a lower dopant density than P+, the etching method is different. The wafers used have resistances of 7-13 ohm-cm. They are boron doped (100) silicon wafers from Siltronix.

The etch solution consists of 1M HF, and 0.1 M tetrabutylammonium perchlorate (TBAP) in acetonitrile (MeCN). All chemicals are mixed in a plastic beaker then the solution is transferred to the etch cell. The etch current is controlled to 3-6 mA/cm^2. The etch time is 45 min. After etching, the wafer is washed with methanol to remove any residue solution. The methanol is removed via air-drying. The etch creates PS with a porosity of 50-80% with the μ pore diameters varying from 0.8 to 1.5 μ m and pore depths varying from 10 to 30 μ m. [51]

2.1.4 N Etch

Etching n-type silicon is different from p-type because of the lack of extrinsic holes in the semiconductor. In order to generate holes for the chemical reaction, a UV light source is used. The UV light generates an electron hole pair in the silicon. The hole travels to the

surface and starts the reaction, thus enabling the n-type silicon to etch.

There are two methods of illuminating the silicon, the first is known as backside illumination. In this method UV light illuminates the back of the wafer while it is being etched. The generated holes from the UV light migrate up to the etch surface and these holes start the chemical reaction which removes the silicon. The other method of illumination is topside illumination. As the name implies, the UV light goes through the etch solution and illuminates the topside of the silicon wafer to generating the necessary holes [136].

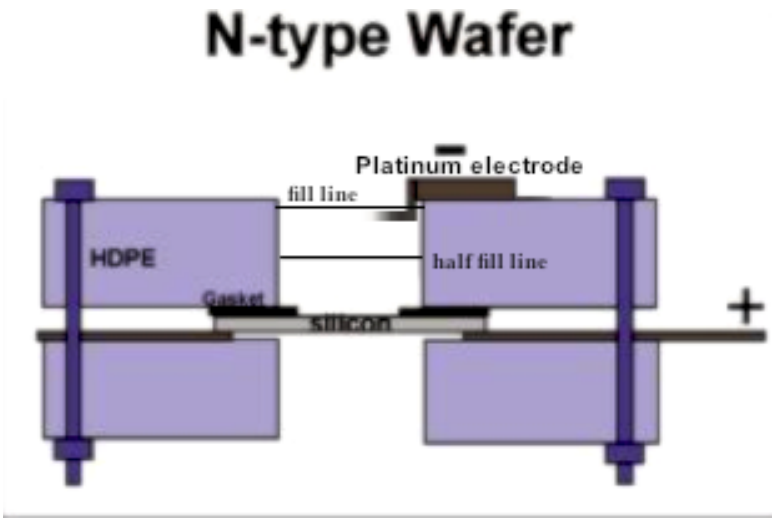

Figure 2.6: Close up side view of the etch cell showing the location of the platinum electrode and the attachment of the screws. The half fill line roughly corresponds to the level when the ethanol is added and the fill line shows the solution level after the HF is added, such that the platinum electrode just touches the solution.

The etch used in the experiments are all carried out using topside illumination. In order for the light to reach the wafer a different etch cell was created. The etch cell was set up in the form of a well. The wafer is put on to the top of a steel plate smooth side up. Then a gasket is placed on the wafer and the HDPE cell is place on top of the gasket. Then four bolts are place through holes in the corners of the HDPE cell and plate and carefully tightened to hold the wafer in place. The bottom HDPE piece was simply used to add depth to the metal screws so the threads. The platinum electrode is placed on the side of the well just touching the solution so the flat end is 2 cm down from the lip.

Into the cell, we place a solution of 7ml of ethanol and 7 ml of 50% by weight HF. The literature suggests modifying the solution to 6 ml of ethanol 7 ml of HF and 1 ml Hydrogen

peroxide. However, there has not been a noticeable difference in the resultant etch between these two solutions. The ethanol is added first in order to check for leaks in the gasket. After a minute and if the solution level has not dropped the HF solution is added. The solution should be almost to the top of HDPE.

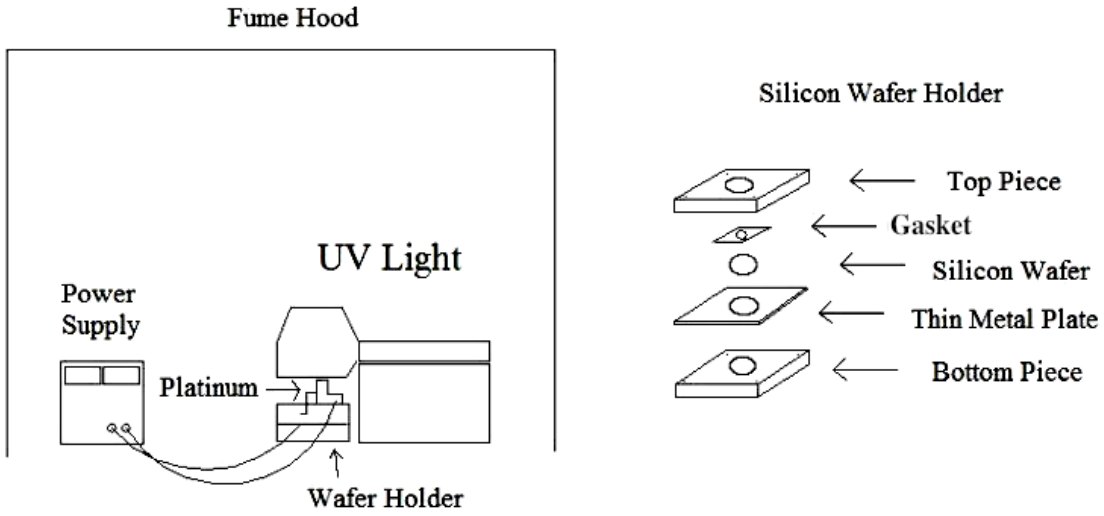

Figure 2.7: Diagram (left side) showing how an n-type silicon wafer is exposed to UV light. The right side of the figureshows how the etch cell was assembled.

A Blak-Ray light 365nm UV lamp is turned on and positioned over the hole so that the highest intensity of UV light is exactly over the hole. The lamp is propped up in order for the light to shine straight down onto the wafer. Normally, the light is turned on before the cell is assembled in order to give the light source sufficient time to warm up and reach steady state operation.

Once the UV light illuminates the wafer, the etch starts. The current is run at 10 mA/cm^2 for 10 min with the negative (black) current hooked up to the platinum and the positive (red) current attached to the metal plate, which is in contact with the wafer.

After the etch is finished the solution is pipetted away into a waste container before the cell is disassembled. The wafer is placed into a dilute (1:20) HF solution of methanol. The HF solution dissolves away the SiO_2 that forms on the wafer once the PS is exposed to the air. Since SiO_2 is an insulator having a layer between the conducting PS and the conducting gold layer would at best increase the resistance of the sensor. At worse SiO_2

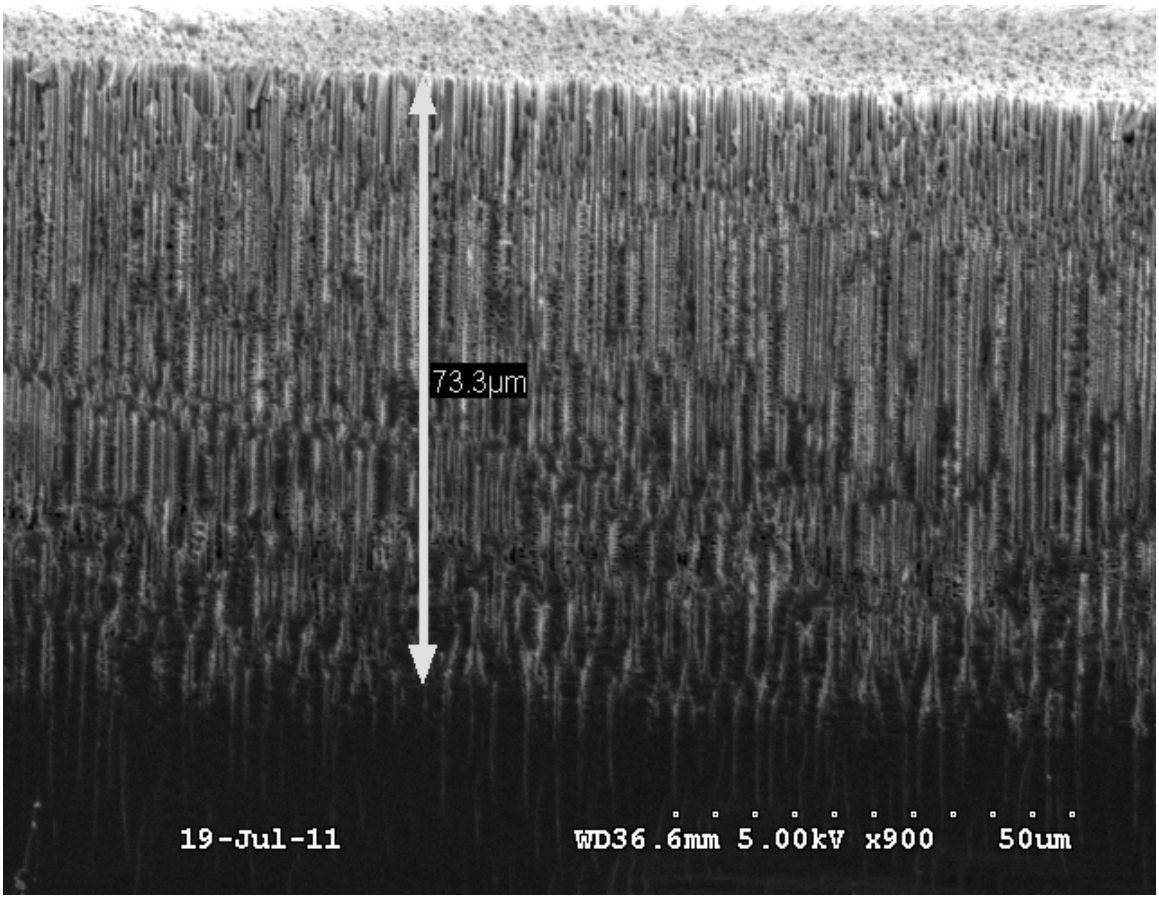

Figure 2.8: Side view of the n-type etch. Notice the depth of the pores. [137]

would completely halt current flow. The resulting etched pores are 0.5-0.7 um in diameter and 50-75 um in depth as seen in Figures 2.8 and 2.9 [137].

2.2 Sensor Creation

In order to make sure the etched silicon is usable and functional, smaller discrete etch areas were used. These smaller areas allow for smaller sensors. Smaller sensors are useful for integration onto a chip. Also smaller sensors allow for more sensors per wafer. In order to create these smaller areas, a protective mask has to be put down onto the wafer. This mask separates the etch areas protecting some of the silicon from being etched. The material for the mask to produce the required regions had to meet the following criteria. First, it must be a good insulator. When etching, the current must flow only to the areas to be etched. With no current flowing in the regions of the protective mask, the selected areas

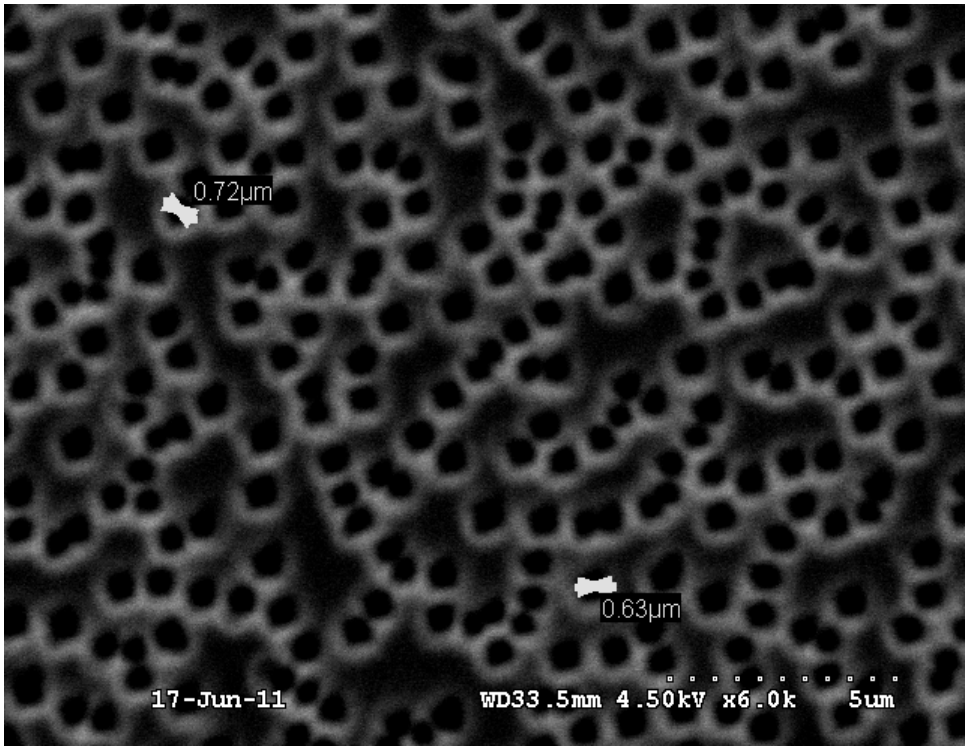

Figure 2.9: Top view of n-type etched porous silicon. The pores are randomly distributed with irregular shapes due to the etch method. [137]

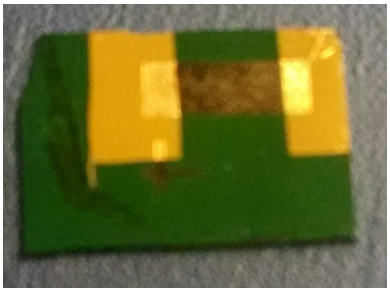

Figure 2.10: Close up of a finished wafer. The green is SiC and the gold is gold contacts and the brown-grey is PS.

have no electrochemical etching. Secondly, it has to be chemically inert, the mask has to withstand 45 min of HF electrochemical etching. SiO_2 and SiN meet the first condition but do not meet the second. SiC meets both conditions; it is extremely chemically inert and nonconductive. [138]

In order to put down a layer of SiC, a plasma enhanced chemical vapor deposition (PECVD) tool is used. This method takes place at much lower temperatures, at around 200 to 300 °C, than other CVD methods. The wafers are placed on a deposition electrode

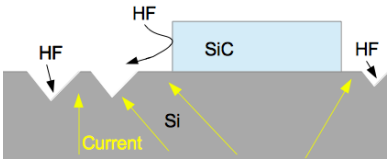

Figure 2.11: The SiC both keeps the HF from the silicon and causes the current to flow to unmasked areas.

in a gas chamber. The chamber is then evacuated and a controlled flow of gas is added. The deposition gases are exposed to a high-powered RF field. This RF field speeds up the electrons in the vapor as a result of their light weight. But the RF field does not excite the ions since they are heavier and thus slower. The electrons attain thermal energies of ten thousand Kelvin creating a plasma. This plasma disassociates the deposition gases into simpler chemical atoms. A small electrical bias is placed over the silicon wafer drawing the positive ions towards the silicon surface. These ions deposit on the surface creating a thin film.

While the initial research used the Unaxis PECVD, in order to increase reproducibility and minimize contamination the process was moved from the Unaxis to the Oxford PECVD 80 plus plasma lab machine in the cleanroom. The Oxford machine is not used to deposit silicon oxide, so in theory the resulting SiC should be cleaner.

The normal recipe for SiC on the Oxford is 13 sccm of SiH_4, 100 sccm of CH_4, and 185 sccm of N_2 at 1000 mTorr in a 50W, 13.6 Mhz electric field with the plate temperature at 250 ^{o}C. The recipe is run for 20 min, enough time to deposit 2000 Å of SiC on to the surface. While higher amounts can be deposited, this depth allows for good contacts to be created with the gold deposits applied later on in this process.

Once a thin layer of SiC has been uniformly deposited across the wafer, holes in the film must be created to expose the underling silicon for etching. In order to do so a photoresist is put on the wafer and the wafer is placed in a spinner. The spinner creates an even coating on the wafer by centrifugal force. The coating thickness (Figure 2.12) depends on the spin rate and type of photoresist [139].

The most important initial classification of the photoresist is whether it is a positive or a negative resist. Positive photoresists, when exposed to UV light, becomes soluble in

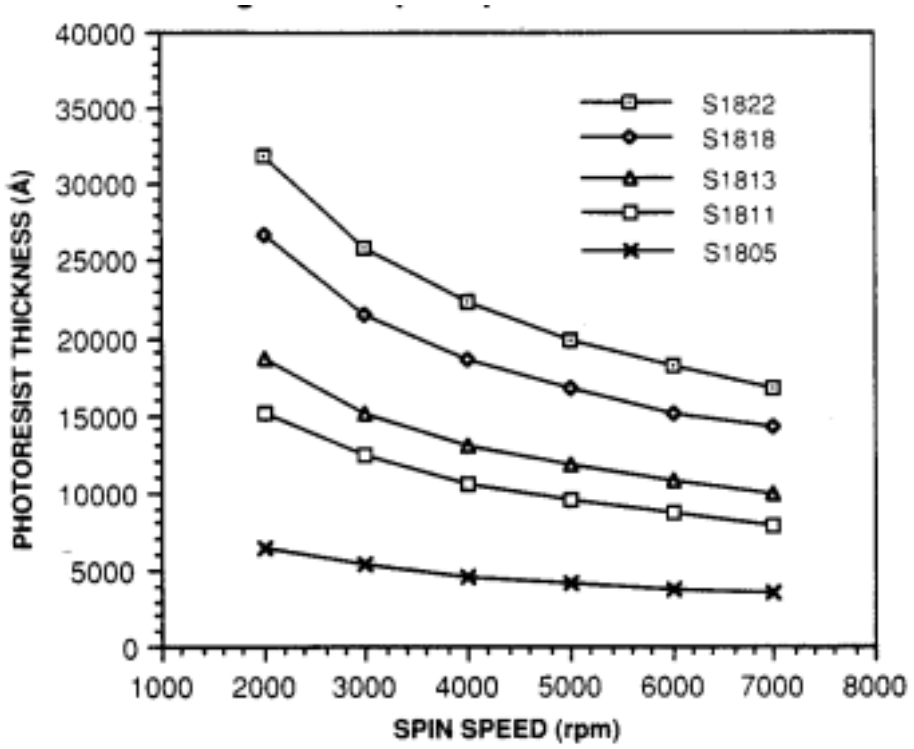

Figure 2.12: Examples of spin speed vs. resist thickness.

the correct developer. For our systems process we employed Microposit sc1813 photoresist. This resist was chosen, since it was available in the G.I.T. cleanroom for no cost and fit all needed parameters.

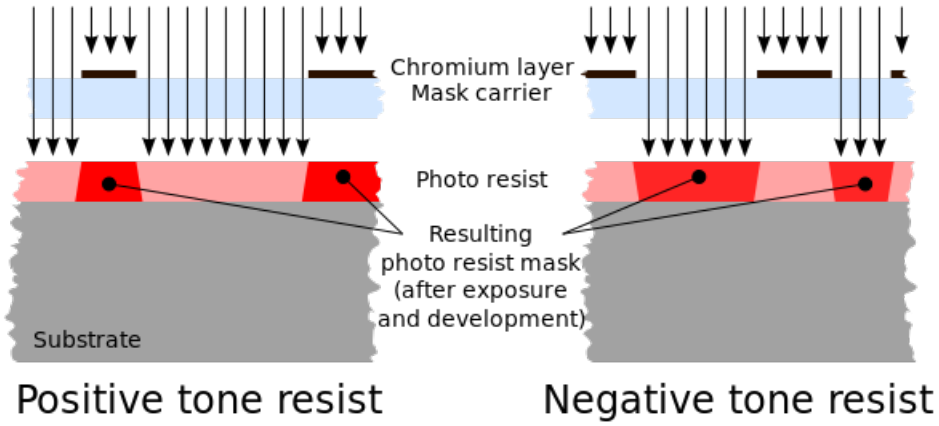

Figure 2.13: When the positive tone resist is exposed to UV light it becomes soluble in developer leaving behind only the dark red. Negative resist when exposed to UV light becomes insoluble in the developed leaving behind the dark red parts.

The method to create the sc1813 photoresist mask is as follows. The wafer is placed in a spin coater, and the photoresist is pipetted onto the wafer. The wafer is spun on the spin coater for 30 sat 3500 rpm with an acceleration of 500 rpm/s. After that the wafer is soft baked at 95 ^{o}C for 2 min. The wafer is then exposed to 365 nm UV light for 30 sthrough a lithography mask using the Klaus Suss MA6 mask aligner. Then the wafer is put into a dish filled with MF-319 developer until the fine features are exposed, generally after 30 s. The developer is washed off with DI water, and the wafer is dried with an air gun. Finally, the wafer is baked at 110 ^{o}C for 10 min.

Negative photoresist becomes insoluble in the developing solution when exposed to UV light as shown in Figure 2.13. During one of the wafer treatments, the positive photoresist mask accidently broke. While transferring the mask from the mask aligner, the mask slipped out and fell. This accident shattered the mask rendering it useless. The exposure mask had to be redone.

While being redone, the mask became light field instead of dark field due to communication issues. This required changing the process to use a negative photoresist. NR71-3000P is the negative resist used. The standard recipe for the NR71-3000P is to place it on a wafer and spin it up to 3000 rpm for 30 s with an acceleration of 1000 rpm/s. The wafer is then baked for 2 min at 150 C in an oven. It is exposed to 365 nm light in the mask aligner and then baked at 100 ^{o}C for 30 min. The resulting coating is developed in Futurrex RD6 solution for 1 minute then dried with nitrogen.

All UV exposures are done on a KSA Mask aligner. This tool was used to properly expose the wafer. The mask aligner holds the wafer and mask in place so that the exposure is perfectly aligned. The wafer is aligned so that the bottom edge was parallel to the outside edge of the mask aligner allowing the crystal structure of the wafer to align with the lithography pattern for smooth dicing as shown in Figure 2.14. All exposures are done with a soft contact at 50 micrometers.

After the photoresist is developed it forms a protective layer for the SiC. The wafer is then placed in a reactive ion etch machine (RIE). The RIE generates a plasma that strips away material on a surface. In this case the RIE is used to remove the SiC allowing the

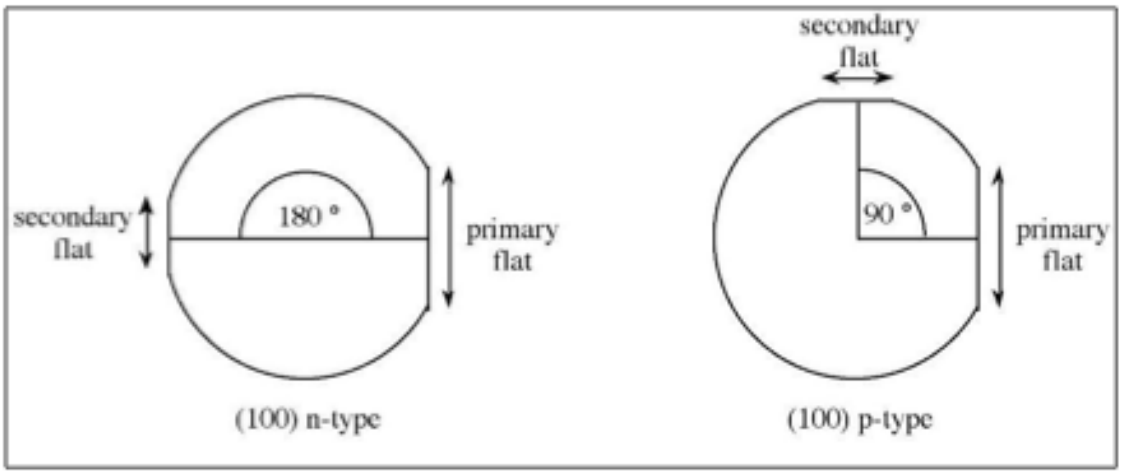

Figure 2.14: Wafer alignment for p and n-type wafers. Note that the primary edge is the same for both wafers.

formation of windows to the bulk silicon underneath. The Oxford endpoint RIE is used to do this with the standard SiC etch using CF_4 and O_2. Before etching, the SiC depth is measured via the Nanospec Reflectometer. Then the etch rate is calculated using a trial run. The etch is run for just enough time to etch the SiC and expose the silicon. If the etch runs over, it eats into the Si. If the Si is etched too deep the SIC will not act as a chemical barrier causing etch problems. If the Si is etched a little bit, the gold deposition will have a hard time covering the larger SiC side walls leading to connection problems.

After the holes have been created in the SiC, the wafer is washed with acetone, methanol, and 2-propanol, in that order, to remove any remaining photoresist resulting in a wafer that looks like Figure 2.15.

The wafer is then etched, depending on the type of wafer, using the methods described previously.

All wafers are soaked in a dilute (1:20) HF solution, just prior to coating with gold, to avoid surface oxidization. Then the wafer is quickly prepared for a metal deposition, first cleaning with methanol and then drying with nitrogen. The metal mask is attached to the wafer using vacuum tape, preventing the mask from moving or falling off. The wafer is then place into an e-beam machine. A 100 angstrom layer of titanium is placed on the surface for good adhesion then a 3000 angstrom layer of gold is quickly deposited on top of the

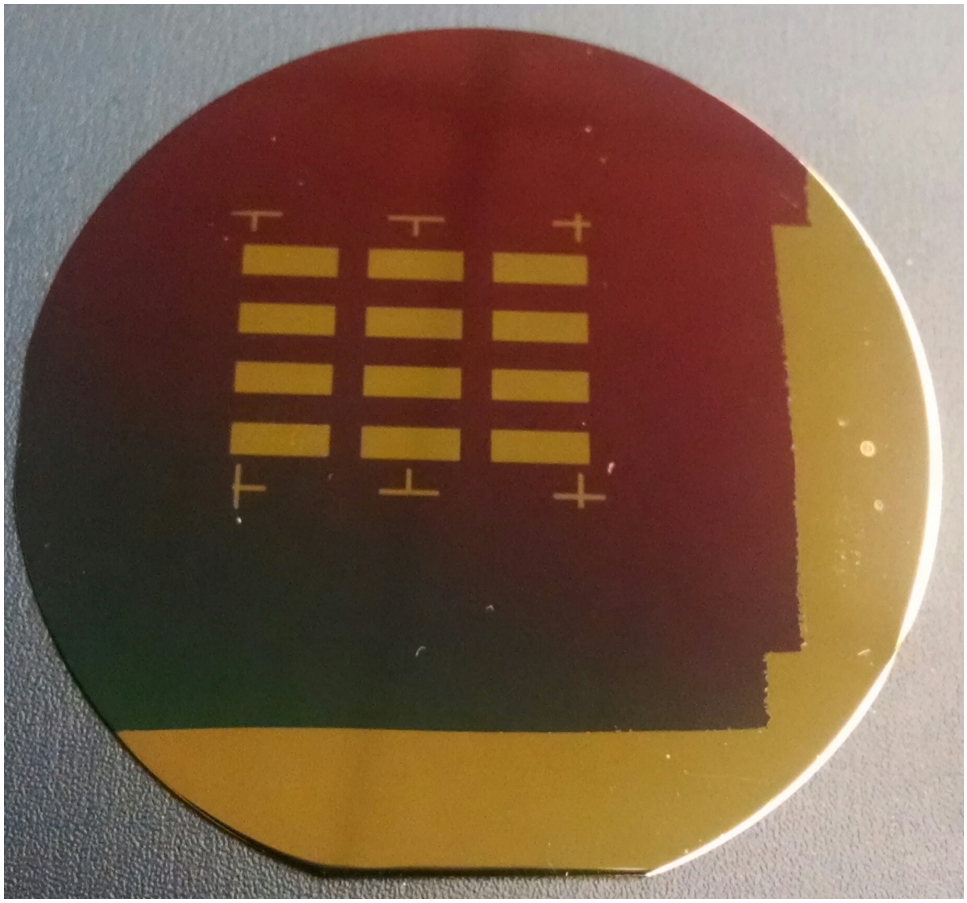

Figure 2.15: Completed silicon etch pattern the purple is the SiC and the reflective grey is the exposed silicon. Note the alignment of the squares with the flat edge at the bottom of the wafer.

titanium for electrical contact as shown in Figure 2.16.

After the deposition the wafer is diced. The wafer is carefully aligned early on to maximize the sensor yield per wafer. We align the directions of fracture with the sensor outline seen in Figure 2.17.

Once the sensors are created and removed from the wafer, they are then tested for their response to the analyte gases. The testing apparatus is described as follows: the diluted analyte gases are stored in gas cylinders. The cylinders are attached to Swagelocked stainless steel lines. These Swagelocked lines are connected to mass flow controllers to allow flow thru an MKS 1179 or 1279 flow controllers. The gas lines are then fed into a main line of ultra high purity nitrogen, which is also controlled by an 1179 MKS flow controller. The nitrogen is used to dilute the analyte gases from either 100 ppm or 1000 ppm to the 1 to 10

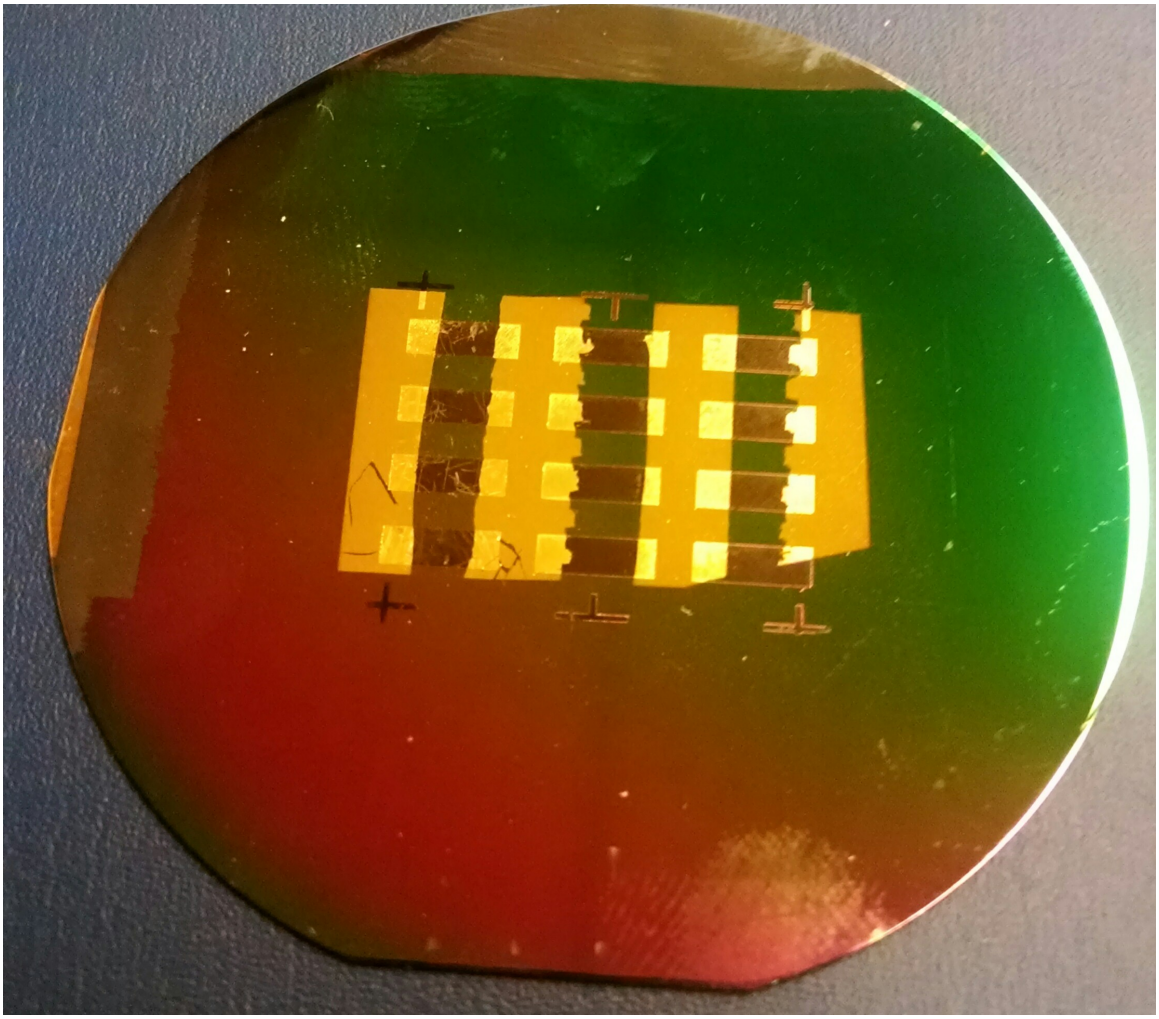

Figure 2.16: A completed wafer of sensors. The gold just touches the PS(grey areas) at the edges allowing current to flow through.

ppm range. The resultant gas mixture exits a 1/8" pipe and flows over the sensor or array of sensors. The basic experimental configuration is diagramed in Figure 2.18 [10].

In order to measure the resistance, precision microprobes are attached to the gold contacts. A square wave is pulsed across the sensors at 1 to 20 Hz. The sensor is in series with a resistor, in order to effectively measure the resistance change. The size of the voltage pulse across this circuit is generally kept at 3 volts for all measurements. 3 volts has been found to have the best signal to noise ratio for measurements with the sensors.

To generate the voltage pulse and measure the voltage drop, the circuit is connected to a data acquisition platform (DAQPad). Initially we used the NI 6015 DAQPad; however,

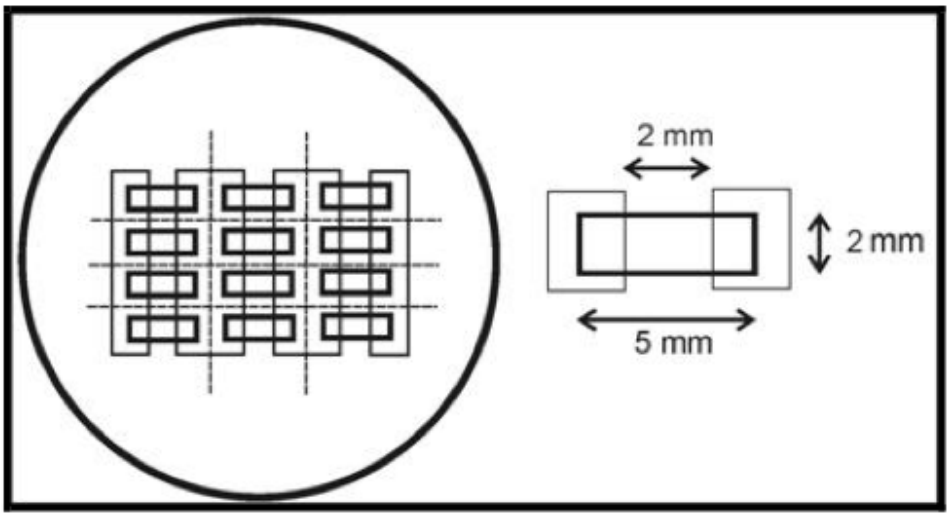

Figure 2.17: Dicing of a wafer into sensors. Since the wafer is properly aligned, the sensors are easily diced along the dashed lines into 2 by 5 mm sensors.

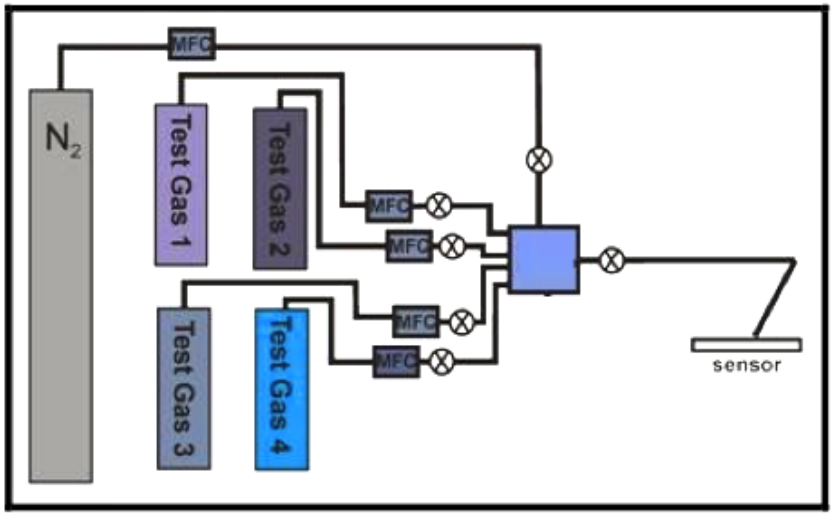

Figure 2.18: Diagram of the gas preparation system. MFC corresponds to a mass flow controller.

we have upgraded to the 6363 NI DAQPad for faster sampling frequencies. The DAQPad is also hooked up to the gas flow controllers via the MKS 246C and MKS 247D power supplies. The DAQPad is connected to a computer running a Labview program to control the gas flow and record the resistance changes [92]. This program is attached in Appendix C.

After testing the sensor response to determine its baseline, the sensor is decorated with various metal oxide nanoparticles. In some cases the decoration is done by placing the

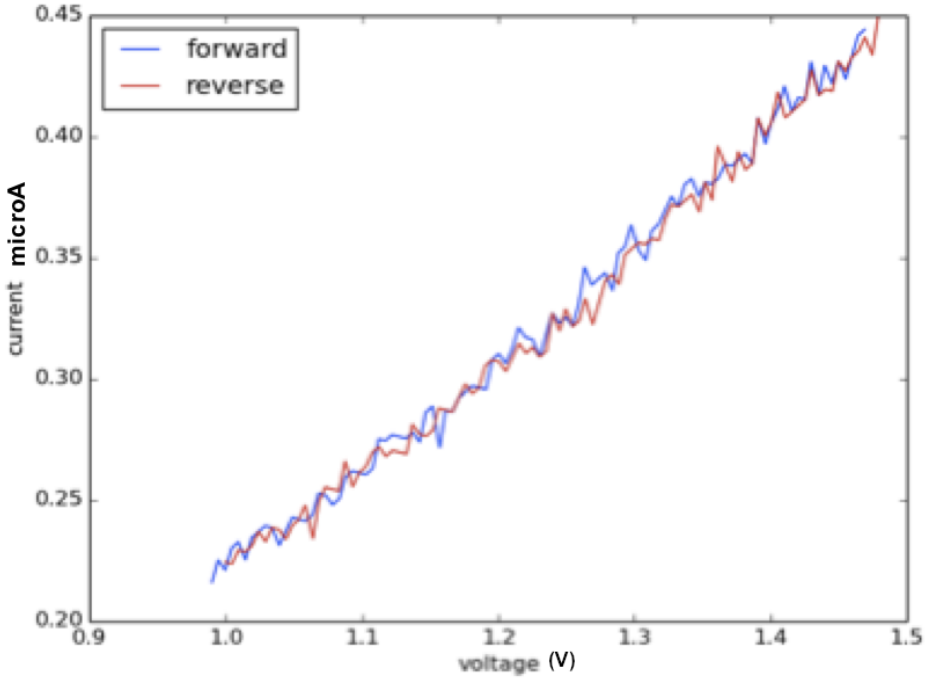

Figure 2.19: IV sweep of a sensor. The sensor has a voltage placed on it from 1 to 1.5 volts with a continuous power consumption of 25 to 60 microwatts. Note that the voltage measured is not the voltage across the complete circuit. The sensor has excellent linearity, following a straight IV curve similar to a resistor with no hysteresis.

sensors in an electroless solution for 10 to 30 s. These include gold, nickel, tin and copper solutions [66, 67]. In order to deposit TiO_2 nanoparticles onto the PS surface, the sensor is directly dipped into a diluted sol-gel solution. These sensors should just be lightly decorated by the metal oxide nanoparticles on the surface [140]. If too many metal oxide nanoparticles are deposited on the surface, this causes crosstalk between the particles. This crosstalk lowers and often kills the sensitivity of the sensor.

After a short soak in the depositing metal oxide solution(10-30 s), the sensors are quickly placed in deionized water for 2 min, to remove the solution. Then the sensors are removed from the water and placed in methanol for another 2 min. The methanol leaches the water from the pores. The methanol easily evaporates out of the pores, due to its low vapor pressure. This evaporation takes place overnight in a fumehood.

After the sensors have been decorated with the metal oxides and dried, they can be also modified by nitration or sulfidization. In order to functionalize with nitrogen the sensor is

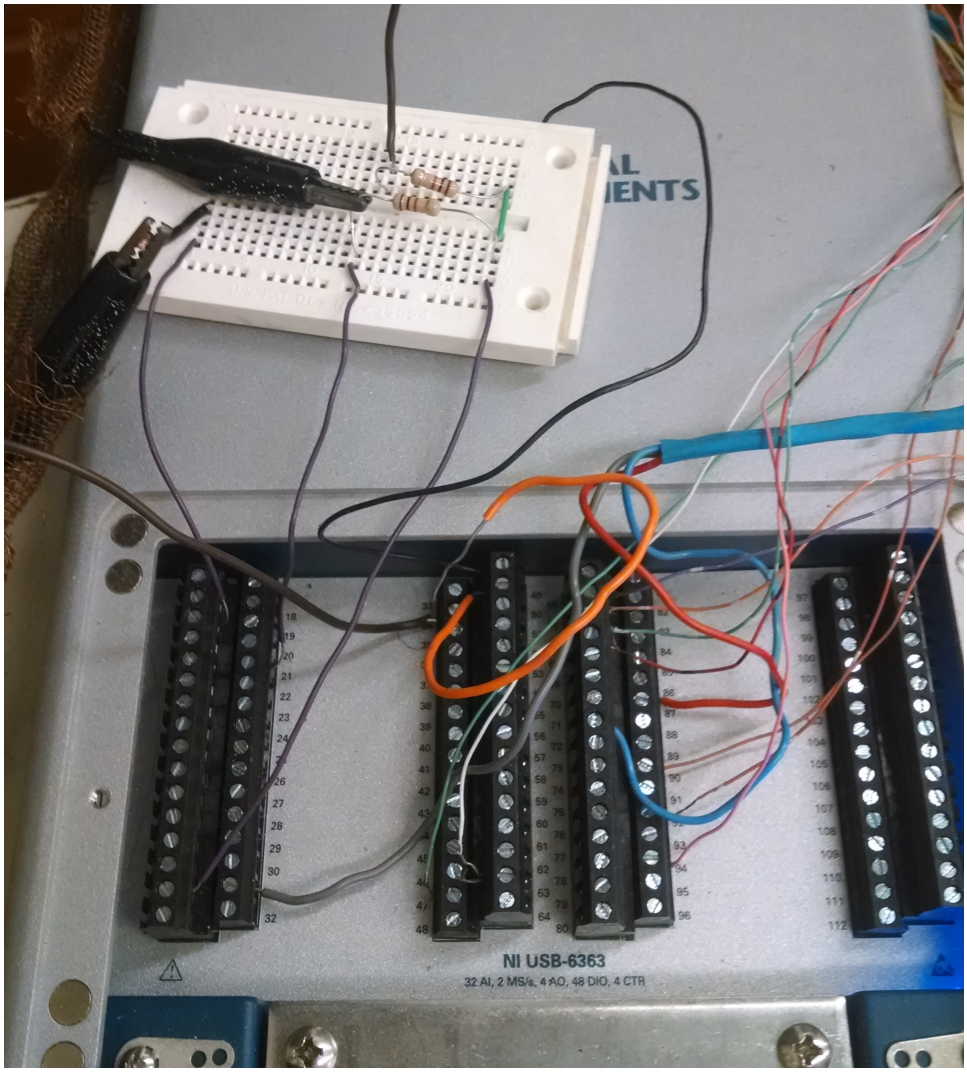

Figure 2.20: Circuit attached to the DAQPad. The purple leads going to the bread board from right to left are voltage output, voltage reading, and ground. The alligator clips go to the sensors. The circuit is a simple voltage divider passing the current across the 1000 ohm resistor. All wires on the right side of the DAQPad go to the gas controllers with the color coded lines corresponding to the different gas flow regulators.

soaked in triethlyamine for 30 s. The sensor is then air dried overnight [68, 129].

A similar method is used to functionialize the sensor with sulfur. The sensor is exposed to diethylene sulfide, butanethiol, or ethanthiol for 30 s, and is allowed to air-dry overnight. [129]

2.3 Simulation and Data Extraction.

All data processing and simulations were done using MATLAB. The initial simulations were done using a simple one dimensional diffusion model. Since there is little to no difference between the pores, instead of simulating multiple pores only one pore is simulated. The pore is assumed to be a symmetric tube with no torsion, so it can be divided into a one-dimensional uniform mesh. Then the analyte gas diffuses into the simulated pore by numerically solving Fick's second law,

$$\frac{\partial \phi}{\partial t} = D\nabla^2\phi \tag{2.1}$$

where ϕ is the concentration of the gases at different points and D is the diffusion coefficient of the gases.

The Fickian equation was numerically solved by subdividing the tube in to a finite number of sections then the gas was allowed to diffuse through each sections by time evolving the system. The Fickian equation was rewritten for a discrete steps in space. The change in the concentration for each section was

$$\Delta C_i = \Delta t * D\frac{C_{i-1} - 2 * C_i + C_{i+1}}{\Delta X} \tag{2.2}$$

Where C_i was the concentration of the gas at the ith section in the tube, C_{i+1} and C_{i-1} are the i+1th section and the i-1th section of the tube, Δt is the time step, and ΔX is the size of the section. Using this equation it is easy simulate the diffusion of a gas into the system. Once the gas is in the pores, the average concentration of the gas is the response function for the simulation. These simulations had a reasonable match with experiment [9].

While this simulation models the actual sensors to first order, modifications are required to better fit the response data. The first thing modified is the turn on of the analyte gas. While the gas ideally would turn on instantaneously, the gas does take a second or so to open up fully, which causes a slight dip in the initial response. Once the gas is allowed to turn on slowly the model shows a better match with the sensor response. The increase in the fit can be seen in Figure 2.21. Other more complicated changes to the model are discussed in Chapter 4.

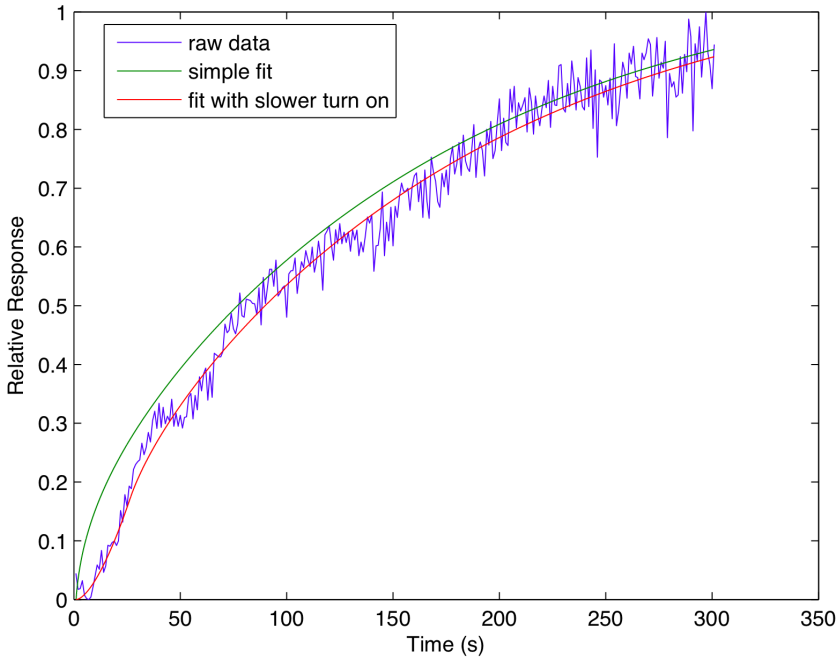

Figure 2.21: Numerical fits for a gas, which increases the resistance, upon increased gas exposure.

While the simulation is important, in order to extract information from the actual data, a numerical derivative was used. While the initial response to the analyte gases is very quick, the time scales for reaching the gas saturation can be longer. By taking the derivative of the data, we deal with this problem. However, real data, in its raw form, is too noisy to take numerical derivatives, so the data has to be smoothed with a weighted moving average. A moving average takes an average of only the last few data points. If the average is weighed, different data points count more for the average. So if we took the last five data points from time T to T +5*dT, the data points at T and T+dT are worth less than T+5*dT. This weighted average allows for smoothing the data without removing the quick response. The derivatives of the data show a correspondence to the initial gas turning on and off. This spike can be measured and the resulting size correlated to the sensor response.

Once the sensor responses are extracted we use a basic form of multiple linear regression (MLR) to find the gas concentrations. This assumes that there is a simple relationship R=B*C+E. where R is the response vector for the different sensors, C is the concentration

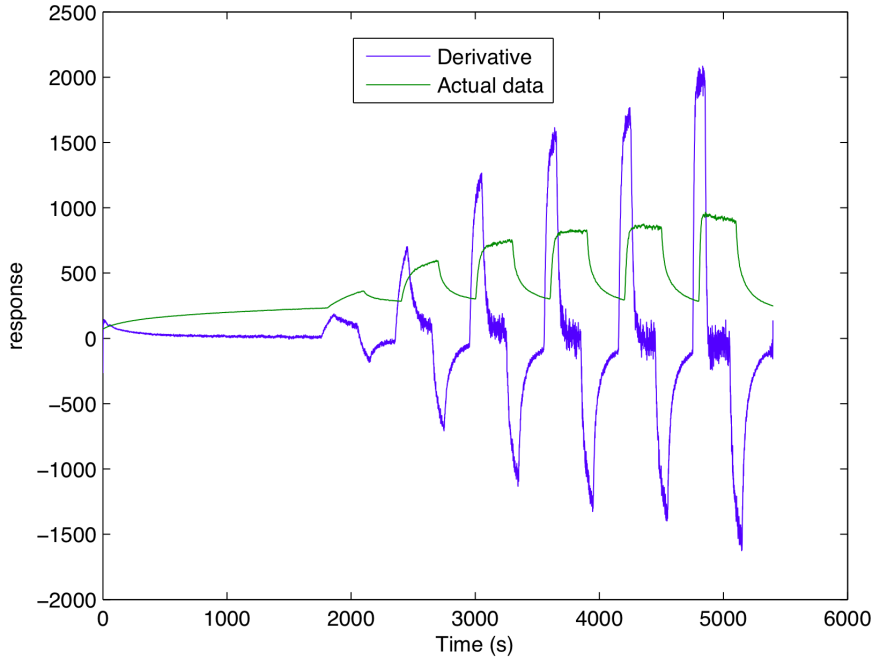

Figure 2.22: Taking a derivative of the analyte response data. The derivative is scaled for easy of viewing. Notice the peaks corresponding to the changes in the analyte gas.

of the different gases, E is the error function of the response, and B is the response matrix. The response matrix is the response of each sensor to each gas. This linear regression should allow us to extract the concentration from the measured sensor data.

CHAPTER III

N-TYPE INTERACTIONS

3.1 IHSAB theory

Porous silicon(PS) is an ideal material for the creation of a gas sensor due to its high surface area and low cost. PS can be used to create conductometric sensors that can be operated at low temperature and can be easily added to integrated complementary metal oxide semiconductor (CMOS) circuits. The high surface area and low cost also make porous silicon ideal for microreactors. Because PS is an extrinsic semiconductor, it is also easy to predict the precise nature of the conductometric response due to the analyte gas.

This prediction requires two fundamental ideas of chemistry and solid-state physics. The first idea is that the resistance of an extrinsic semiconductor depends on the number of majority charge carriers. The more charge carriers, the easier electricity moves through the medium thus lowering resistance.

The other idea needed for this theory is the Lewis definition of acids and bases. By definition, Lewis acids take electrons and Lewis bases donate electrons in a chemical interaction. A molecule could normally be considered mildly acidic, but if in a reaction the molecule donates electrons, it would be the Lewis base in the reaction. This definition is different then the Brønsted–Lowry theory which defines the acid and base on the basis of the exchange of a proton.

Combining those two ideas creates a theory for the nature of the conductometric response to an analyte gas. As an example of this theory, we look at a PS gas sensor created from n-type doped silicon, where the majority carriers in the sensing region are electrons. When the n-type silicon surface interacts with acidic gases, the gases will take electrons from the surface. The electron removal will lower the number of majority carriers and increase the resistance of the sensor. Likewise when basic analyte gases interact with n-type sensors, these gases donate electrons to the porous silicon interfaces. These donated

electrons increase the majority carriers, decreasing the resistance of the gas sensor.

When the analyte gases interact with p-type silicon sensors, where the majority charge carriers are holes instead of electrons, the process is reversed. When acidic gases interact with p-type doped surfaces, electrons are removed increasing the number of holes, and increasing conductivity. If a basic gas interacts with a p-type surface, the donated electrons will cancel the holes. This decrease in the number of holes, increases the resistivity. This theory allows us to predict the direction of the sensors response to the analyte gas with simple chemistry and accurately describes the first order response to all gases used in these experiments.

While being able to predict the direction of the sensor response is important, it is only part of the gas-sensing problem. Selective response to the different analyte gases is vital for any gas sensor application; however, unmodified PS does not give us enough selectivity to differentiate analyte gases. In order to meet the criteria necessary for the detection and monitoring of a diversity of materials and effluents for sensing purposes the porous silicon interface has to be modified.

The literature shows that conductometric gas sensors can be created from a sensitive surface layer, like porous silicon, that can then be transformed through the introduction of nanostructures [66, 67, 141, 142]. These sensors have been shown to respond to rapid transduction of sub-ppm levels of analyte gas with changes in their conduction (resistance); making the sensors ideal for many cases. Because the nanostructures have a dominant effect, it could be possible to create an arrayed configuration of sensors capable of highly distinct, predictable, and inexpensively calibrated responses for a prescribed set of analyte gases, while operating at room temperature.

The Gole group has produced individual gas sensors utilizing a hybrid nano/microporous silicon medium as the sensitive surface layer. These sensors can have selective fractional depositions of nanostructured materials deposited on them. These modified semiconductor interfaces can then be used to create microfabricated arrays for sensing purposes [9, 10, 66, 67, 74, 141–145].

Now we look at how these deposited nanostructures drive the selectivity. It has been

shown that adding various nanostructures to the PS sensors can enhance the sensitivity to different gases; the specific sensitivities will be detailed later [9, 10, 66, 67, 74, 141–145]. The nanostructures have two different methods of enhancing the signal. The first possibility is that the nanostructures increases the number of active surface sites. There are more spots for the gases to adsorb on the surface, so the sensor is more sensitive. However, this answer does not give us the observed selectivity, so it must be the other option. The other concept is that the surface chemistry has changed due to the nanostructures, modifying the surface interaction with the analyte gases.

Looking at these changes in response to different analyte gases due to the fractional deposition of nanostructured materials, Gole and Ozdemir have formulated an approach to describing the complicated interactions of the PS metal oxide nanoparticles and the analyte gases [74]. This approach to classifying and understanding these interactions is the inverse of the hard/soft acid/base principle.

The hard/soft acid/base principle (HSAB) proposed by Pearson provides a semi-quantitative indication of why certain chemicals bond together [146–150]. However for reversible conductometric gas sensors, weak chemical interactions (physisorption) are needed, not the strong chemical interactions (chemisorption) predicted by HSAB. In physisorption the electrons are weakly held by the molecules resulting from a large mismatch of their molecular orbitals. This weak binding allows the chemical interaction to be easily reversible, and this mismatch of electron molecular orbitals allows the physisorpion interaction modifying the bulk conductivity.

The HSAB concept predicts those factors leading to covalent or ionic bonding (chemisorption). If we take the inverse of this concept, it can be shown to predict weak bonding, physisorption. The HSAB concept says that hard acids like to pair off with hard bases in a chemical reaction and form ionic bonds and soft bases like to react with soft acids forming covalent bonds. When Pearson first proposed it, he used empirical observations to categorize the acids and bases. Later it was correlated using chemical reaction rate theory [151]. This followed the use of density functional theory (DFT) which was used to correlate hardness with molecular properties, and later to give it a deeper foundation. [146, 152–156] Conflicts

underlying the correlation of the DFT and CRT theories have largely been resolved by Cohen and Wasserman [151] as well as Zhan et al. who have further refined the concepts of electronegativity and hardness [156].

Hard acids and bases are not necessarily strong acids and bases, instead hardness is defined as having a small physical size, with low polarizability, high oxidation state, and large electronegativity. Since hard acids and base are difficult to polarize, when these molecules come together, they form an ionic bond. On the other hand, soft acids and bases are larger molecules with high polarizability, low oxidation states and low electronegativity. When these soft chemicals combine, they form a covalent bond. Examples of hard, borderline, and soft acids and bases are seen in Table 3.1.

Table 3.1: List of hard, soft, and borderline acids and bases.

	Hard	Borderline	Soft
Acids	H^+, Li^+, Na^+, K^+, Be^{2+}, Mg^{2+}, Ca^{2+}, Cr^{2+}, Cr^{3+}, Al^{3+}, SO_3, BF_3, Sn^{4+}, Ti^{4+}	Fe^{2+}, Co^{2+}, Ni^{2+}, Cu^{2+}, Zn^{2+}, Pb^{2+}, SO_2, BBr_3, Sn^{2+}, NO_2	Cu^+, Au^+, Ag^+, Tl^+, Hg^+, $Pd_2{}^+$, $Cd_2{}^+$, $Pt_2{}^+$, $Hg_2{}^+$, BH_3
Bases	F^-, OH^-, H_2O, NH_3, $CO_3{}^{2-}$, $NO_3{}^-$, O_2	$NO_2{}^-$, $SO_3{}^{2-}$, Br, $N_3{}^-$, N_2, H_2S, C_6H_5N, SCN	H^-, R^-, CN^-, CO, I SCN^-, R_3P, C_6H_5, R_2S

When HSAB was first proposed hardness was not well defined, it took DFT calculations to numerically define the hardness quantity. The first step was to define the electronic chemical potential. Equation 3.1 is used to show how the energy of the ground state of an N electron system, E(N), changes with the addition of an extra electron. Since E is a calculated using the electron density ϱ, we can also look at the change in the energy due the change in ϱ with the nuclei of the molecule held fixed (the Born-Oppenheimer limit).

$$\mu = [\frac{\partial E(N)}{\partial N}]_{v_e} = [\frac{\delta E}{\delta \rho}]_{v_e} \tag{3.1}$$

If we use the three-point finite approximation to determine the electron chemical potential, we arrive at Equation 3.2. μ is approximately equal to the negative of the Mulliken electronegativity. I is the ionization potential and A is the electron affinity.

$$\chi_M \approx -\mu \approx \frac{I + A)}{2} \tag{3.2}$$

In order to calculate the absolute hardness(η) of the chemical of interest, we take the second derivative of the energy with respect to N. Also by definition, this is equal to the first derivative of the chemical potential with respect to N. Since the hardness is the shift in the chemical potential, it is roughly equivalent to the energy gap between the ionization potential (I) and the electron affinity (A).

$$\eta = [\frac{\partial E(N)}{\partial N}]_{v_e} = \frac{\partial \mu}{\partial N}]_{v_e} \approx (I - A) \tag{3.3}$$

Since the ionization potential and electron affinity relate to the outermost orbitals of a molecule, it is useful to define the basic concepts of molecular orbital theory. All electrons in a molecule are assumed to occupy molecular orbitals (MO). The highest occupied molecular orbital (HOMO) is the highest energy orbital occupied by electrons. The lowest unoccupied molecular orbital (LUMO) is the lowest energy electron orbital that does not have any electrons in it. These roughly correspond to the valence (HOMO) and conduction (LUMO) bands in the solid state. Using Koopman's theory for the ionization energy and the electron affinity, we get Equation 3.4 [157]. E_{HOMO} and E_{LUMO} are the energies of the HOMO and the LUMO respectively.

$$-E_{HOMO} = I - E_{LUMO} = A \tag{3.4}$$

Plugging these definitions into Equation 3.3 shows that large gaps between the HOMO and the LUMO cause an atom or molecule to be hard while small gaps correspond to softness. This fact allows us to define the hardness by another physical quantity, the energy gap between the HOMO and the LUMO.

Since the softness is the inverse of the hardness, it is simply defined at the inverse of η. This gives a completely quantitative method for calculating the hardness and softness of molecules.

$$S = \eta^{-1} = \frac{\partial N}{\partial \mu}]_{v_e} \tag{3.5}$$

A problem highlighted with this method is that the difference between the LUMO and the HOMO varies across the molecule, so there can be some variance in the hardness of the molecule. η is only the global average of the system. In order to overcome this difficulty Parr and coworkers have defined a local hardness that can change over the chemical system being studied. Cohen and Wasserman have used a different approach creating a hardness matrix to correlate the reaction rates of the different molecules in the system. [151,158] The molecules have an interactive hardness with themselves and other species in the system being examined. This hardness matrix depends on the interaction distance and becomes diagonal once the species separate in the system. Thus the hardness and softness of a molecule depends on the local context. This theory of local hardness allows for the nanostructured islands to control in interactions of the whole system. This is vital to IHSAB theory.

Using molecular theory it is possible to establish a more general theory of equalization using the MO's involved in the process of electron transfer. When an acid and a base are combined, electrons flow from the system with lower χ to higher χ. This equilibrates the system.

If the electron flow is driven by the difference in each interactant's χ, there should be some resistance to the flow. Since η is correlated to the difficulty in polarizing a molecule (moving electrons around), we get the formula of Equation 3.6 for electron flow [146].

$$\Delta N = \frac{\chi_C - \chi_B}{2(\eta_C + \eta_B)} \tag{3.6}$$

Where χ_{C} and χ_{B} are the chemical potentials of the interacting chemical systems and the η_{B} and η_{C} are the hardness of the chemical systems. This allows for the flow of electrons to be determined by the relative chemical potential between the two chemical systems and their hardness without worrying about the specific electron orbital being used in this exchange. Note that if the chemical potential changes with time, the electron flow can reverse.

Now we look at the sensor response reported by the Gole group [66, 142, 145]. Figure 3.1 shows an excellent example of the signal enhancement for the detection of PH_3 after the surface of the sensor was decorated with Au nanoparticles. PH_3 is known to display a great degree of interaction with a nanostructured surface and has a high sticking coefficient.

[9,66,67,141,144]. This stickiness can be seen in the gradual increase in the sensors baseline. This change is due to the equilibration of adsorption and desorption of the PH_3, also manifest in NH_3. The sensor response and recovery time scales for these gases are distinctly different even though the sensors were only exposed to an unsaturated amount of PH_3, [66, 67, 141, 144]. Weak chemisorptions of PH_3 could also be the cause of the small baseline drift. This chemisorption of PH_3 is in addition to the dominant physisorption [9]. If, after exposure to a 300 s PH_3 gas pulse, the sensor surface is purged with ultrahigh purity (UHP) nitrogen for longer durations(Figure 3.1), enhancing the return to the initial baseline. A more tightly confined gas flow has also been found to speed up the return to baseline. In addition, the application of Fourier fast transform (FFT) pulsing techniques can be used to average out the effects of the baseline drift. However, even with this drift, the gold nanoparticles can be seen to drastically enhance the sensor's response to analyte gases.

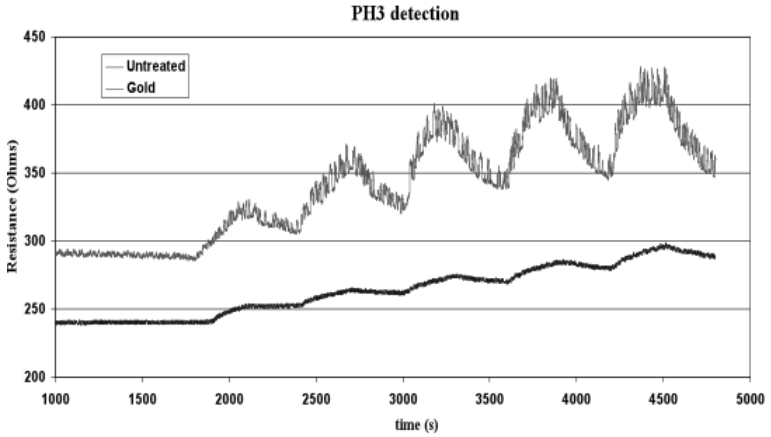

Figure 3.1: Shows the enhanced signal from a gold clustered oxide decorated PS substrate compared to an undecorated PS substrate for PH_3 on p-type silicon. [9].

Figure 3.2 shows actual numerical resistance changes for the response of the sensors to different gases. Here the response of SnO_2 and Au_xO nanoparticle decorated and undecorated PS surfaces are compared for various different analyte gases. Note that all these tests took place at room temperature, much lower than the 300 to 500 ^oC operational temperature of SnO_2 sensors [3].

Table 3.1 identifies Sn as a hard acid and Au as a soft acid. CO is soft base while NH_3 is a hard base. Comparing the response it is clear that the Sn has a better response with the

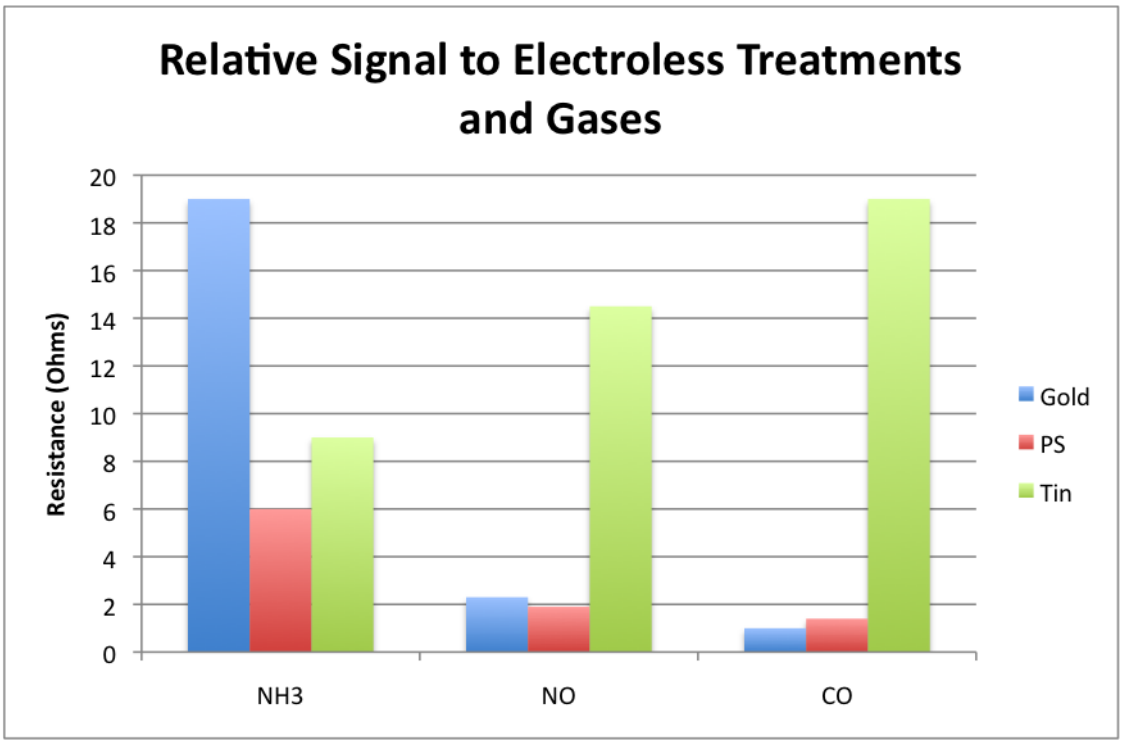

Figure 3.2: The response of the various decorated sensors to various analyte gases. From Seals et al., Lewis et al., and Ozdemir and Gole, [66, 142, 145]

soft base CO then the harder base of NH_3, while Au has a minimum response to CO but has a large response to the hard base, NH_3. Taking this further, Gole and Ozdimer looked at the change in response from an untreated sensor to a decorated sensor for multiple gases and metal oxide nanoparticles and compiled their results in Table 3.2. They looked at the change in the response for 1 ppm of the different gases before and after depositing the metal oxide nanoparticles. Equation 3.6 was used to generate the numbers in Table 3.2 where R_0 is the baseline of the sensor before exposure to the gas and ΔR is the resistance change in the senor due to the exposure.

Table 3.2: Increase in the signal for p-type silicon for various analyte gases after decorating with different metal oxide nanoparticles relative to an undecorated PS surface.

	Tin (SnO_2)	Nickel (NiO)	Copper $(Cu)_xO$)	Gold (Au_xO)
PH_3	2	2.5	4	5
NO	7–10	3.5	1	1.5
NH_3	1.5	(1.5–2)	(2–2.5)	3
SO_2	4	2	1+	2

Reiterating the HSAB concept of Pearson, when hard Lewis acids combine with hard Lewis bases they chemisorb to form an ionic bond. When a soft Lewis acids combine with soft Lewis bases, they chemisorb to form a covalent bond. Physisorption would mainly happen when a weak Lewis acid interacts with a strong Lewis base or a strong Lewis acid interacts with a weak Lewis base. [147–151, 156, 158] Using this principle of physisortion and the data in Tables 3.1 and 3.2, we can begin to compare the data.

The first thing Table 3.2 demonstrates is that the hard to moderate base gases (ammonia and phosphine) have the strongest response (largest transfer of electrons) to a nanostructured Au_xO decorated surface, which creates a soft acid ($Au^{0,+}$) interface. In contrast, the soft bases (CO and NO) display a maximum response (change in resistance) with the borderline to hard acid SnO_x ($Sn^{2+,4+}$). Note also the minimum response of the untreated PS surface to CO and the subsequent decrease for the Au_xO nanostructure treated surface displayed in Figure 3.2. There was a minimum measured response with either an untreated or an Au_xO nanostructure treated PS surface nor any change in that signal. The decrease in a small, almost negligible, resistance response for hybrid PS is consistent with the expected effect of chemisorption for the interaction of a weak acid with a weak base to create a stronger, more covalent, chemical interaction that does not facilitate electron transfer or transduction.

With all this data it is now possible to correlate the interaction of gaseous bases with the nanostructured surfaces. The location of each of these bases in a hard, soft dimension is evaluated based upon their observed interaction with the range of treated PS surfaces. The data in Table 3.2 suggest the combination of a weakly acidic sensor surface with a strongly basic interacting molecule, or vice versa, is the driving force for optimal PS conductometric sensor response.

Describing this observation within the framework of MO theory, we are attempting to promote a mismatch between the HOMO–LUMO gaps associated with the analyte and nanostructure orbitals. This mismatch in orbital gaps is used to produce rapidly responding, "reversible" sensor configurations. By promoting this interaction, we minimize the effect of chemical bond formation that inhibits the transfer of electrons to the modified PS interface

and maximizes a physisorbed interaction that encourages the transfer of electrons to the interface.

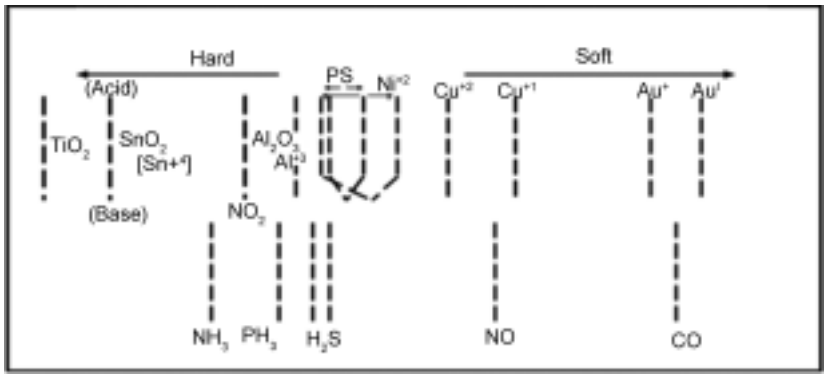

Figure 3.3: Estimated relative positions of the metal oxides and the analyte gases in the IHSAB theory based on observations.

The responses outlined in Table 3.2 in concert with Figure **??**, Figure 3.2, and Table 3.1 can further be correlated to generate the materials positioning depicted in Figure 3.3. This positioning diagram was generated based on the relative responses for the gases studied, with several nanostructured deposits over an extended period. The five base gases NH_3, PH_3, H_2S, NO, and CO are positioned relative to the PS (Si^{1-4+}) and the PS modified acidic interfaces generated with a nanostructured SnO_x ($Sn^{2+,\ 4+}$), Al_2O_3 (Al^{3+}), NiO (Ni^{2+}), Cu_xO ($Cu^{+,\ 2+}$), and Au_xO ($Au^{0,\ +}$) deposit. The basis for the positioning of H_2S in Figure 3.3 is the comparison of the relative responses for one ppm H_2S with a Au_xO deposited surface vs an untreated PS surface [67, 141] and to the data for NH_3, PH_3, and NO in Table 3.2. The ionization potential [159] and proton affinity [160], for H_2S are very close to PH_3. Due to the sensor response, H_2S is placed to the soft acid side of PH_3. The basis for the positioning of CO is its virtually non-existent response to Au_xO and its substantial response to SnO_2 seen over multiple experiments, summarized in Figure **??**. Comparing the data for the response of Al_2O_3 deposits to the hybrid PS interface for PH_3 shows no difference. Thus the acidic strength of the alumina modified PS surface as well as the untreated PS surface and the basic strength of PH_3 are closely aligned.

Now we look at the acidic metal oxide surfaces. We constructed Figure 3.3 within the framework of the acid and base character outlined in Table 3.1 considering, to first order,

the hard acidic strength associated with an Sn^{4+} (SnO_2) configuration, the soft acidic strength associated with a $Au^{0,\,+1}$ (Au_xO) configuration, and the intermediate (borderline) acidic strength associated with the PS hybrid surface. The silicon (Si_xO_y) oxidation state is considered to vary from 1–4+ [161]. From this simple framework, we insert the results outlined in Table 3.2 for the intermediate acid Ni^{2+}, the soft to intermediate acids $Cu^{1+,\,2+}$, and the intermediate to strong acid state associated with Al^{3+} (Al_2O_3).

Additional factors are used to refine Figure 3.3. A greater resistance change associated with SnO_2 suggests that ammonia lies closer to PS than to the strong Sn^{4+} acid. The inherently hard basic character of ammonia is also consistent with the strong resistance change observed for its interaction with the Au_xO nanostructure deposited surface (Table 2). The behavior of phosphine is similar to ammonia. PH_3 displays an expected strong increase in resistance change relative to the "p-type" PS surface modified with Cu_xO and Au_xO nanostructure-modified surfaces. The Ni^{2+} oxide nanostructure deposition does not increase the signal as much as the Cu_xO and Au_xO for PH_3. This suggests that the Ni^{2+} treated surface lies to the soft acid side of the untreated hybrid PS surface. The remaining interactions with NO and NH_3 suggest a Ni^{2+} acid strength in closer proximity to PS. This defines the broader relative response for the Ni^{2+} and hybrid PS regions indicated in Figure 3.3. As noted for phosphine, the Al_2O_3 should be closely aligned with PH_3 in relative hardness. Since tin oxide has a greater response to PH_3, it is consistent with the acid character of Sn^{4+} considerably exceeding that of Al^{3+}. The positioning of TiO_2 in Figure 3.3 is based on the observations in Refs. [74] and [140]. This hard acid is seen to react more strongly with NH_3 than SnO_2 putting it to the harder side of Sn.

NO is a special case since it is a radical with a singly occupied HOMO, as compared to the doubly occupied HOMO of closed shell ammonia or phosphine, and represents a weak base. The open shell nature of NO would suggest a very different interaction with hybrid PS and the nanostructure-treated PS interface. In addition, NO can bind an electron while NH_3 and PH_3 cannot. The soft base–hard acid interaction of NO with a SnO_2 nanostructured coating leads to a substantial resistance change relative to PS. This is the signature of the reversible interaction of a strongly acidic surface with a weak base. Further,

the response to gold, copper, and nickel treated surfaces, while considerably muted relative to the tin treated surface, suggests that NO should be positioned directly below the copper ($Cu^{+,\,2+}$) systems and intermediate to gold ($Au^{0,\,+}$) and nickel (Ni^{2+}). The interaction of NO with Ni^{2+} suggests a greater separation from nickel than from gold. While PS and Ni^{2+} may lie in a similar intermediate region, the greater resistance change observed for NO with a Ni^{2+} surface suggests that the (Ni^{2+}) modified PS surface lies to the hard acid side of PS, acting as a harder acid deposited to the PS surface. This again suggests a broader range for the relative response of the Ni^{2+} and PS regions as indicated in Figure 3.3.

The IHSAB concept offers a plausible mechanistic principal for the PS sensor resistance changes observed for the effectively oxidized gases. This process is amplified and dominated through the interaction of a modified acidic metal oxide surface. In effect, the nanostructures act as gateways to transduce charge due to physisorption.

The IHSAB concept suggests that nanostructured sensor surfaces for conductometric array-based devices can be constructed from a simple table. Once the gas is classified as a hard or soft, acid or base, a suitable range of nanostructured fractional deposits can be created to modify a prepared semiconductor interface to encompass the needed range of acidity and basicity. While there are other factors, including steric effects, polarization [162], and the nature of the open or closed shell character of interacting molecules to consider, the acid/base makeup of the nanostructure modified PS sensor surface and the mismatch of hard and soft acid/base molecular orbitals with the species to be detected appears to be the primary mechanism for sensor gas interactions. As an overriding principle, the maximum physisorption response (resistance change) is to be expected from combinations of hard acid surfaces with soft bases, and vice versa.

It should be noted that there is nothing unique about the silicon substrate for the IHSAB concept. There are alternate extrinsic semiconductor (*e.g.,* GaP, InP, CdTe) onto which a porous nanostructure coated microstructure can be generated [163] In theory, the porous silicon (PS) structures, devices, and methods described in the following discussion can be replaced with these surrogate porous semiconductors.

The IHSAB concept can also predict the response of extrinsic semiconductor sensors in

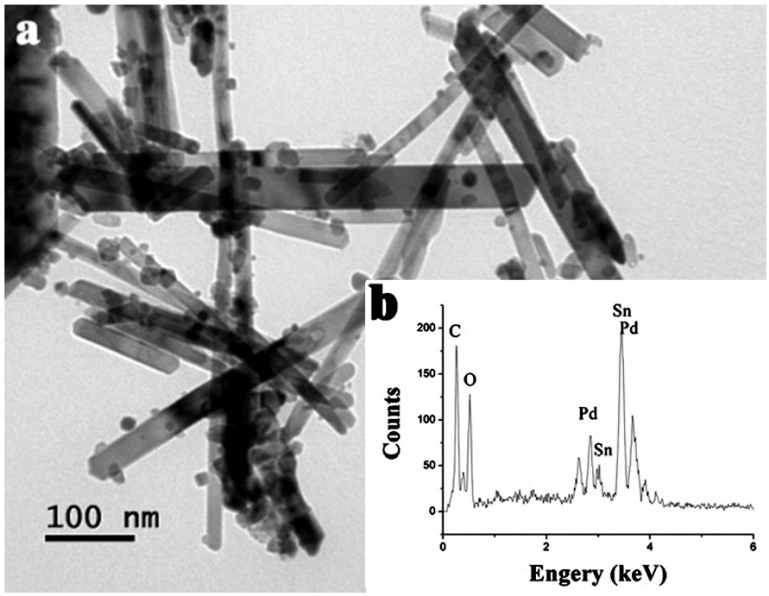

Figure 3.4: (a) Transmission electron microscopy (TEM) image and (b) energy-dispersive x-ray spectroscopy (EDS) (inset) of Pd nanoparticles deposited to SnO_2 nanowires. (Reprinted with permission from Li, et al., [164]Copyright 2010 Elsevier.)

a nanowire configuration if these nanowires are decorated with electrically non-interacting nanoparticles. In one case, Li, et al., placed Pd on SnO_2 nanowires, seen in Figure 3.4, to enhance the sensing to H_2S. This is in line with the IHSAB concept since the palladium is a soft acid and H_2S is a moderate base. The orbital mismatch will enhance the electron transduction interaction on the surface. Thus the nanowire becomes more sensitive. This response would be less if the doping material were Ni or other moderately hard acids with which the orbital mismatch would be less. Since the SnO_2 is considered an n-type system, the interaction with the base H_2S will increase the major carriers (electrons) and thus the sensor resistance will decrease. This predicted response matches this group's results. [164]

Kim, et al., have also studied nanowires for sensing applications. They used In_2O_3 wires to detect the presence of O_2. When they added small amounts of Pt forming islands instead of coating the entire wire with Pt as seen in Figure 3.5, the response increased significantly. Since O_2 is a moderate base, the soft acid platinum has an orbital mismatch with O_2 increasing electron transduction and the O_2 signal. Also since the In_2O_3 is a p-type semiconductor the increased electrons decrease the number of holes causing a resistance increase when sensing O_2. [165]

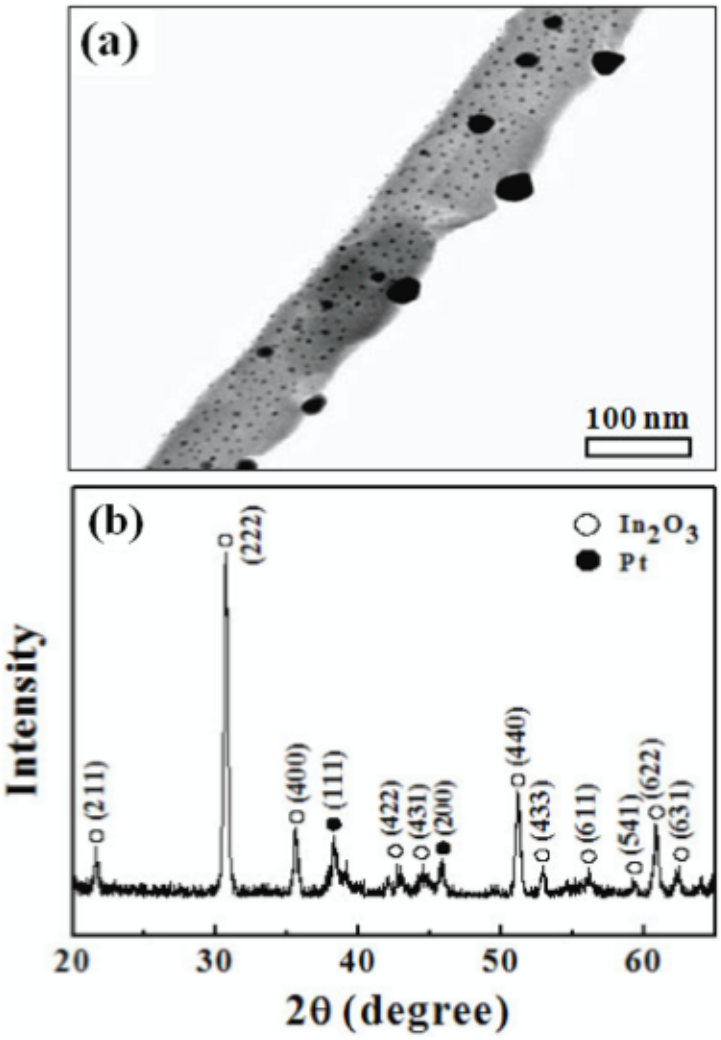

Figure 3.5: a) Low-magnification transmission electron microscopy (TEM) image of an 800C-annealed, core-shell nanowire. (b) Corresponding x-ray diffraction (XRD) spectrum. (Reprinted with permission from Kim et al. Copyright 2010 IOP Publishing.) [165]

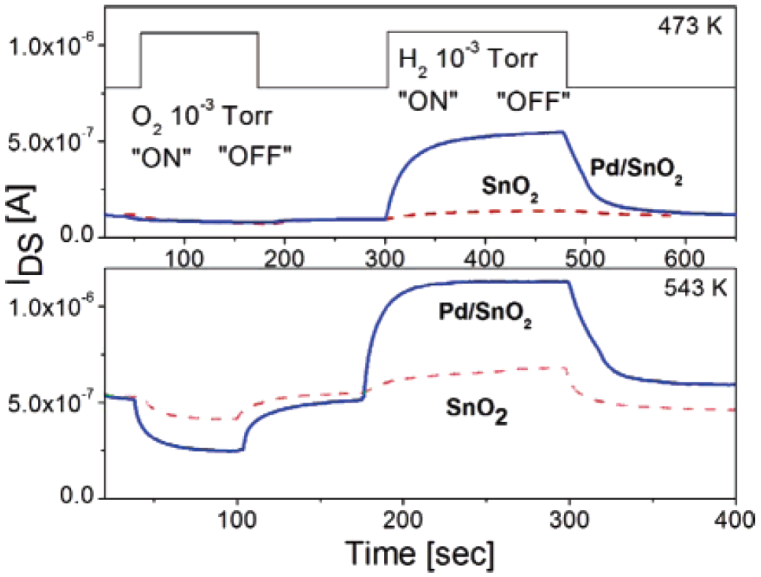

Figure 3.6: (a) Schematic view of the formation of electron-depleted regions beneath and in the immediate vicinity of two Pd nanoparticles. (b) Response of a pristine (dashed line) and Pd- functionalized (solid line) nanostructure to sequential oxygen and hydrogen pulses at 473 K (top pane) and 543 K (bottom). (Reprinted with permission from Kolmakov et al. [166] Copyright 2005 American Chemical Society.)

Finally, we note that Kolmakov et al. studied the response of a Pd-functionalized SnO_2 nanostructure to sequential oxygen and hydrogen pulses at 473 and 543 K (Figure 3.6). There was a strong response to hydrogen at both temperatures where the resistance increased. This resistance increase was enhanced by the Pd. No response was observed for oxygen at 473 K, but a drop in resistance was monitored at 543 K. These results can be readily explained within the IHSAB model. The hard acid hydrogen interacts with n-type SnO_2, removing electrons and leading to an increase in resistance. At the higher temperature, O_2^-, a moderate to hard base, is created on the SnO_2 surface. This base provides additional electrons to increase conductance decreasing the resistance. Again all interactions are enhanced by the presence of the soft acid Pd nanostructured islands. Since the H_2 has a much larger mismatch in its energy orbital with Pd than with O_2, the relative increase in the signal is greater as well [166].

3.2 PH_3 detection

We have obtained results for *p*, *p+* and *n*-type PS interfaces treated with nanostructures of TiO_2 and SnO_2, both strong acids, with the moderately soft acid Cu_xO, and with the soft acid Au_xO (x>>1). These results exemplify the dynamic interplay associated with these systems and the importance of the IHSAB principle. The resistance change with concentration for the *p*-type systems is positive for the PS interface even if it is treated with TiO_2, SnO_x, Cu_xO, or Au_xO fractional nanostructured depositions. This is as predicted by IHSAB.

Table 3.3: Relative increase or decrease in resistance (decrease or increase in conductance) of TiO_2, SnO_x, Cu_xO, and Au_xO (x 1) clustered oxides treated "*n*-type" "*p*-type" and "p^+-type PS interfaces. (a) Ratio of resistance *decrease* vs. untreated PS; (b) Ratio of resistance *increase* vs. untreated PS from Ref. [9]; (c) Ratio of resistance *increase* vs. untreated PS; (d) See Figures 9,11. The table constitutes a response matrix for PH_3.

	TiO_2	SnO_2	Cu_xO	Au_xO
PH_3[a] "n"	2-2.5	—-	—-	—-
PH_3[b] "p"	5	2	4	5
PH_3[c] "p+"	4	2	3-3.5	7[d]

The resistance change for nanostructure deposited vs. untreated *n, p,* and *p+* sensors, is summarized in Table 3.3. The data for *p*-type silicon is taken from previous publications [9] and the response of *p*-type silicon can be seen in Figure 3.7.

Figure 3.9 demonstrates relatively rapid scans of the responses that an untreated (see also Figure 3.8 and compare to Figure 3.9(a)) and nanostructured oxide decorated *p+* interfaces show to PH_3. In these figures, the first 1800 seconds represent a drop in resistance as a nitrogen purge is applied to the *p+* interface. This drop in resistance shown in Figure 3.8 is characteristic of the removal of water, a moderate base from a *p* type substrate. Also the nitrogen is used to remove OH groups and hydrocarbons, deposited from the air, from the substrate.

It can be argued that the oxidized, deposited, metal-based nanostucture islands, which we form on the PS interface, correspond to metal ions that are not accessible due to a combined oxide-surface hydroxide coating. Note that if the surface is completely coated

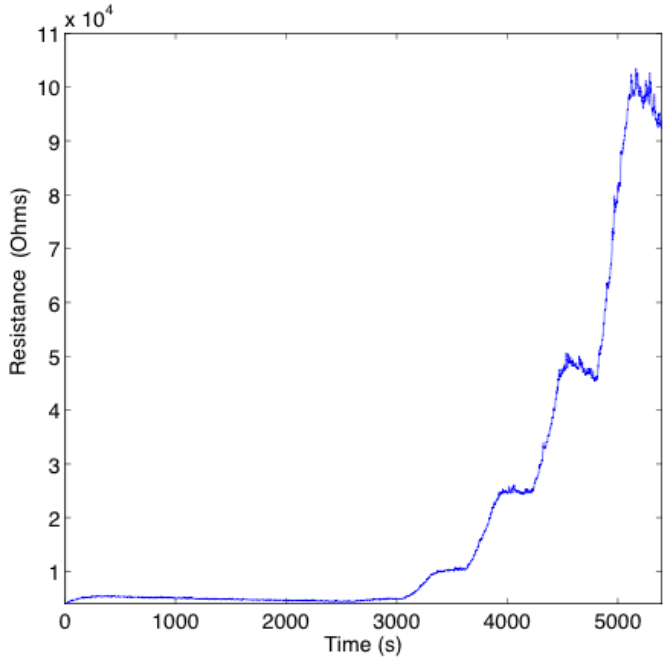

Figure 3.7: Response to 2,3,4,5, and 10 ppm PH_3 for a *p*-type PS interface. After purging with UHP nitrogen for 1800s, PH_3 was pulsed onto the interface with a 300 s half cycle followed by a 300 s half cycle UHP nitrogen cleaning. In all cases the introduction of PH_3 leads to a significant increase in resistance which is enhanced with the introduction of nanostructure metal oxide fractional depositions.

(covered) with hydroxide ions so as to block the exposure of an oxidized metal, this will nullify the effect of the corresponding metal ions rendering moot the observation of clearly dominant changes in sensitivity. This suggests two effects. First there should be little or no differences in the responses to different analyte gases to the metal oxides and secondly a completely OH^- covered surface should act to repel basic analytes,considerably decreasing the response of the sensor.

The sticky nature of PH_3 slows the return to base line in the Figures. Attempts to observe residual PH_3 by chemical analysis (TEM) of the PS modified material after the experimental runs have not been successful, since we use at maximum of 100 ppm of the PH_3 in these experiments and the residual does not survive the vacuum for TEM. However other results discussed below suggest the presence of additional phosphorus compounds at higher PH_3 levels.

The response for the untreated PS interface (Figure 3.9) is linear for 2–5 ppm while the

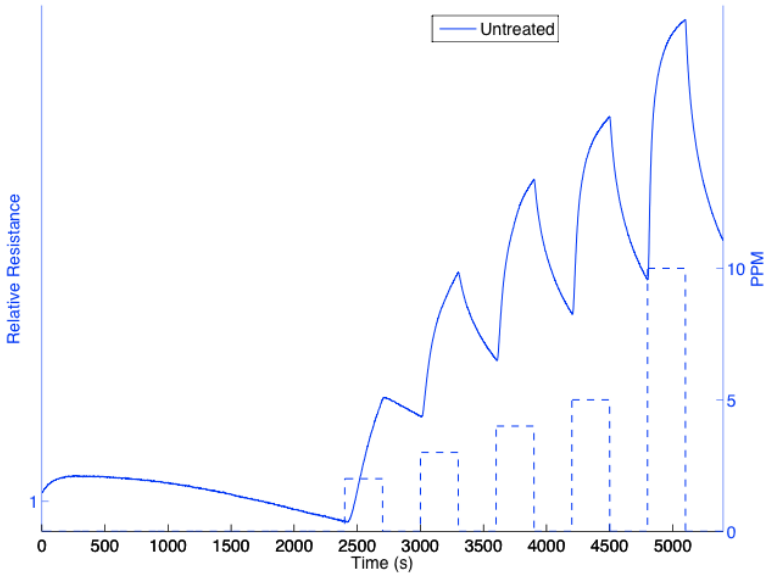

Figure 3.8: Relative response of the p+ type porous silicon to the PH_3 gas. The dashed lines show the ppm levels of the PH_3.

response begins to saturate at 10 ppm. Figure 3.9 demonstrates the effects on a $p+$ PS interface that TiO_2, SnO_x, Cu_xO, and Au_xO fractional nanostructured depositions have on the reversible response to PH_3. The signals are all enhanced from the uncoated p+ PS, due to the nanostructures decorating their surfaces. But the responses are different then the p-type PS systems. The gold deposited sensors are enhanced by a factor of seven compared to the factor of five for TiO_2. This should be compared to the data obtained for the p-type system where enhancement by the nanostructured gold clustered oxide surface appears to be equal to TiO_2. Also the $p+$ system has a decreased enhancement of the signal due to TiO_2 compared to the p-type system.

There appears to be a playoff of these strong (TiO_2) and weak (Au_xO) metal oxide acid depositions in the p and $p+$ systems. The data appear to demonstrate a shift of the sensitivity matrix from one that is virtually symmetrical with similar resistance responses for both the TiO_2 and Au_xO modification of the sensitivity of a p-type interface to a skewed enhancement of the relative sensitivity of the weaker acid coating. These results suggest that the *decorated* $p+$ doped interface is more effectively than the p-type decorated interface at extracting electrons. TiO_2, as a strong acid, and Cu_xO, as a moderate acid, can compete with the $p+$ interface during the electron transduction process decreasing the

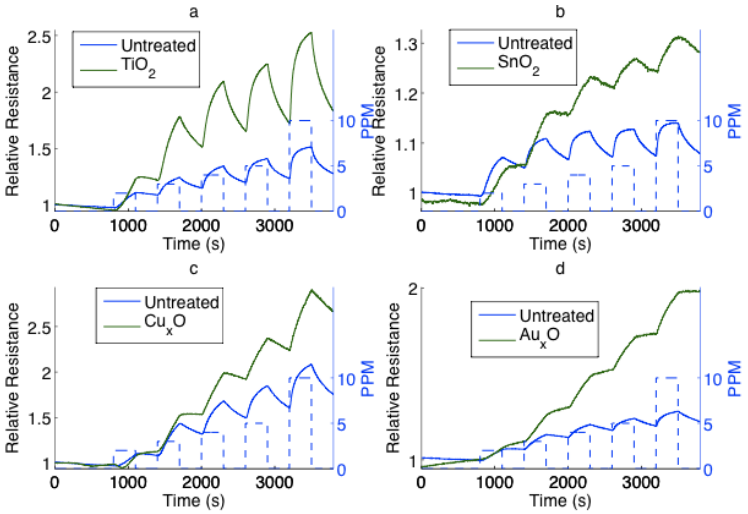

Figure 3.9: PS interface consisting of an untreated $p+$-type interface with those treated with (a) TiO_2, (b) SnO_x, (c) Cu_xO, and (d) Au_xO fractional nanostructured island depositions. PH_3 was pulsed onto the interfaces with a 300 s half cycle followed by a 300 s half cycle UHP nitrogen cleaning. In all cases the introduction of PH_3 leads to a significant *increase* in resistance which is enhanced with the introduction of nanostructure fractional depositions. These systems were purged with UHP nitrogen for 1800s before operation.

response. Au_xO, as a weak acid, does not compete nearly as effectively for these electrons. This lack of competition while enhancing the Si process can lead to an increased electron transfer to the $p+$ semiconductor and thus an increased response for the Au_xO treated $p+$ interface relative to the untreated p-type interface. The data in Figure 3.9 allows us to begin to develop a sensitivity and selectivity matrix for the PS-PH_3 interaction and PH_3 gas detection.

Figure 3.10 indicates the typical error bars associated with the measurement of each of the decorated interfaces. All of the systems outlined in this chapter are characterized multiple times and the data reported in Figures 3.9-15 are accurate and reproducible.

We indicate the data spread for a typical system in Figure 3.11. This is an excellent result in view of the spread in resistivities of the silicon wafers used in this study. Further, since PH_3 is a "sticky" gas (see also above), the return to baseline is notably slower than is the onset of the response when the sensors are exposed to the PH_3. This has been considered in the evaluation of the data in Figures 3.9. Similar comments can be made concerning the data for the untreated p-type PS interface in Figure 3.12, which clearly demonstrates the

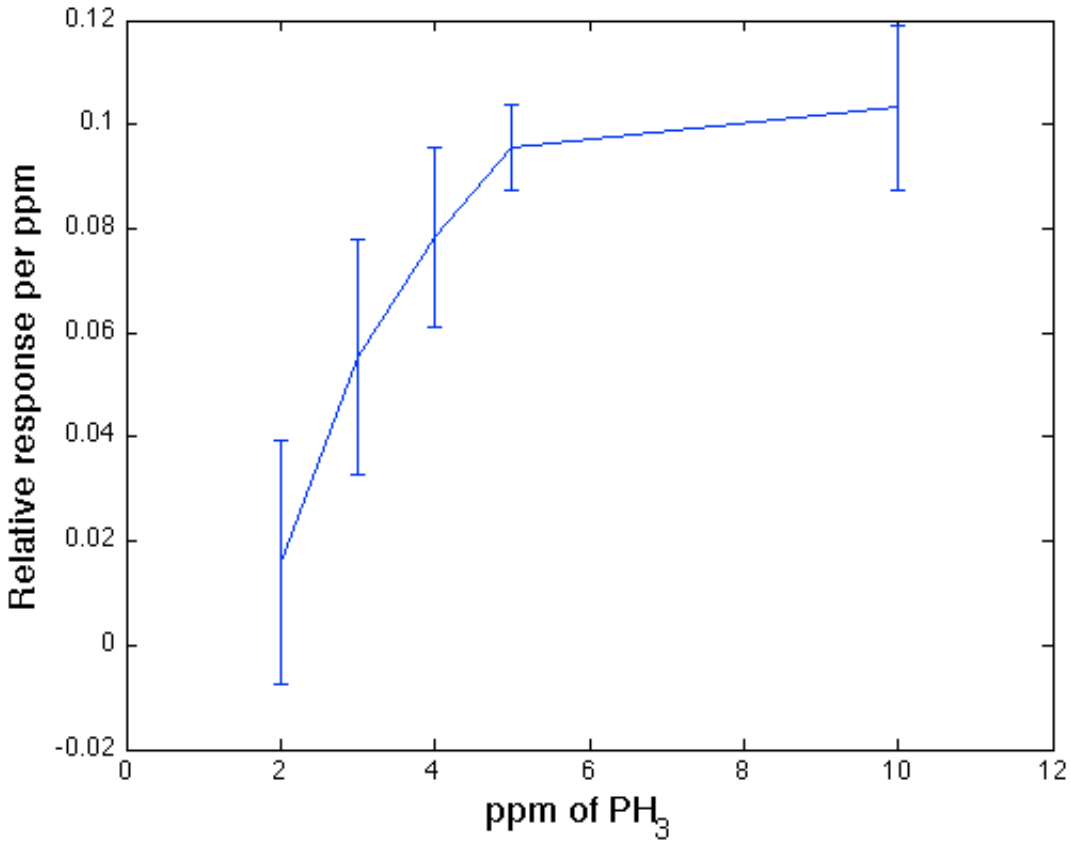

Figure 3.10: Uncertainty in the measured response after measurements of the PH_3 concentration as this analyte is sensed with TiO_2 coated $p+$ sensors.

effects of residual PH_3.

The data for three different gold depositions given in Figure 3.11 exemplifies the importance of fractional nanostructure deposition in these systems. The ratio of the response $p+$ interface with ten seconds of gold deposited, suggests a factor of 1.1 to 1.2 enhancement over the untreated surface(Fig. 3.11(a)). A twenty second gold deposition (Fig 3.11(b) and Table 3) demonstrates a notably higher relative response ($\sim$7) which then decreases to between 3.5 to 4 with a extra ten seconds of nanostructure deposition. Here the gold clustered nanostructures begin to cross talk as they interact electronically. The need to optimize the fractional nanostructured coating in these and other system for optimal detection is clearly show by this data.

PH_3 represents a moderately strong base whose behavior on an n-type surface, as it contributes electrons, should correlate a decrease in resistance with increased concentration.

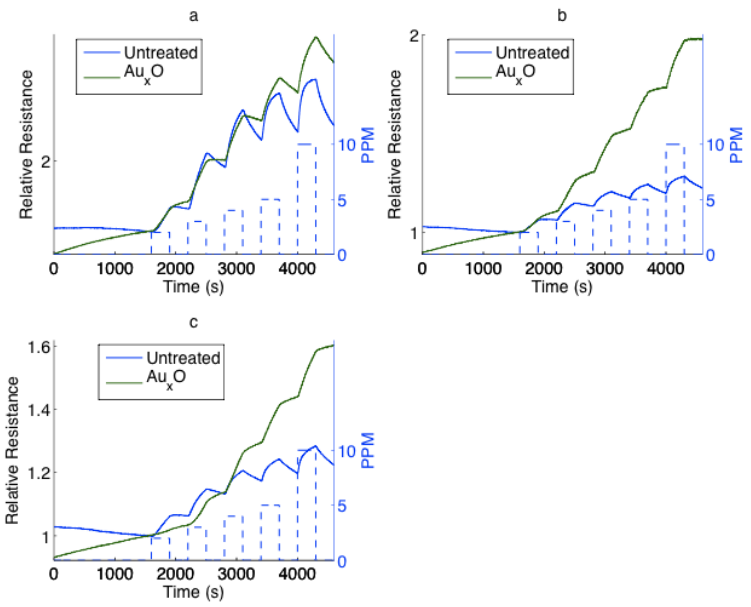

Figure 3.11: Comparison of responses to 2,3,4,5, and 10 ppm PH_3 for a PS interface consisting of an untreated $p+$-type surface with those treated with differing Au_xO fractional nanostructured island depositions. In all cases the introduction of PH_3 leads to a significant *increase* in resistance which is enhanced with the introduction of nanostructure fractional depositions. Figure (a) corresponds to a short ten second exposure to Transcene, the gold source. Figure (b) corresponds to a 20 second optimal exposure. Figure(c) corresponds to a 30 second exposure with an enhancement notably less than scan (b). PH_3 was pulsed onto the interfaces with a 300 s half cycle followed by a 300 s half cycle UHP nitrogen cleaning. The system was purged with UHP nitrogen for 1800 s before operation.

However, the responses observed for the interaction of PH_3 with an n-type interface are more complicated. While we initially observe a decrease in resistance upon the initial exposure to PH_3, the response of the interface is found to transform, especially for these more sensitive decorated interfaces. We observe the transformation from a response, which corresponds to the transfer of electrons from PH_3 at lower concentrations, resulting in a decrease in resistance, to a positive resistance at higher concentrations and/or with increased exposure to phosphine.

The response for the TiO_2 decorated n-type interface depicted in Figure 3.12 is only a factor of two times more intense than the undecorated interface (Table 3). Note that the response rises during the initial nitrogen purge cycle as water is removed from the surface of the n-type system. The observed results suggest the minimal chemical transformation of PH_3 on the p and $p+$ boron doped PS interfaces and a significant chemical interaction

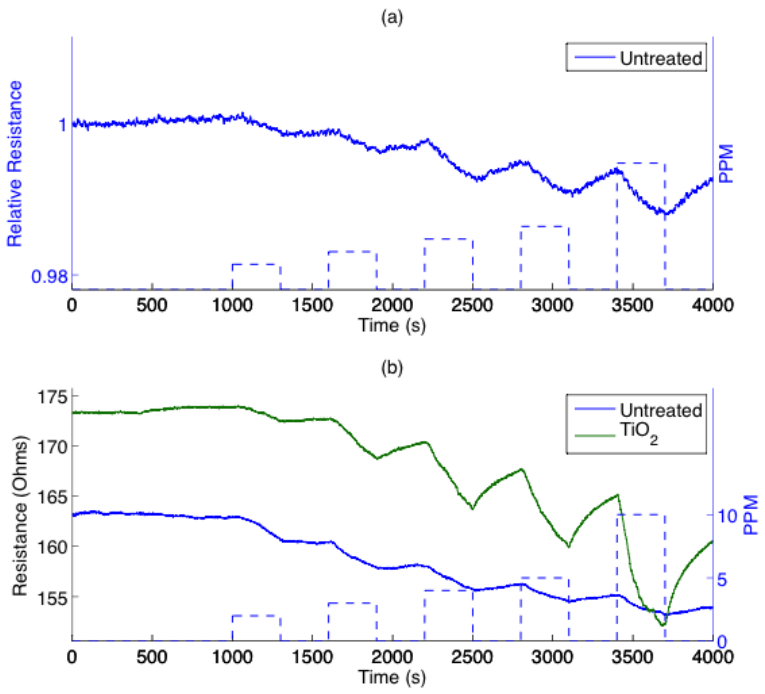

Figure 3.12: Comparison of responses to 2,3,4,5, and 10 ppm PH_3 for (a) a PS interface consisting of an untreated *n*-type surface with that treated with (b) TiO_2 fractional nanostructured island depositions. PH_3 was pulsed onto the interfaces (a, b) with a 300 s half cycle followed by a 300 s half cycle UHP nitrogen cleaning. In all cases the introduction of PH_3 leads to a significant *decrease* in resistance which is enhanced with the introduction of nanostructure fractional depositions of TiO_2. The system was purged with UHP nitrogen for 1800 s before operation.

with the *n*-type interface.

Figure 3.13 demonstrates the response behavior for a Cu_xO decorated PS interface where, at 1–3 ppm of PH_3, we observe a response corresponding to a decreasing resistance (increased conductance). At 3 ppm the conductance has decreased relative to that at 1 and 2 ppm and at 4, 5, and 10 ppm the resistance increases, indicating the interaction with an analyte that extracts as opposed to donates electrons to the PS interface. We theorize that this interaction behavior results from the chemical conversion of PH_3 on the *n*-type PS interface as PH_3 interacts with the phosphorus dopant in the silicon.

Figure 3.14 demonstrates the result observed after an *n*-type sensor system is exposed to a large concentration of PH_3 (80 ppm) for half an hour. The data in Figure 3.14 show the trailing edge of a large phosphine signal where the concentration of PH_3 has been sufficient to saturate the sensor, leaving it with a decreased resistance. The corresponding feature

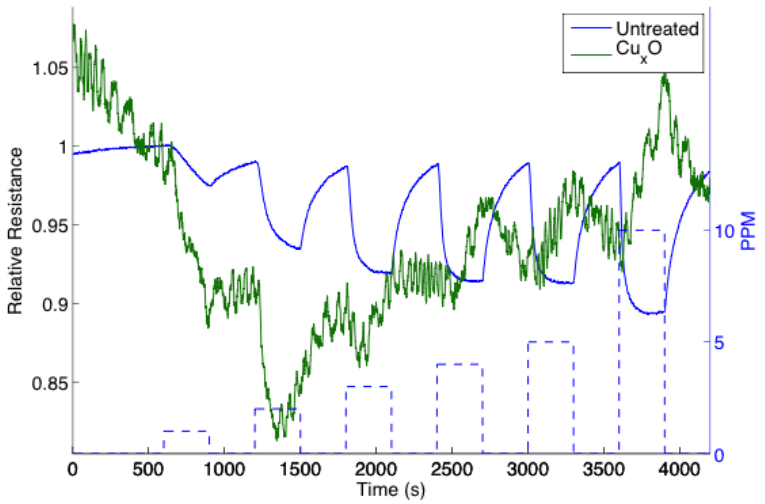

Figure 3.13: Comparison of responses to 1–5, and 10 ppm PH_3 after purging with UHP nitrogen for 1800 s before operation for a PS interface consisting of an untreated n-type surface with that treated with a Cu_xO fractional nanostructured island deposition. The introduction of PH_3 to the Cu_xO decorated interface at first leads to a decrease in resistance. At analyte concentrations in excess of 2 ppm, the response is reversing, suggesting that the PH_3 is converted on the copper oxide decorated PS interface. PH_3 was pulsed onto the interfaces with a 300 s half cycle followed by a 300 s half cycle UHP nitrogen cleaning.

associated with the pulsed PH_3 analyte observed after this treatment cannot be associated with the character of the basic analyte PH_3, its lack of an electron affinity, and its ability to provide electrons which Figure 3.13 demonstrates should lead to a decreased resistance. Rather, the observed signal most likely is from a transient species that has a positive electron affinity generated by the interaction of PH_3 with the n-type PS interface. A strong candidate is the PH_2 free radical whose significant electron affinity (1.25 eV.) [167,168] and ionization potential (9.83 eV.) [167–169] should lead to the extraction of electrons from the PS interface and an increase in the conductometric resistance. This change in the resistance suggest a change in the charge density of 340% or around 1.6 e13 per cm^3, which is an order of magnitude smaller than the density of the PH_3 at 80 ppm.

The results presented in Figures 3.8–3.12 for the interaction of PH_3 with untreated and fractional nanostructure treated p, $p+$ and n-type porous silicon clearly indicate a diversity of dynamic reversible interactions for basic phosphine with majority electron charge carriers and holes. The data presented in Figures 8–11 demonstrate important correlations with the schematic temperature dependence of an extrinsic semiconductor. First the temperature

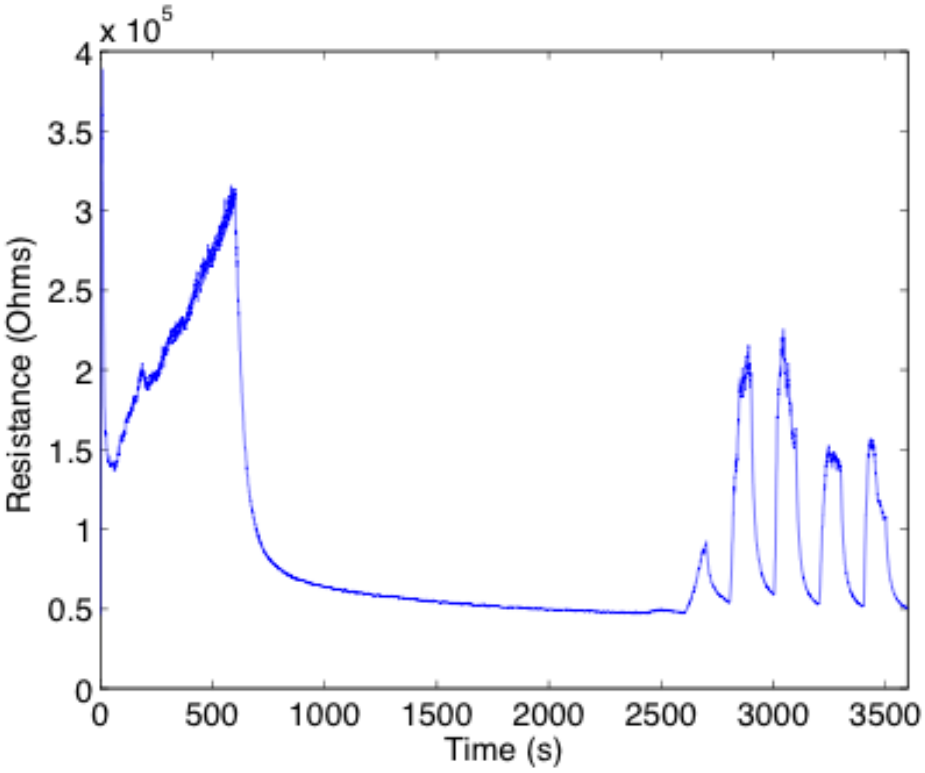

Figure 3.14: Sensor response after exposure to a high concentration of PH_3 (80 ppm) for half an hour. In this figure, the high concentration of PH_3 produces a positive signal, which for the concentration applied is quenched relative to the responses in figures 3.9, 3.12 and 3.13. The subsequent response spectrum after a period of 1500 seconds, indicative of the formation of an analyte with non-negligible electron affinity, is tentatively associated with PH_2.

dependence for the p-type semiconductors is such that one can expect available holes for a p-type system at room temperature [170]. PH_3 corresponds to a moderately strong base with a doubly occupied HOMO similar to ammonia. As Figure 3.2 demonstrates, PH_3, induces an increase in the resistance of a "p-type" porous silicon (PS) surface as would be expected when a base contributes electrons to "p-type" PS and thus diminishes the majority carrier concentration. The nanostructured metal oxide islands [74, 126, 171] we have deposited to the surface of PS to increase the surface activity are selected to modify and direct a dominant electron transduction for rapidly responding, reversible PS gas sensors.

PH_3 is a moderately strong base. Thus, its position among several bases as indicated in Table 3.1 which summarizes primarily the acid-base strength of ions associated with the oxides. From this table, the IHSAB model suggests that PH_3 will give the best reversible

response with either a TiO_2 or an Au_xO (x>>1) modified PS surface since Ti^{+4} represents a much stronger acid whereas Au_xO represents a very weak acid. Cu_xO represents a borderline to weak acid (Cu^{+1},$^{+2}$), and provides a decreased response as it lies closer in molecular orbital makeup to PH_3.

3.3 Interaction with an untreated Porous Silicon Interface for other gases

We now consider the interaction with the gases NH_3 NO and NO_2. NO_2 represents a moderately strong acid [172] whereas NH_3 corresponds to a strong base [173]. We expect these analytes to induce the opposite response from an n-type and p-type semiconductor interface. NO, however, is an amphoteric free radical [174] and, for this reason, its interactions are far less straightforward as will be seen later. In Figure 15, we display the typical response changes for an untreated n-type PS interface to NO_2, NO, and NH_3.

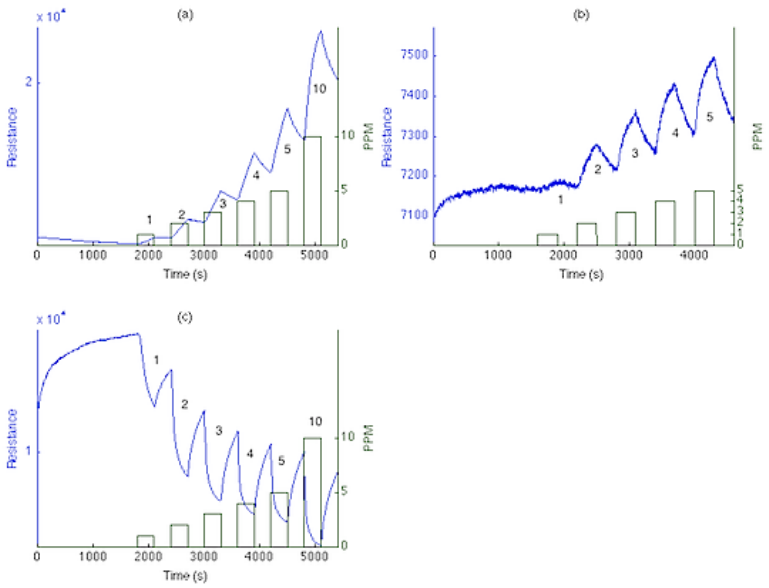

Figure 3.15: Response of n-type PS micro/nanostructured interface to 1,2,3,4,5 and 10 ppm NO_2 (a) and NH_3 (c) and 1-5 ppm NO (b) after purging with UHP nitrogen for 1800s. These gases were pulsed onto the PS interface with a 300s half-cyclefollowed by a 300s half-cycle UHP cleaning.

The positive resistance changes for NO_2 and NO vary linearly and correspond to an exposure to 1,2,3,4,5 ppm (10 for NO_2) of test gas. The recorded signal for NO_2 on n-type PS, is that of an acid which has a significant electron affinity [172] and withdraws electrons from the PS interface. In contrast, we observe a decrease in resistance as NO_2 withdraws electrons from p-type PS [10]. The absolute recorded signal for NO on n-type PS corresponds to 100 Ohms/ppm [137] which considerably exceeds the 2 Ohm/ppm signal recorded for p-type PS [10]. For both n- and p-type PS, the observed change in response corresponds

to an increased resistance. Thus, with n-type PS, the amphoteric NO radical acts like an acid withdrawing electrons whereas with p-type PS, the NO radical acts like a soft base, contributing electrons but at a much lower rate. The response for the moderately hard base, NH_3 (Fig. 3.15(a)), corresponds to a significant drop in resistance which, while it appears linear to 4ppm, begins to saturate at concentrations around of 5 ppm and definitely is partially quenched at 10 ppm.

3.3.1 Interaction with Nanostructure Modified Porous Silicon Interfaces

Table 3.4 summarizes the changes in response observed when n-type porous silicon is treated with fractional nanostructured depositions of several metal oxides including TiO_2, SnO_x, NiO, Cu_xO, and Au_xO. These data should be compared with the results obtained for the fractional deposition of nanostructures on a p-type PS interface (Table 3.2). This comparison indicates that there are clear and significant differences between the n- and p-type systems. While Table 3.5, shows the changes in the derivative of the observed response. Note that the derivatives are similar to the observed response changes and follow the IHSAB principle.

Table 3.4: Response change due to nanostructured metal oxide depositions on n-type silicon.

	Titanium (TiO_2)	Tin (SnO_2)	Nickel (NiO)	Copper (Cu_xO)	Gold (Au_xO)
NO	-12	-2*	4	1.2	1.5-2
NO_2	0.75**	0.5**	(0.9-1)	1	1.1
NH_3	(3.5-4)	2.5	1.5	2	3
Relative increase or decrease in resistance of TiO_2, SnO_x, NiO, Cu_xO, and Au_xO clustered oxide treated "n-type" PS interfaces. The table constitutes a response matrix for the gases NO, NO_2, and NH_3. a-dynamic time response, * indicates reversal in responce with analyte exposure, ** indicates initial response.					

Table 3.5: The derivative response change due to nanostructured metal oxide depositions on n-type silicon.

	Titanium (TiO_2)	Tin (SnO_2)	Nickel (NiO)	Copper (Cu_xO)	Gold (Au_xO)
NO	-3	-1	3	1.3	2
NO_2	0.75	0.5	3	2	1.1
NH_3	6	4	3	1.4	1.5

Figure 3.16 compares the response of a prepared " n-type" PS interface to NH_3 with that for the same PS interface treated with SnO_x, NiO, and Au_xO nanostructures. The responses are distinct and do not have the same magnitude for the same concentration of the tested gas. This feature allows us to begin to develop a selectivity matrix for PS gas detection.

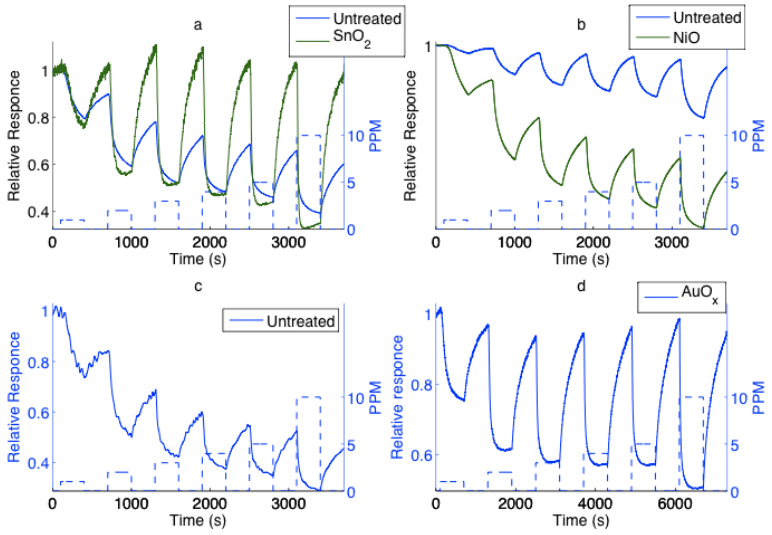

Figure 3.16: Comparison of sensor responses to 1,2,3,4,5 and 10 ppm NH_3 (a) before and after treatment with SnO_2, (b) before and after treatment with NiO, (c) before and (d) after treatment with Au_xO.

The fractionally deposited nanostructures clearly enhance the transfer of electrons from NH_3 to the *n*-type PS interface. The degree of enhancement follows the tenants of the IHSAB principle as physisorption (electron transduction) is greatly enhanced by the moderately strong base ammonia as it interacts with the very strong acid SnO_2 and the very weak acid Au_xO.

The enhancement observed for the NiO nanostructure deposited interface is less than that for either the SnO_2 or Au_xO treated interfaces. The borderline acidity of NiO (Table 3.1), intermediate to that of SnO_x and Au_xO, places the hard/soft nature of the NiO nanostructures in much closer proximity (Figure 3.3) to ammonia in orbital differences. This match up results in the diminished enhancement of reversible electron transduction. These results are consistent with observations of the interaction of NH_3 with nanostructure treated *p*-type silicon (Table 3.2). However, the absolute resistance changes are more pronounced in all the sensors as the NH_3 molecules now interact with the highly mobile donor electrons of the extrinsic semiconductor.

While the response of the untreated PS interface varies linearly with concentration over the range 1-5 ppm, this is not the case for the SnO_2 and Au_xO treated systems. Here, especially for the Au_xO treated interface, the resistance reaches a limiting lower value. The

nanostructured oxides enhance the rate of electron transfer to the PS interface via electron transduction. In all of the cases outlined in Figure 3.16, the ratio of the 10 to 5 ppm resistance change does not double, again indicating a saturation effect and a limit on the conductance.

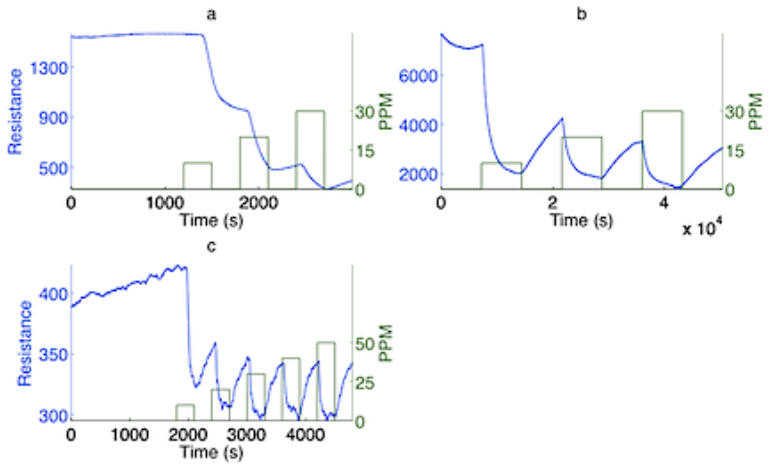

Figure 3.17: Comparison of responses for NH_3 in the concentration range 10-250 ppm. (a) and (b) correspond to the response of untreated and Au_xO treated n-type PS interfaces to 10, 20, and 30 ppm NH_3. (c) corresponds to the response of an untreated n-type PS interface to 50-250 ppm of NH_3. With the exception of the NH_3- Au_xO data whose time scale is indicated in the figure, the gases were pulsed onto these interfaces with a 300s half-cycle followed by a 300s half-cycle UHP cleaning.

Figures 3.17 (a) and (b) demonstrate a slightly different behavior for the response of untreated and Au_xO treated n-type PS interfaces to higher concentrations of NH_3. The interaction of ammonia with an n-type PS interface demonstrates a significant drop in resistance associated with exposure to 10 ppm of NH_3, (Figure 3.17(a)). After the initial drop in resistance, the system reaches a plateau response that appears to saturate and remain at the lower resistance even though there is nothing on the surface to limit this reaction. The subsequent exposure to 20 ppm NH_3 again decreases the resistance, however, it is clear that there is a minimal concentration dependence. The introduction of a second nitrogen purge again leads to a plateau in the response to a lower resistance. Upon introducing 30 ppm of NH_3 to this sensor we observe a significantly muted resistance decrease even though the introduced gas concentration has increased. Removing the NH_3 leads to a slight increase in the baseline established upon exposure to 30 ppm NH_3. This behavior could be related to

the nature of the majority carriers, electrons, in this n-type semiconductor and the interaction as these electrons, contributed to the donor level population of the PS interface by NH_3, reach a saturated level where the electrochemical potentials are equal .

The results obtained for an Au_xO treated prepared n-type PS interface are considerably more pronounced. Figure 3.17 (b) demonstrates a very significant resistance drop upon introduction of 10 ppm NH_3 after an extended nitrogen purge. This is followed by a series of very much smaller and virtually constant decreases in the resistance with introduction of progressively higher NH_3 concentrations after nitrogen purging. This behavior is directly related to the combination of the weak acid nature of the Au_xO nanostructured islands deposited to the PS interface, their ability to enhance the rate of electron uptake and interaction with the majority carriers, again electrons, in the semiconductor, and the saturation of electron donation.

Figure 3.17 (c) displays the observed response to NH_3 at concentrations ranging from 50 to 250 ppm. This very high ppm response is very similar to that for the Au_xO treated n-type PS interface in the range 10-30 ppm. It is clear that, in both cases, we are observing a bottoming-out of the resistance as NH_3 contributes electrons to the donor level population. This implies a limit to the electron contribution to the donor levels of the semiconductor.

3.3.2 NO on *n*-type silicon

The data obtained for the amphoteric free radical NO are intriguing. Figure 3.18 compares the response for a prepared "*n*-type" PS interface with that for the same PS interface treated with TiO_2, SnO_2, NiO, Cu_xO, and Au_XO nanostructures. In all cases relative measurements for the treated and untreated PS samples exposed to NO at 1,2,3,4,5, and 10 ppm are considered.

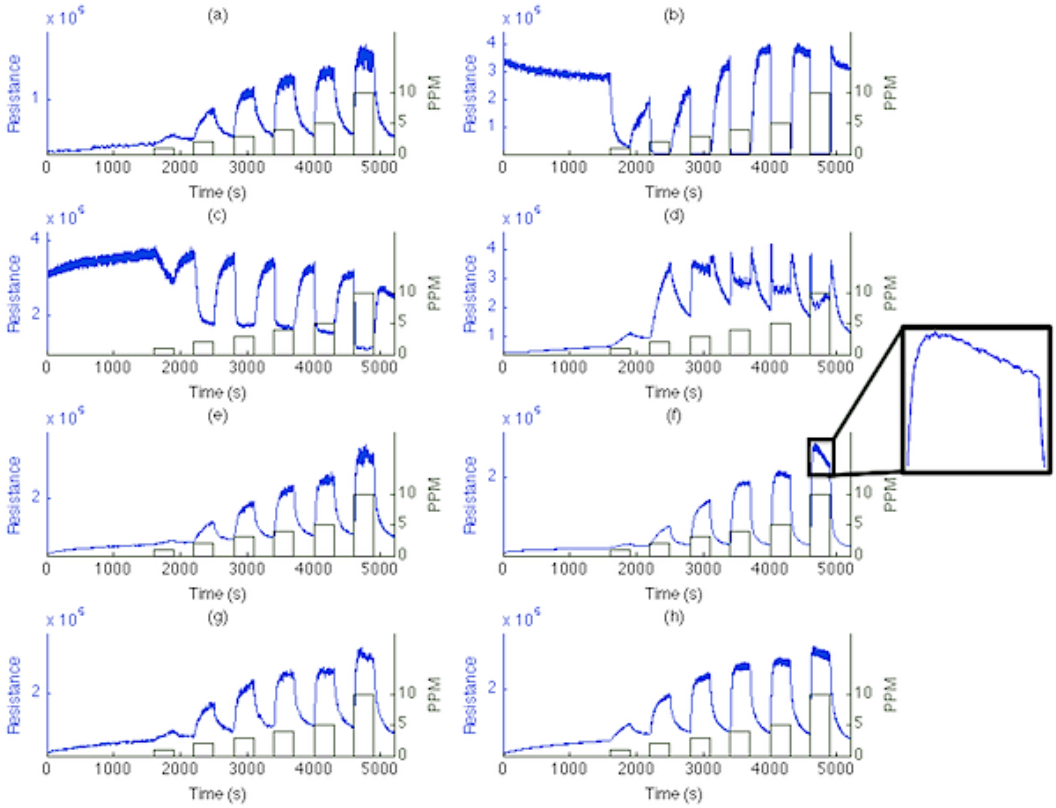

Figure 3.18: Comparison of responses for 1,2,3,4,5, and 10 ppm NO for (a), (e), (g) sensors consisting of an untreated *n*-type PS interface with those treated with (b) TiO_2 , (c) SnO_2 , (d) NiO , (f) Cu_xO , and (h) Au_xO fractional nanostructured island depositions. The untreated PS interface in (a) is that treated with TiO_2 in (b). The response for the untreated PS interface in (a) is duplicated precisely for the untreated PS interfaces to which we compare in (c) for SnO_x and (d) for NiO . The untreated PS responses in (e) and (g) correlate with the Cu_xO (f) and Au_xO responses in (h) respectively. NO was pulsed onto these interfaces with a 300s half-cycle followed by a 300s half-cycle UHP nitrogen cleaning.

The data in Figs. 3.18 (a), (e), and (g) correspond to untreated PS interfaces. The responses show a rise in resistance indicating that NO acts as a weak acid, removing electrons from the *n*-type PS interface, and leading to an increase in resistance (decrease in

conductance) associated primarily with the depletion of donor level electrons. The observed responses for the untreated samples are virtually linear to 5 ppm although a slight delay in the gas system flow to the sensor and response is evident below 2 ppm. The observed response again does not double from 5 to 10 ppm, indicating a saturation of the available levels manifest as a decrease in the rate of conductance increase at the highest NO concentrations.

The variations in response observed for the nanostructure treated PS interfaces, while reflecting the donor level population, demonstrate the important role played by the deposited nanostructures and the nature of acid/base interaction they direct. The observed trends are remarkable and correlate well with the relative responses observed as NO interacts with "p-type" PS (Table 3.2) [10]. These data, for *p*-type PS lead to the positioning of NO ($\approx$ weak base) below Cu^{+2}- Cu^{+1} in Table 3, based on the relative response matrix for SnO_2, NiO, Cu_xO, and Au_xO.

The acid strength of the nanostructures deposited to the *n*-type PS interface decreases from the strongest acid TiO_2 to the weakest acid Au_xO in the order $TiO_2 > SnO_2 > NiO > Cu_xO > Au_xO$. Figs. 18 (e) - (h) demonstrate that the deposition of both Au_xO and Cu_xO nanostructures increases the response of the PS interface (Table 3) and that the increase is greater for the weaker acid Au_xO. As observed for the nanostructure modified *p*-type interface, the data suggest that the acid/base strengths of NO and Cu_xO are comparable. Here, Au_xO and Cu_xO act to slightly enhance the electron withdrawing power of the NO radical which suggests that they represent softer acids on the *n*-type PS interface. The effect of the enhanced rate of transfer in Figs. 3.18(e) and (f) are shown by both a decrease in the rate of conductance increase with concentration and a decrease in response with time at the highest concentrations.

The observed response for the more acidic metal oxides is in distinct contrast to that for Cu_xO and Au_xO. By comparison, the response depicted in Fig. 3.18 (a) for the untreated prepared PS interface is identical for the three samples used for the TiO_2, SnO_2, and NiO treated systems. The nanostructure deposition of *n*-type PS with the strong acids TiO_2 and SnO_2 results in a significant reversal of response as the treated PS interface acts to

remove electrons from the NO radical. The amphoteric NO radical thus acts as a base. The effect is far more pronounced for TiO_2 then in the SnO_2 decorated surface indicating a much greater acid strength for TiO_2. This relative acid strength is also apparent for the PH_3 interaction with a p-type PS interface mentioned earlier in the chapter [9].

When NiO nanostructures are deposited to the prepared *n*-type PS interface, the observed dynamic response is indeed intriguing. NiO is an intermediate acid. Figure 3.18 (d) demonstrates that at the lowest NO concentrations, the response of the *n*-type PS interface is enhanced as the ratio of the response 2ppm/ 1ppm increases significantly relative to that for the untreated *n*-type PS. However, at an NO concentration of 3ppm, the dynamic response increases to a maximum, then decreases, oscillates, and finally increases once the gas is turned off. This nonlinear behavior is even more pronounced at 4, 5, and 10 ppm.

An explanation for this phenomenon is that as the NO concentration increases, the transfer of electrons to NO increases to a maximum. This transfer reaches a limit when the decorated *n*-type PS interface is sufficiently depleted of electrons that the interface acts as a stronger acid than the amphoteric NO radical. At this point electrons are extracted from NO (acting as a base) accompanied by a decrease in the measured dynamic resistance (increase in conductance) as the semiconductor donor levels are repopulated. In other words, at the lowest concentrations the NiO nanostructure deposited interface mimics the simple behavior of the weak acids Cu_XO and Au_xO. At higher concentrations, the dynamic interplay between the metal oxide particles, the available surface electrons, and the analyte gas transmute the surface. The surface then acts like it was treated with the stronger nanostructured acids TiO_2 and SnO_2. In summary, NO acts as both an acid and a base as a function of concentration for the intermediate acid sites of NiO.

The intermediate behavior observed for NiO would appear to correlate to the results obtained for *p*-type systems as exemplified in Figure 15. Here, NO as an analyte interacting with the *p*-type PS interface was placed as a weak base [74] in a region close to the region between Cu^{+2} and Ni^{+2} . This is, in effect, the fulcrum region, which is also observed for the *n*-type PS interface.

3.3.3 NO_2 on *n*-type silicon

NO_2 represents a moderately strong acid. The behavior of this acid with an *n*-type surface, and the corresponding increase in resistance (Figure 15(a)) with concentration is not surprising. However, unlike NO, NO_2 has a large and substantial electron affinity; this affinity causes a significantly different behavior than that of the NO radical for a similar interface preparation.

The electron affinity of NO_2 greatly enhances electron withdrawal and can deplete the donor level population. However, this depletion happens at much higher concentrations then NO. The extent of this process, while it depends on the initial PS donor level population, is such that the *n*-type interface, once depleted, can become more electron withdrawing than NO_2, in a similar manner to the results seen for NO with TiO_2 and SnO_2. This interaction can subsequently produce a response for both SnO_2 and Au_xO nanostructure treated surfaces, which mimics that of NH_3 (Figure 3.16,17).

Care must be taken while making the measurements with the NO_2 system. While NO_2 is a moderate acid, NO_2^- , a byproduct of NO_2 extracting an electron from the *n*-type PS interface, is a moderate to strong base. Figure 3.3 suggest that a *p*- or *n*-type PS surface corresponds to a borderline acidic surface. For this reason, we expect the chemical interaction (chemisorption) with NO_2 and NO_2^-, as dictated by the IHSAB/HSAB principle, to be minimal. If, however, the PS surface is treated with nanostructured SnO_2, we expect a strong chemical interaction between this strong acid and NO_2^-. A significant dynamic interaction also characterizes the interaction of NO_2 with a TiO_2 nanostructured surface. In contrast, the fractional nanostructure deposition of Cu_xO has virtually no effect on the PS interface and the fractional nanostructure deposition of Au_xO creates an interface (Table 4), which appears to promote a modest enhancement of the rate of electron transfer to NO_2.

The data in Figure 3.19 corresponds to exposures of 1, 2, 3, 4, 5, and 10 ppm of test gas, as denoted by the green saw-teeth in the figures, which indicate the time range over which the gas is turned on and off. The untreated sensor interface in Figure 3.19(a) and the Cu_xO treated interface in Figure 3.19(d) for which the NO_2 signal varies linearly to 3ppm are distinct from those for the untreated sensors in Figures 19(c) and 19(e) which are somewhat

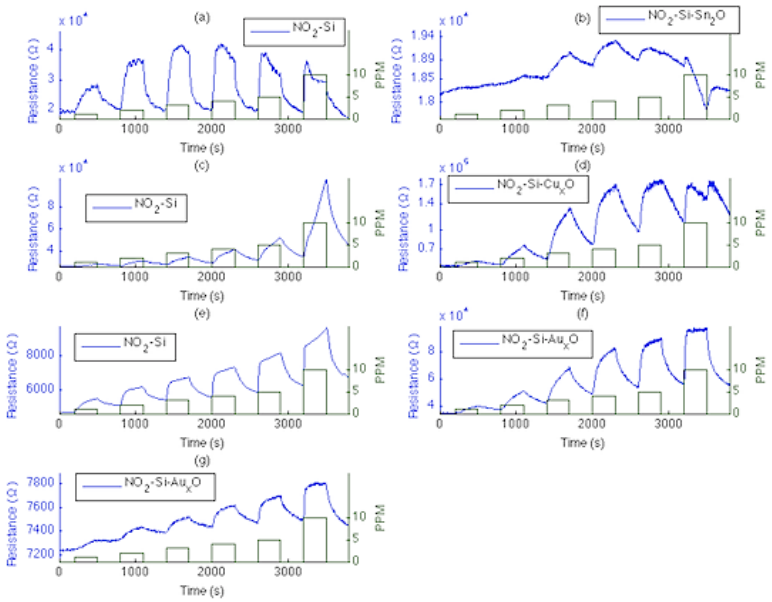

Figure 3.19: Comparison of responses to 1,2,3,4,5, and 10 ppm NO_2 for (a), (c), and (e) PS interfaces consisting of an untreated n-type surface with those treated with (b) SnO_x , (d) Cu_xO , and (f,g) Au_xO fractional nanostructured island depositions.

less responsive but display a linear response to 5ppm. This less than linear increase in signal with concentration indicates a more rapid response to the limit of electron depletion, which is reached at lower concentrations for the more sensitive interfaces. At concentrations in excess of 5ppm all of the systems begin to display a quenching of the resistance response.

The results obtained for the PS interface treated with nanostructures of TiO_2 and SnO_x, both strong acids, with the moderate to weak acid Cu_xO, and with the very weak acid Au_XO, exemplify the dynamic interplay for these systems and the importance of the coupling to the PS interface created by the nanostructure deposits. The IHSAB principle and the acid/base character of theses metal oxides dictate the degree of this coupling. The results obtained with TiO_2 also demonstrate the important dynamic interplay induced by this strongly acidic nanostructure as it competes with NO_2 for electrons. Remnant effects further characterize the manifestation of this electron dynamics and donor level electron depletion for the SnO_x and Au_xO system. At elevated pressure, we observe the time dependent interaction of NO_2 and NO with an untreated PS surface.

Figure 3.19(b) demonstrates the IHSAB effect, which the strong acid SnO_x has on the

NO_2 interaction with the PS interface. Here, both an acidic analyte and the nanostructure modified PS surface compete for electrons. If NO_2 and SnO_x compete effectively for electrons, the competition might be expected to diminish the sensitivity of the interface, influencing directed electron transduction as measured by a significantly diminished resistance change. We do observe a muted response. However, the weak and diffuse nature of the observed response after SnO_x treatment suggests that it is equally likely to be strongly influenced by chemisorption. While NO_2 is a moderate acid, NO_2^-, which can be formed as NO_2 extracts an electron from the *n*-type PS interface, corresponds to a moderate to strong base. Figure 3.3 suggests that an *n*-type PS surface corresponds to a borderline acidic surface. For this reason, we expect chemical interaction (chemisorption) with NO_2 and NO_2^- as dictated by the IHSAB/HSAB principle to be of only moderate effect. If, however, the PS surface is treated with nanostructured SnO_x , we expect a strong chemical interaction between this strong acid and NO_2^-. The muted and diffuse response with concentration in Figure 3.19(b) signals this chemisorption. It is to be emphasized that the base strength of NO_2^- and the acid strength of SnO_x are much more closely matched than those of the much stronger acid, TiO_2, or the weaker acids Cu_xO and Au_xO. For this reason we expect a chemisorptive interaction. [74]

In contrast to SnO_x, the nanostructured deposition of Au_xO, a weak acid (Table 3.1) significantly enhances the rate of electron transfer to NO_2. However, in comparing Figure 3.19(f), where the Au_xO nanostructures are deposited in a ten second exposure, and Figure 3.19(g), where the PS interface is deposited for a 30 second exposure, with the data for the untreated PS interfaces in Figures 19(e), we observe a significant enhancement at 10s which is considerably diminished on exposure for 30s. The decrease in sensitivity at higher Au_xO concentrations results as the second exposure over-deposits the PS interface with electroless gold. Cross talk between the deposited nanostructures decreases the efficiency of electron transduction and leads to a notable decrease in response. This emphasizes the requirement for careful fractional deposition to the PS interface. For the optimally deposited Au_xO system, the response verses the untreated PS surface is multiplied by a factor of approximately 5. We find that the deposition of Cu_xO nanostructures in fractional

deposition to the prepared n-type interface of Figure 3.19(c) (deposited surface 19(d)) increases the system response by in excess of a factor of 2. The response of the Cu_xO treated interface rises linearly, but much more rapidly than that of the untreated interface to 3 ppm. This response, however, corresponds to an increase in the rate of electron removal, which begins to quench at 4 ppm in contrast to the untreated PS interface. Further at 10 ppm we observe directly the effect of the dynamic behavior of the electron transduction. The resistance first increases sharply as NO_2 is extracting electrons. However, this extraction is soon countered as the donor level population is depleted to the extent that the decorated Cu_xO-PS interface begins to act as a stronger acid than NO_2. This effect is even more apparent in the TiO_2-based systems discussed below.

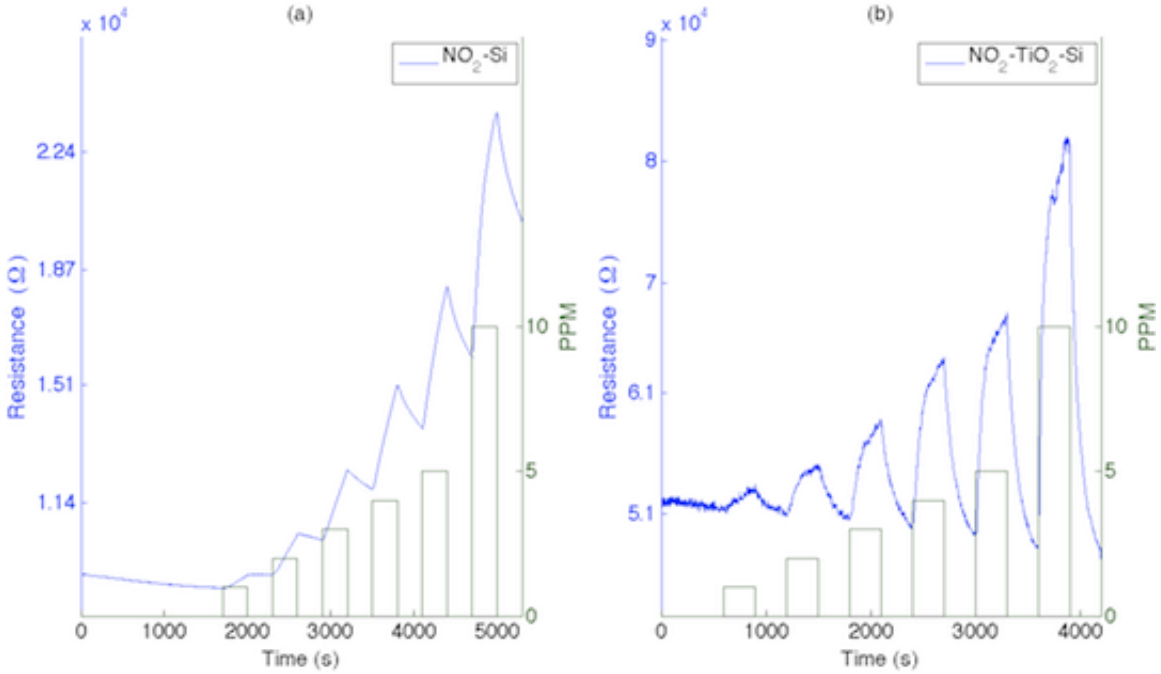

Figure 3.20: Comparison of NO_2 response to (a) an untreated and (b) a TiO_2 nanostructure deposited PS interfaces for low TiO_2 deposition. In both cases the response corresponds to an increase in resistance with NO_2 concentration as NO_2 dominates the TiO_2 nanostructures and extracts electrons.).

Figures 3.20-22 demonstrate the effect that TiO_2 fractional nanostructured depositions have on the response of an n-type PS interface to NO_2. Figures 3.20(b) corresponds to the results obtained for low TiO_2 deposition times ($\leq$10s) or under conditions that do not produce sufficient concentrations of the strongly acidic TiO_2 to facilitate its ability

to dominate NO_2 and attract electrons that are transferred to the PS interface. Here, the response to NO_2, which extracts electrons, leads to a resistance increase (conductance decrease). The TiO_2 treated system has a similar but weaker response than the untreated interface .

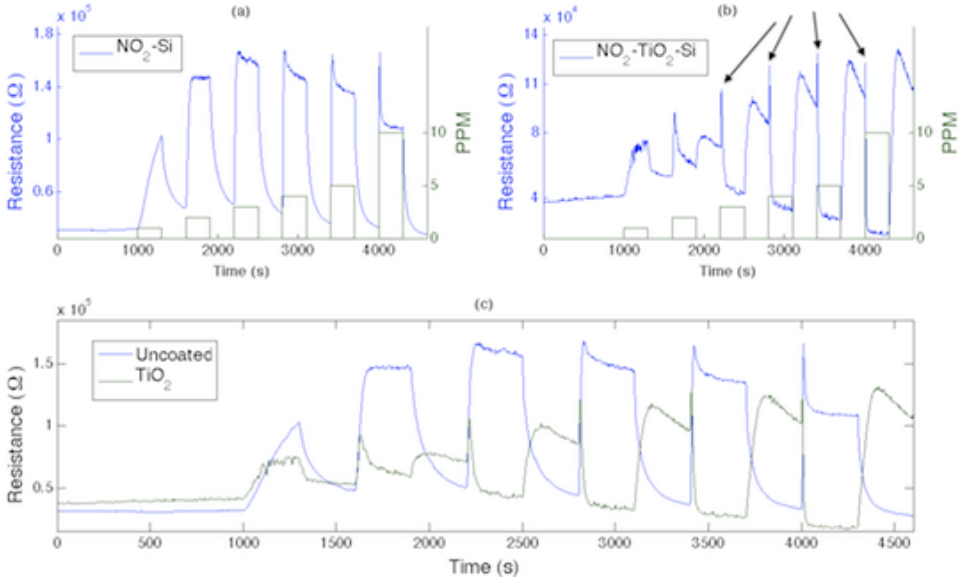

Figure 3.21: Comparison of responses to 1,2,3,4,5, and 10 ppm NO_2 for (a) a PS interface consisting of an untreated n-type surface with (b) that treated with TiO_2 fractional nanostructured island depositions. The figure (c) corresponds to the overlap of the response observed for the untreated PS interface (blue) to that modified with TiO_2 (green). The arrows point to the measured peaks for the TiO_2 island system.

Figures 3.21 (a-c) demonstrate the effect that an intermediate TiO_2 fractional nanostructured deposition (20s) has on the response of an n-type PS interface to NO_2. Figure 3.21(a) corresponds to the response of the prepared untreated PS interface while Figure 3.21(b) demonstrates the response after TiO_2 is introduced. The results, demonstrated also in the overlapped response data of Figure 3.21(c), are striking. Here at the fractional concentrations deposited, the strong acid, TiO_2 [74], competes quite effectively with the moderately strong acid, NO_2, for the available electrons in this system. The untreated PS interface (Figure 3.21(a)) displays a significant increase in resistance as NO_2 attracts electrons and depletes majority carriers. However, at the higher NO_2 concentrations, we observe a peaking in the resistance followed by a near exponential decay of the resistance. The rate of exponential decay observed in Figure 3.21(a) is seen to increase in magnitude with

increasing NO_2 concentration in the range 4- 10 ppm. The intensity is seen to maximize at ˜3 ppm and the initial intensity maxima are similar for 3,4,5,and 10 ppm. The effects of electron depletion and subsequent repopulation are manifest at the higher concentrations.

Figure 3.21 (b) demonstrates results obtained at an intermediate TiO_2 nanostructure deposition. For those NO_2 analyle concentrations in excess of 2 ppm, as the response begins to increase with the introduction of NO_2, it is suddenly and rapidly quenched. This behavior is more pronounced at higher analyte concentrations. The spike-like response is also illustrated in Figure 3.21(c). As NO_2 attempts to extract electrons from the decorated PS interface, the resistance rises rapidly to a point when the electron depletion reaches a limiting value. Here, the nanostructured TiO_2 islands coupled to the PS interface interact, preventing further electron withdrawal, and reversing the electron flow so as to increase the donor and conduction level electron concentrations. This is manifest by a sharp decrease in the resistance. The affect clearly onsets at 2 ppm and increases in a manner proportional to concentration. The dynamic nature of this interplay is further evident as the resistance drops to a minimum value and then begins to again increase when the NO_2 is removed. As NO_2 is introduced in a new cycle the spike-like increase in resistance is again observed followed by a sharp drop in resistance. This behavior is explained as TiO_2 competes with and counteracts the extraction of electrons by NO_2, insures the flow of electrons to the decorated n-type PS interface, and leads to the significant decrease in resistance. The process of interaction is a dynamic one as TiO_2 and NO_2 vie for the available electrons. As a result the observed increase in resistance decreases by ˜25% relative to the untreated PS interface.

Table 3.6: Observed dynamic interplay resulting from the depletion of donor levels and subsequence reversal electron exchange associated with the interaction of NO_2 and a TiO_2 treated PS interface (Figure 3.21). The elapsed time follows a linear inverse with concentration..

	2 ppm	3 ppm	4 ppm	5 ppm	10 ppm
Elapsed time till peak maximum	32 s	15 s	11 s	9 s	4 s
Peak width s	57 s	14 s	8 s	5 s	1 s

The spike like features depicted in Figures 3.21(b) and (c) show a clear dependence on the NO_2 analyte concentration. These features show a concentration dependence as the elapsed time to their appearance displays an inverse linear proportionality to the concentration. In addition as the concentration of analyte increases the peak width decreases and displays a sharp exponential decay. This time dependent behavior and the features that are observed are distinct from those associated with analyte diffusion. Figure 3.21(a) would suggest that the desorption kinetics associated with NO_2 is quite efficient. While adsorption to the PS interface influences the observed process this unusual behavior is difficult to relate to the adsorption/desorption process as it appears more closely related to the interplay associated with electron exchange. As opposed to the adsorption and desorption kinetics associated in part with gaseous diffusion the observed behavior appears to be characteristic of systems where analyte and interface compete for electrons.

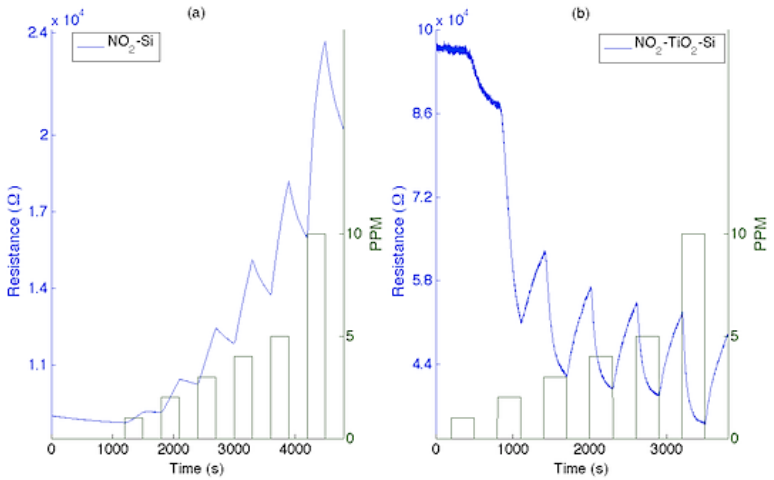

Figure 3.22: Comparison of NO_2 response to (a) an untreated and (b) a TiO_2 nanostructure deposited PS interface for TiO_2 depositions notably higher than those associated with Figures 4 and 5. The response curve for the untreated n-type interface corresponds to an increase in resistance with NO_2 concentration; the TiO_2 decorated surface displays a decrease in resistance (increase in conductance) as TiO_2 facilitates electron extraction from NO_2. Here, the signal begins to saturate between 3 and 4 ppm*.

Figure 3.22 (b) demonstrates results at a somewhat higher TiO_2 concentration (30s deposition time) Here, the TiO_2 coupled to the PS interface creates a surface which can overcome the electron withdrawing power of NO_2. Now, the response is that of a system which attracts electrons to the PS interface leading to a decrease in resistance (increase in

conductance). By comparison the data in Figure fig:c23 is intriguing in that it represents a variation of response as a function of NO_2 concentration. Here, we have converted the TiO_2 nanostructures deposited as in figrue 3.22 to their corresponding oxynitride, $TiO_{2-x}N_x$ [66,171]. This creates a more basic interface and thus diminishes the ability of the deposited nanostructures to attract electrons. At NO_2 concentrations $\leq$ 5ppm, the system again responds to the gas by removing electrons from NO_2. This corresponds to a decrease in resistance although the decrease is less than that for the TiO_2 decorated system. However, an NO_2 concentration of 10 ppm is now sufficient to reverse this response, leading to a positive resistance change, which results from a dominant electron extraction by NO_2.

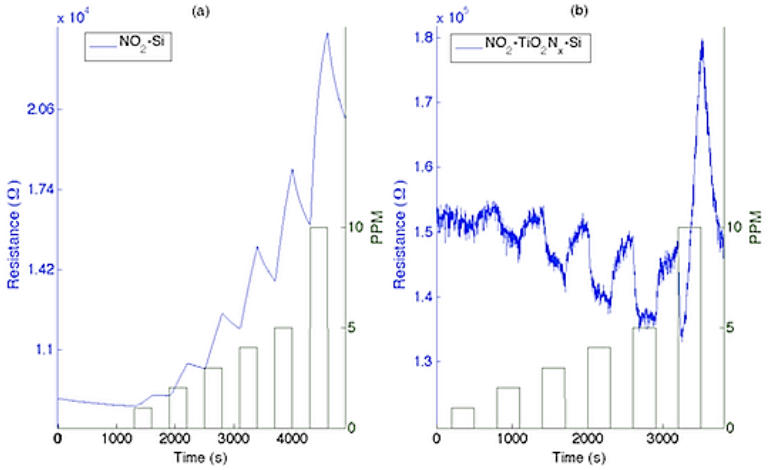

Figure 3.23: Comparison of NO_2 response to (a) an untreated and (b) a $TiO_{2-x}N_x$ treated PS interface.

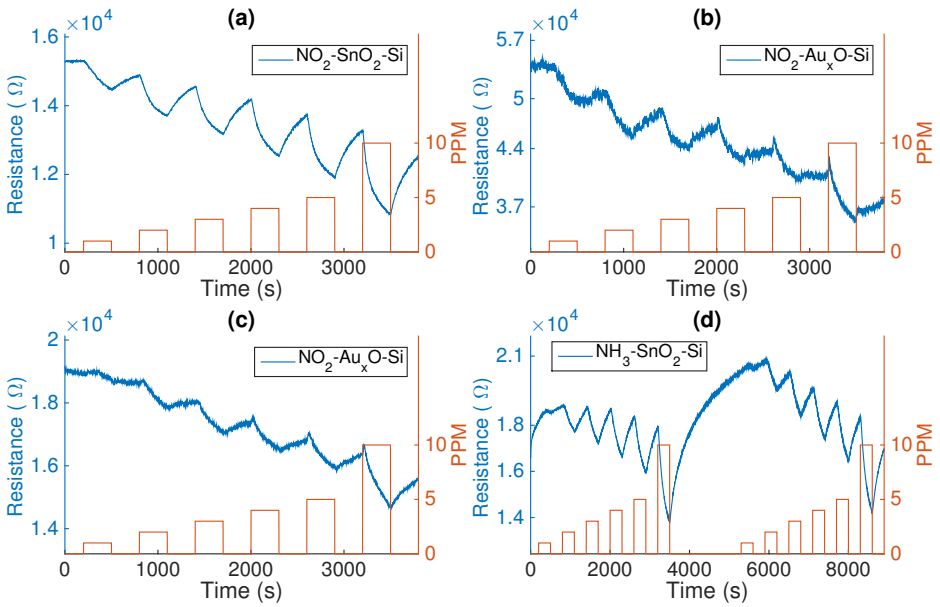

Figure 3.24: Comparison of responses to 1,2,3,4,5,and 10 ppm of analyte gas. 3.24(a) NO_2 interacting with an SnO_x treated n-type PS surface 24 hours after an initial exposure produced the response in Figure 3.19(b). Figure 3.24 (b and c) corresponds to the response of Au_xO treated (10 and 30s exposures) PS surfaces for the surfaces generating the responses in Figures 3.19 (f and g) 24 hours earlier. Figure 3.24(d) corresponds to the response (two cycles) to NH_3 of an SnO_x treated n-type PS surface also used in Figure 3.24(a). Note that the scale for this figure is compressed relative to Figures 3.24 (a,b,c).

In all of the systems studied here, the electron affinity of NO_2 enhances its ability to withdraw electrons, eventually depleting the donor level electron population. The extent of this process and the dynamics of its time dependent reversal is pronounced as the interface, once depleted, becomes more electron withdrawing than NO_2. In compliment to the time-dependent behavior of the electron transduction in TiO_2, we find that the depletion process can lead to significant remnant effects. Figures 3.24(a-d) demonstrates these remnant effects as we observe a response for both the SnO_x and Au_xO nanostructure modified and depleted surfaces which mimics that observed for interaction with an electron donating analyte. Figure 3.24(a) depicts the response of the SnO_x treated PS interface 24 hours after the initial experiments as described in Figures 19(a) and 19(b). The observed response is that which would be expected of an analyte that is contributing electrons to the SnO_x/n-type PS interface. The decorated PS sample is now extracting electrons from NO_2. A similar

behavior is observed for the Au_xO decorated PS (initially Figure 3.19(f) and 19(g)), which now extracts electrons from NO_2. Figure 3.24 (b) demonstrates a resistance decrease for the 10 s exposed interface and Figure 3.24(c) indicates a slightly smaller decrease for the 30 s Au_xO exposed interface. Even more compelling are the results obtained in Figure 3.24(d) when the system, treated for 10 s with Au_xO, is subsequently treated with NH_3, again 24 hours after the experiments depicted in Figure 3.19. Figure 3.24(d) indicates a significant resistance decrease and minimal quenching even at concentrations of 10 ppm. NH_3, as a strong base, contributes electrons, which leads to the repopulation of a strongly depleted donor level population.

The IHSAB principle which we describe briefly above and elsewhere [9,74] dictates the means to obtain an initial dominant directed electron transduction and minimal chemisorption with respect to the acidic analyte NO_2. Because of the potential for the chemisorbed interaction-reaction of SnO_x with surface generated NO_2^-, the interaction leading to directed electron transduction enhanced via coupled gold clustered oxide Au_xO ($x >> 1$) nanostructure deposits provides a more efficient means for the initial "reversible" extraction of donor level electrons (Figs. 19). However, Figure 3.24 demonstrates that this previously treated and apparently depleted tin oxide surface now appears to act similarly to the depleted Au_xO surfaces capturing electrons to populate the donor levels and subsequently decreasing the system resistance (increasing conductance).

The dynamic nature of electron depletion and exchange is demonstrated as elevated concentrations of NO_2 and NO interact with an untreated PS interface. Figure 3.25 depicts observed responses for an untreated PS interface to NO, and NO_2 at concentrations in excess of 10 ppm. The data for NO and NO_2 in Figures 3.25 (a)-(d) reflect a clear dynamic interplay. The data for NO at 10 ppm display a rise to a maximum resistance as electrons are attracted by this analtye. A similar rise is observed for NO_2 although the change in resistance is considerably greater. At 20 ppm and again at higher concentrations, the NO response at first peaks and then decays. On the time resolution of Figs. 25(a) and (c) these features appear as a sharp initial resistance increase, which at higher time resolution, is seen to decay as a slow, near exponential tail to a subsequent limiting value. The NO_2 responses

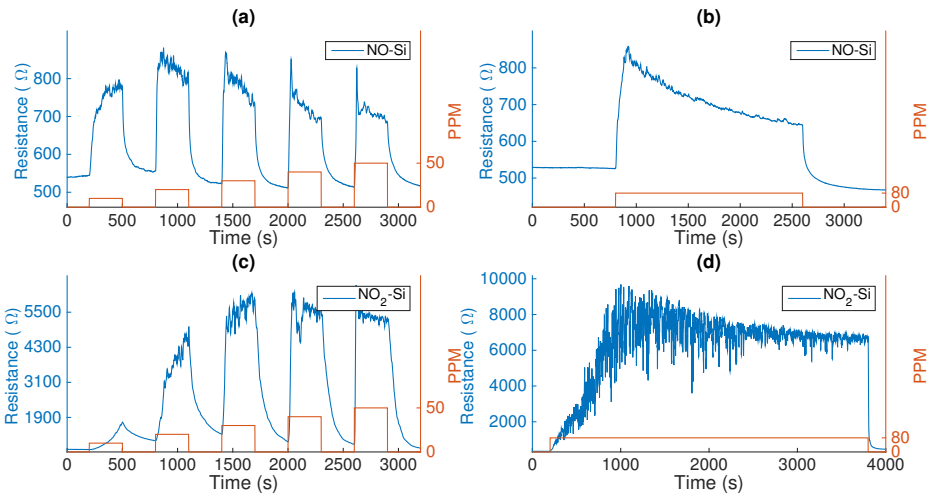

Figure 3.25: Comparison of responses for NO_2 and NO in the concentration range 10-80 ppm. Figures (a) and (b) for NO and (c) and (d) for NO_2 depict the response to 10, 20, 30, 40, 50, and 80 ppm of these gases. Figures (b) and (d) represent higher resolution time scales . The maximum response is seen to peak and then slowly decay as the system approaches an equilibrated resistance level. The change in resistance for NO_2 is a substantial 10,000 Ohms but the NO only approaches 800 Ohms.

at 20 and 30 ppm again display a rise to a maximum resistance during exposure, although the rise appears muted at 30 ppm. At 40 and 50 ppm, NO_2 also displays a signal, which first peaks and then decays at a much faster rate than that observed at lower concentrations.

An indication of this slow near exponential decay at higher time resolution and analyte gas concentrations of 80 ppm is presented in Figures 3.25 (b) and (d). The onset of this behavior at lower concentrations for the NO system would suggest an origin for this phenomenon. NO_2 has a substantial electron affinity [72, 172, 175–177] compared to NO, which has a small if not negligible electron affinity [174, 178, 179]. This fact dictates that NO_2 withdraws electrons considerably more efficiently than the amphoteric NO radical. As NO_2 and NO withdraw donor level electrons, the n-type PS interface is depleted to the point where it begins to compete for available electrons. Because of its much more substantial electron affinity, NO_2 competes more favorably for these available electrons than does the amphoteric NO radical. Hence the dynamic signal decay onsets at higher concentrations or higher resistances. The near exponential decays depicted in Figures 3.25 (b) and (d) correspond to the process whereby the degree of electron extraction reaches a maximum

and is then counteracted by the depleted n-type PS interface that now acts as a stronger acid than either NO_2 or NO.

3.3.4 Depleted System Responses

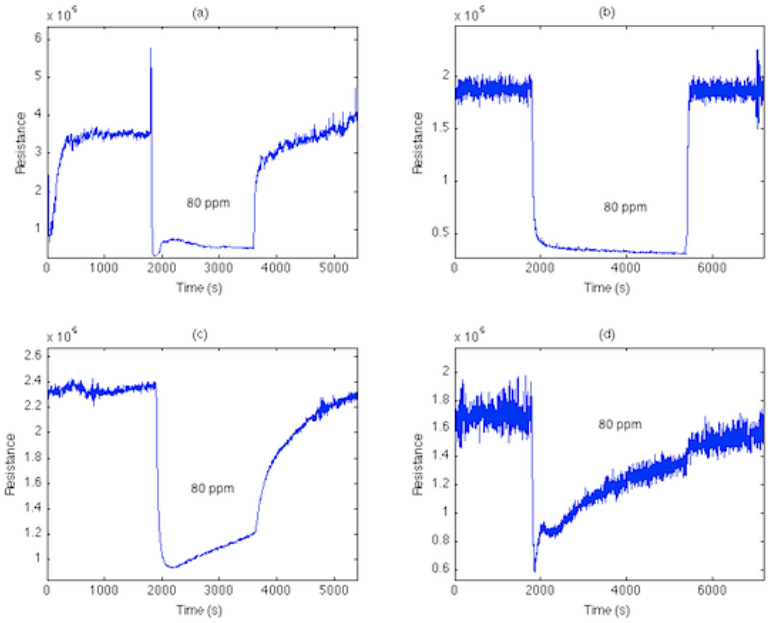

Figure 3.26: Comparison of responses for depleted or near-depleted n-type PS interfaces to 80 ppm (a,b) NO_2 , (c) NH_3, and (d) NO. The gases were pulsed onto these interfaces with a 1800s half-cycle followed by a 1800s half-cycle UHP cleaning. The system was purged with UHP nitrogen for 3600s before operation.

It is possible to so severely deplete the n-type PS systems to the extent that these systems become inverted. The resulting responses observed after depletion provide additional relevant information. Figure 3.26 (a) and (b) demonstrate the response of a PS interface, which has been depleted to near p-type character, to a concentration of 80 ppm of NO_2. The data in Figure 3.26 (a) were obtained for a system with an extremely small residual donor electron population whereas that in Figure 3.26(b) was obtained for a thoroughly depleted system. Figure 3.26(a) displays a spike-like rise in resistance (decrease of conductance) suggestive of the removal of electrons due to the interaction of NO_2 with the residual donor level population. In both Figure 3.26(a) and 26(b) we observe the rapid drop in resistance indicative of the interaction with a p-type system (depleted n-type) and with holes in the valence band (as opposed to electrons in the donor level). Further note the slow decrease

in resistance following the sharp drop in resistance as NO_2 extracts electrons (Fig. 26(b)) and compare this response to that for 80 ppm NH_3 in Figure 3.26 (c). After the initial resistance drop indicative of an ammonia interaction with a small residual concentration of donor electrons, the NH_3 response now *increases*, indicative of the interaction with holes in the valence band [143]. The rate of increase in resistance over this intermediate time period is notably greater than the corresponding decrease observed for NO_2. The thoroughly depleted system for NO_2 (Fig. 26(b)) displays an extremely sharp return to baseline as the NO_2 gas flow is terminated. The return to baseline is much slower for the NH_3 system and for the NO system depicted in Figure 3.26(d). These results suggest that extracting electrons from these depleted systems (NO_2) is much more difficult than donating electrons (NH_3 and NO).

3.3.5 Discussion

The underlying IHSAB principle dictates the physisorption directed response that we have observed from an acidic (NO_2), basic (NH_3), and amphoteric (NO) analyte as they interact with a treated *n*-type PS interface. A first order comparison of the response data in Tables 2 and 4 with the exemplary list of hard, borderline, and soft acids and bases in Table 3.1 clearly demonstrates that hard bases such as NH_3 respond most strongly when exposed to an Au_xO nanostructure treated PS surface. Within the framework of the IHSAB principle, this is not surprising since Au_xO is a soft acid ($Au^{0,+1}$).

The results presented in Figures 15-26 for the transduction of NO_2, NO, and NH_3 with *n*-type porous silicon indicate a more dynamic reversible interaction for acids and bases with majority electron carriers than with holes. Further, the influence of the nanostructured metal oxides, fractionally deposited to the PS interface, is notably more pronounced as these metal oxides influence the modification of the initial donor level concentration. The materials selected in this study for the nanostructured islands serve the role of guiding antennas to force a dominantly physisorbtive (vs. chemisorbtive) interaction at the decorated extrinsic semiconductor interface. We have established that the process of selectivity is best implemented on a nanopore coated microchannel array. The nanoporous coating provides

a phase match for the *unique fractional deposition of select nanostructures.* The nanostructured islands provide the gateways for a physisorptive (electron transduction) interaction at the decorated PS interface .

The IHSAB model [9, 10, 74, 137, 140]suggests that the proper combination of nanostructure deposition techniques could be employed to produce combinations of array based multiple sensor devices of varying sensitivity to a variety of gases and that a matrix of array responses might be correlated to selectivity for a given gas mixture. This is because the selection of the nanostructures that are deposited to the nanopore covered microchannels and the variable surface sensitivities that are produced, as they form in-situ metal/metal oxide deposits, can now be predicated not in a random fashion or based on limited previous observations but in a clearly designed procedure based on established molecular properties.

The plateau resistance observed for the NH_3, NO, and NO_2 systems at elevated concentration (Figure 3.17 and 25) seems to correspond to the equilibration of the Fermi levels for the analyte- semiconductor interface to a position intermediate to that above the donor levels and the limit of energy corresponding to the Fermi level for the intrinsic semiconductor (Figure 3.27). Here we make note of the changes in the Fermi level with temperature.

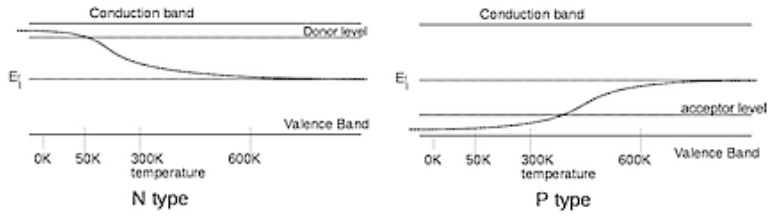

Figure 3.27: Fermi level of extrinsic semiconductors as a function of temperature.

Figure 3.27 describes the variation in the position of the Fermi level with temperature for n-type and p-type semiconductors [170]. This temperature dependence forms a basis for our considerations of electron transfer to and from an extrinsic semiconductor, the nature of the interaction with majority carriers in that semiconductor, and the corresponding influence, which this transfer has on the semiconductor conductance and transduction. For an n-type semiconductor, donor electron levels lie just below the conduction band (Fig. 27(a)). At 0 K, the Fermi level lies at an energy E_d ($\approx$0.025eV)/2 below the conduction band. At

moderate temperatures, the vast majority of donor level electrons have been excited into the conduction band as eventually the semiconductor practically reverts to that of an intrinsic material at temperatures above 600 K. Here, the Fermi level has shifted to the energy $E_{Fi} \approx E_g/2$ where E_g is the intrinsic semiconductor bandgap energy. A similar situation holds for a *p*-type semiconductor (Fig. 27(b)) as electrons are excited to acceptor levels (holes are excited into the valence band) at an energy $E_a \approx 0.036$ eV. above the valence band. At 0 K , the Fermi level lies at an energy $E_a/2$ above the valence band, however , Figure 3.27(b) depicts the corresponding shift of E_{Fp} as it transcends with temperature to the value $E_{Fi} \approx E_g/2$ for the corresponding intrinsic semiconductor.

From the temperature dependent behavior depicted in Figure 3.27, it is apparent that vacant donor level sites and valence band hole sites increase with temperature. From the temperature dependent behavior depicted in Figure 3.27, it is apparent that the addition of electrons to an "*n*-type" system should contribute to and eventually "top-out" the donor level population whereas the removal of electrons and increase in resistance is very much analogous to the effect of temperature rise. In contrast, the removal of electrons from a "p-type" system can potentially maximize conductance (decrease resistance to a minimum value) whereas an influx of electrons is very much analogous to the effect of temperature rise. These effects, resulting from analyte interface interactions, the preparation of the interface, and the population of donor and/or acceptor levels, have now been clearly observed. Further, the Fermi level shifts that accompany these dynamic interactions are significant.

The data presented in Figures 3.17-3.26 demonstrate important correlations with the schematic temperature dependence of an extrinsic semiconductor presented in Figure 3.27. First the temperature dependence for both p and *n*-type semiconductors is such that one can expect vacant donor levels for an *n*-type system and available holes for a *p*-type system at room temperature [170]. If an analyte acts to add electrons to the vacant donor electron levels of an *n*-type extrinsic semiconductor, we anticipate that the population of these levels will " top-out" and the resistance will reach a limiting lower value. This minimum resistance is demonstrated for the interaction of basic NH_3, especially for the exposure to SnO_x (Fig. 3.16(b)) and Au_xO (Fig. 3.16(f)) treated *n*-type PS , at elevated concentrations

in the range 10-30 ppm for interaction with Au_xO treated PS (Fig. 3.17(f)), and at even higher concentrations in excess of 50 ppm for the exposure of ammonia to untreated PS (Fig. 3.17(g)). An analogous decrease to a minimum resistance is observed for the *p*-type PS system. Here, however, NO_2 extracts electrons and enhances conductance. Figure 3.25 demonstrates the bottoming-out of the resistance associated with the removal of electrons as would be expected from Figure 3.27.

The outlined correlations associated with Figure 3.27 point to an additional aspect of the dynamic nature of these systems. The Fermi level is dynamic and the change in the Fermi level energy must be evaluated as we consider processes initiated with extrinsic semiconductor interfaces. This could have significant consequences as one attempts to employ these prepared interfaces in transduction processes which include any type of dynamic electron transfer and, for that matter, solar pumping involving these systems. While many approaches to transduction focus on the bandgap when considering interactions associated with an extrinsic semiconductor, this focus lacks appropriate dynamic considerations. The effect of the intraction process on energy increments in a dynamic system and especially on the Fermi level should be strongly considered.

NO and NO_2 are found to extract electrons from the untreated *n*-type PS interfaces that we have prepared in this study. From the data in Figures 3.15 and 3.25, it is apparent that NO_2, with its significant electron affinity, is more effective at electron extraction than is the amphoteric NO radical. The data in Figures 3.18-3.25, however, demonstrate finer detail in the dynamic process of electron withdrawal. The data in Figures 3.18-3.25 provide a window to the dynamic process of electron withdrawal and exchange. At lower concentrations, it is apparent that the nature of the nanostructure deposition can have a strong and variable impact on the control of analyte electron extraction. This is demonstrated by the variations in the TiO_2 decorated PS interfaces in Figs. 3.20-3.23. The possibility exists to reverse the process of electron extraction whenever an acid is countered by a strongly acidic nanostructured deposition (Figures 3.18-3.25).

It is also apparent, for both NO and NO_2, that without the nanostructures, the interaction with the extrinsic semiconductor donor electrons reaches a limit where electron

withdrawal can no longer proceed. The extrinsic semiconductor is depleted to the extent that it, in effect, becomes a stronger acid than NO or NO_2. This, of course, occurs first for NO, as demonstrated from the comparison of Figures 3.25(a) and (c). As demonstrated vividly at these elevated pressures, the dynamic process corresponding to a resistance rise to a maximum and the limit of electron removal, is followed by a near-exponential decrease to a plateau resistance (Figures 3.25(b) and (d). Here, the electron population of the semiconductor interface now is depleted to the extent that it becomes a stronger acid and begins to remove electrons from NO or NO_2.

The results presented in Figures 3.18-3.25 for the transduction of NO_2 and NO with both untreated and fractional nanostructure treated n-type porous silicon indicate a very much more dynamic reversible interaction for acids and bases with majority electron carriers than with holes [10, 145].

CHAPTER IV

MULTIGAS SENSING AND MODELING

4.1 Simulation

While enhancing the sensor response to analyte gases is important, equally important is the ability to extract analyte gas concentration data from a sensor array [107,120,180]. For that purpose, a basic two-sensor array was created and the sensor response data analyzed. We also ran two gases at once on these sensors, giving a better understanding of the interactions of the analyte gases with themselves and the extrinsic semiconductor surfaces. In order to extract the gas concentrations from the sensor response, the response mechanism has to be understood. One method to understand the response is to start with a simple model, then modify it with various other models to fit the recorded sensor response. While there are many complicated models for gas diffusion [181, 182] we began these studies using a simple model of diffusion into a 1-D tube [66,183]. The gas diffusion into a 1-D tube model is simulated using a basic numerical diffusion code, described previously [66], the code is in Appendix A. While analytic solutions do exist for the 1-D diffusion problem, they are extremely dependent on initial conditions and do not handle the dynamic flow back and forth of the pulsing of the analyte gas. This difficulty requires us to use a numerical solution for the gas diffusion [183]. For the simulation, the pore is assumed to be uniform for its entire length, so the diffusion coefficient is constant in the tube. No major adsorption is assumed to happen at the bottom of the tube. The simulated response is the average concentration of the gas diffused in the tube. While this is a simplistic model, it does give a good fit to the basic features of the sensor response. An example of a simulation using a simple diffusion model is seen in Figure 4.1, where the calculated response amplitude is very similar to the actual response data seen previously.

The simulated data is much smoother than the recorded data and allows us to easily take first and second order derivatives. The amplitude of the spikes in the derivatives correlates

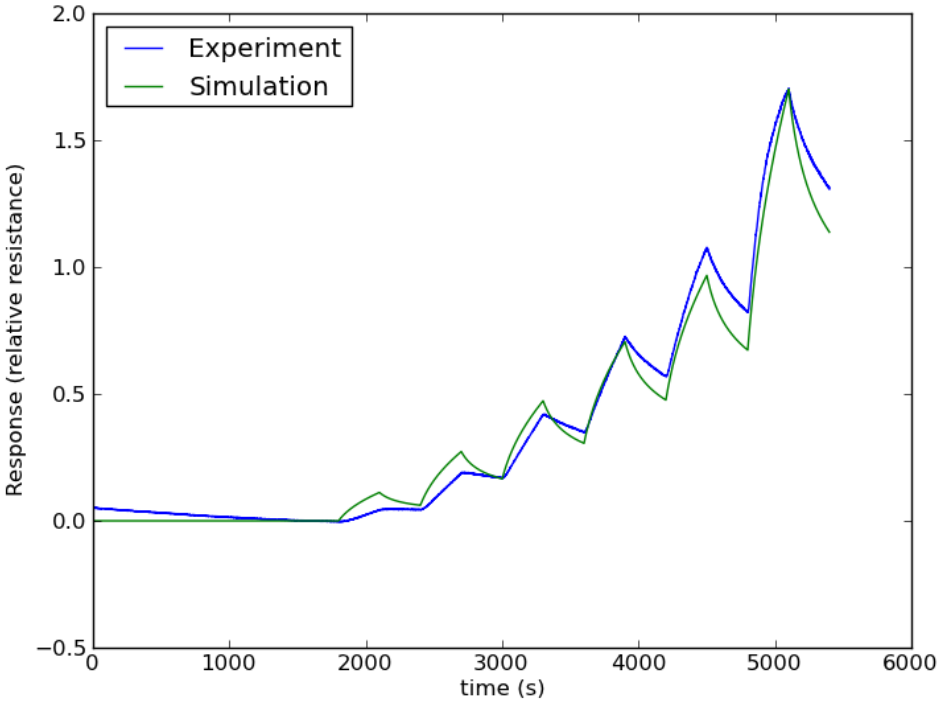

Figure 4.1: Basic diffusion model of the response. The calculated sensor response is green and actual experimental results are in blue. With a simulated diffusion constant of D=5X10^{-12}m^2 per second much slower than the calculated diffusion of NO in air of 2x10^{-4}m^2 per second at standard pressure and temperature [184].

almost perfectly with the gas concentration. The size of the spike translates to the size of the gas concentration pulse as seen in Figure 2.22. Another advantage of the derivatives is that they spike early in the gas pulse and don't require the sensor to reach saturation allowing for a quick response, as mentioned earlier in Chapter 2. Using the information gleaned from this simple model, we attempted to extract gas concentrations from the raw sensor responses. Figure 4.2 shows the normalized resistance response to NO on *n*-type PS. This is the resistance change of the sensor in the presence of the analyte gas divided by the baseline. This baseline can fluctuate due to the variation in the resistivity of the wafers. Also shown is the normalized conductance response to NH_3 for *n*-type sensors. For ease of comparison, the inverse of the normalized response (the conductance) is shown. The average response in Figure 4.2 is over several different sensors with different coatings; however, they all have a similar response curve, which is similar to the PH_3 response on

$p+$-type sensors [185]. The response is near linear at very low ppm (1-4 ppm). However, the response begins to saturate at higher ppm.

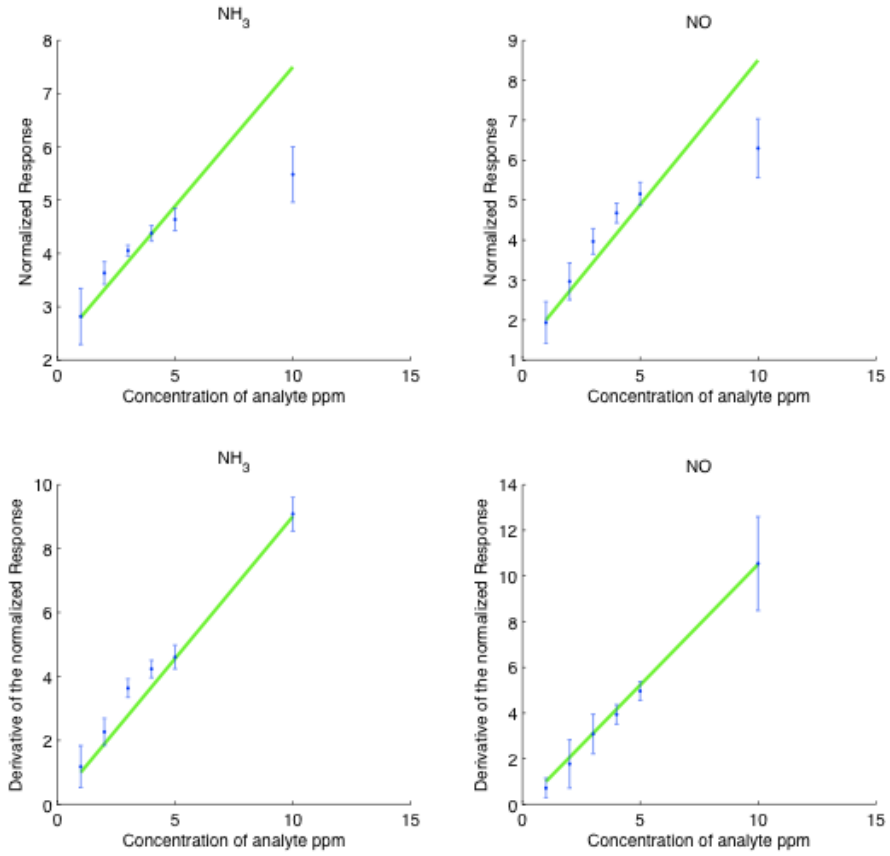

Figure 4.2: (Top) Normalized response to NH_3 (left) and NO (right) for several different n-type sensors and the magnitude of the 1st derivatives(Bottom) of the normalized response. Blue points are the actual data along with error bars and the green line is the linear fit.

The nonlinear response of the sensors at higher concentrations makes it difficult to use the raw response to find the analyte gas concentration. The saturation curves go roughly as the square root of the concentration; however, the inverse power can vary from sensor to sensor. Another issue with using the raw response from the sensor is the saturation of the analyte gas. The sensors require an extended time to reach their saturated response. The required time to saturation can be as short as 2 min to more than half an h of exposure to the analyte gas dependent upon the nature of the analyte gas and the exact shape of the etched pores.

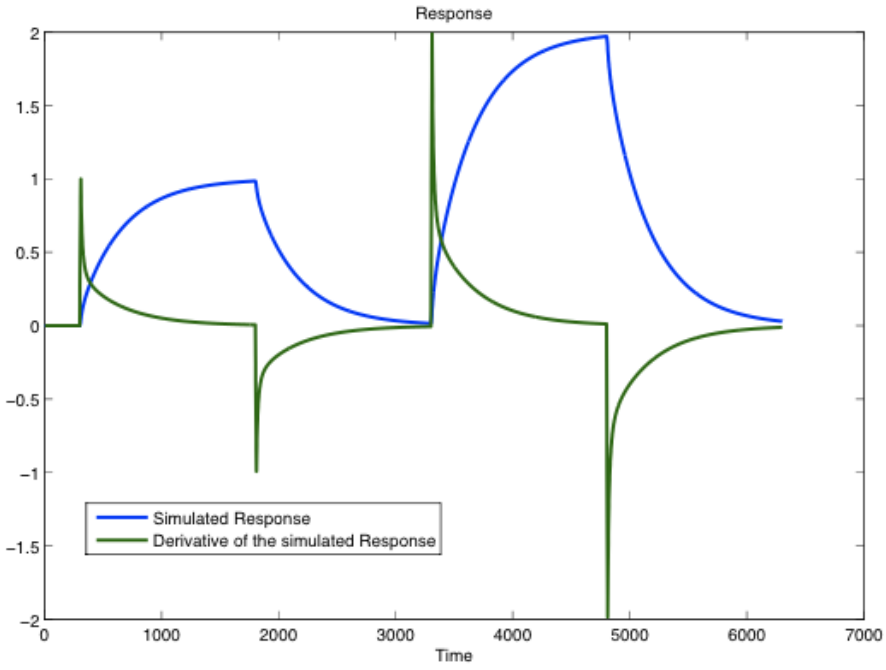

Figure 4.3: The figure shows the derivative of the simulated response in green. The sharp spikes correspond to the gas turning on and off.

Taking the derivative of the response both quickly determines the concentration of the gas, and the maximum size of the spike in the derivative correlates linearly with the concentration of the analyte gas. The spike in the derivative appears almost instantaneously once the gas interacts with the surface; however, the spike quickly tapers off until the gas concentration changes again. While taking the time derivative of the simulated conductrometric response is easy, the raw sensor data has some noise in it, causing large false signals in the derivative. In order to remove the noise, a moving average is used [186]. The moving average takes some previous number of points and averages over these points. The moving average reduces the high frequency noise in the system clearing up the derivatives. After taking the moving average the spikes in the derivative of the sensor response can be easily seen and measured. Figure 4.2 shows that the height of the spikes correlates linearly with the analyte gas concentration. The linearity in the response even at higher ppm values is very encouraging, both for being able to extract concentrations from the response and showing that even a basic model can point the analysis in the correct direction. Expanding

upon the success of the basic model, a simplistic two gas interaction was simulated. Using an additive model for the gas response, we simulated a two-sensor response to two different gases. The gases were non-interacting and the sensor response was a linear addition of the concentration for each gas that diffused into the sensors. We then tried to extract the concentration from the simulated response for the two sensors.

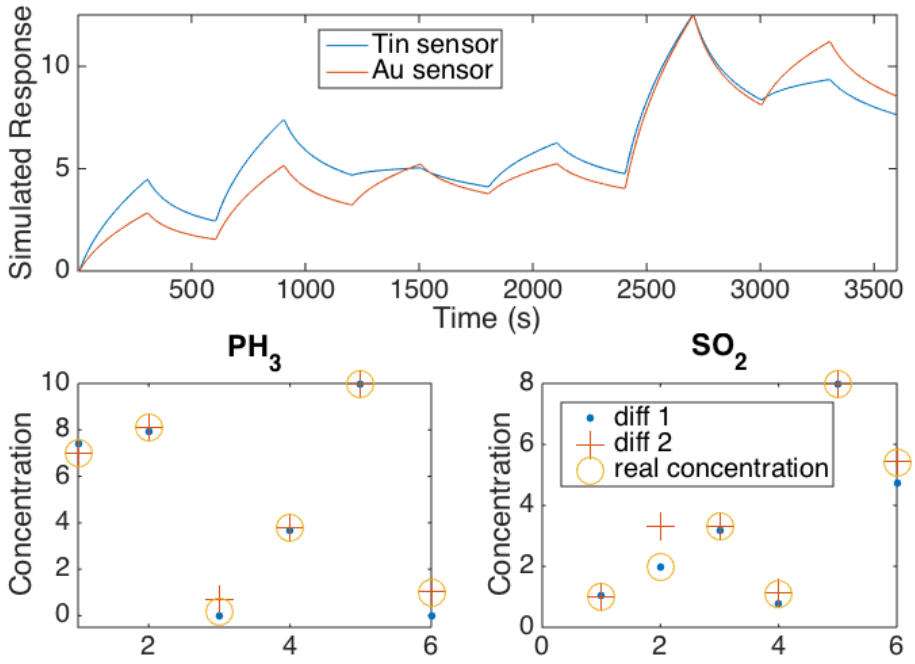

Figure 4.4: Extracted gas concentrations from the simulated response. Gas simulations of two sensors without any noise are presented at the top. The extracted concentration vs the actual concentration is seen at the bottom of the two simulated gases. Diff 1 represents the extracted concentration using only the first derivative while Diff 2 represents the extracted concentration using the second derivative.

The simulated response was modeled using the data from Table 3.2. We simulated SO_2 and PH_3 pulsing on a gold and tin decorated surface. Using the table we created a simple response matrix. Assuming that the sensors had equal responses to the two gases before they were treated with metal oxide nanoparticles. The matrix says that the tin decorated sensor resistance increases by 2 for 1 ppm of PH_3 and 4 for 1 ppm SO_2, while the Gold decorated sensor has a response that increases by 5 for 1 ppm of PH_3 and 2 for 1 ppm of

SO_2. This would create a response matrix M such that $M = \begin{pmatrix} 2 & 5 \\ 4 & 2 \end{pmatrix}$

Using this response matrix derived from the data, we have found that the optimal method for extracting the concentration from the simulation involved taking a second derivative of the data and then multiplying the derivatives with the inverted response matrix for the sensors and gas response. The program is included in Appendix B. Once the responses were calibrated, the code extracted the concentration data from the simulated data with high accuracy.

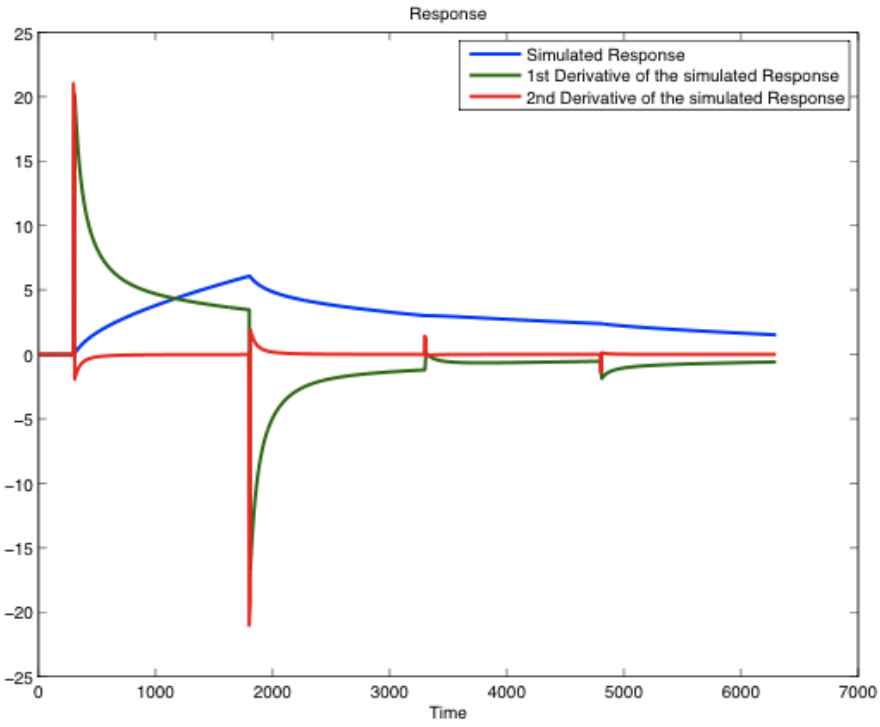

Figure 4.5: Here a large pulse of gas is followed by a small pulse of gas. While the simulation does not show any change, finding the size of the change in the 1st derivative requires applying the 2nd derivative.

The code was able to handle a wide variety of gas concentrations. One important problem with only using the first derivative is if you had a very large pulse of gas followed by a very small amount, the system might not have enough time to recover. However, there still would be a discontinuity in the first derivative. Using the second derivative removes

this problem as shown in Figure 4.5. The code, shown in Appendix B, could also handle two gases diffusing into the sensor at different rates. For different molecular masses, the diffusion rates of different gases also differ. However, the code was able to address the simulation even for significantly different rates of diffusion varying by over two orders of magnitude. This happened when the response to the gases Another problem to consider was the orthogonality of the different gas responses. It should be easier to separate out two gas responses if a dominate response to each gas is provided by only one of the two sensors. As an example NO and NH_3 both have a strong response to SnO_2 and Au_xO clustered oxides respectively. However, nickel and copper have a similar response to these two analyte gases. The further apart the response vectors are for a set of analytes, the stronger their orthoginality. While a decrease in orthogonality could pose a problem, the code was able to correctly identify each gas. While the results obtained with this approach were promising, two issues remained. First, we assume that the dependence of the sensor response on concentration will always be constant. However, as we have seen, the response does vary as the concentration changes. So the response of the sensor at 10 ppm of the analyte gas is not 10 times the response of the same sensor at 1 ppm of the analyte gas.

The other issue arises dealing with the second derivative. The second derivative by its nature is very sensitive to noise in the system. This sensitivity is seen in Figure 4.6 where we take the same system as in Figure 4.4 and add a small amount of random noise to the sensor response. Even using a smoothing function to correct for this small amount of noise can cause some issues in determining the gas level. This can be seen in the shifts away from the actual gas levels in Figure 4.6. This problem can be dealt with using multiple sensors to increase redundancy and decrease the noise in the system. Since the sensor array will have noise, the more sensors used will allow the noise to average out to a small value. A slightly different way of viewing the problem is that the more sensors in the array the greater can be the orthogonality of the sensor arrays responses to the different analyte gases, easing the extraction of the analyte concentration.

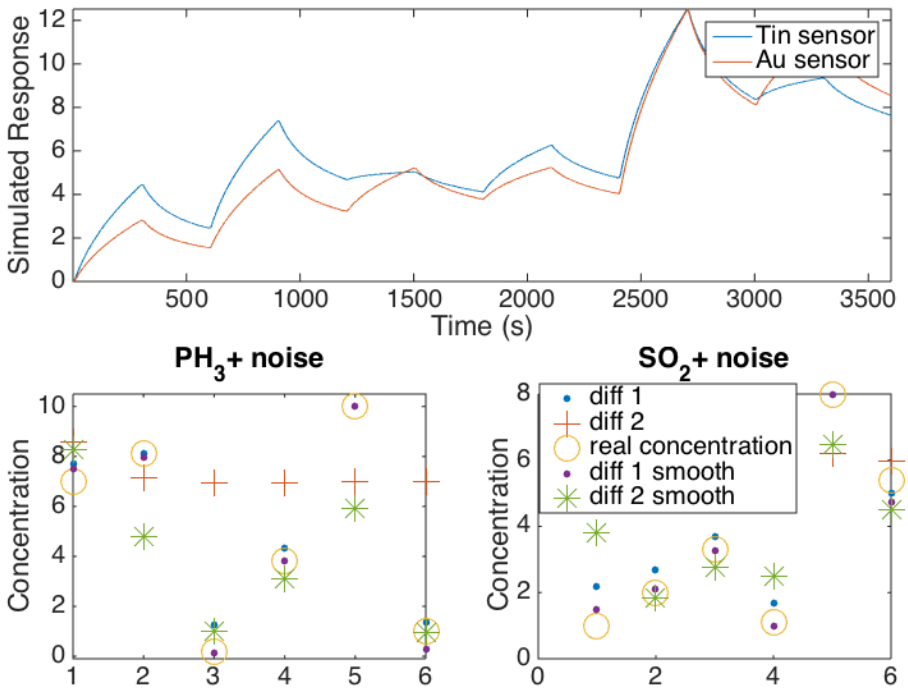

Figure 4.6: Adding small amounts of noise to the two simulated sensors shown at the top. Extracted gas concentrations from simulated results with noise are seen at the bottom. Note how little noise is needed to frustrate the data analysis. Diff 1 represents the extracted concentration using only the first derivative. Diff 1 smooth is the extracted concentration using only the first derivative after smoothing the data. Diff 2 represents the extracted concentration using the second derivative and Diff 2 smooth is the result using the same algorithm only smoothing the data first.

4.1.1 Nonlinear response

While the results from the simulated responses are encouraging, we have not addressed the major problem with all the simulations. The mechanism for the nonlinear response at higher concentrations is not understood. The simulation code assumes that the response has a simple linear relationship. If there is 10 ppm of gas the response is 10 times larger than the 1 ppm response. While this model works at very low concentrations; the response to the studied gases at higher ppm values is not linear as seen previously in Figure 4.2. Understanding the nonlinearity will allow a reduction in the uncertainty of the concentration by correlating the measured sensor response with the derivative measurements.

Several methods were used in an attempt to address this issue of nonlinear response.

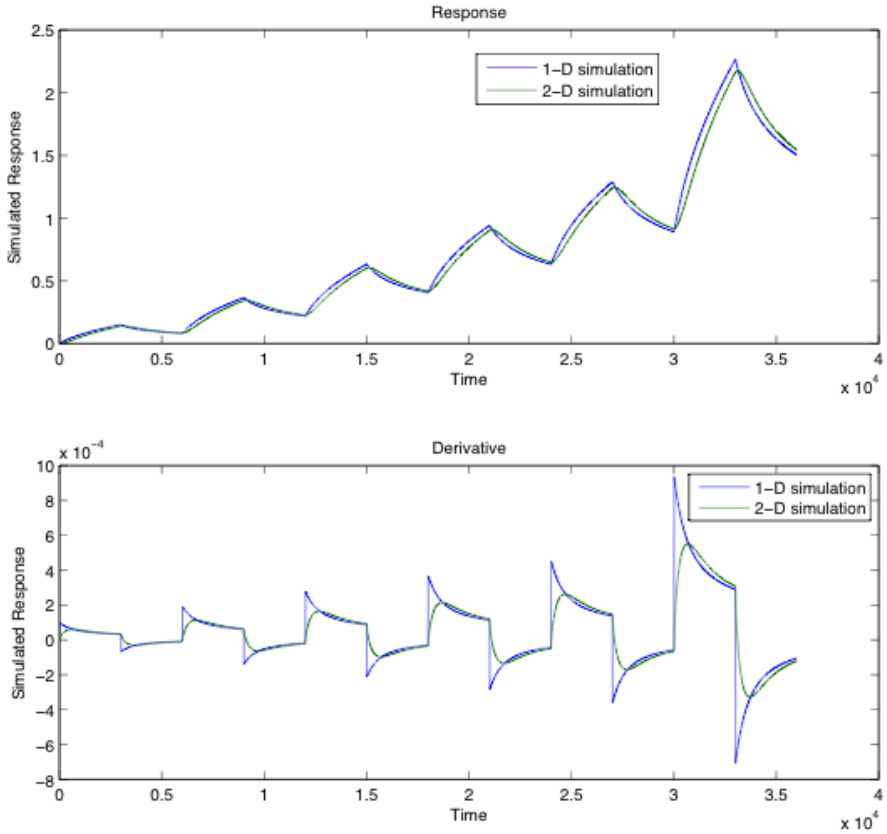

Figure 4.7: The difference between the 1-D diffusion and the 2-D diffusion models of response. The only major change can be seen in the time derivative of the responce where the sharpness of the derivative is muffled in the 2-D simulation.

We modified the diffusion and the response simulation trying to better fit the collected data from the PS sensors. When iterating the code, we looked not only at the observed response but also at the calculated derivative. Since the actual sensors do show a linear response in the derivative of the resistance, it is important that any change to the code also correctly modifies the time derivative of the response.

The first approach to this problem was to model 2-D diffusion into the pores. We modeled the gas diffusing into the micropores and then into the nanopores on their surface, adding the extra dimension. The nanopores are assumed to be smaller but with a larger surface area. These nanopores are where the majority of the gas interactions occur. However the resulting response from the 2-D simulations did not significantly differ from those

achieved by doing a simple one dimensional simulation, as seen in Figure 4.7. The only major change observed in the results was the sharpness of the derivative, due to the time delay for the gases to diffuse into the set of pores. This time delay results as the analyte gas travels down the main pore and then diffuses into the nanopores. Since the simulation takes an average of the all the nanopores, the delay in the gas diffusing into the bottom pores smooths out the derivative. This smoothing of the derivative is the only major change in the modeled sensor responses observed.

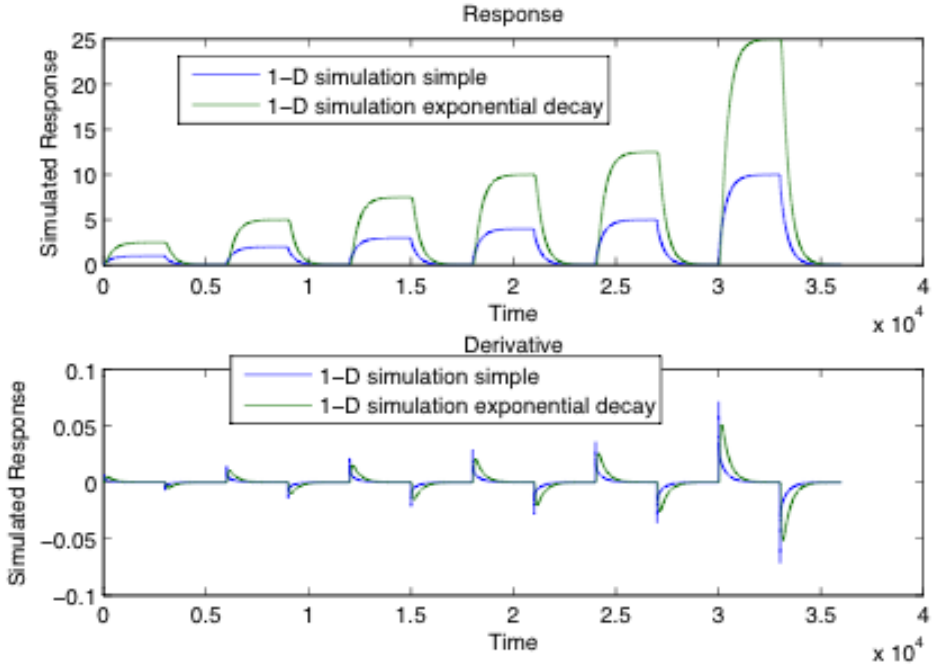

Figure 4.8: Comparison of the exponential decay model to the straight mean method for calculating the response with a fast diffusion constant (4.9e-10 m^2/s).

Another method was used by Lewis et al. [66] to model the nonlinearity. The model assumes that the response decays exponentially from the bottom of the pores. which works out to

$$\Omega_i(t) = \Omega_0 + S_i \int_0^L C(x,t) \frac{Be^{Bx}}{1 - Be^B L} dx \tag{4.1}$$

Where $\Omega_i(t)$ is the resistance value measured by the sensor, Ω_0 is the baseline resistance of the sensor, S_i is the sensitivity of the sensor to the analyte gas ,C(x,t) is the concentration of the gas in the pore as a funtion of time and distance into the pore, and B is the fitting

parameter of the gas used. The simulated results are shown in Figure 4.8. However using the Lewis model to simulate the sensors did not give a nonlinear response to the sensor. The only advantage seen with this model is that the tops of the peaks take longer to reach a saturation value. As the gas diffuses into the pores it reaches the saturation limit slowing down, but the Lewis model has an exponential term enhancing this small final change, thus modeling the actual response of a gas a bit better. The slow change also smoothes out the derivatives seen in Figure 4.8. However, at much lower diffusion constants the response doesn't seem to fit as well. At the slower diffusion rates, the calculated response is smoothed so much as to lose all sharp peaks, no longer fitting the observed gas sensor responses shown in Figure 4.9.

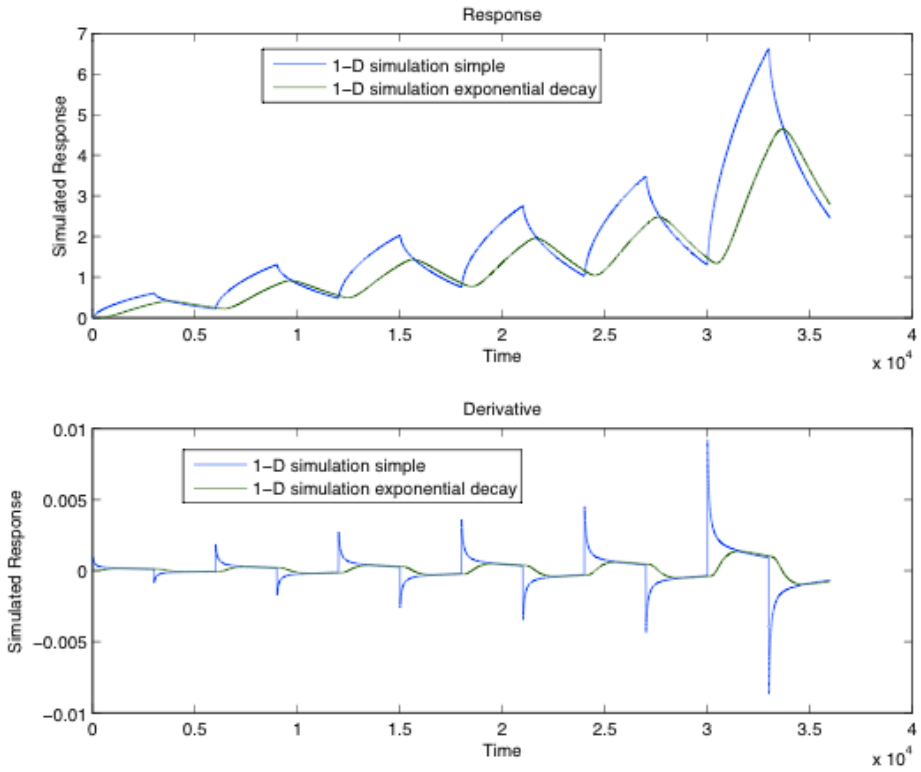

Figure 4.9: Comparison of the exponential decay model to the straight mean model for calculating the response with a slower diffusion constant (4.9e-13 m^2/s).

A term that models the stickiness of the gas to the pore surface wall can be added to the simulation for better modeling. This gas adhesion has been observed and mentioned

previously [9, 66, 137]. Therefore, for the simulation, the diffusion constant of the gas out of the pore was different than the diffusion into the pore by 50 percent. The slowed down diffusion models "simulate" the gas adhesion to the surface. This gas adhesion model roughly approximates the actual gas adhesion to the surface. However, this is a very simple model to deal with the adsorption dynamics. There are other more complicated models used to deal with adsorption dynamics, but these models generally deal with effects that appear at much higher concentrations of the analyte gas. [187,188] Despite the simplicity of the model, it does seem to have some resemblance to how the actual gas in the sensor acts. Figure 4.10 shows a very strong sticking factor modifying the simulation. The major effect on the simulation to notice is the asymmetry in the size of the spikes in the derivative when the gas is turned on versus when the gas is turned off. This same asymmetry is seen in the derivative of actual data, though to a much smaller degree. The simulation is modeling something similar to the response; however, it still does not create a non-linear response to the gas concentration.

4.1.2 Decreasing Resistance Simulation Issues

Another simulation problem is how to model decreasing resistance (increasing conductance). The decreasing resistance cannot be linear otherwise we would get zero or a negative value for the resistance at high enough ppm levels, which is not physically possible. Instead the sensor saturates as seen for NH_3 on an n-type PS sensor. Any simulation where the conductance increases has to take this behavior into account. In addition, the data in Figure 4.2 suggests that inverting the change in resistance will describe the concentration. The simplest function to describe this requires that we have the response mechanism be the inverse of the concentration. However, there is no discontinuity in the response or the derivative of the response when the resistance decreases below the baseline. This tells us there is one mechanism for the analyte gas interacting with the surface that describes both the resistance increasing and decreasing. So a piecewise function where the response increases linearly with resistance increase and then goes as the inverse of the concentration

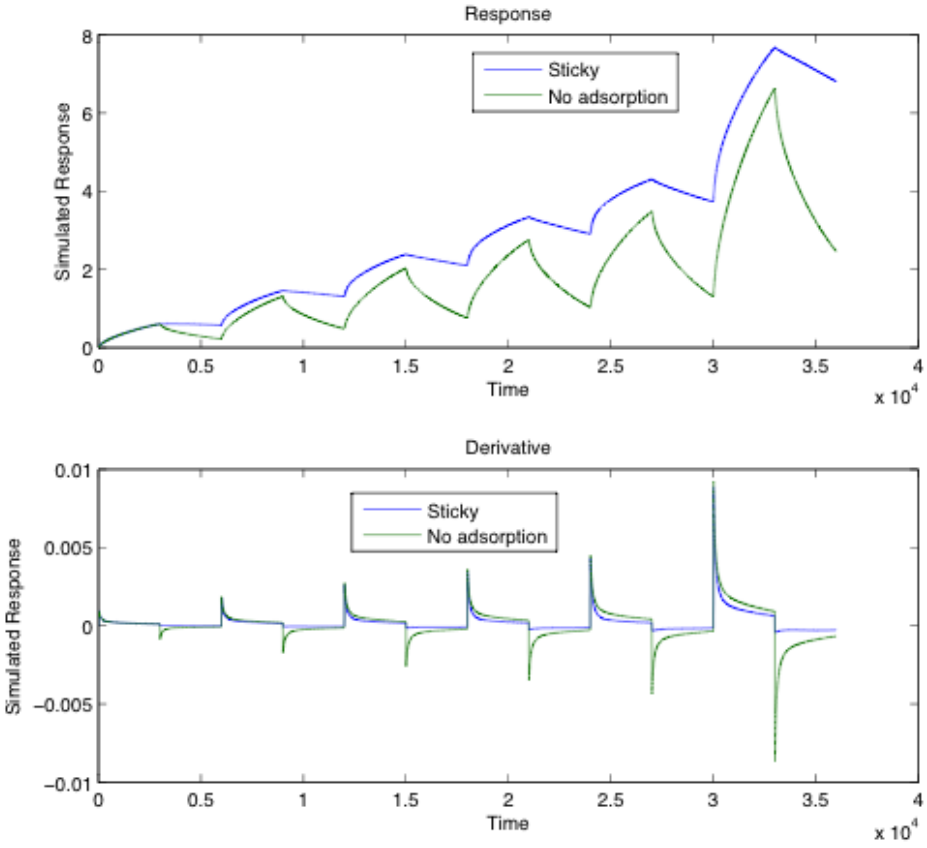

Figure 4.10: Using a slower desorption then adsorption in blue. Notice the linearity even though the gas does not diffuse off easily.

when the resistance decreases below the baseline, like this

$$f(x) = \begin{cases} C + \Omega_0 & : \Omega \geq \Omega_0 \\ \Omega_0 / C & : \Omega < \Omega_0 \end{cases}$$

does not work. One mechanism must handle both increases and decreases in the resistance.

4.2 Saturation Effects

While the use of derivatives is very useful for a pulsed analyte gas configuration, other methods must be used for non-pulsed systems where there is a slow increase in the analyte gas concentration. This requires that we study and classify the nonlinear response of the gas impingent on the PS sensor.

The first step to understanding the saturation effect requires that we measure it. Several

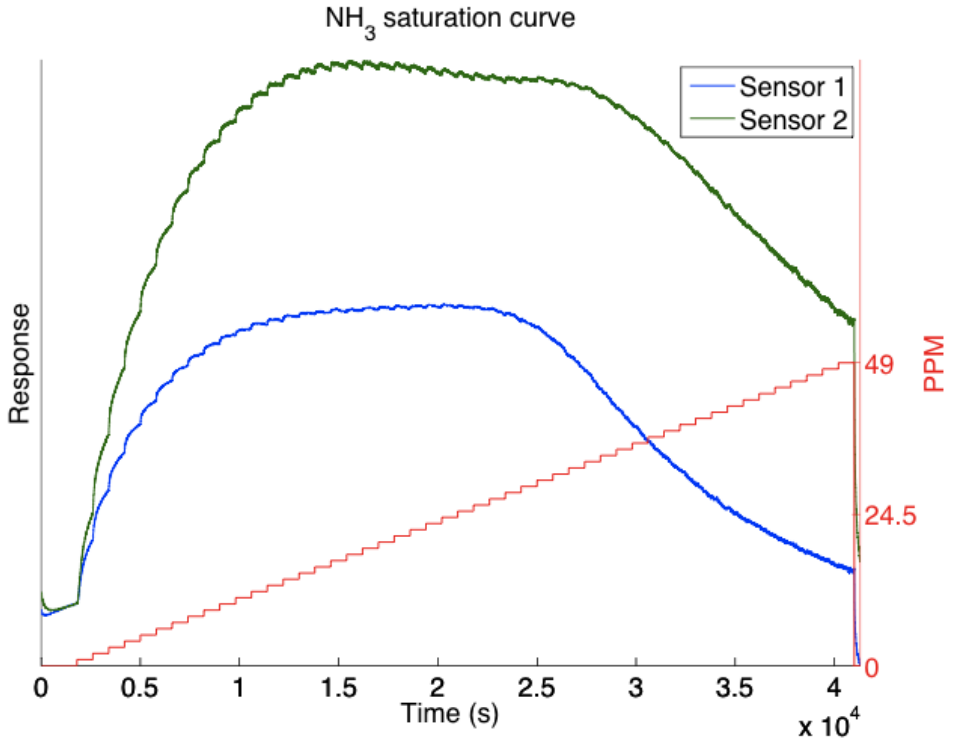

Figure 4.11: The sensor response to 800 seconds of increasing ppm from 1-49 ppm of NH_3 in red. The response for two different uncoated p-type sensors is shown in blue and green.

sensor runs were used to study how the gas response changed over 12 hours of increasing ppm levels. The analyte gas was run for 800 seconds at 1 ppm then it was instantly increase to 2 ppm for 800 seconds without a purge of N_2 between subsequent ppm levels. The concentration of the NH_3 analyte gas was increased in the same manor until it reached 49 ppm, the maximum concentration for the gas configuration.

The first gas adsorption curve studied was NH_3 on an uncoated p-type surface. The results of the data collection are seen in Figure 4.11. On this system the response increases, levels off at high concentration, and then begins to decrease at even higher concentrations. Special note should be made to the bumpy looking response at higher concentrations (Figs. 4.11,4.12). Every time the gas concentration increases at higher ppm values, the sensor response increases then decreases, causing the observed bumps in the response (Fig. 4.13).

The sensor response for NH_3 on an untreated p-type surface, versus concentration, was extracted from the data. Graphing the concentration and response on a log-log plot

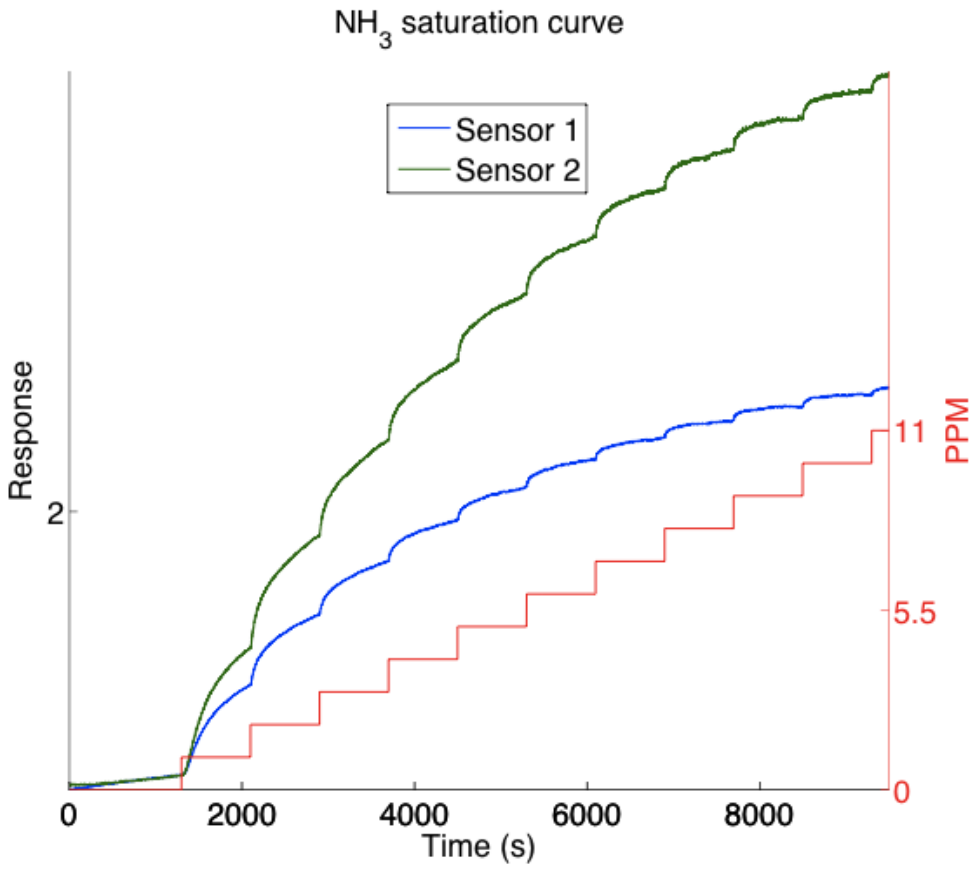

Figure 4.12: Close up of the first few gas steps for the NH_3 saturation curves.

shows a straight line at lower concentration levels and another straight line at the higher concentration levels as depicted in Figure 4.14. The straight line on the log-log plot is an indicator of Freundlich adsorption. The Freundlich adsorption model is an empirical model for adsorption. It was empirically created for very low partial pressures and the model breaks down at higher pressures as other effects dominate [189]. The exact form of the equation is shown in Table 4.1. Theoretical calculations show the presence of heterogeneous adsorption sites give rise to the Freundlich adsorption [190, 191]. The smaller the slope of the log-log plot in the adsorption curve, the more heterogeneous the surface is. The adsorption slopes are different for different sensors suggesting that they are caused by slightly different etch conditions.

The *p*-type PS sensors were then treated with the metal oxide nanoparticle. Sensor 1 was treated with Au_xO and Sensor 2 with SnO_2 nanoparticles. These decorated sensors

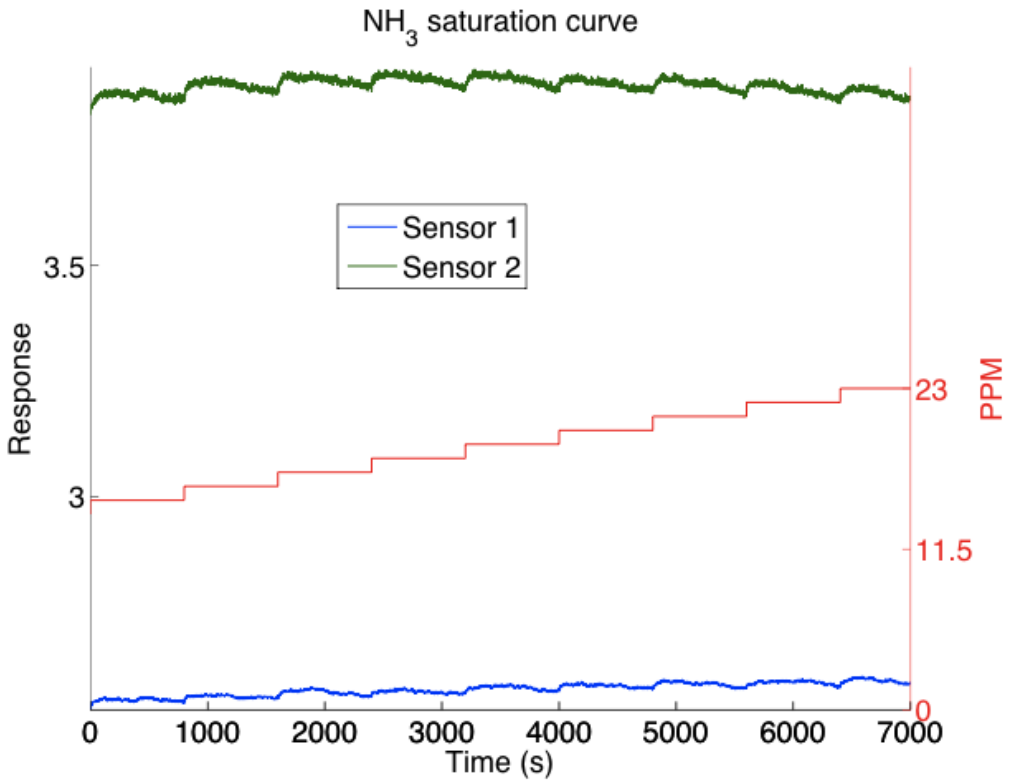

Figure 4.13: Close up of the higher ppm values: note how the resistance goes up with each increase in concentration then decreases

were exposed to the same conditions used to generate the data in Figure 4.11. The results of the response versus concentration curves are seen in Figure 4.15. Note that this figure does not have the sharp drop off in response at higher ppm concentrations. Note also that there is no pulsed roughness in the response. The response does not increase and then decrease with increase in analyte concentration as seen in Figure 4.11. Also since Au_xO increases the sensor response more for the NH_3 than the SnO_2, Sensor 1 now has a larger response to NH_3 than Sensor 2. Since Figures 4.11 and 4.15 are so different, something must have changed the interaction between the sensor and the analyte gas. The only candidate is the metal oxide nanoparticles deposited on the surface. There are a couple of theories as to how the sensor interaction with the gas changes with the addition of the metal oxide island sites. There might be a size effect as the nanoparticles are much smaller than the PS surface and thus effectively confining the electron transfer. Another possible theory is that, at higher concentration, the effect of the uncoated *p*-type sensors is analogous to the

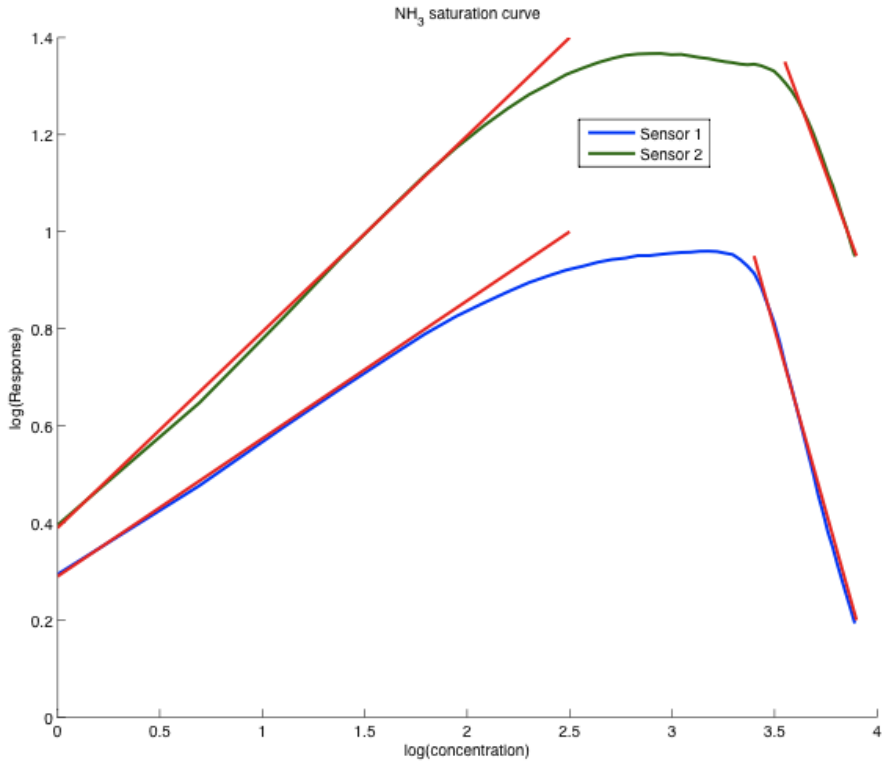

Figure 4.14: log-log plot of the maximum resistance vs gas concentration. Note the straight lines at low and high concentrations.

effect observed for the response to NO of an n-type interface [137]. An n-type interface for which enough electrons are removed so that the surface becomes more acidic then NO, subsequently extracting electrons from the NO gas. In a similar manor, donated electrons could change the acidic nature of a p-type surface, weakening the acidity. If the p-type surface becomes more basic than NH_3, this would result in the surface donating electrons to the gas and decreasing the resistance or alternatively not accepting the electrons which would stabilize the resistance changes. An n-type sensor subsequently deposited with strong acids such as TiO_2 and SnO_2 metal oxide nanoparticles has been shown to make the surface more acidic removing the electrons from the NO. The metal oxide nanoparicles on the p-type sensor also increase the surface acidity. This increase in acidity prevents the back donation of electrons at higher concentrations. A more complicated theory for the untreated surface starts with the assumption that the analyte gas is physisorbed to the silicon surface. The

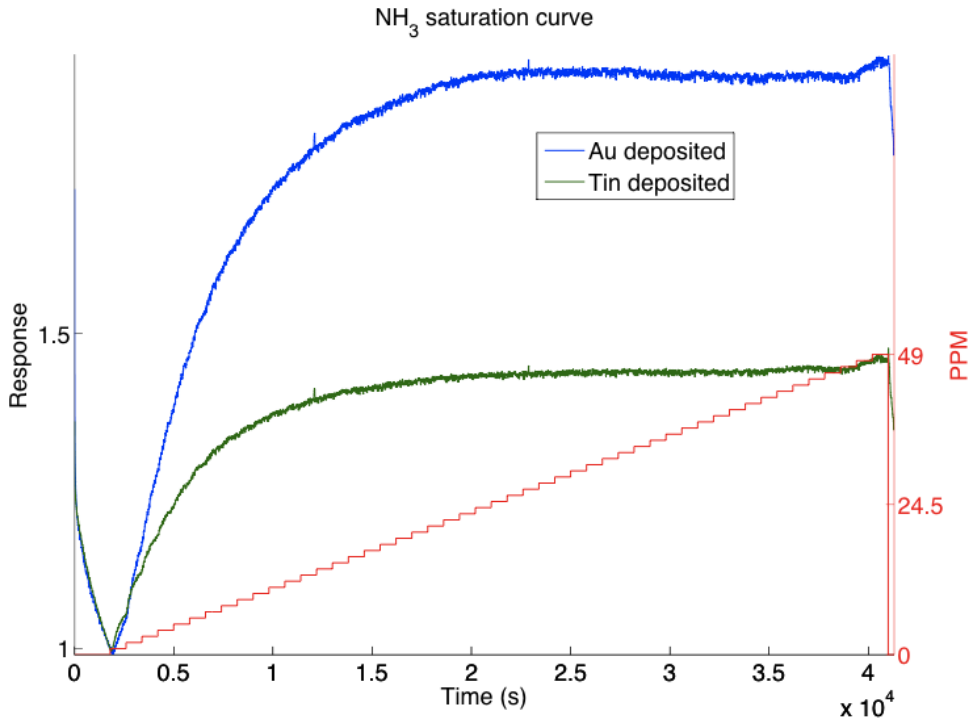

Figure 4.15: Response of Au_xO coated (blue) and SnO_2 coated (green) p-type sensors to increasing NH_3 concentration. Notice the minuscule drop in the response over time with the Au deposited sensor compared with the relatively stable response of the SnO_2 deposited sensor. There is no huge drop off in resistance for SnO_2 and there is only a small increase at the end of the run.

number of electrons donated to the surface per adsorbate can be modeled approximately by the previously seen equation,

$$\Delta N = \frac{\chi_C - \chi_B}{2(\eta_C + \eta_B)} \tag{4.2}$$

We note that the hardness is defined as the change in the chemical potential with respect to the number of electrons. Since the bulk silicon can take extra electrons without radically changing its nature, we can rewrite the equation, as there are no other interactions to govern the hardness, to

$$\Delta N = \frac{\chi_C - \chi_B}{2(\eta_C + \frac{\partial \mu_B}{\partial N})} = \frac{\chi_C - \chi_B}{2(\eta_C - \frac{\partial \chi_B}{\partial N})} \tag{4.3}$$

This expression is a differential equation that can be solved for χ_B to create an equation relating the chemical potential of the silicon and the number of electrons donated:

$$\chi_B = \chi_C + N * \eta_C * (Q - log(N)) \tag{4.4}$$

,where Q is a dimensionless quantity created from solving the differential equation. Since there are only a limited amount of electrons a gas can exchange, when the concentration of the analyte gas increases so does the number of electrons donated to the surface, N. This allows us to relate the concentration of the analyte gas to N by an arbitrary factor.

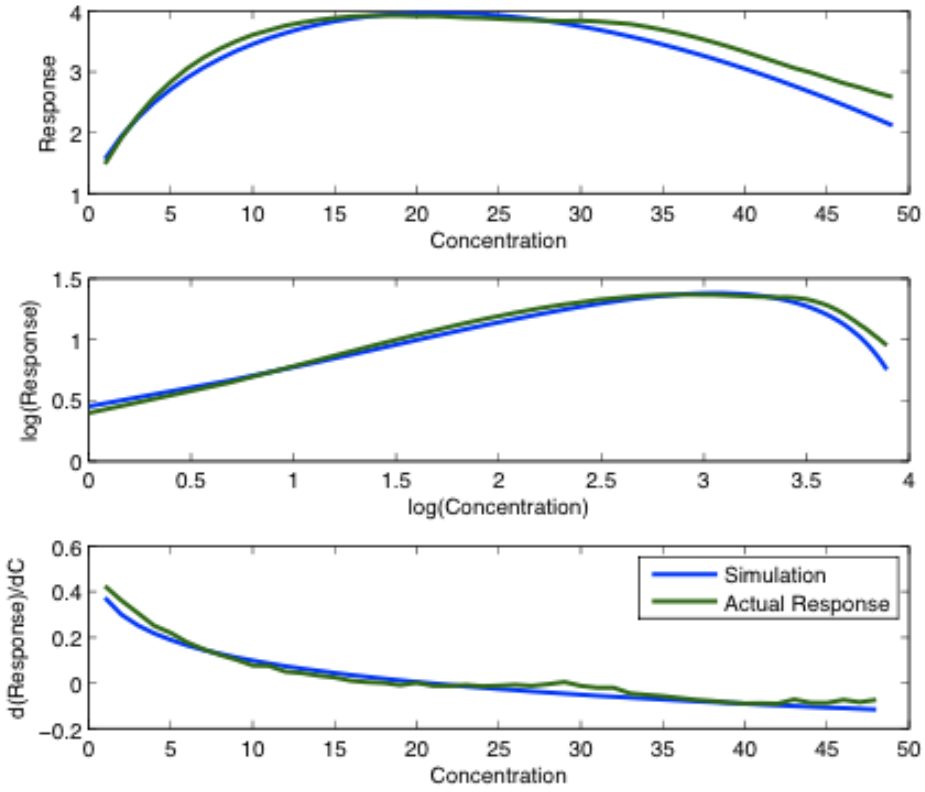

Figure 4.16: Best fit using a simulation in blue and the actual response of untreated p-type silicon with NH_3 in green. The equation appears to roughly describe the experimental results.

Now we relate the resistance to the chemical potential. The electron chemical potential is related to how many electrons are in various bands, and the number of electrons in the various bands controls the conductance. Using this substitution we create a relationship between the concentration and the resistance

$$R = (Q - \log(C)) * B * C + \Omega_0 \tag{4.5}$$

, where C in the gas concentration R is the resistance, Ω_0 is the baseline resistance, B is

the sensitivity of the sensor to the gas, and Q is the parameters that controls the saturation point. Graphing the formula gives decent agreement with the results seen in Figure 4.11 shown in Figure 4.16. The formulation requires that the hardness of the silicon only be determined by the changes in the electron electrochemical potential. Once metal oxides decorate the PS surface, they set the hardness at a fixed value, and the equation doesn't apply, allowing other effects to dominate the interaction. While this formulation is fairly tenuous, but it does at least fit the uncoated response to the analyte gas, and gives a more comprehensive reasoning behind the difference between the response of the decorated and undecorated sensors. The interactions mediated by the nanoparticles are dominated by a response mechanism, which appears to be of simpler form. It is more important to find a function that deals with the decorated surfaces, since the surface will correspond to the majority of sensors that are used in a sensor array.

To study the analyte gas interactions with the metal oxide decorated silicon surface, we took the concentration responses and attempted to fit an adsorption model to them. This model should reflect the actual interactions causing the concentration dependence. Multiple isotherms were tested. One isotherm was the Langmuir isotherm, which is mainly used for modeling a monolayer of gas adsorbing on a homogeneous surface [192]. It is one of the most commonly used isotherms. Another common isotherm is the Freundlich isotherm, which has been described earlier [193]. The Dubinin-Radushkevich isotherm is used to model subcritical vapors on micropores [194]. It is an empirical model with a built-in temperature dependence. It is mainly used to distinguish between physisorbed and chemisorbed ions. The Temkin isotherm is used to model close packed uniform adsorption [195]. However, since the PS surface is not homogeneous, the isotherm does not apply here. Another isotherm that assumes uniformity is the Hill isotherm [196]. This model is useful when adsorbed molecules enhance the adsorption process and is a specific case of the NICA (Nonideal competitive adsorption) model. The Redlich-Peterson isotherm is a combination of the Freundlich and the Langmuir isotherms [197]. It's an empirical model designed to mimic Freundlich isotherms at low pressure and Langmuir isotherm at high pressures. Sips is another combination of the Freundlich and Langmuir isotherms, sometimes referred

Table 4.1: List of adsorption isotherms. q_e is the quantity adsorbed, C_e is the concentration of the gas, and RT is the temperature. All other numbers are simply fitting parameters. Adapted from Foo and Hameed [191] .

Isotherm title	Basic equation	Axes for a linear plot	Reference
Langmuir	$q_e = \frac{A*B*C_e}{1+B*C_e}$	$\frac{1}{q_e}$ vs $\frac{1}{C_e}$	[192]
Freundlich	$q_e = A*(C_e)^{(1/N)}$	$\ln q_e$ vs $\ln C_e$	[193]
Dubinin-Radushkevich	$q_e = A*e^{-\frac{RT}{B}*(\eta^2)}$ $\eta = \ln(1+\frac{1}{C_e}))$	$\log q_e$vs η^2	[194]
Temkin	$q_e = \frac{RT}{B}\log(C_e*A)$	q_e vs $\log C_e$	[195]
Hill	$q_e = \frac{A*C_e^N}{B+C_e^N}$	$\ln \frac{q_e}{A-q_e}$ vs $\ln C_e$	[196]
Redlich-Peterson	$q_e = \frac{A*C_e}{B+C_e^N}$	$\ln(A\frac{C_e}{q_e}-1)$vs $\ln C_e$	[197]
Sips	$q_e = \frac{A*C_e^N}{1+B*C_e^N}$	$\ln \frac{A}{q_e}$vs $\ln C_e$	[198]
Toth	$q_e = \frac{A*C_e}{(B-C_e)^{1/N}}$	$\log \frac{A}{q_e}$vs $\log C_e$	[199]
BET	$q_e = \frac{A*D*C_e}{(B-C_e)(1+A-(C_e/B))}$	$\frac{C_e}{q_e(B-C_e)}$vs $\frac{C_e}{B}$	[200]
FHH	$\ln(\frac{C_e}{B}) = -\frac{A}{RT}(\frac{D}{q_e})^N$	–	[201]
MET	$q_e = B(\frac{A}{\log(D/C_e)})$	–	[202]

to as the Frendlich-Langmuir isotherm [198]. The Toth isotherm is a modification of the Langmuir isotherm for odd adsorption energy distributions [199], which does not seem to be the situation in the current study, since the plot doesn't linearize in Figure 4.13.

The multi-layer isotherms(Table 4.1) correspond to the Brunauer-Emmett-Teller (BET) [200], Frenkel-Halsey-Hill (FHH) [201], and MacMillan-Teller (MET) [202] models. The BET model is generated from assuming a multilayer Langmuir adsorption. The MET model is a modification of the BET model assuming surface tension. The FHH model is an isotherm model constructed on the basis of potential theory.

The first way to test a group of adsorption models is to attempt to linearize the data. Several of the adsorption models have techniques to linearize the data. If the actual data follows one of the adsorption curves once the data is linearized it should form a straight line over the entire concentration range. The list of linearizations is found in Table 4.1. The resulting attempts to linearize the data are seen in Figure 4.17. Here we attempt to linearize the response data using eight different adsorption curves. While the Langmuir plot does appear to be linear throughout the concentration range, there still is a small curve at the beginning of the data. The Redlich-Peterson equation has the second best fit of the linearized isotherms, but it does have a significant bow in the line seen in Figure 4.17. The Freundlich isotherm and the isotherms derived from it do have a linear fit at lower concentrations up to 10 ppm; however, once saturation effects take over, the line has a sharp bend to it. This suggest that Freundlich can be used to approximate the response at low ppm.

For the more complicated adsorption curves that could not be linearized, we simply tried to get the best fit using the different models seen in Figure 4.18. Here the multilayer adsorption models do not seem to fit the response. The BET model has the best fit of the group, but even this model does not have a correct curve. It was very difficult to fit the data using the FHH and MET models. These two models did not describe any of the important features of the saturation curve. The unimpressive results of the multi-layer adsorption models suggest that the saturation curve is not due to any multilayer effect. This would be expected based upon the low concentration of the analyte gas used in the experiment and

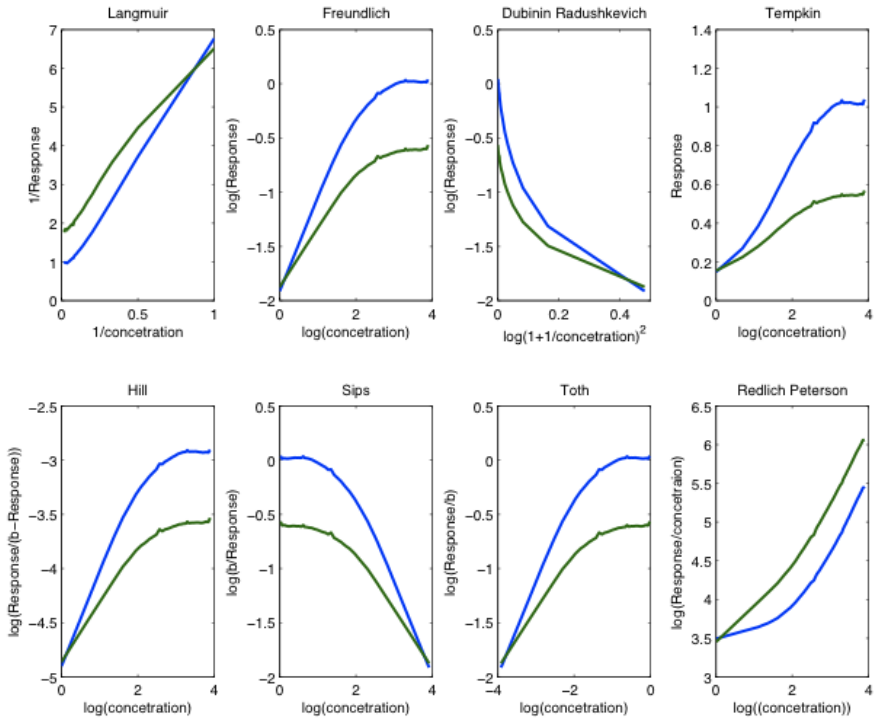

Figure 4.17: Attempts to linearize the response for two different sensors (in blue and green) to NH_3 using 8 different adsorption curves. The different adsorption curves are linearized using different variables so that the curves change depending on the nature of the adsorption. Only the Langmuir and the Redlich-Peterson adsorption curves have a consistent linear shape.

the sparse nature of the decorating metal oxide nanostructure islands.

The Langmuir model appears to be the best fit to the response curve for the metal oxide decorated surfaces. However on closer inspection, the Langmuir model does not faithfully describe the important aspects of the porous silicon isotherm. For example in the log-log plot of the data in Figure 4.19, the Langmuir isotherm curve is curved when the actual response is linear and linear where the response is curved at lower concentrations. The Redlich-Peterson fit handles the log-log plot; however, it doesn't seem to fit the derivative plot very well. This is important at lower concentrations, where the data must fit well for accurate measurements [203]. We need to look for a function that increases and plateaus like the response seen for NH_3. In looking for another function that increases and then plateaus, we used the Fermi distribution function (FDF). If electrical effects cause the saturation curve,

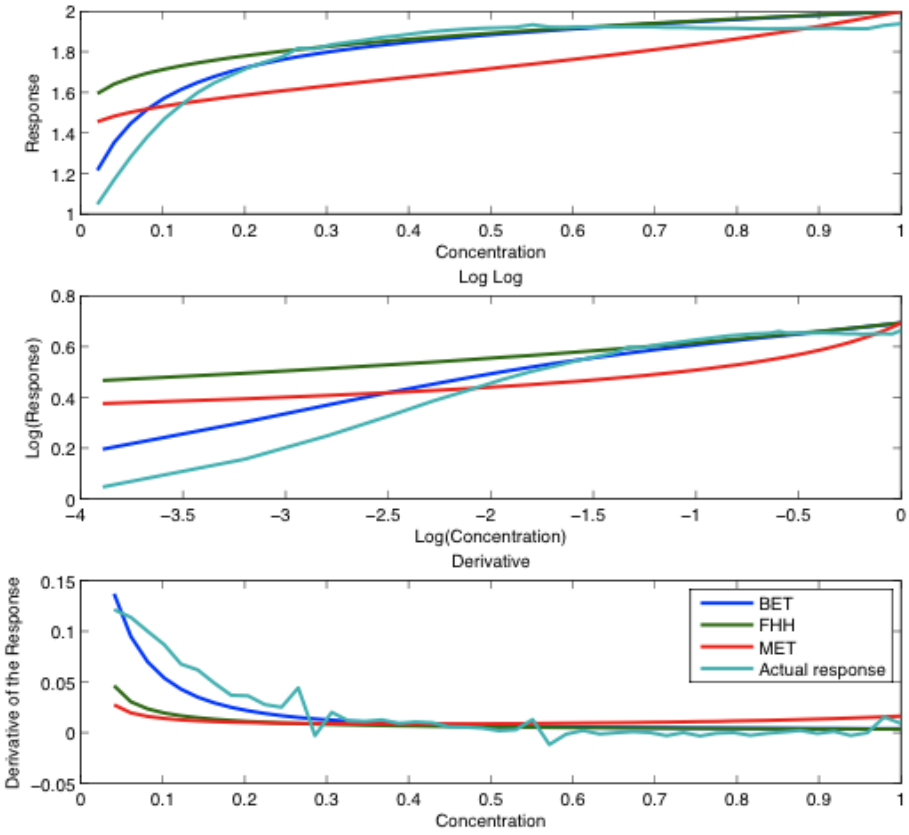

Figure 4.18: Best fits for BET, FHH, and MET models to the experimental data. The modeled responses are examined using a log-log scale and the concentration derivative.

than what is saturating are the electrons in the available conduction bands. This electron saturation can be described using the FDF. The FDF would appear to give a better fit then the Langmuir equation for the analyte gas saturation data.

4.2.1 Theory behind FDF

The foundation of the FDF model starts with the relation between the Fermi level and the resistance. Resistance is linked with the mobility and density of the charge carriers. Since the analyte gas does not change the mobility of the charge carriers, the gas must change the density of the charge carriers. When the density of the charge carriers changes, it shifts the location of the Fermi level at room temperature. Depending on whether electrons flow from the surface to the analyte or vice versa, the Fermi level will shift up or down. This

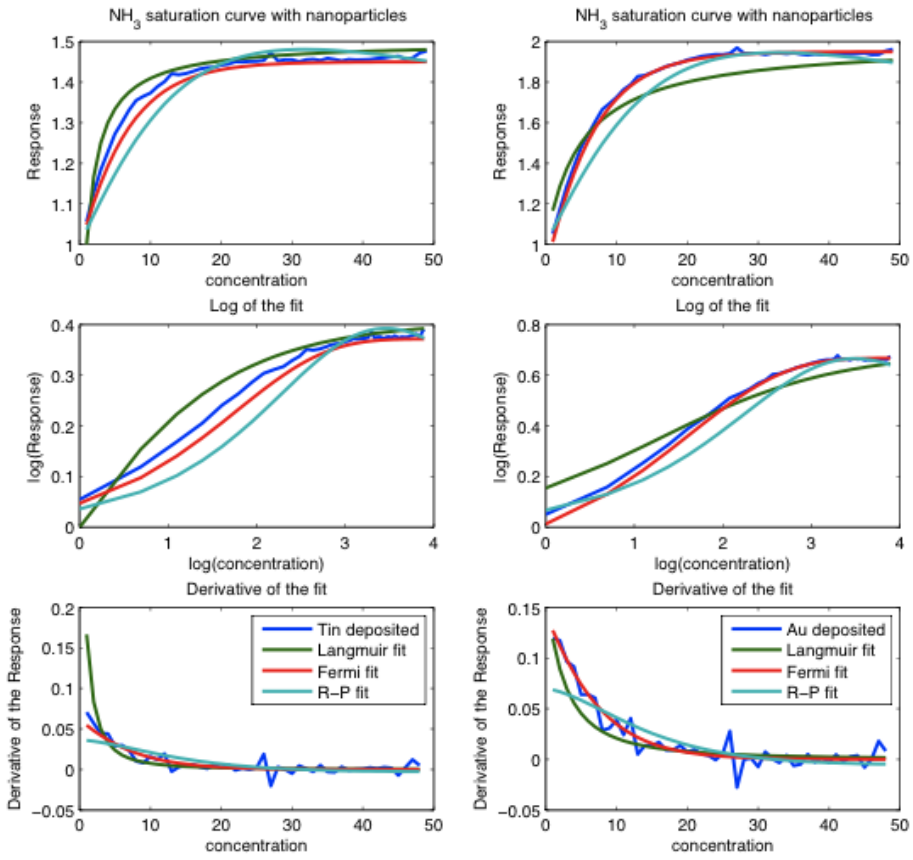

Figure 4.19: The sensor response to NH_3 is in blue. The best fits using a Langmuir model are in green, the FDF fits are in red, and the Redlich-Person fit is in cyan. The fits have been checked against the log-log plot (middle) and the derivative of the concentration (bottom), for higher accuracy.

room temperature occupation suggests that the Fermi level is tied directly to the resistance of the sensor. As an example of the electrochemical potential and its correlation with the resistance, we look at the interaction of NO with an n-type PS interface. As previously mentioned the surface can become more acidic then the amphoteric NO analyte. At high enough concentration, when the surface becomes more acidic than the NO, the electrons reverse their flow. This shift in response suggests that the Fermi level (a.k.a the electron chemical potential) of the PS drops lower than that for NO, and the electrons flow from the higher potential to the lower one. This reversal can be seen in Figure 4.20. Here the resistance increases while the NO, acting as an acid, removes electrons from a NiO decorated

PS surface. As the electrons are removed from the surface, the Fermi level drops. The lower Fermi level indicates that the donor levels are depleted. This allows the interface to capture electrons, increasing the conduction. Since this switch appears to happen at roughly the same resistance level, the resistance should be heavily tied to the Fermi level of the porous silicon surface.

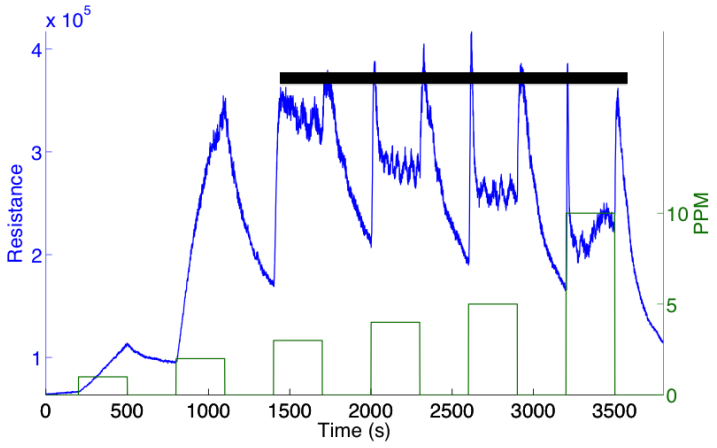

Figure 4.20: NO interacting with a NiO enhanced n-type silicon interface. Notice that the tipping point is at a specific resistance both when the gas is applied and when the gas is turned off shown by the black bar.

To describe the number of electrons in the different bands we use simple statistical mechanics. The density of electrons available in the conduction band corresponds to

$$N_e = \frac{8\pi\sqrt{2}}{h^3} * m_e^{*3/2} \int_{E_c}^{\infty} \frac{\sqrt{E - E_c}}{1 + e^{\frac{E - E_f}{kT}}} \, \mathrm{d}E \tag{4.6}$$

where E_c is the lowest energy of the conduction band E_f is the Fermi level, kT is the energy at the temperature, T, and N_e is the denisty of electrons in the valence band. Similarly, the density of holes available in the valence band correspond to:

$$N_h = \frac{8\pi\sqrt{2}}{h^3} * m_h^{*3/2} \int_{-\infty}^{E_v} \frac{\sqrt{E_v - E}}{1 + e^{\frac{E_f - E}{kT}}} \, \mathrm{d}E \tag{4.7}$$

Where E_v is the highest energy of the valence band E_f is the Fermi level and kT is the energy at the temperature, T [170]. We then assume that the electronic chemical energy of the air is equal to the Fermi level of the extrinsic semiconductor, since they are in equilibrium. The electron chemical potential of the air is thus equal to

$$E_f = \chi_{air} = \sum \chi_i \, C_i = E_{f_i} - \chi_a * C_a \tag{4.8}$$

where χ_{air} is the electron chemical potential of the air. χ_i is the electron chemical potential of each individual species in the air mixture and C_i is the concentration of the chemical species in the air. If we assume that the χ_{air}, without the analyte concentration, is equal to the initial Fermi energy E_{fi}, we can write the linear change in the Fermi level with the concentration of the analyte C_a. For a semiconductor the Fermi level is always in the band gap, so it is safe to assume that $E_c > E_f > E_v$. In that case the exponential term dominates leading to the easy evaluation of the integral.

$$N_e \approx 1 + e^{\frac{E_c - E_{f_i} - \chi_a * C_a}{kT}} \tag{4.9}$$

for n-type sensors. The conductivity of an n-type semiconductor is directly related to the number of electrons in the conduction band [170],

$$\sigma = N_e e \mu_e + N_h e \mu_h \tag{4.10}$$

However N_h is small in an n-type system and can be ignored. Because the resistivity is the inverse of the conductivity, substituting in the equations gives the following formula

$$\rho = \frac{1}{\sigma} = \frac{1}{N_e e \mu_e} \approx \frac{1}{e\mu_e(1 + e^{\frac{E_c - E_{f_i} - \chi_a * C_a}{kT}})} \tag{4.11}$$

. A similar method can be used for p-type sensors where holes are considered instead of electrons. The only major change in the final formula is switching from E_c to E_v and μ_e to μ_h. As mentioned earlier the response mechanism needs to handle both increases and decreases in the resistance, and should have a saturation limit. The FDF does seem to meet these requirements. Also, importantly, this suggests a thermal dependence on the response of the order E^{-kT}. In order to test this thermal dependence, the sensitivity of a sensor was tested at room temperature. Then the temperature was increased using a hot plate, and the sensitivity was tested again. The temperature was increased multiple times and sensitivity measurements were done at each temperature. The results are shown in Figure 4.21. In Figure 4.21, the response of the sensor to the analyte gas decreases as the temperature increases, just as the FDF theory predicts.

This temperature phenomena does lead credence to the FDF theory. There are other things that might cause this Arrhenius dependence such as an increased reaction rate with

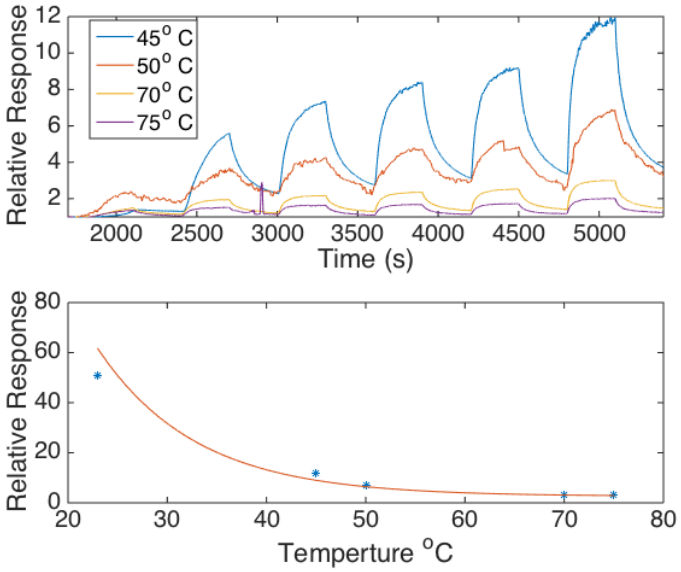

Figure 4.21: (Top) temperature response curves for p-type silicon to NH_3 at different temperatures. (Bottom) The resulting maximum response of the sensors at each temperature with 10 ppm NH_3 shows an exponential decay with a slope of 1 meV.

chemisorption; however, the ease of returning to baseline in these sensor runs does not support this conclusion. So the Fermi level model remains the most viable way of explaining the data.

4.2.2 Fitting the results for NO

While the FDF seems to work for NH_3, the theory should hold for other gas interactions. One interaction we looked at was the interaction of NO on a p-type PS interface. After exposing the PS sensor to increasing amounts of NO concentration in exactly the same manner as used in Figure 4.11 and 4.15, we fit the saturation curves for NO on p-type surfaces. The results are shown in Figure 4.22.

In the figure, the Langmuir model doesn't fit the saturation curves while the FDF model does. The log-log plot shows greater cohesion for the FDF model than the Langmuir model. The FDF model is slightly modified from the model used in Figure 4.19. While in Figure 4.19 the NH_3 is adding electrons to the surface, NO is removing them. While the coefficient in front of the NH_3 concentration of the fit is positive, the coefficient in front of the NO concentration is negative. This minor change gives a very good fit to the NO response

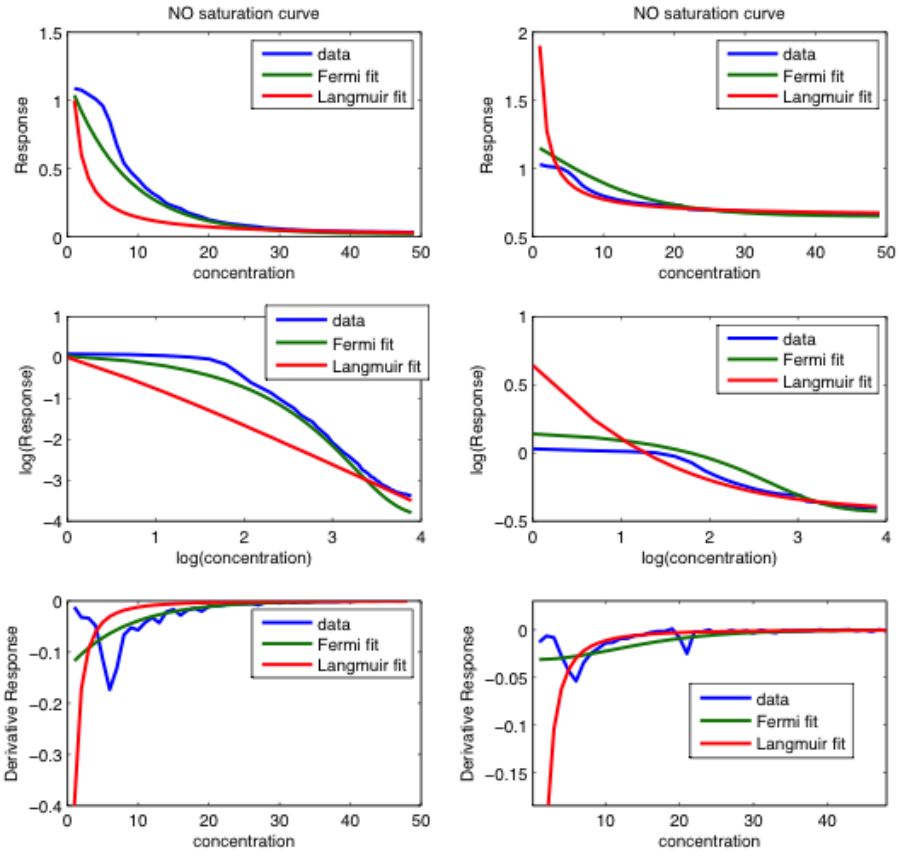

Figure 4.22: The sensor response to NO is in blue. The best fits using a Langmuir model are in red and the FDF fits are in green. The fits are checked against the log-log plot and the derivative of the concentration, for higher accuracy. The left side and right side are two different runs on the same sensor after 12 hours have passed. The Redlich-Peterson curves were not used to maintain image clarity.

curves. Instead of a complicated formula to take into account the response mechanisms of adding versus subtracting electrons, the FDF has the required features built into the equation.

All together these results point to an FDF-like response curve for the PS interface. While FDF does not describe the more complicated curves associated with response inversion at the higher ppm levels seen in Figure 4.11, it does give a better fit then a Langmuir isotherm for both NO and NH_3. This suggests that the results are more closely associated with an electronic band structure saturation than adsorption saturation. This is important because the saturation curve must be accounted for in order to both properly model the

gas response and to extract data from the sensor at higher concentrations. For example Grate and Wise [180] in order to extract data from an array of chemometric sensors where the gas adsorbs on to a polymer had to take a logarithm of the response in order to handle the nonlinearity. A similar transform will have to be implemented in order to extract the concentration data from the current sensor response [204].

4.3 Multiple Gas Interactions

We have measured the conductometric response of NO and NH_3 on an undecorated PS sensor interface followed by combinations with the analytes H_2S and CO on several nanostructured metal oxide treated PS interfaces. When measuring multiple gases, as Figure 4.23 demonstrates, it is important to note that the NO and the NH_3 responses on p-type silicon do not add together. This nonlinearity of the response must be understood otherwise the sensors cannot be used to analyze multiple gases simultaneously. While the gas responses do not add together linearly, the multi gas response is repeatable and independent of any initial gas on the surface. This independence is shown by the similar responses of the gas sensors to NH_3 NO mixtures. Further , we have demonstrated26 that diffusion dominates the sensor conductometric response and modeled this process with the aid of the relative sensitivities determined previously for the metal oxides. Both the direct conductometric response and the derivative of this response are used to evaluate and model the sensor response. The first derivative, is found to be linear in concentration. Taking the derivative of the response both quickly determines the concentration of the gas, as the maximum size of the peak in the derivative is found to correlate linearly with the concentration of the analyte. A spike in the derivative appears almost instantaneously once the gas interacts with the PS surface and quickly tapers off until the gas concentration changes.

Because NO and NH_3, which represent respectfully a weak acid and a strong base, have distinctly different interactions with a decorated PS interface, leading to their respective responses, simpler interactions were analyzed to demonstrate the principles to of modeling mixed gas response. First we looked at a p-type sensor response to H_2S and NH_3, two moderate to strong bases, shown in Figure 4.24. These basic gases add electrons to the PS

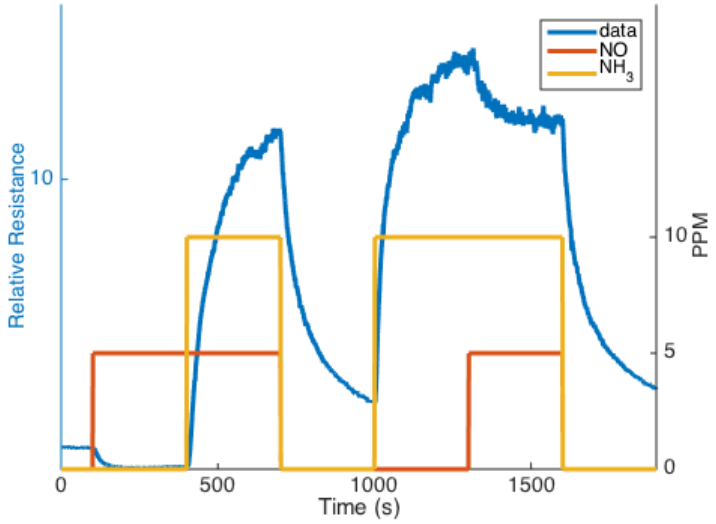

Figure 4.23: Example of the response of a p-type gas sensor to NH_3 and NO simultaneously. Note that the response of the mixed gas levels off to specific value independent of which gas was exposed to the sensor first.

interface decreasing the number of holes in a p-type system, and increasing the sensor resistance. The H_2S, NH_3 tests were all done on an Au_xO decorated PS interface. Initially NH_3 was exposed to the decorated PS surface with the analyte concentration increasing slowly over 15 minutes. After the NH_3 treatment was initially ceased, a background level of H_2S was added to the sensor. The Au_xO treated sensor was then exposed to the same increasing concentration profile of NH_3. The Au_xO treated sensor displays a greater response to NH_3 with H_2S present than in its absence.

We examine the reverse dosage in Figure 4.25 where, first, H_2S is slowly introduced and cycled to the Au_xO treated p-type interface. A baseline of NH_3 was then introduced onto the Au_xO decorated p-type surface, followed again by cycling the H_2S. The NH_3 background did not increase the response to H_2S as much as the H_2S background increased the response to NH_3, however,NH_3 was at a much lower concentration due to the required experimental design. Significant is that even with the much smaller NH_3 concentration, an enhancement of the H_2S signal was seen on the Au_xO treated sensor.

In both Figures 4.24 and 4.25 the introduced background gas interacts with the decorated PS interface. As H_2S interacts, it lowers the Lewis acidity of the nanostructured Au_xO island

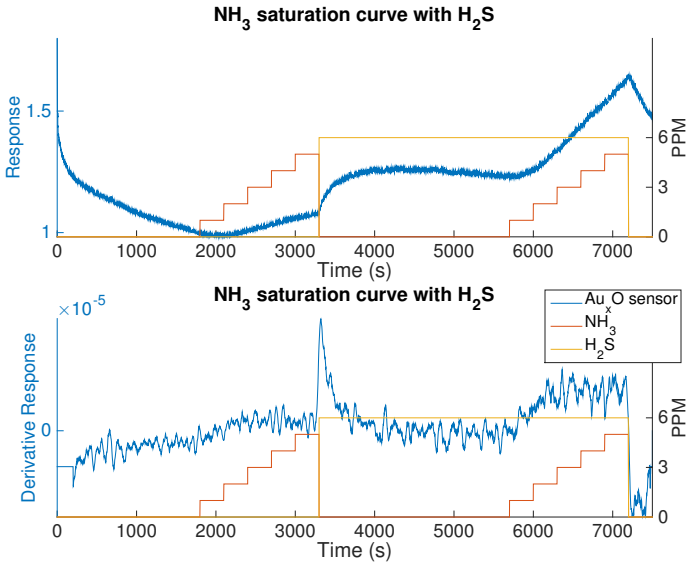

Figure 4.24: The Au_xO *p*-type sensor response to NH_3 and H_2S. The sensor is allowed to come to a base line after treatment with 1800 S of UHP N_2 have flowed over the sensor. Then NH_3 is slowly added to the decorated interface. Once the NH_3 is turned off, H_2S is added to the sensor and the sensor is allowed to equilibrate. The NH_3 is slowly added again to the interface. The response of the sensor to NH_3 is greater with the H_2S background. In the figure, we denote the onsets of H_2S and NH_3 with an asterisk. H_2S dominates NH_3 and the onset of NH_3 points downward (dominant H_2S turning off as NH_3 turns on).

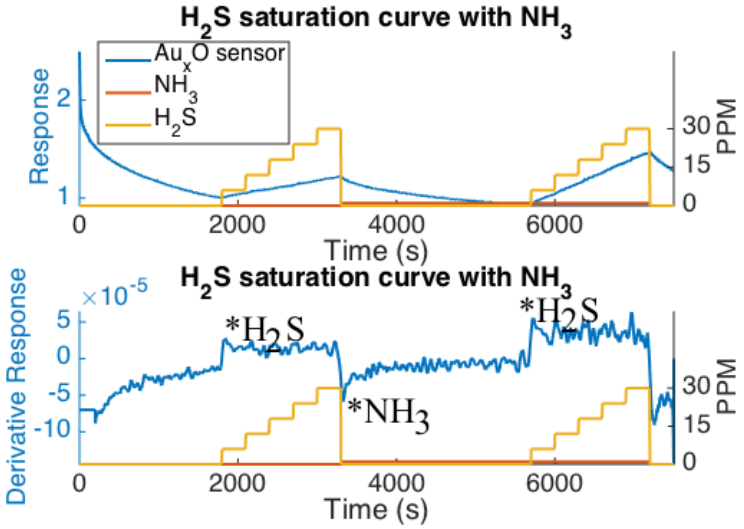

Figure 4.25: The Au_xO *p*-type sensor response to NH_3 and H_2S. The sensor was allowed to come to a base line after treatment with 1800 S of UHP N_2. Then H_2S is slowly added to the surface. Once the H_2S was turned off, NH_3 was added to the sensor and the sensor was allowed to equilibrate. The H_2S is slowly added again to the surface. The response of the sensor to H_2S is greater with the NH_3 background.

sites. This means that the orbital mismatch with NH_3 will increase. As NH_3, acting as a background gas, interacts with Au_xO , it lowers the Lewis acidity to a lesser extent and the effect on H_2S will be less. In summary, the addition of both H_2S and NH_3 will decrease the Lewis acidity of the Au_xO site, shifting the Au_xO site to the soft acid side of Figure 4.26. This enhances the orbital mismatch of the gases with the PS interface and thus increases their reversible response. The shift corresponding to a decreasing Lewis acidity is indicated in Figure 4.26. Figure 4.26 represents the adjustments of the Hard/Soft acid/base diagram. As the deposited metal oxides change the interface response of PS, so also can adsorbed gases change the interface response of a decorated PS surface. As they interact with the metal oxides depending on their acidity or basisicity and their relative location in Figure 4.26 the analyte gases can increase or decrease orbital mismatch. To test this concept, we compared the responses of a *p*-type plain PS sensor to that of a SnO_2 deposited interface in Figures 4.27 and 4.28. Duplicate experiments were conducted with the plain PS sensor and the SnO_2 deposited sensor.

The plain PS sensor, Figure 4.27, also demonstrates an increased response to NH_3 when an H_2S background is present, in analogy to the Au_xO decorated sensor of Figure 4.24. As H_2S interacts with PS, the Lewis acidity of the PS decreases. In Figure 4.26, this leads to a shift away from both NH_3 and H_2S, increasing the orbital mismatch and causing the reversible response to increase. This effect is greater with the plain undecorated PS sensor of Figure 4.27 than the Au_xO deposited sensor of Figure 4.25 because of the closer location of H_2S to PS on the hardness scale (Fig. 4.26. As seen in Figure 4.28, the SnO_2 decorated *p*-type interface has a decreased response for NH_3 when an H_2S background is present. This again is due to a compounded behavior. The SnO_2 lies to the hard acid side of H_2S and NH_3 and when H_2S contributes electrons to SnO_2, its Lewis acidity decreases. This decreases the mismatch between SnO_2 and NH_3, the diminished mismatch leads to an decrease in the sensor response to NH_3.

The SnO_2 decorated *p*-type interface has a decreased response for the H_2S when an NH_3 background is present as seen in Figure 4.28. This also is in line with the IHSAB concept. The SnO_2 nanoparticles are strongly acidic so when the basicity increases, it also decreases

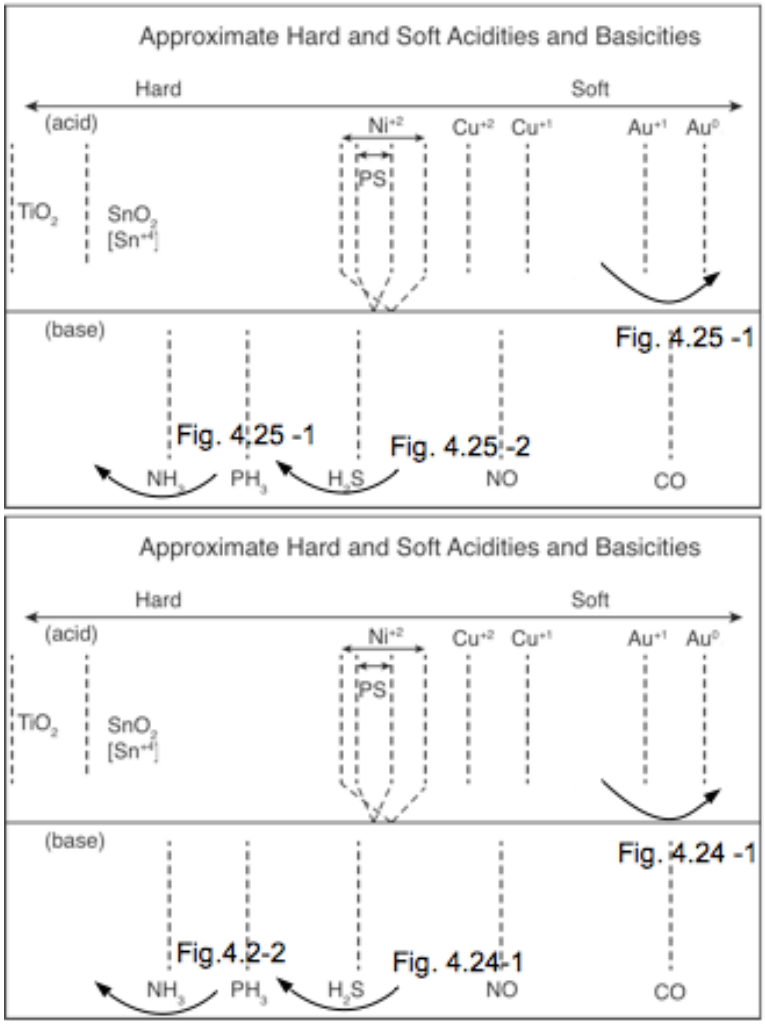

Figure 4.26: The IHSAB interaction matrix showing how the different metal oxides would shift if they became less acidic due to the presence of the basic gases NH_3 and H_2S. In Figure 4.25 NH_3 gas interacts with the Au_xO decorated PS interface (noted by the Fig. 4.25-1). This interaction decreases the hardness of the Au_xO. When the H_2S interacts (displayed by Fig. 4.25-2) with the shifted Au_xO, the orbital mismatch with H_2S has increased and the response increases. In Figure 4.24 the H_2S interacts with the Au_xO decorated PS interface.. This interaction decreases the hardness of the metal oxides. When the Au_xO interacts with NH_3, the mismatch between the soft acid and the moderate base has increased causing the conductometric response to increase.

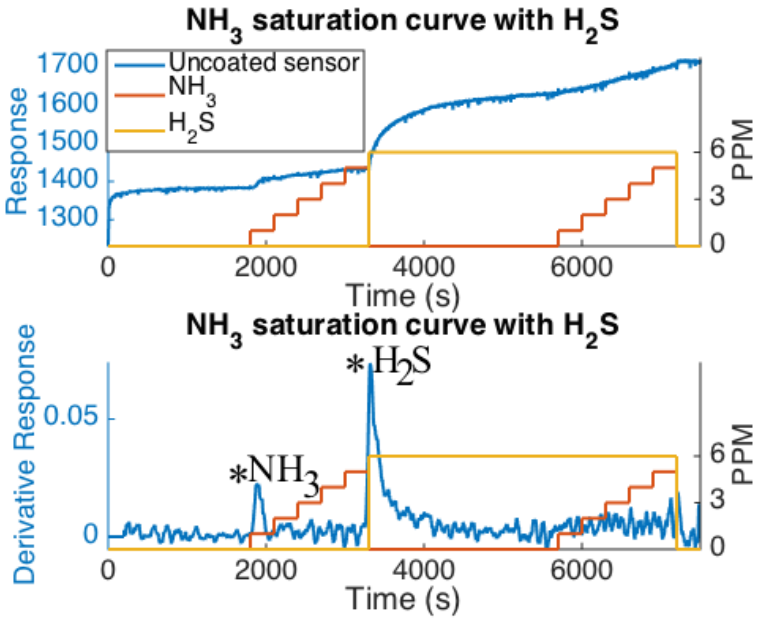

Figure 4.27: Uncoated p-type sensor response to NH_3 and H_2S. The sensor was allowed to come to a base line after treatment with 1800 S of UHP N_2. NH_3 was then slowly added to the interface. Once the NH_3 is turned off, H_2S was added to the sensor and the sensor was allowed to equilibrate. NH_3 is slowly added again to the surface. The response of the sensor to NH_3 is greater with the H_2S background. * Refers to the initial onset of NH_3 and H_2S exposure to the sensor interface. H_2S again dominates NH_3.

the mismatch between the SnO_2 and the NH_3 and H_2S. The increased orbital matching leads to a decrease in the sensor response to H_2S.

We next examined the interaction of two weakly acidic gases on a p-type PS interface decorated with SnO_2 (Figures 4.29 and 4.30). NO and CO acting as weak acids remove electrons from the decorated PS surface and increase the number of holes which are the majority charge carriers. This leads to an increase in conductance and a decrease in the resistance of the sensor. Each gas was exposed to the surface then the alternate gas was run to create a baseline in the same way as done for the H_2S, NH_3 experiments. The first gas was then pulsed again. A concern with these test gases was the level of response for each gas. PS is much more responsive to NO than to CO. Despite this limitation, it can be seen that the gases increase the reversible sensor response to each other for the SnO_2 decorated surface. For NO pulsed with and without a CO background we observe an increase in the

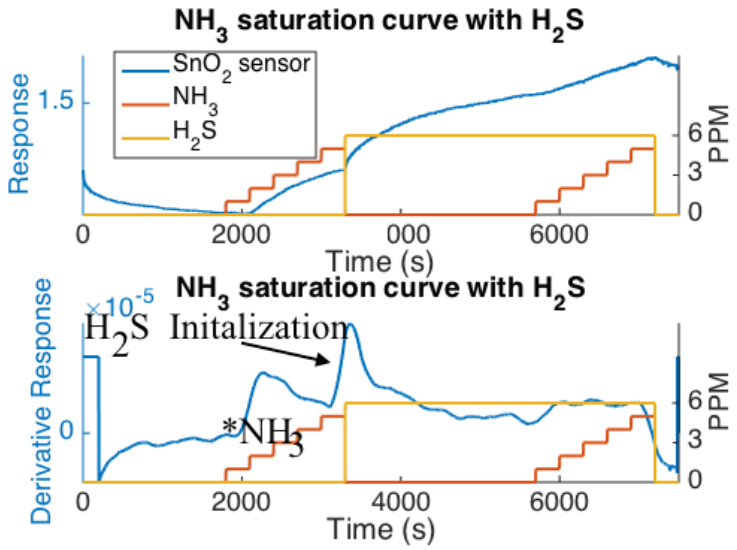

Figure 4.28: (Top) SnO_2 decorated p-type sensor response to NH_3 and H_2S. (bottom) the derivative of the sensor resistance. The sensor was allowed to come to a base line after an 1800 S treatment of UHP N_2. NH_3 is slowly added to the surface. Once the NH_3 was turned off, the H_2S was added to the sensor and the sensor was allowed to equilibrate. The NH_3 was added again to the surface. The slope of the response response of the sensor to NH_3 decreases in the presence of the H_2S. This can be seen more clearly in the derivative than in the plot of resistance. The average slope (the height of the derivative) is greater without the H_2S than the slope when the H_2S is present * There is a small enhanced peak for NH_3 initialization. The onset of H_2S again dominates NH_3.

saturated response to NO in the presence of a CO background for the SnO_2 decorated p-type PS interface. Here, CO on SnO_2 leads to an interaction which increases the separation and orbital mismatch with NO. The effect of the CO background on the NO response is significant, although not as great as the H_2S ?NH_3 interaction. For the reversed experiment on the SnO_2 decorated sensor, the CO pulse appears virtually lost in the NO background. However there is a slight change in the response suggesting that the CO response might be added to that of NO for a small enhancement of the signal. As CO interacts on an SnO_2 decorated PS interface, the NO (background)- SnO_2 interaction increases the orbital mismatch with CO. In contrast, with Au_xO decorated PS sensors the interactions with NO and CO are greatly modified as shown in Figures 4.31 and 4.32.

While the effect of the CO on the NO response is significant, although not as great as the H_2S-NH_3 interaction, the CO pulse appears lost in the NO background for the reversed experiment on the SnO_2 decorated sensor. However there is a slight change in the response

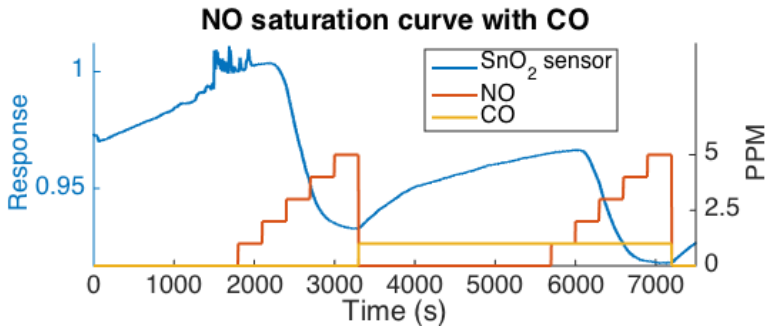

Figure 4.29: The response of a SnO_2 decorated *p*-type sensor response to NO and CO. The sensor is allowed to come to a base line after treatment 1800 S with of UHP N_2. Then NO is slowly added to the surface. Once the NO is turned off, CO is added to the sensor and the sensor is allowed to equilibrate. Then the NO is added again to the surface. The red line represents the ppm values of NO, and the yellow lines the ppm values of CO. The saturated response of the sensor to NO is greater with the CO.

suggesting that the CO response might be added to the NO for a small enhancement of the signal. Au_xO enhanced PS sensors were also run and they tell a slightly different story as shown in Figures 4.31 and 4.32.

In the Au_xO decorated *p*-type PS sensor runs the CO response is slightly diminished when run with NO present (Figure 4.31). The Au_xO Lewis acidity increases due to the interaction with the NO background gas. This, in turn, decreases the mismatch with CO and the conductance. As CO interacts with Au_xO, its Lewis acidity increases. The NO response decreases as it interacts with the CO deposited on and interacting with the Au_xO *p*-type surface (Figure 4.32) and the conductance level is lower with CO present. As CO interacts with Au_xO and its Lewis acidity increases, Au_xO shifts toward the hard acid side of Figure 4.26 ,closer to the NO. This decreases orbital mismatch and the reversible interaction with NO.

NO and CO mixtures have also been examined on NiO and Cu_xO deposited *p*-type sensors. These systems both see a change in the response for NO in the presence of CO. The NiO *p*-type system sees an increase in the conductance when the NO interacts with it. As the initial exposure to NO ceases, the CO does not increase the conductance of the system further. When the NO cycle is returned, the conduction increases (resistance decreases) and saturates to a higher value in the presence of the CO. This results as the

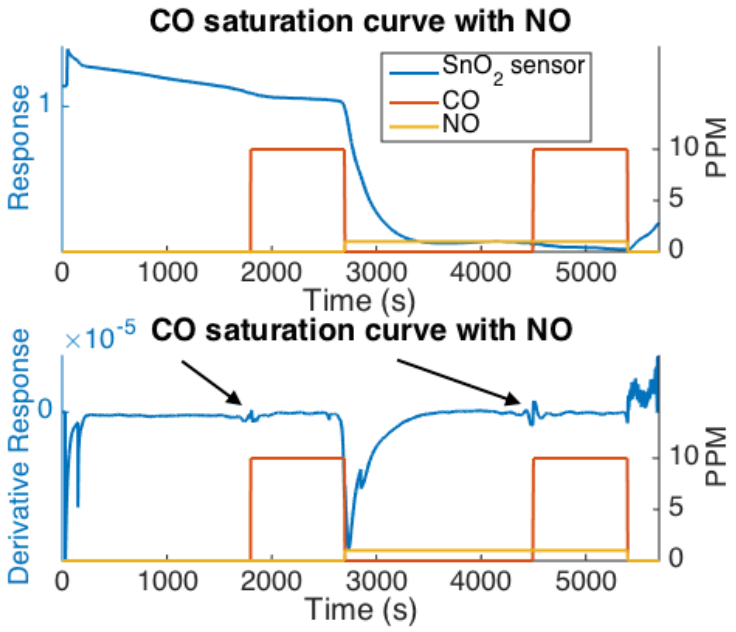

Figure 4.30: xResponse of the SnO_2 decorated *p*-type sensor response to CO and NO (Top). (Bottom) Derivative of the resistance. The sensor is allowed to come to a base line after treatment with 1800 S with of UHP N_2. The CO is slowly added to the surface. Once the CO is turned off, NO is added to the sensor and the sensor is allowed to equilibrate. Then the CO is added again to the surface. The red line represents the ppm values of the CO, and the yellow line the ppm values of NO. The response of the sensor to CO is greater when NO has been introduced to the interface. This is observed in the derivative as the spikes, denoted in the figure by with black arrows indicate that the response to CO is larger with the NO present. The dip at 3000 s indicates the introduction of NO.

CO extracts electrons and increases the Lewis acidity of the nickel oxide. This increases the orbital mismatch with NO and leads to an increase in the conductance due to NO as shown in Figure 4.33 . In concert the change in the responses for the NO-CO system indicate a tighter positioning for NO and especially CO in Figure 4.37 . The observed interactions result if CO is directly to the hard acid side of Au_xO and NO is to the soft acid side of Cu+2/ Cu+1.

The Cu_xO decorated sensor also shows an increase in the conductance when NO interacts with background CO. This is again results as CO interacts with Cu_xO and increases the Lewis acidity of the Cu_xO This increases the orbital mismatch with NO leading to an increase in the conductance as shown in Figure 4.34 . Here, CO interacts with and shifts Cu_xO, increasing the reversible interaction with NO. It should be noted that the increase in

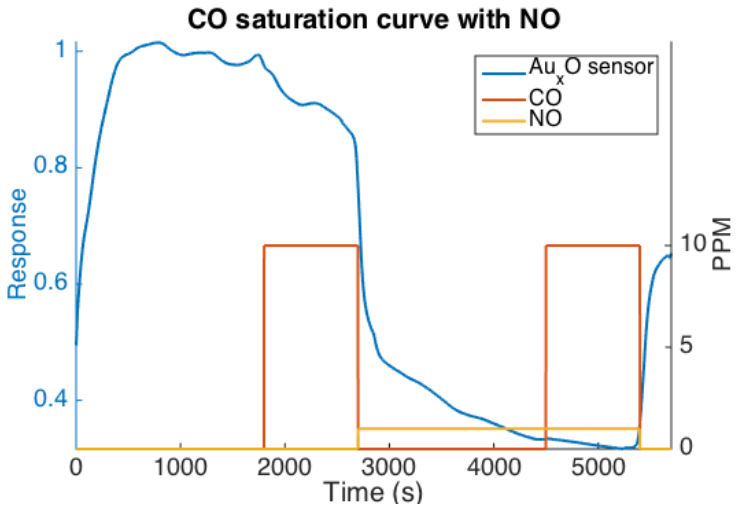

Figure 4.31: Response of an SnO_2 decorated *p*-type sensor response to CO and NO. The sensor is allowed to come to a base line after treatment with 1800 S of UHP N_2. Then CO is slowly added to the surface. Once the CO is turned off, NO is added to the sensor and the sensor is allowed to equilibrate. CO is then added again to the surface. The red line represents the ppm values of the CO, and the yellow lines the ppm values of NO. The response of the sensor to CO is less in the presence of NO.

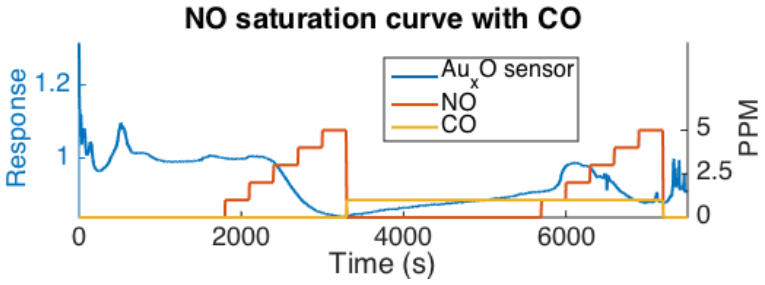

Figure 4.32: Response of an Au_xO decorated *p*-type sensor response to NO and CO. The sensor is allowed to come to a base line after treatment with 1800 S of UHP N_2. Then NO is slowly added to the surface. Once the NO is turned off, CO is brought to the sensor and the sensor is allowed to equilibrate. NO is then added again to the surface. The red line represents the ppm values of the NO, and the yellow line the ppm values of CO. The response of the sensor to NO is less with the CO background.

conductance with the NO-CO mixture is greater for Cu_xO than the change in conductance associated with NiO. This results since Cu_xO lies closer to NO so that any small shift will change the response for the Cu_xO more than that associated with NiO. The NiO and the Cu_xO sensors respond only weakly to CO for the alternate runs (Figures 4.35 and 4.36). However, the CO appears to have an effect on the response of the sensor to NO. This fact suggests that the gases can subtly change the nature of the metal oxides even though they are barely detected in the normal sensor resistance changes.

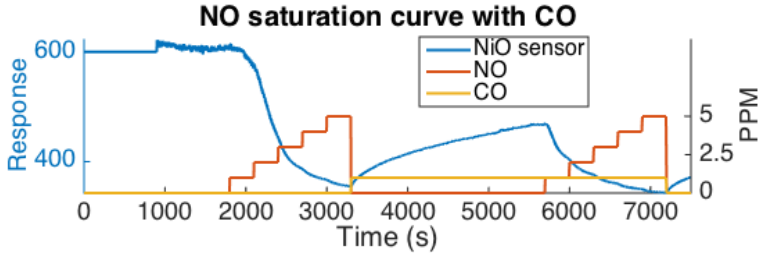

Figure 4.33: Response of a NiO decorated *p*-type sensor response to NO and CO. The sensor is allowed to come to a base line after treatment with 1800 S of UHP N_2. Then NO is slowly added to the surface. Once the NO is turned off , CO is added to the sensor and the sensor is allowed to equilibrate. NO is then added again to the surface. The red line represents the ppm values of the NO, and the yellow lines the ppm values of CO. The response of the sensor to NO is greater with the CO background.

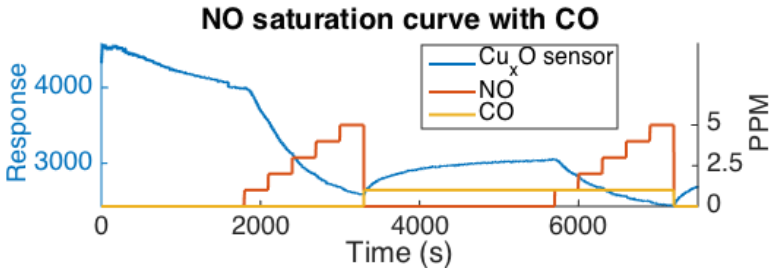

Figure 4.34: Response of a Cu_xO decorated *p*-type sensor response to NO and CO. The sensor is allowed to come to a base line after treatment with 1800 S of UHP N_2. Then NO is slowly added to the surface. Once the NO is turned off , CO is added to the sensor and the sensor is allowed to equilibrate. NO is then added again to the surface. The red line represents the ppm values of the NO, and the yellow lines the ppm values of CO. The response of the sensor to NO is greater with the CO, since the NO saturates at a higher conductance in the presence of NO than without it.

The changes in response associated with CO and NO mixtures are due to the metal oxides shifting to a more acidic character (Lewis acidity increases). The Au_xO shifts closer to the NO when exposed to CO and the conductance decreases. The other metal oxides

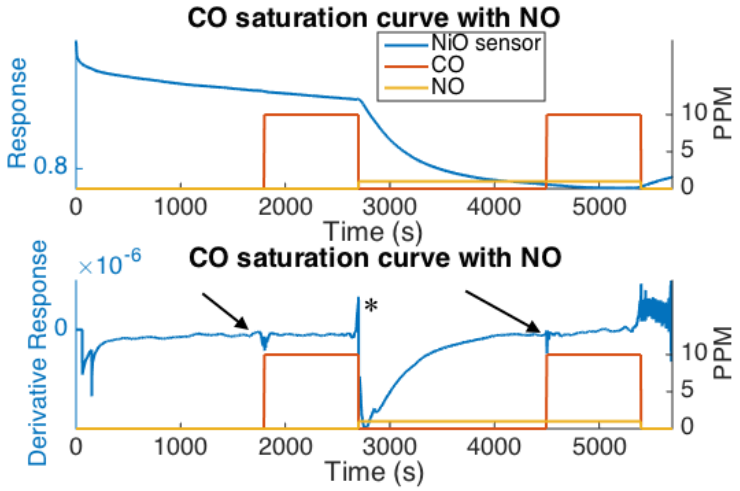

Figure 4.35: Response of an NiO decorated p-type sensor response to NO and CO. The sensor is allowed to come to a base line after treatment with 1800 S of UHP N_2. Then CO is slowly added to the surface. Once the CO is turned off, NO is added to the sensor and the sensor is allowed to equilibrate. CO is then added again to the surface. The red line represents the ppm values of the CO, and the yellow lines the ppm values of NO. There appears to be a slight increase in the response to the CO in the presence of the NO, shown by the larger spike in the derivative, indicated in the figure by the black arrows, when the CO is brought to the interface in the presence of NO. *indicates the introduction of NO

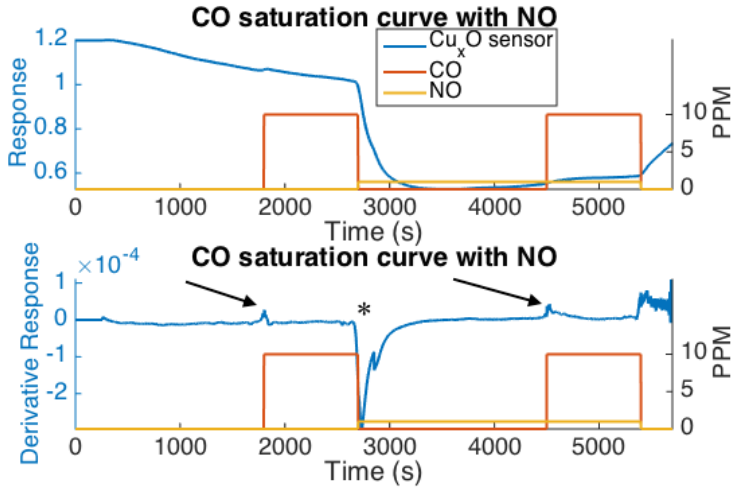

Figure 4.36: The response of a Cu_xO decorated p-type sensor response to NO and CO. The sensor is allowed to come to a base line after treatment with 1800 S of UHP N_2. Then CO is slowly added to the surface. Once the CO is turned off, NO is added to the sensor and the sensor is allowed to equilibrate. CO is then added again to the surface. The red line represents the ppm values of the CO, and the yellow lines the ppm values of NO. There appears to be a slightly increased response to the CO in the presence of the NO. This can be clearly seen in the rise in the derivative of the response when the CO is brought into contact with the NO treated interface. * indicates the introduction of NO.

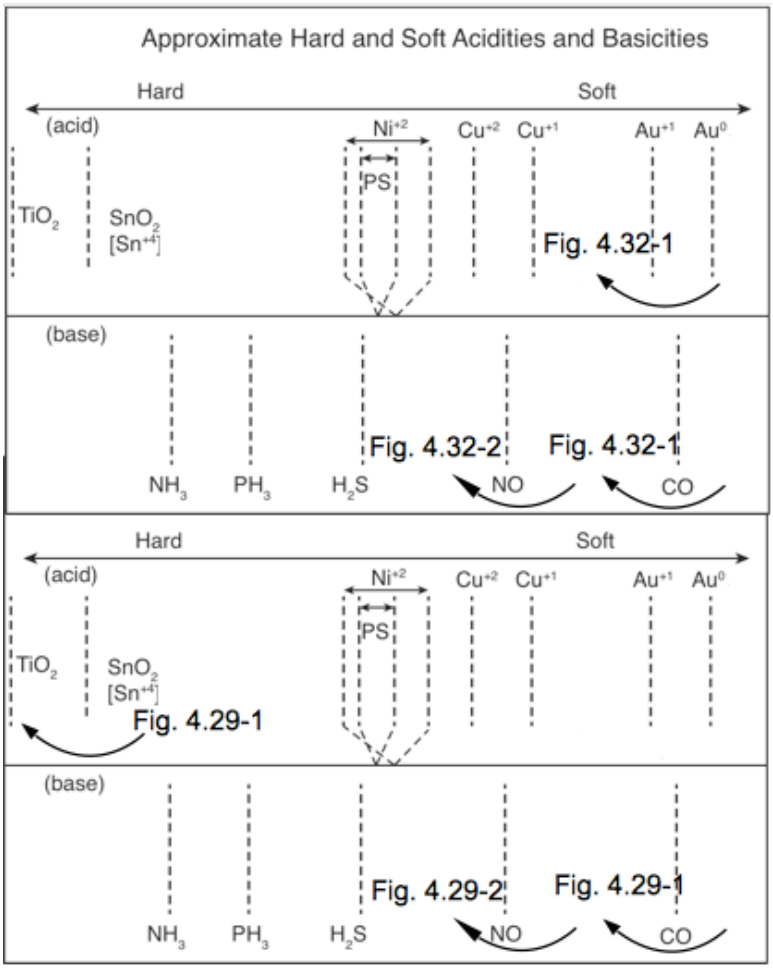

Figure 4.37: IHSAB chart showing the effect of the NO and CO on the acidity of the metal oxides. In Figure 4.32 CO interacts with the Au_xO decorated PS interface.. This interaction increases the hardness of the Au_xO (noted in Fig. 4.32-1). When the Au_xO interacts with the NO (Fig. 4.32-2) the decreased mismatch between the Au_xO and the CO causes the conductometric response to decrease. In Figure 4.29 the CO interacts with the SnO_2 decorated PS interface (noted by the Fig. 4.29-1). This increases the hardness of the SnO_2 nanoparticle deposit. When the NO interacts (displayed by Fig. 4.29-2) with the shifted SnO_2, because the orbital mismatch has increased, the response increases.

shift away from the NO so their conductance increases with the NO. The NO shifts the Au_xO closer to the CO decreasing the reversible response.

4.3.1 Modeling multigas interactions

With a basic understanding of the analyte gas interaction we began to model it. In order to model the response we must take into account the previously mentioned fact that the two-gas interactions are independent of the order the gases are introduced to the system. This independence can be seen in the NO-NH_3 mixtures where the response settles down to a similar resistance value independent of the order of gas. Any theory that describes the response change has to take this fact into account. It is also, important is to note the low concentrations of the gases being used. This fact along with the response enhancements of specific gases do not suggest that there are any strong binary diffusion constant effects [205, 206].

To test the different theories for gas interaction, attempts were made to fit the data for NO and NH_3 interacting using a Langmuir fit, a simple cross term fitting model, and the FDF model. Each model required a few fitting parameters, which were calculated from the heights of the different responses for each data set. These parameters are listed in in the appropriate tables. The gases were simulated diffusing into the surface. We then applied the different models to the diffused gas and used these to generate a response from the simulated diffusion. Then in Figures 4.38-4.40 each model was assessed visually to the accuracy of fit.

The Langmuir formula for multiple gases was used to describe the two gas interactions. The Langmuir formula was implemented for modeling the interaction of NO and NH_3; however, it had two flaws. The first flaw is that the model does not fit a simple one-gas case, and the second issue is that the enhancements of some gas responses are not well described. While the sharp rise of the response in the Langmuir simulation is an issue, the major issue with the model is with the derivative of the response. In the derivative, the data does spike up when an analyte gas is added or removed, then the spike quickly decreases. However, in the Langmuir simulations, the derivative is seen to slowly increase and then slowly decrease as seen in Figure 4.41. This broad symmetric response in the derivative severally limits the accuracy of any simulation using the Langmuir formula for the response. This result suggests that we look at other classes of functions for the multi

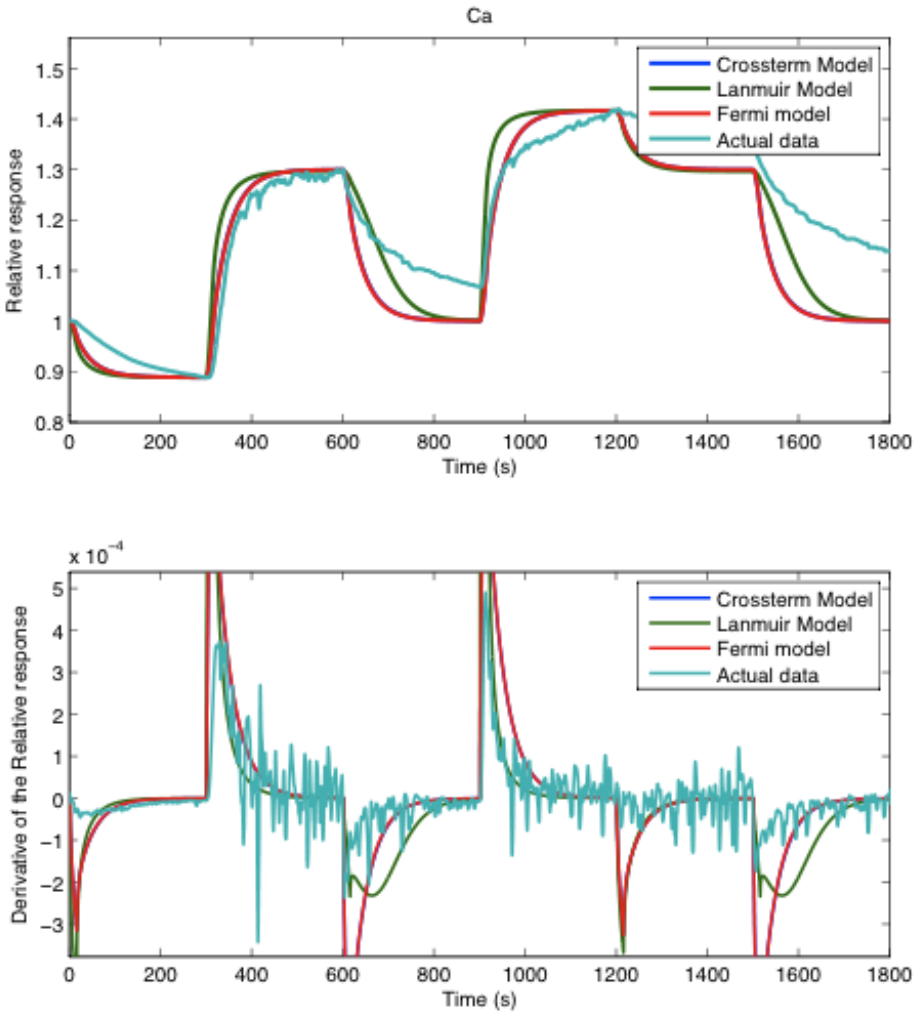

Figure 4.38: Ca oxide decorated sensor exposed to NO and NH_3 (cyan) along with simulation of the response in red, green, and blue. Top is the actual data and simulated responses bottom is the derivatives of the actual response and the simulated data.

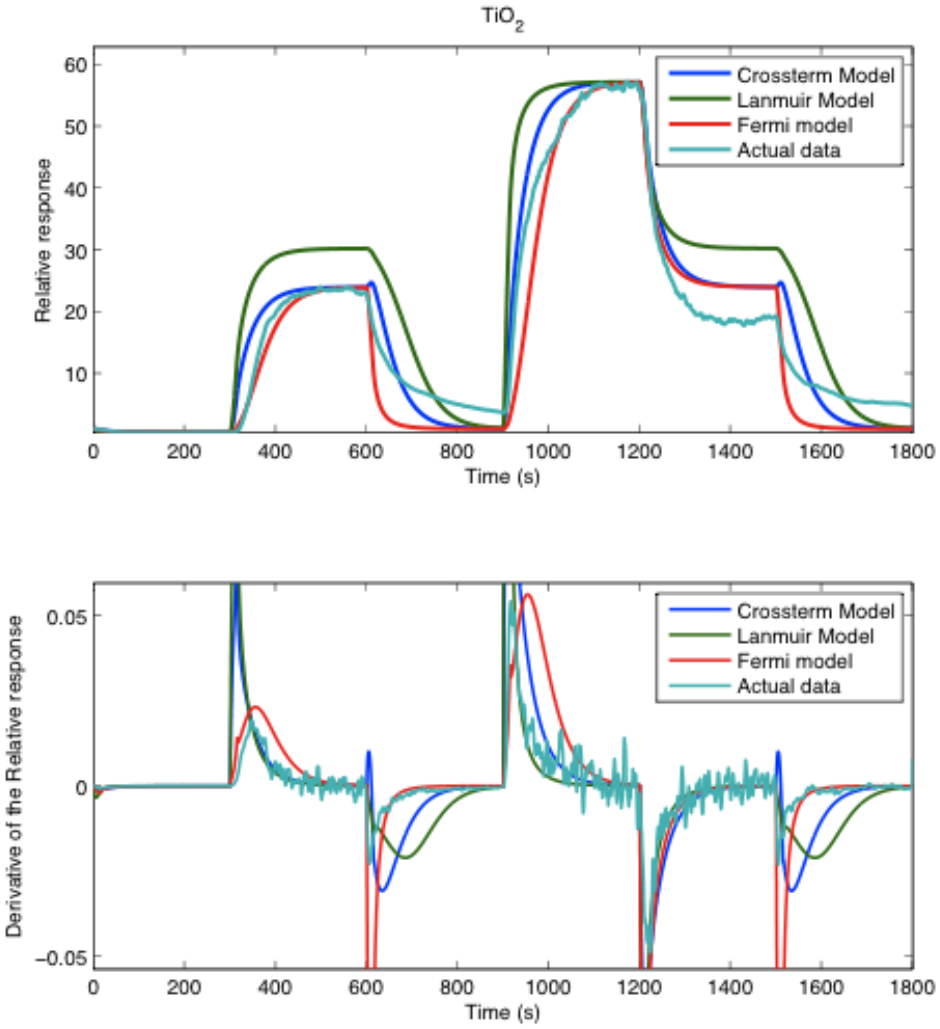

Figure 4.39: Ti oxide decorated sensor exposed to NO and NH_3 (cyan) along with simulation of the response in red, green, and blue. Top is the actual data and simulated responses bottom is the derivatives of the actual response and the simulated data.

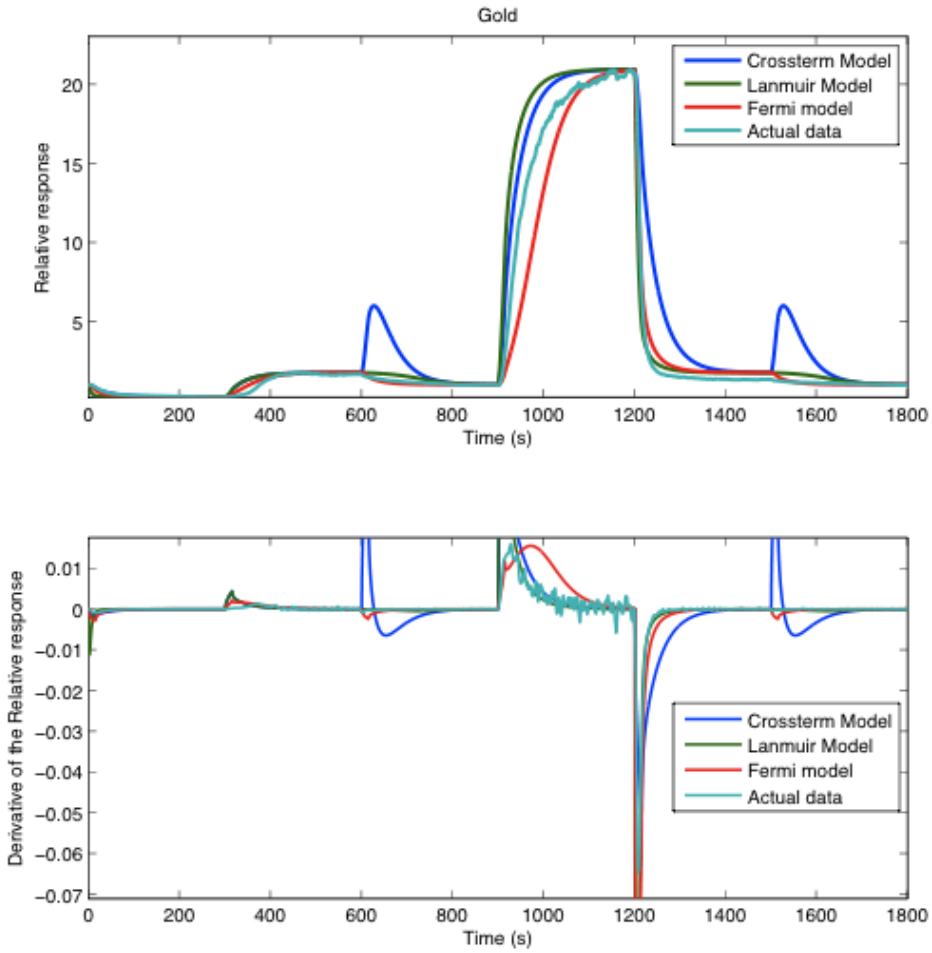

Figure 4.40: Au oxide decorated sensor expose to NO and NH_3 (cyan) along with simulation of the response in red, green, and blue. Top is the actual data and simulated responses bottom is the derivatives.

gas response. All fitting parameters for the Langmuir equations are shown in Table 4.2.

Another model was based on the assumption that there is a cross term effect between the two gases. So instead of a straight linear function like y=a*C1+b*C2 we add a cross term in the response, resulting in a response function like y=a*C1+b*C2 +d*C1*C2 were C1 and C2 are the concentrations of the analyte gases. This function is more of a test case for complicated interactions than an actual theory. However, while the cross term model describes the basic features, it has difficulty describing largely mismatched gas sensor responses. For example, the response of the Au_xO decorated p-type surface to NH_3 is around

Table 4.2:
Fitting parameters for the Langmuir equation for different metal oxide coatings. Where C_{NO} and C_{NH_3} are respectively the concentrations of the NO and NH_3. $R = \frac{A*B*C_{NO}+D*E*C_{NH_3}}{1+B*C_{NO}+D*C_{NH_3}}$.

Metal oxides	A	B	E	D
Gold	-0.27	14.4	24.76	0.47
Ca	-0.21	0.2267	0.527	0.3777
TiO_2	-0.737	0.921	69.76	0.4117

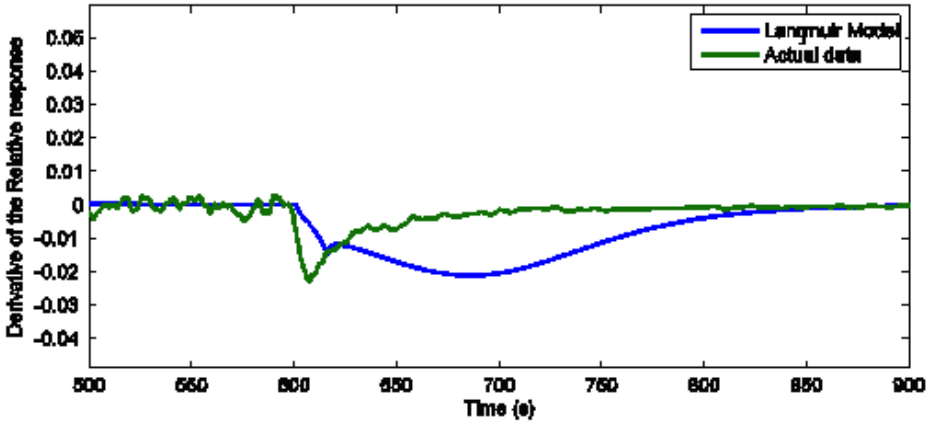

Figure 4.41: Close up of the hump in the derivative generated from the Langmuir model which is both huge in duration and fairly symmetric unlike the derivative of the actual response which has a short duration and is very asymmetrical.

10 times greater than the response with NH_3 and NO. So in order to properly model it, the cross term has to be very large. This large cross term which makes a slight change in the ratio of the gases causes a large bump in the response when the gas concentrations change. The close up of this feature is shown in Figure 4.42. This bump is feature when the gas changes suggesting that any function of the gas interaction does not have a strong cross term in it.

Finally we used the FDF model and simply modified it to include the two gases modifying the Fermi level in the exponential. While this might not be the optimal way to model these interactions, it does have some advantages. It does model the shift in sensitivity of the analyte gas interaction. And even if the function is not linear then it is at least easy to reverse, since it is a single value function without any cross terms.

Table 4.3:
Fitting parameters for the Cross fit equation for different metal oxide coatings. Where C_{NO} and C_{NH_3} are respectively the concentrations of the NO and NH_3. $R = A * C_{NO} + B * C_{NH_3} + D * C_{NO} * C_{NH_3}$.

Metal oxides	A	B	D
Gold	-0.1542	1.9943	-0.3682
Ca	-0.0223	0.0417	-0.0001
TiO_2	-0.121	5.612	-0.651

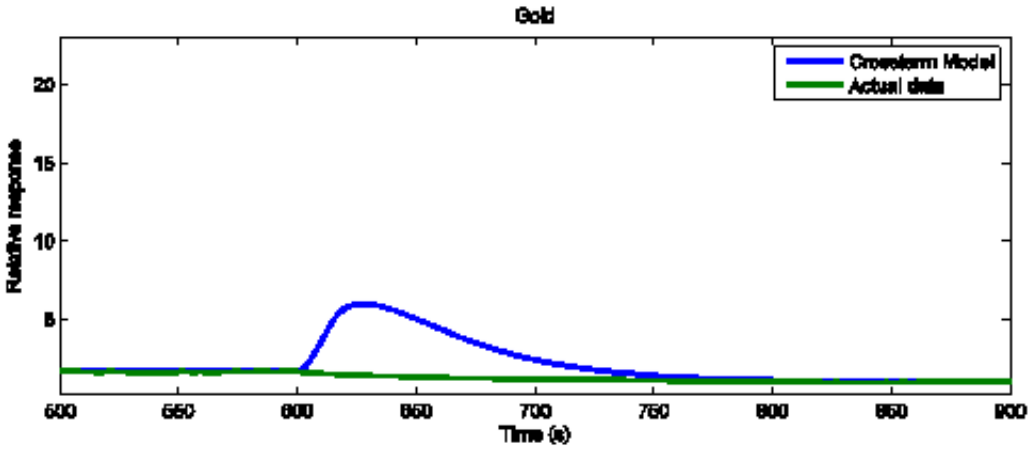

Figure 4.42: Close up of the predicted broad response rise caused by the cross term for the Au_xO decorated interface.

While none of the fitting methods works perfectly the overall result is that, the FDF model gives the best fit of all the methods. None of these models handle the gas stickiness in the pores, which is a problem with the diffusion simulation, not the interaction models. The response models only take the gas concentration from the diffusion model, but do not modify it.The problem of concentration changes is only calculated from the diffusion simulation. Despite this the FDF model does seem to fit and model the multi gas interactions quite well of short runs. In addtion we have a fundamental understanding of how the FDF model works instead of only empirical proof.

4.3.2 Electronic conduction calculations

Now let us look at the fitting parameters for the Fermi model and see if the numbers make sense for the change in the charge carrier density . In order to calculate the change in the

Table 4.4:
Fitting parameters for the Fermi equation or different metal oxide coatings. Where C_{NO} and C_{NH_3} are respectively the concentrations of the NO and NH_3. $R = \frac{1+A}{1+Ae^{B*C_{NO}+D*C_{NH_3}}}$
.

Metal oxides	A	B	D
Gold	7.922	0.2767	-0.1868
Ca	2.472	0.038	-0.068
TiO_2	575.1	0.186	-0.415

charge carrier density, we must know the initial charge carrier density of the doped silicon wafer. Using the formula for resistivity ρ=1/N_e *e*μ_e we can calculate that a 8-13 ohm-cm resistivity p-type wafers with mobility around 397 Vcm^2/s will have a doping level of between 1.70 to 1.04 e15 boron atoms per cm^3 of silicon. For n-type wafers with resistivity between 1-20 ohm-cm and mobility of 1396 Vcm2/s the doping levels are between 4.96 e15 to 2.24 e14 phosphorus atoms per cm^3, much greater than the intrinsic charge density of e10 charge carriers per cm^3.

For comparison to the charge density of silicon, 1 cm^3 of air at normal pressure and temperature has 2.65 e19 molecules. If there is 1 ppm of NH_3 in the air, there are 2.65 e13 molecules of NH_3 per cm^3, so the theoretical maximum possible charge carrier change is 2.65 e13 per cm^3. The charge carrier density of the analyte gas is two orders of magnitude smaller than the number of majority charge carriers in the porous silicon. The difference in density implies that the shift in the charge carriers is not due to the addition or removal of electrons by the analyte gas, but instead the manipulation of the Fermi level. The metal oxide nanostructure island sites can control this shift in the Fermi levels as they dictate. a focused transfer of electrons governed by the IHSAB theory. This transfer of electron to the island sites acts to force a larger change in the Fermi levels of the PS, enhancing the response.

But the electron density calculations are for bulk silicon, we must examine what happens to the electron properties when the PS is etched. The studies by Timoshenko, et al., have shown that the charge carrier density of the porous silicon do not change after etching in

the bulk porous silicon [207]. However, the porous silicon does have a different band gap then the bulk silicon, so this causes a depletion of the charges when the porous silicon is in contact with the bulk silicon [208]. This depletion causes a diode effect at the PS-silicon junction, suggesting that small changes of the Fermi level will lead to large changes in the conduction. [209–211]

Also when the PS is etched, the mobility of the electrons decreases by at least three orders of magnitude from the bulk silicon [207, 212]. The decrease in mobility increases the resistivity of the PS. This means that the charge carriers will minimize travel in the PS and flow through the porous-bulk silicon interface, which has been seen to act as a diode. Rough estimations of the resistance breakdown suggest that the PS-silicon layer accounts for at least 99% of the base resistance measured. So changes in the density of the charge carriers in the PS-silicon layer will greatly affect the measured resistance.

The numerical data from the Fermi fits seen in Table 4.4 are multiplied by 0.0257 eV(kT at room temperature). This gives a Fermi level shift of 0.05 eV to 0.001 eV per ppm. These numbers are around the energy of physisorption. The base Fermi level is seen to be around 0.05 to .16 eV away from the valence band. The resulting shift in Fermi level should increase the electron density by around 1014 electrons per cm^3 per ppm. For example the shift in the p type TiO_2 decorated surface is an increase in the range of 1.04 to .66 e12 holes per cm^3 for exposure to 1 ppm NO and a decrease of around 3.02 to 1.86 e11 holes per cm^3 for 1 ppm of NH_3. For gold the concentration change is in the range of 5.03 to 3.09 e13 holes cm^3 for 1 ppm of NO and 2.08 to 1.28 e13 holes cm^3 for 1 ppm of NH_3. These changes in the charge carrier density are range over two orders of magnitude; however, they are consistent with the variation in the sensitivities between sensors. In general the shifts in charge carrier density are on the same order of magnitude as the analyte gas. However some are larger than the density of the analyte so, it is likely that a shift in the Fermi level causes the resistance change. These shifts are likely governed by the metal oxide nanoparticles interacting with the analyte gases, which then leads to a modification of the PS Fermi level.

This does not change the results of the acids and bases interacting with the semiconductor. As an acid has a lower electrochemical potential, it will shift the Fermi level down

decreasing the number of electrons in the conduction band and increasing the number of holes in the valence band. A base has a higher electrochemical potential and shifts the Fermi level higher, increasing the number of electrons in the conduction band and decreasing the number of holes in the valence band, as shown in Figure 4.43. So acids are still shifting electrons away from the semiconductor and bases are a shifting electrons into the semiconductor.

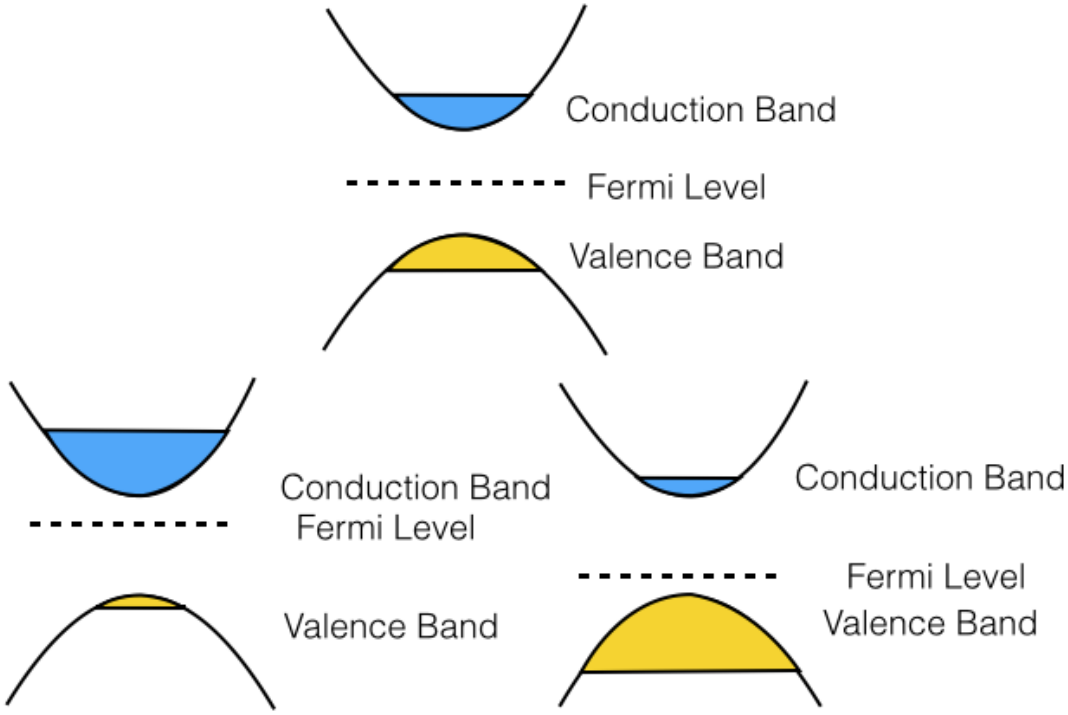

Figure 4.43: Top normal semiconductor, left semiconductor interacting with an base with the bands bent up. right semiconductor interacting with an acid with the bands bent down

4.3.3 Advanced Testing

For a more advanced test, longer sensor runs with more gas interactions were recorded as shown in Figure 4.44. Here, we attempted to take the response for the first half of a response measurement and use that to simulate the response in the second half of the run. However, the adsorption effects began to pile up and none of the simulation models accurately described the sensor response of the gases as the models give too high a response for one gas interaction and too low a response for the final gas mixture. However, while

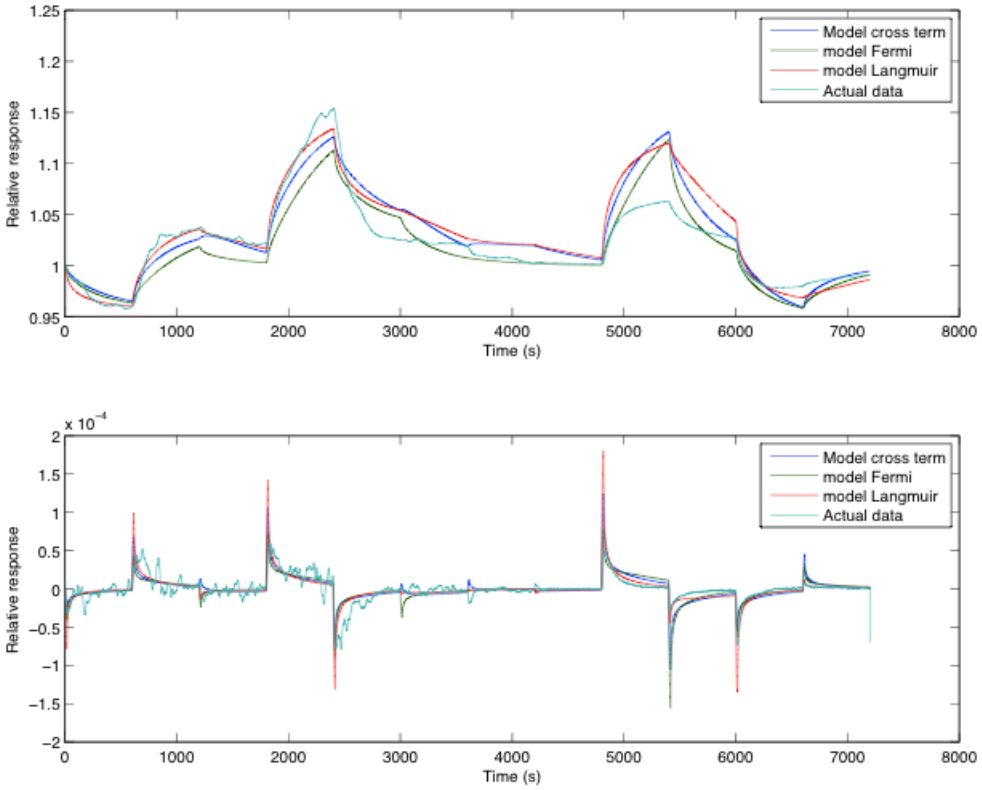

Figure 4.44: Simulation of more advanced gas interactions. Saturation effects seem to dominate the response at later times.

the data extracted from a variety of simulations was not perfect, the FDF model does show promise.

4.4 Multivariate Analysis

We also looked at a more qualitative method to extract gas concentrations from the sensor data, starting with Clustering analysis. We attempted to improve accuracy of the sensor response by clustering the sensor response datasets [213]. The idea of clustering is to extract values from the raw data so that the extracted values group similar stimuli together. In our case, the raw data would be the resistances (conductances) from an array of sensors and the stimuli would be pulses of analyte gas.

In the ideal scenario, the clustered responses of the stimuli would indicate the gas type. So for example, if we pulse 3 ppm of H_2S on to an array of sensors, we could extract the highest recorded resistance of each of the different sensors. Then we could repeat the pulse of 3 ppm of H_2S onto the sensor array and again extract the highest resistances of each of the sensors. Ideally, the maximum values of the different sensors would all be at the same value for the two pulse sequences of 3 ppm H_2S. However, because real data has variance, we can expect that there would be some spread in the points from the ideal case where the points have zero variance. In order to minimize the spread of the points, we will try and pick a value to extract from the raw data that gives the most variance between different gas pulses. This will be the main thrust of these experiments.

In order to determine the best values for the clustering method, we pulsed short bursts of H_2S and NH_3 onto a two sensor array and measured the resistances of the two sensors. The results are shown in Figure 4.45. We then extracted various data points from the responses. For each gas pulse, we collected the highest resistance value (the peak), the amplitude of the derivative peak, the difference between the highest resistance value for a pulse and the lowest resistance value, and finally we created a vector combining the first set of values (highest resistance) with the second set (amplitude of the derivative peak).

We then took each of the aforementioned data sets and plotted the responses of one sensor against the other, looking at how the points clustered. Ideally there would be a clear separation between the different types of analyte gas pulses.

Clustering analysis was able to differentiate between the analyte gases. Each of the different sets of values are plotted in Figures 4.46 to 4.49. All the different value sets show

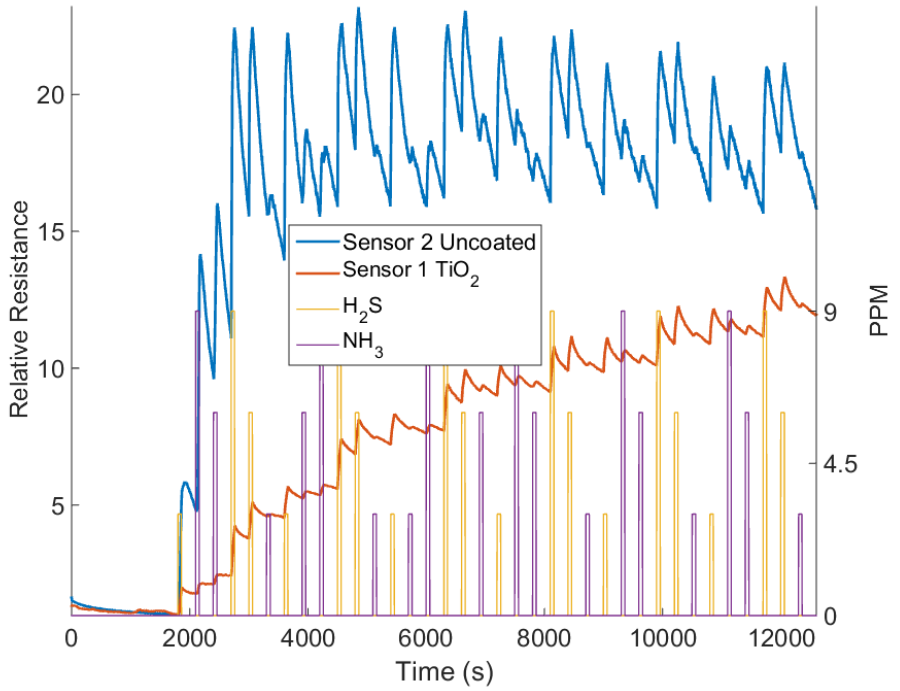

Figure 4.45: Results from a sensor run for a two sensor-array, composed of one uncoated and one TiO_2 decorated sensor, interacting with pulses of NH_3 and H_2S gas. There were 36 pulses of differing ppm values and analyte gas. Each pulse was 60 seconds long with 240 seconds of purging with N_2.

a definite separation in the data between the H_2S pulses and the NH_3 pulses. There are no H_2S responses in the NH_3 area or vice a versa. In Figure 4.46 the two highest values for the resistance are plotted against each other. For this data set the NH_3 pulses are in the bottom two thirds of the graph while the H_2S pulses are in the top third. There seems to be some separation of the H_2S ppm values each ppm level makes a small curve in the top; however, the curve for the 9 ppm of H_2S is between the curves for the 3 and 6 ppm pulses. There seems to be no trend in the grouping of the NH_3 pulses.

The data in Figure 4.47 shows a slightly different clustering. Here the H_2S pulses takes up the right half of the plot while the NH_3 pulses take up the left half. The 9 ppm pulses of H_2S are separate from the other H_2S pulses; however, the 3 and 6 ppm pulses are meshed together. On the NH_3 pulse side there seems to be no clear clustering of the data.

While the method is not as straightforward as the other two, the data in Figure 4.48 does have a clear separation. The H_2S pulses takes up the right half of the plot while the

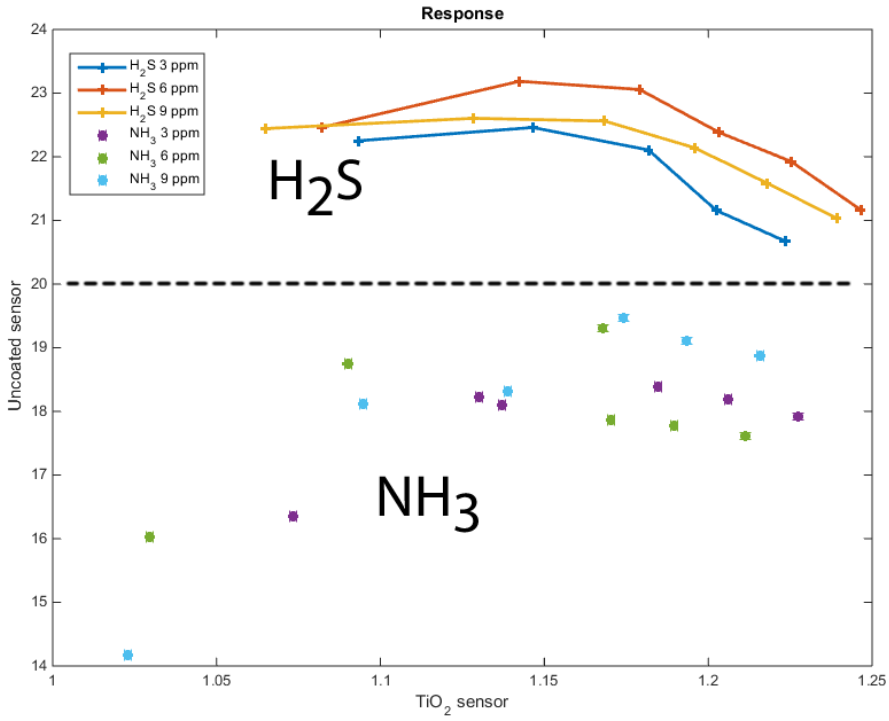

Figure 4.46: Plotting the highest response of the two sensors.

NH_3 pulses take up the left half. The 9 ppm pulses of H_2S are again separate from the other H_2S pulses but again the 3 and 6 ppm pulses are meshed together as in Figure 4.47. The NH_3 pulses are more tightly grouped than in Figure 4.47. The only advantage that this data set has over the derivative set is that the separation between the two analyte gases is much more distinct. Because the clustering analysis did not show much to distinguish the NH_3 ppm data points apart, we used Principle Components Analysis (PCA) to try to solve this problem. PCA takes multidimensional data and finds the axes of the data that have the most variance (a.k.a. the most spread). PCA does this by finding the eigenvectors and eigenvalues of the covariance matrix of the data. The amount of variance of the data in the direction of the eigenvector is related to the size of the eigenvalue.

In this stage of the analysis, we compared the highest response to the gas with the largest spike in the derivative, finding the resulting component axes, and we then plotted the two major axes [113, 114]. The results are shown in Figure 4.49. In the figure the H_2S pulses cluster mostly in the bottom right half of the plot while the NH_3 pulses cluster in

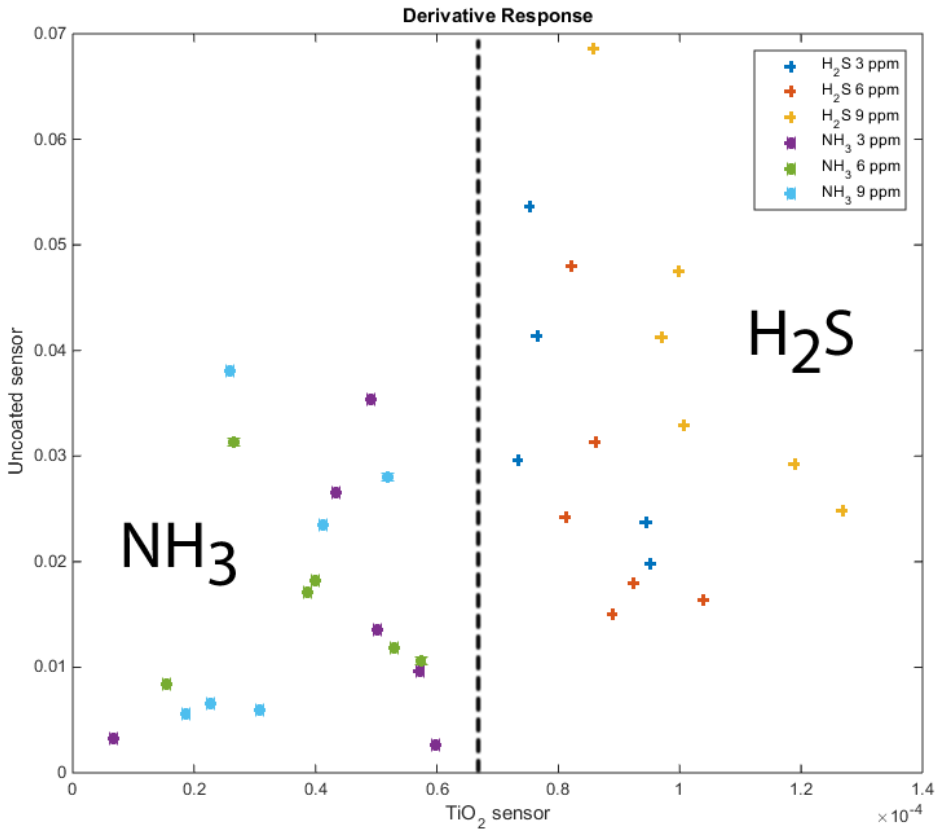

Figure 4.47: Plotting the height of the derivative peak from the two sensors for each gas pulse against each other.

the top left half. Otherwise, there appears to be no significant separation of the pulses. The eigenvalues of each axis are included in the figure. There is a large variance in the left to right axis and a smaller variance in the top to bottom axis. Despite the failure to easily separate the different gas pulses, the fact that the different gases clustered together shows the promise of this analysis and we can easily separate out the 9 ppm H_2S pulses from those of smaller value. Improvements would account for saturation effects, which would take into account the previous pulsed gas studies and could show the promise of this analysis for sensor applications [119].

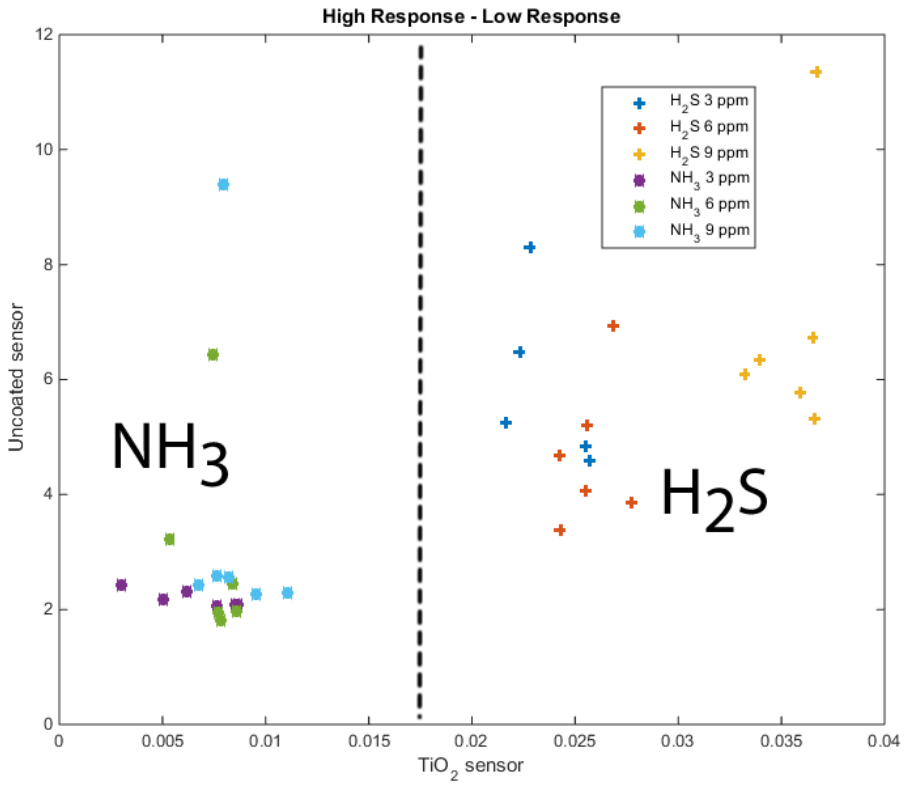

Figure 4.48: Plotting the difference between the lowest part of the response peak and the highest for the two sensors.

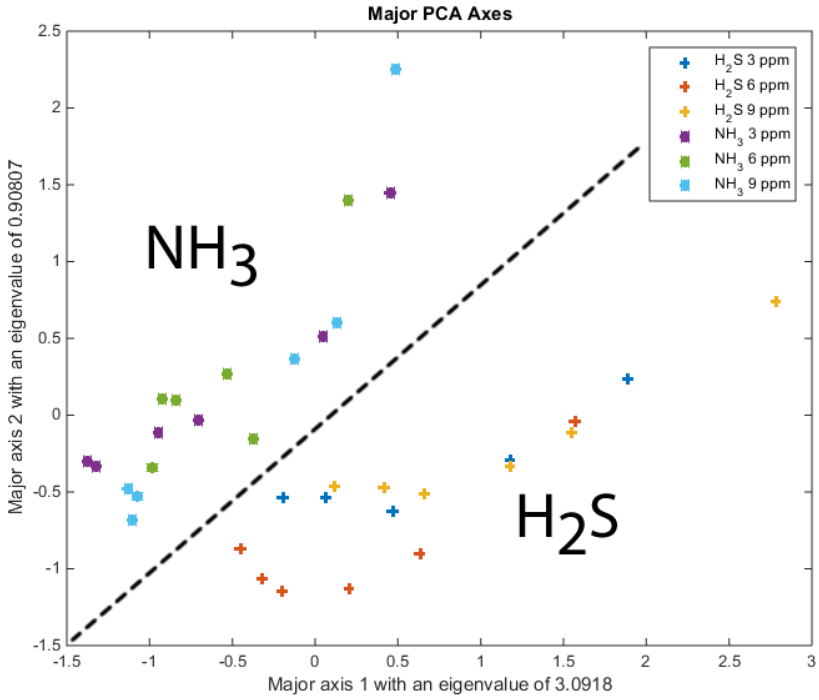

Figure 4.49: The major PCA axes for combined values of the highest resistance and the height of the derivative of the resistance.

4.5 Summary

In summary we have looked at saturation and multi-gas effects and noted that the FDF model of saturation does seem to model both phenomena. While this model does not explain higher concentration effects nor does it deal with adsorption effects, it does provide a better understanding of the extrinsic semiconductor analyte gas interactions. One area of future research must involve understanding the desorption effect which should allow us to model the interactions more effectively [191]. Another promising method would be to apply more complicated techniques to manipulate the response data to allow clustering analysis. This would include the consideration of previous gas pulsing experiments. In concert, this should allow cheap effective gas monitoring [119, 213].

CHAPTER V

IN-SITU MODIFICATION OF METAL OXIDES

5.1 Direct Nitridation of Metal Oxide Nanostructures

The addition of nitrogen to a molecular structure, Nitridation, is used to create basic sites in organic molecules, such as the nucleotides of DNA [214], and inorganic compounds, like metal oxide particles. The Lewis acidity of the metal sites will change with the addition of the nitrogen. The nitridation of metal oxides can be done with a variety of methods [122, 215–217]. Exposing the metal oxide to NH_3 for several hours at temperatures exceeding 500 ^oC is one method [122]. This process has been applied to TiO_2 to produce the oxynitride, TiO_xN_y. a More recently, in searching for microscopic strongly basic catalysts, Dogan et al. [216] have created heavily nitrogen doped zeolites, treating these zeolites with NH_3 at temperatures in excess of 750 ^oC. This process replaces the oxygen in both the Si-O-Si and Si-O-Al framework. These experiments give precedence to the use of amines in the nitridation process, as the Lewis acidity of the substituted metal oxide framework increases, in part, due to the lower electronegativity of nitrogen with respect to oxygen, as seen using Density Functional Theory (DFT) [215, 217, 218]. The highly active nature of metal oxide nanoparticles allows for an alternative nitration technique. Porous anatase titanium dioxide nanocolloids in a size range 5-20 nm can be generated using sol-gel techniques [126,171,219]. These smaller particles can be nitridated directly within seconds using alkyl ammonium compounds at room temperature to yield the visible light absorbing titanium oxynitride,TiO_xN_y. This chemical reaction produces significant heat as it forms the anatase oxynitride nanocolloid. By contrast, purified micron sized anatase Degussa TiO_2 requires many hours to produce a weaker transformation to the oxynitride than does the nanocolloid. Similar unfruitful results with microscale particles and the direct amination treatment suggest the important role played by the TiO_2 nanocolloid porous form and its interaction. The photocatalytic efficiency of the oxynitride formed from the nanocolloid

also exceeds that of Degussa P25 [126, 171, 219, 220].

The nitridation process is important in order to harvest white light from the TiO_2 photocatalysts. In remote sensing where electrical power is costly, using white light (or minimal UV light) excitation to create a sensor response at room temperature is a valuable asset. Since white light represents the major component of the solar spectrum, a light absorption process that subsequently leads to directed electron transduction corresponds to "solar pumped" sensing. These light enhanced or even light operated sensors, could be reconfigured to sequester and destroy analytes in addition to sensing them.

The creation of highly stable and inexpensive pollutant mediating photocatalysts which have significant activity under visible light excitation utilizing the solar spectrum or interior room lighting can be promising due to the availability and cost of the light [122, 221]. These photocatalysts can also offer the potential for the significant improvement of sensor devices [67]. An extrinsic n-type semiconductor was treated with the strong acid, TiO_2, and its visible light absorbing and more basic counterpart, TiO_xN_y, to mediate electron transduction at the interface at room temperature.

A light accessible nanostructure decorated nanopore coated microporous array of n-type silicon was decorated with active metal oxide nano-photocatalysts [67,74] (Figure 5.1). This framework was used to study the effects of light enhancement on TiO_2 and the more basic TiO_xN_y. This study was done by measuring the change in the conduction of the doped PS with and without light along with an undecorated surface after exposure to analyte gases. The nanostructure deposition has to be maintained at a sufficiently low level so as to avoid cross-talk between the nanostructures which can lead to a noisy device and the loss of functionality. [67, 74]

As a refresher, Figure 5.2 presents a schematic diagram of the donor level population and the level structure as a function of temperature for an n-type extrinsic semiconductor where the basic anayltes can eventually saturate the donor electron level population [137]. Similarly, an acidic analyte depletes and can eventually "bottom out" the donor level population. Deposited nanostructures of TiO_2 and TiO_xN_y to the PS interface can influence, direct, and enhance this process. Optical excitation of the nanostructures can also influence,

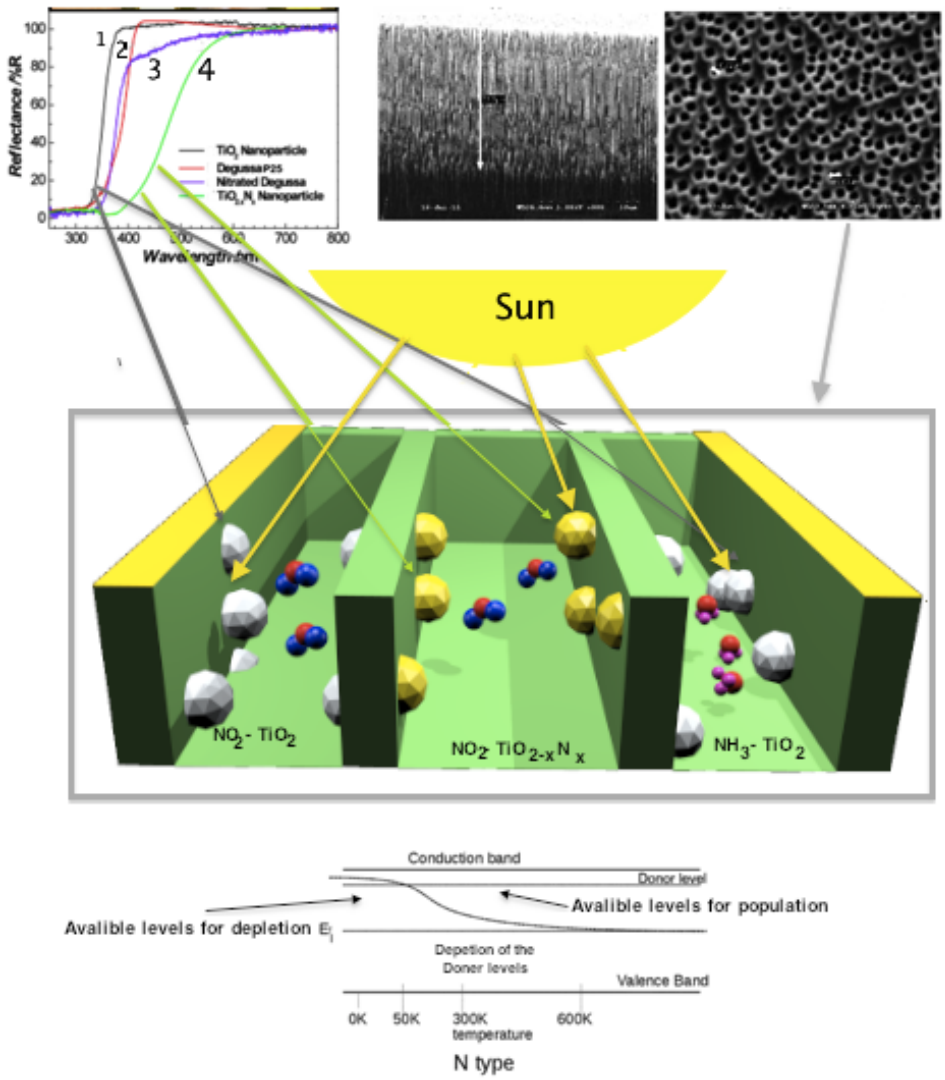

Figure 5.1: (Top left) UV-visible reflectance spectra of (1) TiO_2 nanocolloid particles; (2) Degussa P25 TiO_2 powder; (3) Degussa P25 TiO_2 powder nitridated with triethylamine; and (4) nitridated TiO_xN_y nanocolloid particles. (Top right) Pore structure of etched n-type PS, (Bottom) Schematic representation of portion of PS nanopore coated microstructure (large green structure) treated with active TiO_2 (grey sphere shape) and TiO_xN_y nanostructures (yellow spheres) acting to enhance solar pumped sensing.

direct, and enhance this process. The energy level and density of states structure for TiO_2 and its oxynitride have been discussed previously [122, 137] as have the onsets for optical pumping [124, 126, 171, 222, 223]. The energy levels shift notably on conversion to TiO_xN_y; however, the change in electronic level structure as a function of temperature range in these experiments varies by a very small energy increment [122] as kT is only of the order 208 cm^{-1} (0.025 eV) at 298 K and $k\Delta T$ is a small fraction of this energy increment.

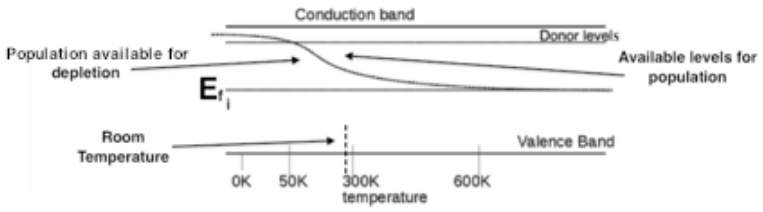

Figure 5.2: Schematic of n-type extrinsic semi-conductor level structure and populations

5.1.1 Results

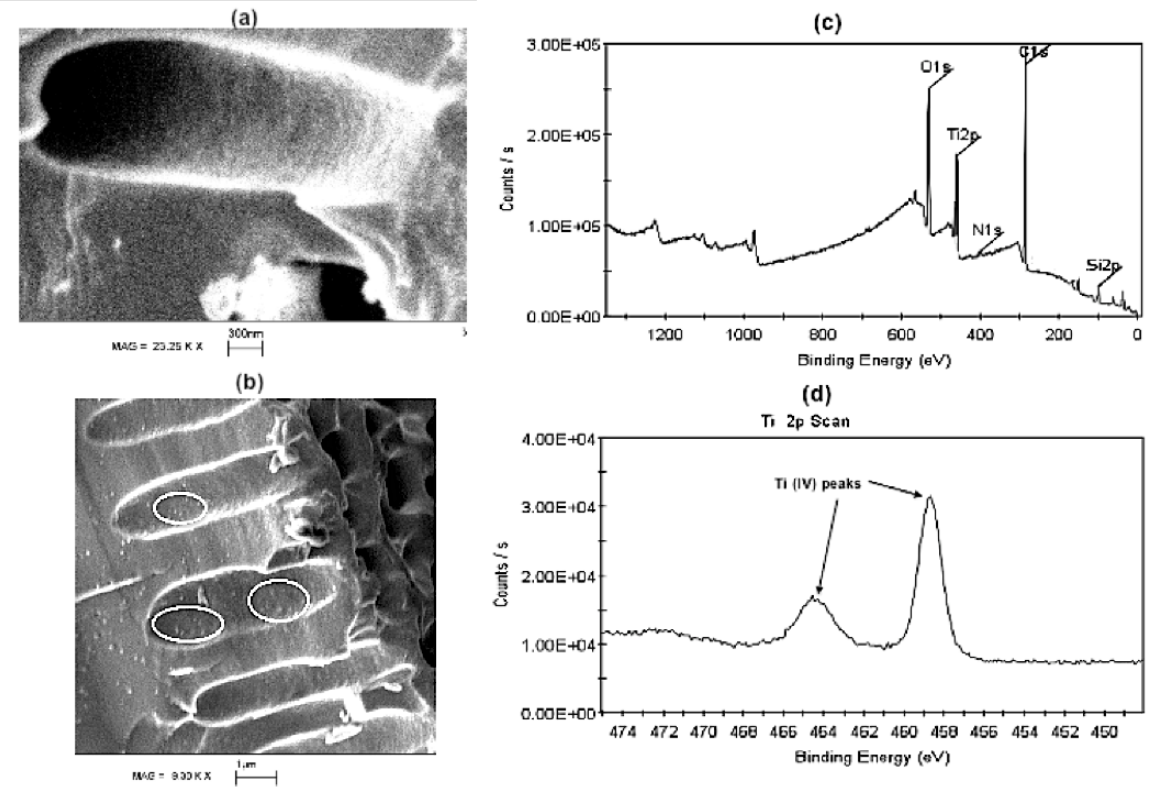

Figure 5.3: (a) SEM image of undecorated porous silicon pore structure. The pore is approximately one micron in diameter and 4 microns in length. (b) SEM image of porous silicon structure deposited with TiO_2. Some of the TiO_2 nanostructures (10-20 nm) are encircled in white. (c) XPS spectrum for the decorated porous structure showing the overall XPS spectrum including background peaks and (d) close-up of Ti 2p XPS region.

Figure 5.3 shows that TiO_2 had been deposited onto the surface of the PS. Figure 5.3 (a) and (b) correspond to SEM images, which compare the pore structure for the undecorated porous silicon surface and that for the TiO_2 decorated pores. The corresponding XPS spectra associated with the TiO_2 decorated pores are depicted in Figures 5.3 (c) and (d). Figure 5.3 (c) shows the whole XPS spectra where a strong Ti(IV) peak is clearly seen. Figure 5.3 (d) shows a close up of the Ti peaks.

Figures 5.4, 5.5, and 5.6 shows examples of NH_3 interacting with both an untreated and a nano-photocatalyst (TiO_2, TiO_xN_y) deposited *n*-type PS interface. The decreasing resistance of *n*-type silicon is due to the increase in charge carrying electrons donated from the Brønsted base NH_3. Figure 5.4 demonstrates that both white light and UV light have

no effect on the response of an "untreated" PS interface to NH_3. This PS response can be viewed as a backdrop for comparison to the data in Figures 5.5 and 5.6.

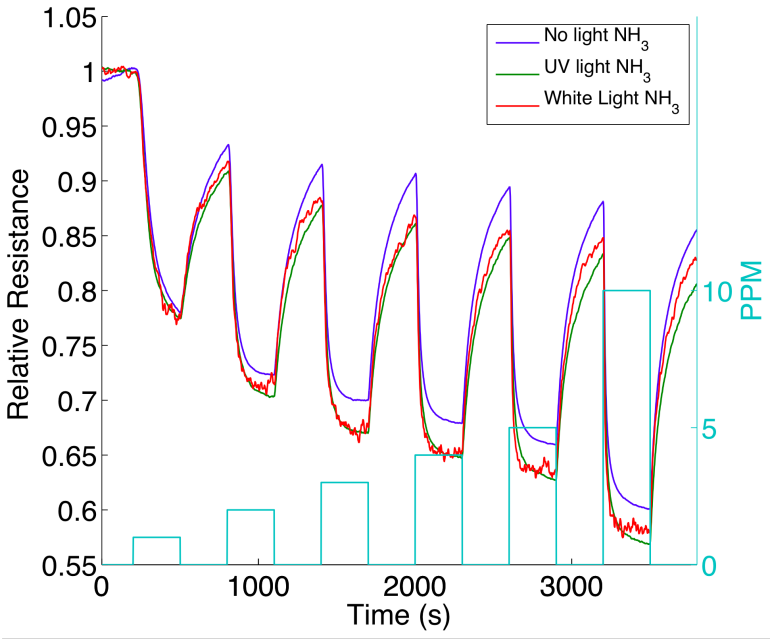

Figure 5.4: Comparison of responses for a PS interface exposed to white light (red), to UV light (green), and in the absence of light (blue). The magnitude of the response changes upon UV and white light exposure are identical to those in the absence of light. The cyan saw-tooth boxes indicate the analyte concentration and the range over which this concentration is exposed to the sensor interface.

Figure 5.5 shows the response to pulses of NH_3 for a surface before being treated with TiO_2 nanostructures, after being treated with the with TiO_2 nanostructures and after the in-situ conversion from TiO_2 to TiO_xN_y. [74, 126, 137, 171]. Here, the TiO_2 concentration may be somewhat less than that necessary to produce an optimal response [140]. TiO_2 is a strong (hard) acid that enhances the capture of electrons and increases the response relative to the undecorated interface. TiO_xN_y, has gained considerable basic character and does not capture electrons as efficiently as does the untreated PS interface since the nanoparticles are less acidic and thus have a better HOMO-LUMO orbital match with the NH_3. Therefore, the interface conductance response decreases. The observed trends are explained within the framework of the Inverse Hard/Soft Acid/Base concept [74, 137], which we have outlined earlier.

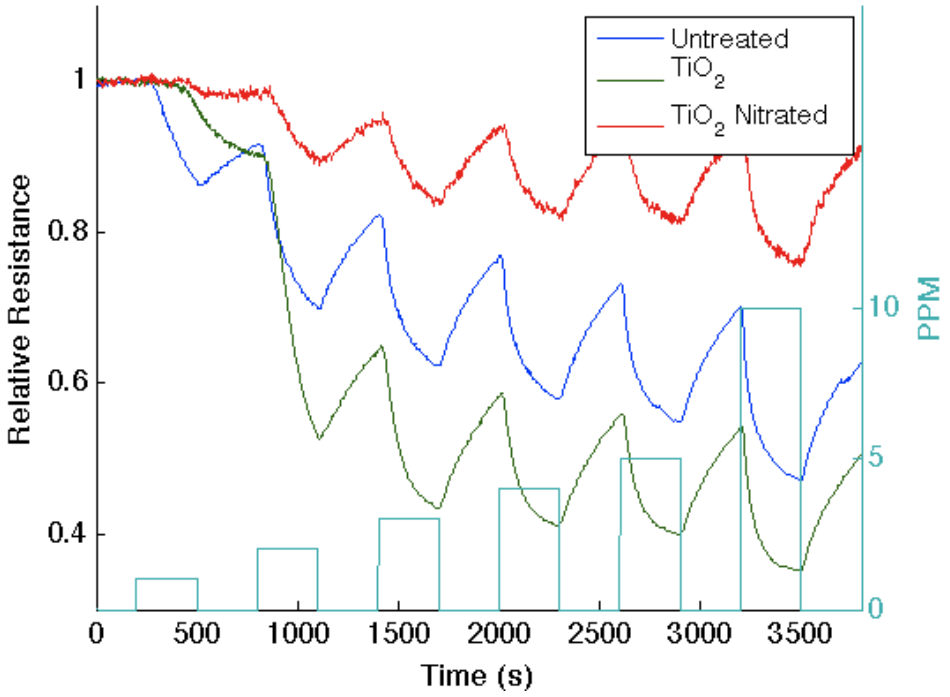

Figure 5.5: Response corresponding to decreasing resistance as NH_3 contributes electrons to an untreated porous silicon (PS), TiO_2, and a TiO_xN_y treated PS interfaces. The TiO_xN_y treated interface is basic relative to the PS and TiO_2 treated PS acidic sites. The boxes (aqua) denote the analyte concentration. Nitridation for 15 seconds results in a decrease in the interface response as monitored as a decrease in conductance.

Figure 5.6(a) indicates the response of a TiO_2 nanostructure treated PS interface before and during exposure to both "white light" and UV radiation. Visible radiation has a negligible effect on both the untreated and TiO_2 treated PS interface. When illuminated by 365 nm (3.4 eV) UV light, the signal from the TiO_2 decorated sensor interface, where the anatase TiO_2 has a bandgap of 3.2 eV, is improved by well over 100%. The photoexcited electrons increase the acidity of the TiO_2 nanoparticles. These more acid nanoparticles enhance the transfer of electrons from the analyte gas to the decorated PS interface leading to an increase in conductance. The exposure of a 25 W "white light" source to this TiO_2-PS interface does not photoexcite the electrons and does not enhance the transfer of electrons. The decrease in the signal for the white light exposure indicates the effect of a slight interface heating (carefully avoided in all additional experiments). The signal observed in the absence of surface heating is identical to that of the untreated PS interface. Optical pumping of the TiO_2 decorated interface and the enhancement of interface sensitivity occurs at energies

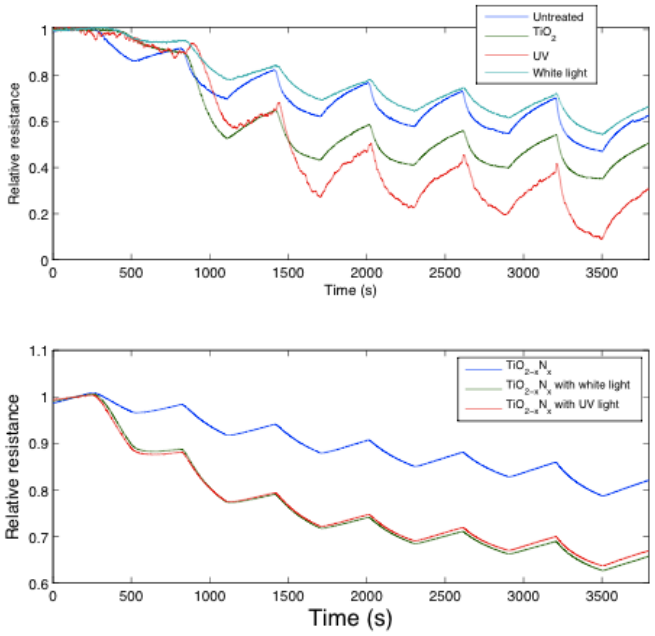

Figure 5.6: (a) Response to NH_3 of a TiO_2 treated PS interface without light exposure (green) and exposed to "white light" (cyan) and UV radiation (red). The untreated PS response is inserted for comparison. (b) Response of a TiO_xN_y treated PS interface with no light exposure (blue) and exposed to UV (red) and white light (green). Light exposure produces a moderately higher response at higher analyte concentrations.

exceeding the TiO_2 bandgap.

Figure 5.6(b) depicts the response of a TiO_xN_y treated interface to UV and white light. Here, the response of the sensor is seen to increase by 100+ % as a result of UV and "white light" excitation. The TiO_xN_y is excited by both light sources, enhancing the acidity of the structure, which in turn enhances the orbital mismatch with NH_3 and an increase in the signal. However, this increase occurs for a strong base, NH_3, whose contribution of electrons to the n-type semiconductor may be sufficient to "top out" the donor level population [74,137,140]. The optical pumping of the TiO_xN_y decorated PS interface is seen at energies well into the visible spectral region. The ability to electronically excite TiO_xN_y with visible radiation is consistent with its "effective bandgap" which is on the order of 2eV [122–124, 171, 220, 223].

As seen in Figure 5.2 the addition of electrons to an n-type system can contribute to the eventual saturation of the donor level population. The data in Figure 5.5 and 5.6(a)

demonstrate a saturating effect as the response to the increasing analyte gas begins to decrease between 3 and 4 ppm [137].

Figures 5.7 and **??** show the moderate Lewis acid, NO_2, interacting with and attempting to extract electrons from a TiO_2 and TiO_xN_y nanostructure decorated n-type interface. In these experiments, the relative strength of the electron withdrawing power of NO_2 versus that of the metal oxide and oxynitride decorated semiconductor interface must be considered. When the electron withdrawing power of NO_2 dominates, the analyte gas depletes electrons from the majority charge carrier concentration and increases the sensor resistance [137]. However with enough TiO_2, the strong acid nanostructures can reverse the electron flow. Therefore the electron exchange depends on the both the analyte gas and the decorated surface acidity [74, 137].

Figure 5.7 demonstrates the effect of TiO_2 fractional nanostructured depositions on the response of the PS interface to NO_2. The untreated PS interface (Figure 5.7(a)) displays a significant increase in resistance as NO_2 attracts electrons and depletes majority charge carriers. Figures 5.7(b) shows that low TiO_2 deposition times ($\leq$10s) do not deposit sufficient concentrations of nanostructured TiO_2 to facilitate its ability to compete with the removal of electrons by NO_2. The response to NO_2, as it extracts electrons, corresponds to a resistance increase. Figures 5.7 (c) displays the interaction between an intermediate TiO_2 fractional nanostructured deposition (20s) on n-type PS and the NO_2. The TiO_2 is now a strong enough acid to compete effectively with the moderately strong acid, NO_2, for the available electrons. At NO_2 analyte concentrations in excess of 2 ppm, as the response begins to rapidly increase with the introduction of NO_2, it is suddenly and rapidly quenched. This behavior is associated with the dynamics of electron transduction, and is more pronounced at higher analyte concentrations.

As NO_2 attempts to extract electrons from the decorated PS interface, the resistance rises rapidly to a point where the electron depletion reaches a limiting value. The nanostructured TiO_2 islands, coupled to the PS interface, now begin to compete with the NO_2 for the electrons preventing further electron withdrawal. Then the TiO_2 reverses the flow

of electrons causing an increase the donor and conduction level electron concentrations resulting in a sharp decrease in the resistance. The flip in electron flow increases in direct proportion to concentration [140]. More evidence for the dynamic nature of this interplay between the NO_2 and the TiO_2 is shown after the resistance drops to a minimum value but increases once the NO_2 is removed. As NO_2 is again introduced the same spike-like behavior in the resistance is again observed followed by a sharp drop in resistance. The process of interaction is a dynamic one as TiO_2 and NO_2 vie for the available electrons.

At higher fractional depositions (Fig. 5.7(d)-30 s deposition time) the TiO_2 coupled to the PS interface overcomes the electron withdrawing power of NO_2 at all concentrations and the response corresponds to a system that attracts electrons to the decorated PS interface, leading to a decrease in resistance.

To obtain the data in Figure 5.7(e) the TiO_2 nanostructure deposit of Figure 5.7(d) have been converted *in-situ* to the corresponding oxynitride, TiO_xN_y, diminishing the ability of the deposited nanostructures to attract electrons. At NO_2 concentrations $\leq$ 5ppm, the system again responds to the analyte by removing electrons from NO_2. This corresponds to a decrease in resistance although the decrease is notably less than that for the TiO_2 decorated system (Fig. 5.7(d)). However, an NO_2 concentration of 10 ppm is now sufficient to reverse this response, leading to a positive resistance change, which results from a dominant electron extraction by NO_2. It is against the dynamic changes outlined in Figure 5.5 that we consider the response upon exposure to visible and ultraviolet light.

Figure 5.8. Response corresponding to increasing resistance as NO_2 extracts electrons from a TiO_2 treated PS interface compared to the same interface exposed to UV and white light. The response corresponds to a decrease in resistance for the UV pumped interface

Figure 5.8 compares the response of a TiO_2 treated n-type PS interface not exposed to light against the same interface exposed to UV and "white light" excitation for NO_2 concentrations of 1-5 and 10 ppm. The TiO_2 is at a sufficiently low concentration, so the NO_2 dominates the TiO_2, depleting the majority charge carriers from the extrinsic semiconductor interface [74, 137] (Fig. 5.7(b)). The depletion saturates at a concentration of 10 ppm as the resistance increase does not double that at 5 ppm.

Figure 5.8 demonstrates that at the lower TiO_2 depositions, the introduction of "white light" somewhat diminishes the ability of TiO_2 to compete with NO_2 as indicated by a slight increase in resistance. By contrast, the exposure to UV light creates an interface, which competes so effectively for the available electrons that the resistance response decreases and subsequently reverses. So the treated interface extracts electrons from NO_2, causing the conductance increase (resistance decrease) with analyte concentration. The effect is quite pronounced at 10 ppm where there is a significant signal reversal relative to the dark TiO_2 treated interface. Optical pumping has created a strongly acidic electronically excited TiO_2^* modified interface which is much more efficient at attracting and transferring electrons to the PS interface.

Figure 5.9 depicts the response of a TiO_xN_y treated PS interface to NO_2. The conversion to TiO_xN_y lowers the acidity of the sites. This change weakens the sites so that they don't effectively compete with the acidic NO_2 for electrons. Further, the more basic TiO_xN_y fractional deposition contributes electrons more effectively than can TiO_2 [137, 224]. When the decorated sensor is exposed to a low level of "white light" its enhanced acidity, which also translates to visible light absorption, results in an enhanced electron transfer from TiO_xN_y to NO_2 due to the mismatch in the electronic bands. The response of the interface resistance increases to levels, which are well over 100% for 1-3 ppm of the analyte gas. However it begins to saturate at concentrations in excess of 3ppm. At 5ppm the measured signal is virtually identical with and without white light excitation, since the excited TiO_xN_y begins to counter electron extraction by NO_2. At even higher NO_2 concentration, the analyte gas induces a swift response from the oxynitride decorated interface. The "white light" excited excitation of the TiO_xN_y interface then no longer encourages the extraction of the electrons from the surface, instead it slowly extracts electrons from the NO_2 at the higher gas concentrations.

At a 10 ppm NO_2 exposure, the response of the TiO_xN_y interface at first increases with NO_2 electron extraction, however, the response begins to decrease with time as the ability of NO_2 to extract electrons is countered more rapidly by the far more acidic "white light" excited decorated surface. The observed dynamic behavior resembles the back transfer

process depicted in Figure 5.7(c). Once the NO_2 is introduced to the sensor interface, the electrons are extracted till the response reaches a resistance comparable to the 5 ppm maximum response. The resistance then decreases as a function of time, indicating the back transfer of electrons to the interface and an increase in conductance as the considerably more acidic $TiO_xN_y^*$ interface is now more efficiently extracting electrons. There is a corresponding spiked increase in resistance once the NO_2 concentration is rapidly removed. This a dynamic electron transduction process which is analogous to those observed in Figure 5.7(c) but now resulting from the interaction of a strongly acidic $TiO_xN_y^*$ excited state on the PS interface instead of the higher concentrations of TiO_2.

Figure 5.10 depicts the response to NO_2 where the TiO_xN_y is optimized at a considerably higher fractional deposition level analogous to that in Figs. 5.7(d) and 5.7(e). At concentration levels of 1-5 ppm NO_2, this leads to a dominance of the oxynitride. Electrons, extracted from NO_2 by the TiO_xN_y, increase the majority charge carrier concentration and decrease the resistance. In a reverse of the dynamic behavior observed in Figure 5.9, 10 ppm of NO_2 is sufficient to overcome the TiO_xN_y decorated interface acidic strength. This is seen by the increase in resistance where the NO_2 extracts the electrons decreasing the majority charge carriers. All of the "white light" responses now show a significant increase in the response (over 100%) versus the unexposed oxynitride treated surface, so the "white light" enhances the electron capturing power of the oxynitride. This enhancement leads to the increasing conduction response for the 10 ppm NO_2 exposure.

"White light" excitation greatly amplifies the sensitivity of the decorated interface as seen in Figures 5.9 and 5.10. The optical pumping of the TiO_xN_y decorated PS interface at energies well into the visible is clearly shown. This effect is expected from the light response curves indicated in Figure 5.1. Further, while more basic than TiO_2, the concentrated oxynitride still possesses a sufficient acidic character to overcome the electron withdrawing power of NO_2.

The response is clearly enhanced by "white light" excitation independent of the relative strengths of the NO_2 and the oxynitride-decorated interface. The response enhancement can both increase the resistance as in Figure 5.9 or by a conductance increase as in Figure

5.10. The effect of optical pumping clearly amplifies the signal obtained at both high and low depositions of nanostructures.

The results presented in Figures 5.8 and 5.9 must be considered with respect to the response of NO_2 to light as it interacts with the PS interface. Figure 5.11 demonstrates that the response to NO_2 decreases for both white light and UV excitation as NO_2 extracts electrons at a decreased rate. This decreasing response is counter to the increase in resistance observed in Figure 5.9. So the observed increase in resistance in the presence of TiO_xN_y represents a lower bound on the enchantment of the signal. The data in Figure 5.11 suggests the optical pumping decreases the electron extraction by NO_2. Despite the decrease in the signal, NO_2 in the presence of PS alone still extracts electrons. This fact is compared to the data in Figure 5.8 showing the decorated interface extracting electrons under UV excitation. So while the NO_2 is affected by the optical pumping, the dominating influence of the interface is the optically pumped conversion of TiO_2 and TiO_xN_y to their acidic excited states.

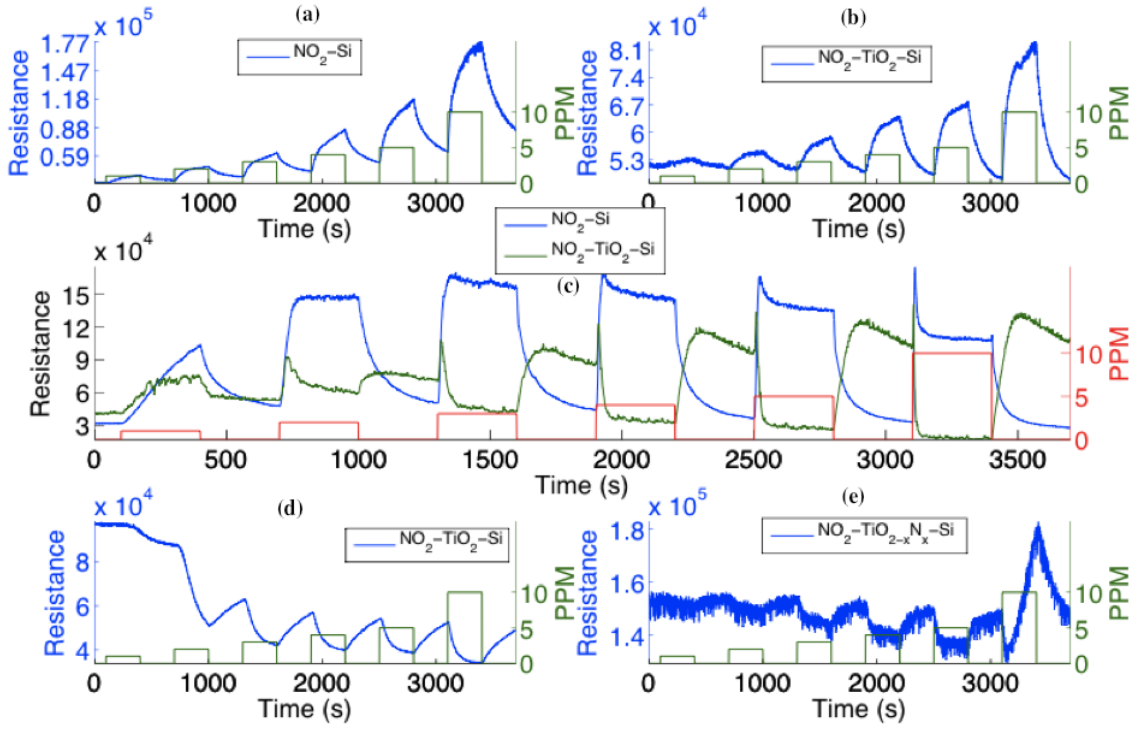

Figure 5.7: Comparison of responses to 1,2,3,4,5, and 10 ppm NO_2 for (a) a PS interface consisting of an untreated n-type surface with (b) a TiO_2 nanostructure deposited PS interface for low TiO_2 deposition, with (c) that which corresponds to the overlap of the response observed for the untreated PS interface (blue) to an interface modified with an intermediate concentration of TiO_2 (green), with (d) a TiO_2 nanostructure deposited PS interface for TiO_2 depositions notably higher than those associated with (b) and (c). Whereas the response curve for the untreated n-type interface corresponds to an increase in resistance with NO_2 concentration, the TiO_2 decorated surface displays a decrease in resistance (increase in conductance) as TiO_2 now facilitates electron extraction from NO_2. The signal begins to saturate between 3 and 4 ppm. (e) A TiO_xN_y treated PS interface obtained by treating the TiO_2 surface (d) which has now been made more basic. The green and red saw-tooth boxes indicate the analyte concentration and the range over which the concentration is exposed to the sensor interface.

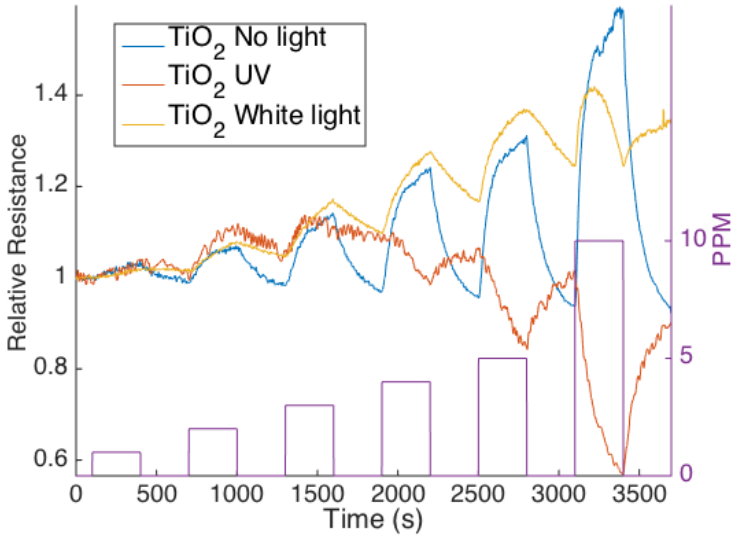

Figure 5.8: Response corresponding to increasing resistance as NO_2 extracts electrons from a TiO_2 treated PS interface compared to the same interface exposed to UV and white light. The response corresponds to a decrease in resistance for the UV pumped interface.

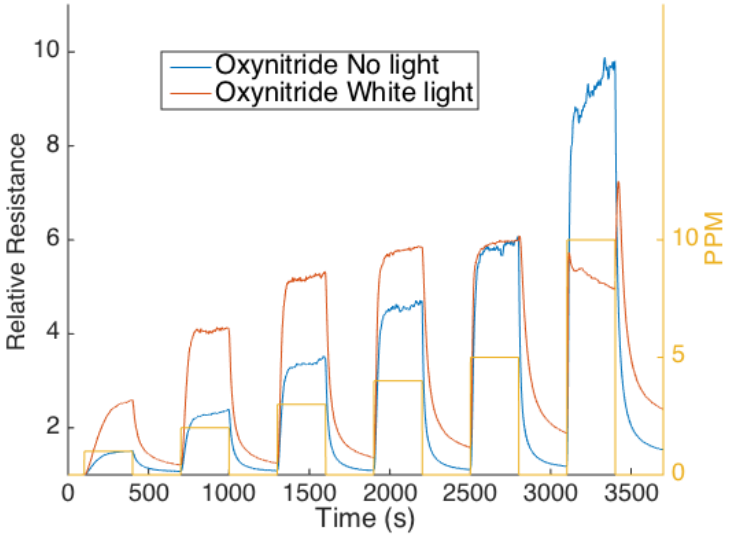

Figure 5.9: Response to NO_2 of a TiO_xN_y treated PS interface without light exposure and exposed to white light corresponds to a lower fractional deposition such that NO_2 dominates TiO_2. Looking at the response of TiO_xN_y decorated PS interface at an NO_2 concentration of 10ppm, The response at first begins to rise during the initial exposure to NO_2 and subsequently decreases rising again sharply as the NO_2 flow ceases.

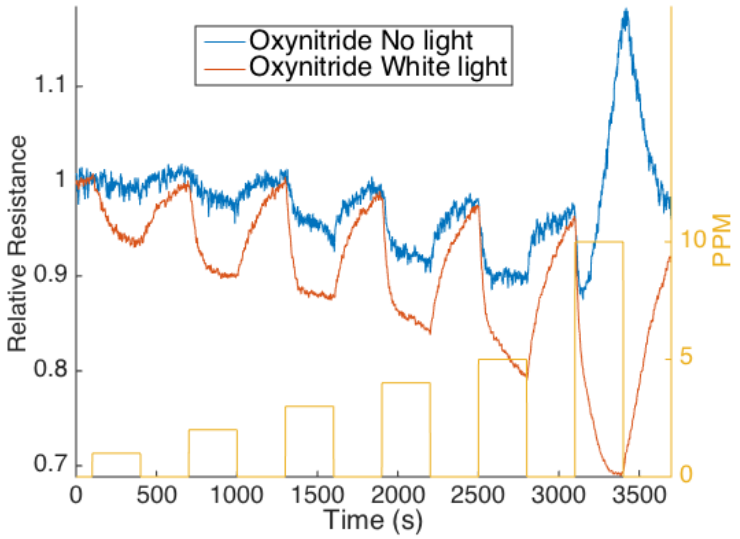

Figure 5.10: Responses to NO_2 of a TiO_xN_y treated PS interfaces without light exposure and exposed to white light. The white light exposure greatly enhances response.

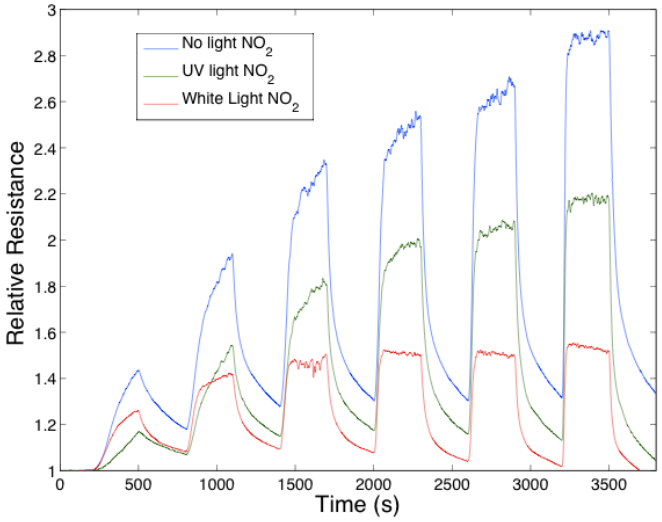

Figure 5.11: Response of untreated porous silicon sensor (a) to NO_2, (b) to NO_2 in the presence of ultraviolet light excitation, and (c) to NO_2 in the presence of white light excitation.

5.1.2 Discussion

The results indicate that light adsorption can influence the electron transduction dominated interaction of an analyte to the PS decorated interface. The semiconductor interface can be modified through treatment with nanostructured metal oxides, many of which are photocatalysts of varying degrees and levels of acidity. These oxides can also be converted to more basic oxynitrides. This nitridation provides a range of materials that can provide a variable enhancement of the response from a given extrinsic semiconductor interface and can be further enhanced through solar pumping.

The previous results significantly improve the nanostructure interactions with the environment by pumping the sensor with solar energy. This pumping will be useful for sensing applications where electrical or battery power is at a premium i.e. off the grid sensing. Here, solar radiation can be used to significantly enhance the sensor response. The average spectral brightness of the sun is its luminance divided by the bandwidth of the sun's visible output, which is 300 nm for the visible wavelength region, 400-700 nm. The average spectral brightness of the sun is L $_{\mu\lambda} \approx 1.5\text{x}10^5$ lumens/cm^2 -steradian/300 nm = 500 lumens/cm^2 -sterad-nm, the 300nm is the bandwidth of visable light. The white light used in these experiments comes from an incandescent light bulb positioned 10 cm from the sensor interface. The light source corresponds, at most, to a few lumen/cm^2 -sterad-nm. This light level can easily be obtained with solar radiation.

Care must be taken only that a fractional deposition of the TiO_2 and TiO_xN_y is placed on the sensor interface [9, 137, 140]. Carefully monitoring of the deposition process can avoid over depositing and/or the creation of a surface coating [9, 137]. Further care must be taken so that the source of the optical pumping, light or UV bulb, does not create a significant thermal excitation of the TiO_2, and TiO_xN_y nanostructure treated surface. Coating, as opposed to fractional deposition, and thermal excitation is found to greatly diminish sensitivity.

5.1.3 Summary

Just as the TiO_2 deposition greatly enhances the NH_3 response, a similar increase in response is seen when UV light impinges on the decorated sensor due to the increase in the acidic character of TiO_2. For the moderate acid NO_2, which extracts electrons from a PS interface, limited concentrations of TiO_2 enhance this extraction. However, the UV light can increase the acidity of the optically pumped TiO_2 treated interface causing the electrons to be extracted from the NO_2, decreasing or even completely reversing the direction of the sensors signal.

In-situ nitridation of the deposited TiO_2 forms the oxynitride, TiO_xN_y. This change lowers the acidity of the decorated surface and enhances its visible light response. One effect of this change is that the NO_2 dominates low depositions of TiO_xN_y and extracts electrons. When the white light excites theses lower depositions, the sensor response to NO_2 increases. However, when higher deposition of TiO_xN_y, are enhanced by white light, it causes the extraction of electrons from the NO_2 increasing the conductance of the sensors. Using average light intensities less than a few lumens/ cm^2-sterad, the responses can be enhanced up to 150% through interaction with visible (and UV) radiation. These light intensities should be compared to the sun's higher radiation level of $\tilde{5}00$ lumens/cm^2 – sterad-nm suggesting the possibility of solar pumped sensing.

5.2 Nitridation Concept and Reduced Acidity Associated with the Formation of Oxynitride Sites.

The combination of tailored active interfaces, the ability to confine processes at the nanoscale, and the ability to manipulate nanostructured materials and their interaction at these select interfaces, offers the opportunity to develop economically viable, energy efficient, and sensitive basic sites for direct sensing and the heterogeneous base catalytic transformation of chemical species. The site preparation and interaction process driven largely by nanostructure-focused Lewis acid-base chemistry can provide array-based rapidly responsive and sensitive platforms [74, 92, 137, 140, 141, 225]. Now, we extrapolate from the nitridation of the titanium oxide nanocolloids and focus on the in-situ transformation of the

metal oxides. Their Lewis acidity can be reduced by substitution of nitrogen for oxygen, generating the more basic oxynitride material [106, 126].

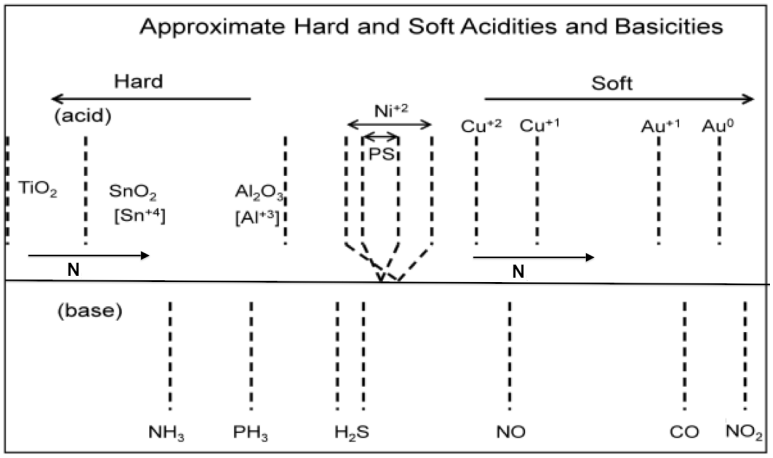

Figure 5.12: Estimated hard and soft acidities and basicities based on resistance changes relative to a *p*-type and *n*- type porous silicon interface. The acidic metal oxides that decorate the semiconductor interface can be modified through *in-situ* nitridation, decreasing their Lewis acidity. The analytes remain as positioned. A horizontal line is used to separate the metal oxides used to modify the interface (above) and the analytes below in the figure.

As previously mentioned the IHSAB concept allows us to predict the response to nanoparticle decorated interfaces and understand what happens to the interface. We have obtained initial evidence for the facile *in-situ* transformation of the metal oxides to their corresponding oxynitride at the nanoscale. While the transformation to a light pumped system was the focus previously we now look closer at the nitration effects on the metal oxides.

In Figure 5.12 the analyte scale is fixed in terms of acid/base properties as determined by the energy of the lone pair (lone electron) donating to the positive metal site as previously discussed. The analyte lone pair energies can be evaluated from their ionization potentials or proton affinities (gas phase basisity). Substituting nitrogen for oxygen donates electron density into the metal, which can vary the sensor acidity scale in Figure 5.12 but does not seem to change the oxidation state of the titanium. This lowers the Lewis acidity of the metal sites in the metal oxide. This transformation is easily accomplished at the nanoscale through direct amination in a manner analogous to that applied to the facile conversion of TiO_2 to TiO_xN_y. [126, 171] The *in-situ* formation of the oxynitrides shifts the transformed oxides toward the soft acid side of Figure 5.12, adding breadth to this materials selectivity

table and promoting a significant change in interface (sensor) response.

We will consider the measurement of the *in-situ* change in response resulting from nitridation, as predicted by the IHSAB concept and its correlation with an enhanced basic character, gauged alternately by the softening of acidity (lowering of Lewis acidity) for the metal sites located within the deposited metal oxides.

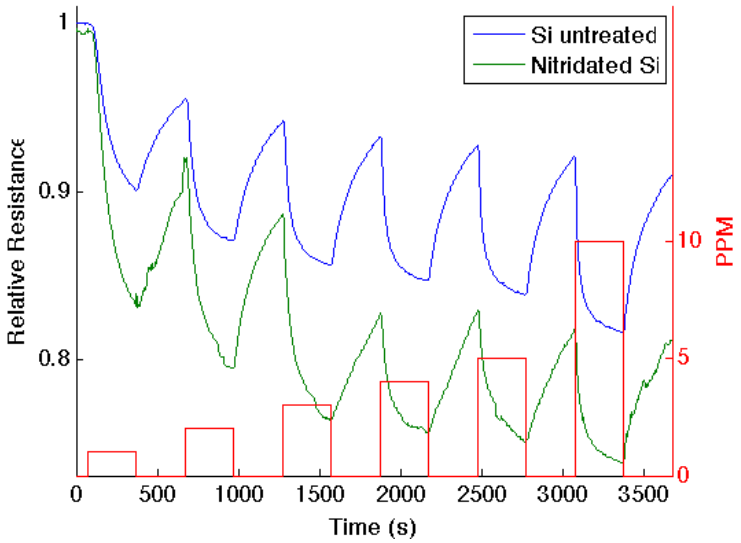

Figure 5.13: Response of an untreated PS interface to NH_3 (blue) and after nitridation of the interface for 15 seconds with triethylamine (green). The boxes (red) denote the analyte concentration. Nitridation produces an increase in the interface response as monitored as an increase in conductance (decrease in resistance).

This behavior will be examined by comparing the interactions of NO and NH_3 with a porous silicon and nitridated porous silicon interface and by studying the effect of nitridation on TiO_2, SnO_x, NiO, and Cu_xO nanostructure deposited PS interfaces [137].

Figures 5.13 and 5.14 compare the response for NH_3 and NO to untreated and nitridated *n*-type PS interfaces. Figure 5.13 corresponds to the responses observed when NH_3 contributes electrons to an untreated [137] and nitridated PS interface. For this figure the PS interface is treated for 15 seconds with triethylamine. The interaction of NH_3 contributes electrons and increases the conductance for both the nitridated and the untreated PS interfaces [137]. However, the increase in conductance is greater for the nitridated interface. While the nitridation process decreases the Lewis acidity of the PS surface corresponding to

a shift toward the soft acid side of Figure 5.12. The increase by nitridation thus is predicted by the IHSAB model. Figure 5.14 demonstrates that the nitridation process extended to one hour produces a similar, if not more pronounced, modification of the PS interface response. We observe a more rapid increase in conductance as well as signal decay as the gas flow is removed. While the untreated PS interface appears to display a $t^{1/2}$ dependence, the interface after nitridation appears to display a more exponential response indicative of a degree of pore expansion upon nitridation.

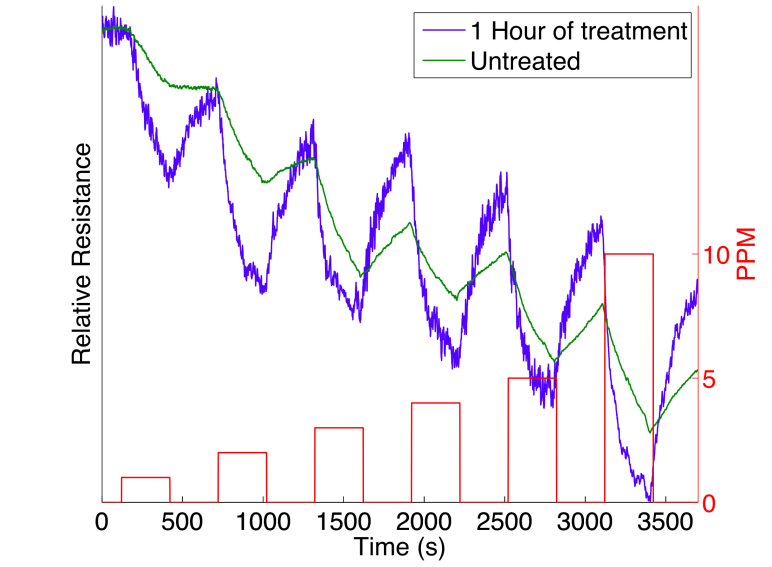

Figure 5.14: Response of an untreated PS interface to NH_3 (blue) and after nitridation of the interface for one hour with triethylamine (green). The boxes (red) denote the analyte concentration. Nitridation produces an increase in the interface response as monitored as an increase in conductance (decrease in resistance).

Figure 15 corresponds to the response observed when NO interacts with an n-type PS interface. Here, with the untreated PS interface, the amphoteric NO radical acts as a weak acid [137, 226], withdrawing electrons and increasing the resistance.

However, nitridation of the PS interface inhibits the extraction of electrons by NO and leads to a decrease in the resistance response. The nitridation of the PS interface decreases the HOMO-LUMO orbital mismatch. The data in Figures 5.14-5.15 provides a backdrop for the consideration of those changes, which accompany the nitridation of the metal oxide nanostructure deposited surfaces.

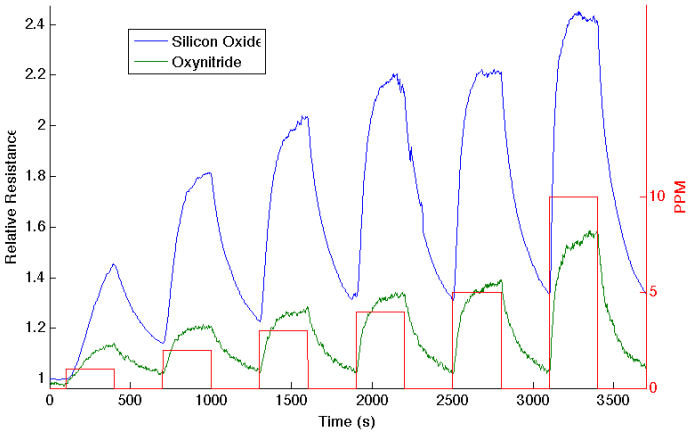

Figure 5.15: Response of an untreated PS interface to NO (blue) and after nitridation of the PS interface with trimethylamine for 15 seconds (green). The boxes (red) denote the analyte concentration. Nitridation results in a decrease in the interface response as monitored as a decrease in resistance.

Figures 5.5 and 5.16 compare the response for NH_3 and NO to a TiO_2 nanostucture deposited *n*-type PS interface, before and after nitridation. Figures 5.16 corresponds to the response observed when NO interacts with a TiO_2 treated *n*-type PS interface. Although, with the untreated interface, the amphoteric NO radical acts as a weak acid [137], withdrawing electrons and increasing the resistance (decreasing conductance), the strong acid TiO_2 completely overcomes this electron withdrawal as the TiO_2 decorated PS interface extracts electrons resulting in a significant increase in conductance(drop in resistance).

The TiO_2 concentration can be optimized further to produce a greater drop in resistance [124]. Nitridation of the TiO_2 decorated PS interface inhibits this electron extraction and leads to a considerable decrease in conductance.

Figures 5.17 and 5.18 compare the responses to NH_3 and NO for an SnO_x nanostucture deposited *n*-type PS interface, before and after nitridation. Nanostuctured SnO_x, especially as SnO_2, corresponds to a strong acid, however, its acid strength is notably less than that of TiO_2. The oxynitride, "SnO_{2-x} N_x", once formed, through *in-situ* treatment of the SnO_2 deposited interface shows a decreased Lewis acidity and thus gains considerable basic character.

Figure 5.17 corresponds to the responses observed when NH_3 contributes electrons to

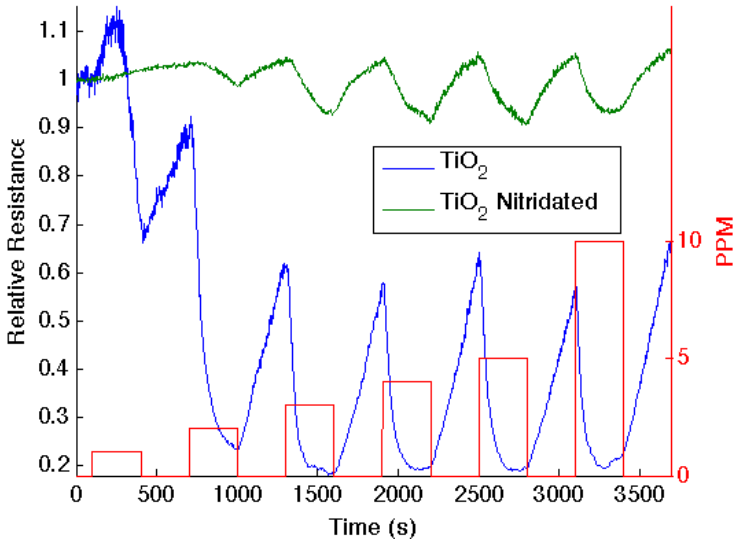

Figure 5.16: Response of a TiO_2 treated PS interface to NO(blue) and after nitridation for 15 seconds with triethylamine (green). The boxes (red) denote the analyte. The signal for TiO_2 on the same scale for the oxynitride actually bottoms out. Nitridation results in a decrease in the interface response as monitored as a decrease in resistance.

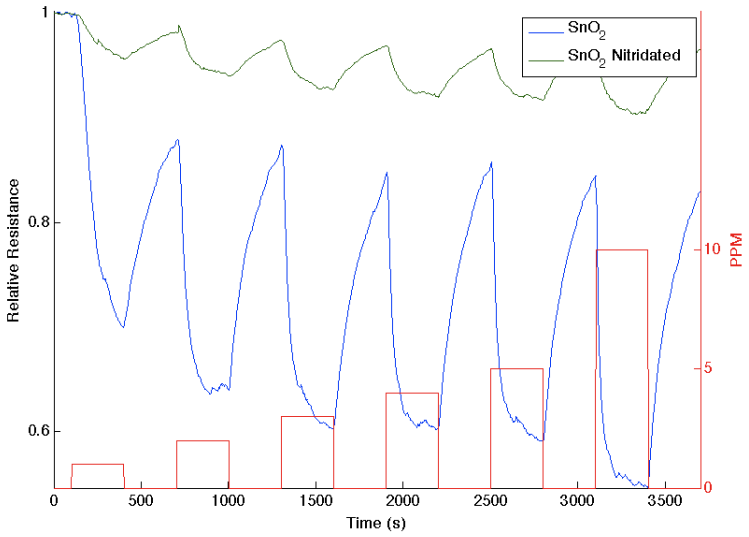

Figure 5.17: Response of a SnO_2 treated PS interface to NH_3 (blue) and after nitridation for 15 seconds with triethylamine (green). The boxes (red) denote the analyte concentration. Nitridation results in a decrease in the interface response as monitored as a decrease in conductance.

an interface treated with SnO_2, formed from electroless deposition [74, 137, 226] and subsequently nitridated. The data in Figure 5.17 compare the response of an untreated n-type PS interface, upon exposure to 1-5 and 10 ppm of NH_3 for the interface treated with a deposition

of acidic SnO_2 nanostructures, and this same interface where the deposited nanostructures are converted *in-situ* from SnO_2 to the more basic SnO_{2-x} N_x.

Figure 5.18 corresponds to the responses observed when NO interacts with an SnO_2 treated *n*-type PS interface [137]. Although, with the untreated interface, the amphoteric NO radical acts as a weak acid [137], withdrawing electrons and increasing resistance, the strong acid SNO_2 decorated interface again overcomes this electron withdrawal, although not to the extent of the TiO_2 decorated PS interface. Electrons are extracted from NO, resulting in a significant increase in conductance (drop in resistance). Nitridation of the SnO_2 decorated PS interface again inhibits the electron extraction as the nitridation lowers the Lewis acidity of the tin centers.

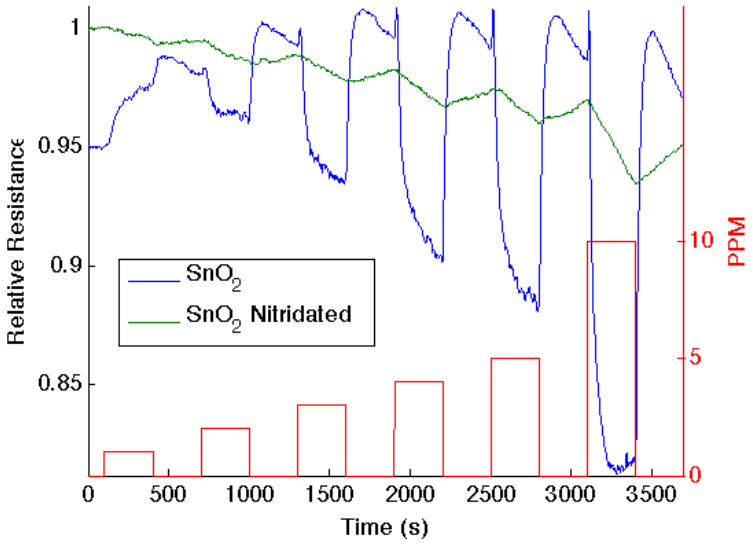

Figure 5.18: Response of a SnO_2 treated PS interface to NO(blue) and after nitridation for 15 seconds with triethylamine (red). The boxes (red) denote the analyte concentration. Nitridation results in a decrease in the interface response as monitored as a decrease in conductance.

Figures 5.19 and 5.20 compare the response for NH_3 and NO to a NiO nanostucture deposited *n*-type PS interface, before and after nitridation. The *in-situ* treatment of the NiO deposited interface creates an oxynitride "$NiO_{1-x}N_x$" that has a lower Lewis acidic character then the original nickel oxide sites, which were moderately acidic.

The data in Figure 5.19 compares the response to exposures of 1-5 and 10 ppm of NH_3

for the interface treated with a deposition of NiO nanostructures, and this same interface where the deposited nanostructures are converted *in-situ* from NiO to the more basic "$NiO_{1-x}N_x$". Here, after nitridation, the response to ammonia increases. This surprising response can be explained within the framework of the IHSAB principle.

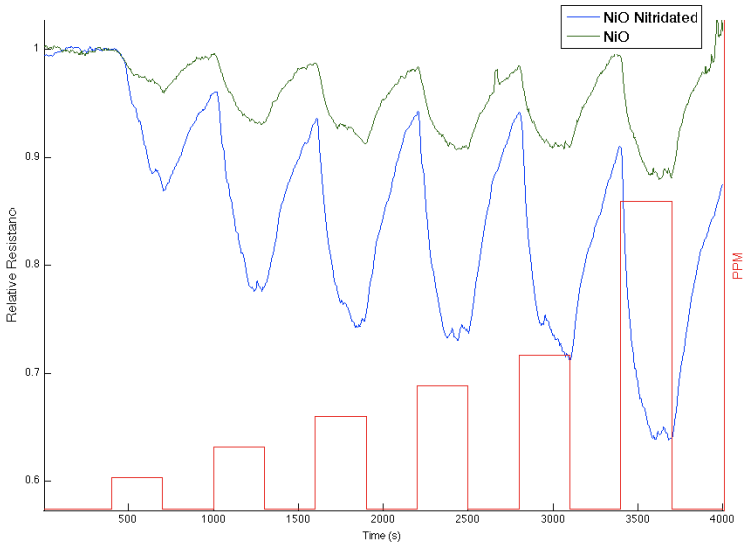

Figure 5.19: Response of an NiO treated PS interface to NH_3 (green) and after nitridation for 15 seconds with triethylamine (blue). The boxes (red) denote the analyte concentration. Nitridation produces an increase in the interface response as monitored as an increase in conductance (decrease in resistance.

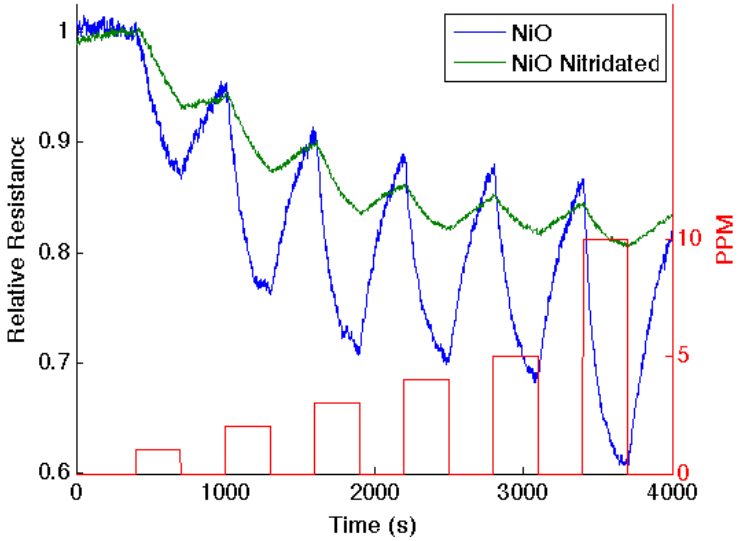

Figure 5.20: Response of an NiO treated PS interface to NO (blue) and after nitridation for 15 seconds with triethylamine (green). The boxes (red) denote the analyte concentration.

Figure 5.20 corresponds to the responses observed when NO interacts with an NiO treated *n*-type PS interface [137]. Although with the untreated interface, the amphoteric NO radical acts as a weak acid [137], withdrawing electrons and increasing the resistance (decreasing conductance), NiO and NO compete for the available electrons in this system, especially at higher NO concentrations [137]. The process is dynamic and, under the conditions of the present experiment NiO dominates. Nitridation of the NiO decorated PS interface again inhibits electron extraction by the decorated interface and leads to a considerable decrease in conductance.

The observed processes associated with nitridation in Figures 5.19 and 5.20 taken together are consistent with a greater HOMO (donor) –LUMO (accepter) molecular orbital mismatch for NH_3 and NiO and a decrease in the HOMO-LUMO molecular orbital energy mismatch for NO and NiO dictated by the IHSAB principle.

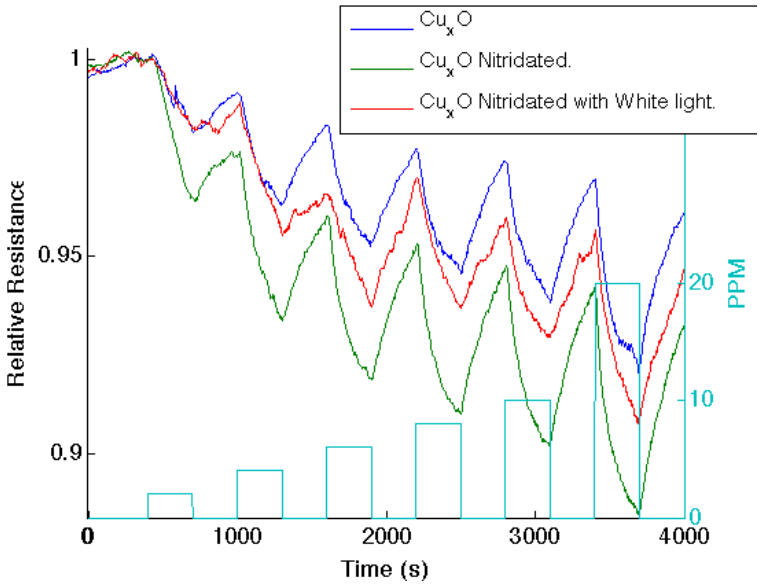

Figure 5.21: Response of a Cu_xO treated PS interface to NH_3 (blue), after nitridation with triethylamine (green), and after white light excitation of the nitridated sample (red). The boxes (aqua) denote the analyte concentration. Nitridation produces an increase in the interface response as monitored as an increase in conductance (decrease in resistance).

Figures 5.21 and 5.22 compare the response to NH_3 and NO of a Cu_xO nanostucture deposited *n*-type PS interface, before and after nitridation. Nanostuctured Cu_xO corresponds to a moderate to weak acid. The *in-situ* treatment of the Cu_xO deposited interface

gains considerable basic character by the formation of the oxynitride, "$Cu_xO_{1-y}N_y$ ". The data in Figure 21 compare the response upon exposure to 1-5 and 10 ppm of NH_3 for a PS interface treated with a deposition of Cu_xO nanostructures, and this same interface where the deposited nanostructures are converted *in-situ* from Cu_xO to the more basic "$Cu_xO_{1-y}N_y$". Here, after nitridation, the response to ammonia increases. This surprising response can be explained within the framework of the IHSAB principle.

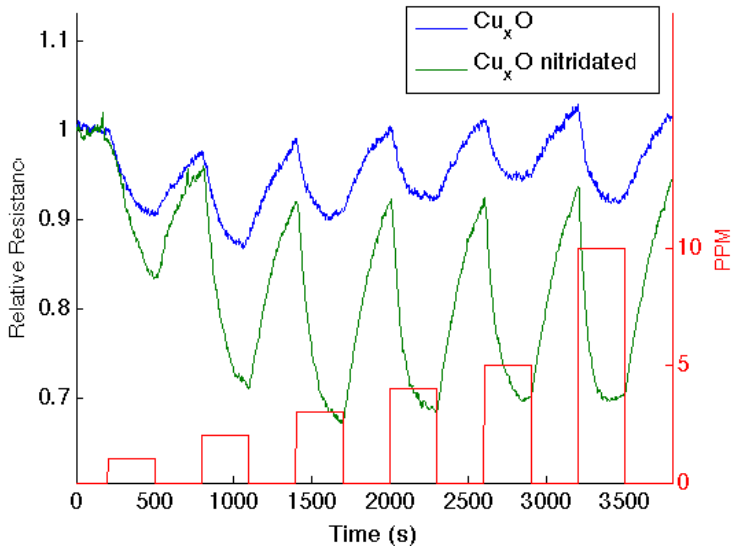

Figure 5.22: Response of a Cu_xO treated PS interface to NO (blue) and after nitridation with triethylamine (green). The boxes (red) denote the analyte concentration. Nitridation produces an increase in the interface response as monitored as an increase in conductance (decrease in resistance).

Figure 5.22 corresponds to the responses observed when NO interacts with a Cu_xO treated *n*-type PS interface [137]. The amphoteric NO radical and the metal oxide (this time Cu_xO) again compete for the available electrons in this system [137] and, under the conditions of the present experiment Cu_xO dominates. Nitridation of the Cu_xO decorated PS interface increases the electron extraction and leads to a considerable increase in conductance. This is again consistent not with a simple increase in the basic character of the interface but is consistent with the IHSAB principle.

5.2.1 Response Matrices and Their Modification on Nitridation

The data in Tables 5.1 and 5.2 summarize the changes in response of the sensors to the analyte gases as seen above for the metals oxides and oxynitrides. The equation for calculating the response is

$$\Delta = \frac{\Delta R(deposited)/R_0(deposited)}{\Delta R(untreated)/R_0(untreated)}] \tag{5.1}$$

Where Δ is the change in the response. $\Delta R(deposited)$ and $\Delta R(untreated)$ are the change in the resistance away from the baseline for the metal oxide deposited and untreated sensor respectively. $R_0(deposited)$ and $R_0(untreated)$ are the baselines for the deposited and untreated sensor respectively.

The importance of this data is that it indicates that the nitridation process creates additional distinct response matrix elements that can be used to test for a given analyte. Further, these response matrix elements are determined by the acid/base strength of the analyte relative to that of the nanostructure deposited interface. The dependence is not a simple one but is dictated by the manner in which the nitridation process modifies the molecular orbital makeup of the metal oxides as the nitration process adjusts the HOMO (donor) – LUMO (acceptor) separation. Since this can enhance or diminish the molecular orbital matchup of the analytes and decorating nanostructures, all the changes in responses can be predicted by the IHSAB principle.

Table 5.1: Changes in the relative conductometric responses of nitridated metal oxides vs. nanostructured metal oxides decorated sensors to NO and NH_3.

	NO	NH_3
TiO_2	1/40	1/9
SnO_x	1/3.5	1/7
NiO	1/2	3
CuO_x	2	1.5

Table 5.2: Changes in the relative conductometric responses of nitridated metal oxides vs. untreated porous silicon (PS) sensors for NO and NH_3.

	NO	NH_3
PS nitrated 15 seconds	1/2	2
PS hour nitration	N/A	2.2
TiO_2	-1/4	
SnO_x	-1/2	1/3
NiO	2	4.5
CuO_x	2.4	4

5.2.2 X-Ray Photoelectron Spectroscopy (XPS)

XPS profiles for TiO_2, SnO_x, NiO, Cu_xO and their corresponding nitridated counterparts are show in Figures 5.23-5.30. Here, we monitor the electron binding energy of sites a few nanometers from the decorated interface surfaces. We have examined seven areas of the XPS spectrum, the C 1s, Ti 2p, Sn 3d, Ni 2p, and Cu 2p, regions, the N 1s region near 400 eV, and the O 1s region near 530 eV.

Looking at the metal spectra for the different coated PS interfaces shows evidence of a change in the chemical binding for the metals. Figure 5.23 shows the specta of the TI 2p region with and without nitridation. There is a slight shift of the Ti binding energy from 458.8 eV, decreasing to 458.6 eV upon nitrogen incorporation, a shift of approximately 0.2 eV to lower binding energy. The Sn 3d binding energy associated with SnO_x (Figure 5.24) has a slightly bigger shift after nitration then the Ti, shifting by 0.3 eV to lower binding energy. The Ni 2p binding energy associated with NiO (Figure 5.25) is at $\tilde{8}53.7$ eV and shows a slight red shift of approximately 0.2 eV upon nitridation.

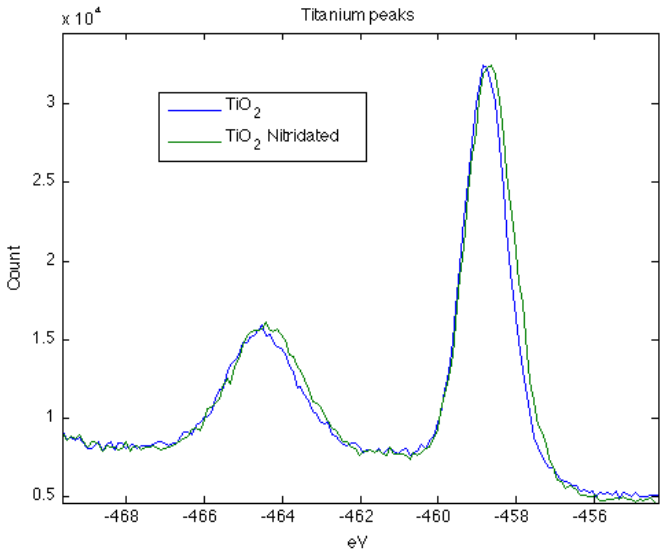

Figure 5.23: Ti 2p XPS spectrum showing a lower binding energy for the nitridated form of TiO_2.

In contrast to the XPS spectra for TiO_2, SnO_x, and NiO, the Cu 2p peaks for the nitridated Cu_xO sample show not only a weakening and broadening of the XPS features

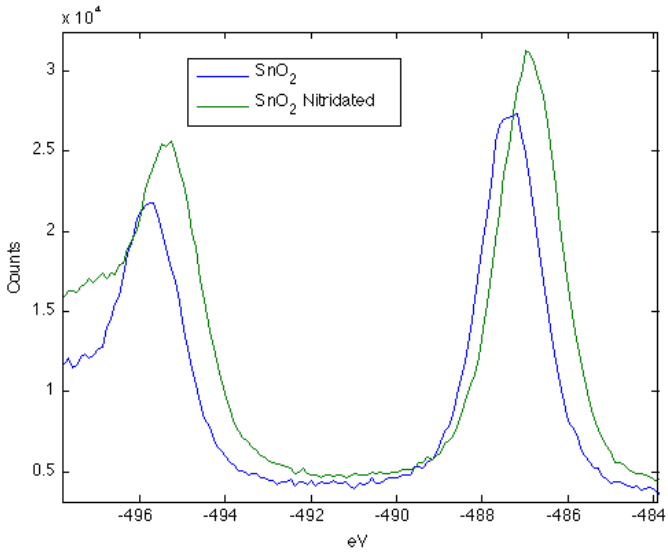

Figure 5.24: Sn 3d XPS spectrum showing a lower binding energy for the nitridated form of SnO_2

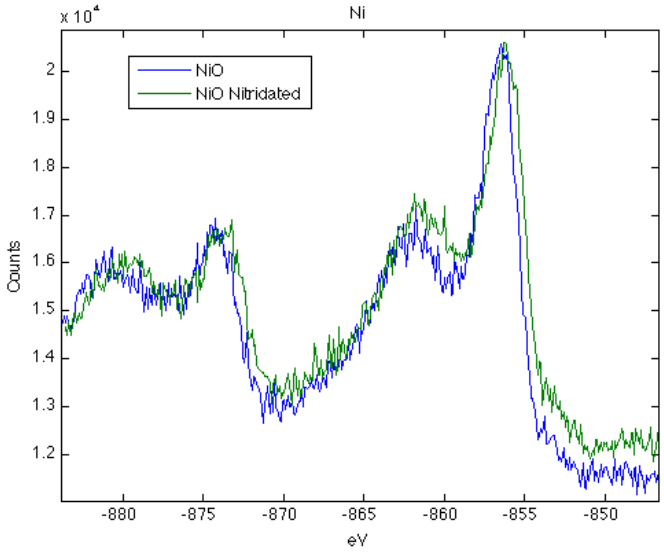

Figure 5.25: Ni 2p XPS spectrum showing a lower binding energy for the nitridated form of NiO.

but also a shift to *higher* binding energy (Figure 5.26).

The N 1s XPS binding energies observed for the N-doped oxides (Figure 5.27) are broad and extend from $\tilde{3}98$ to 403 eV with the exception of SnO_2 which extends to 401 eV. In all cases, this range exceeds the binding energy of 397.2 eV in TiN [8, 227]. The shift in the N 1s features to higher binding energy results when the nitrogen is more positive. It

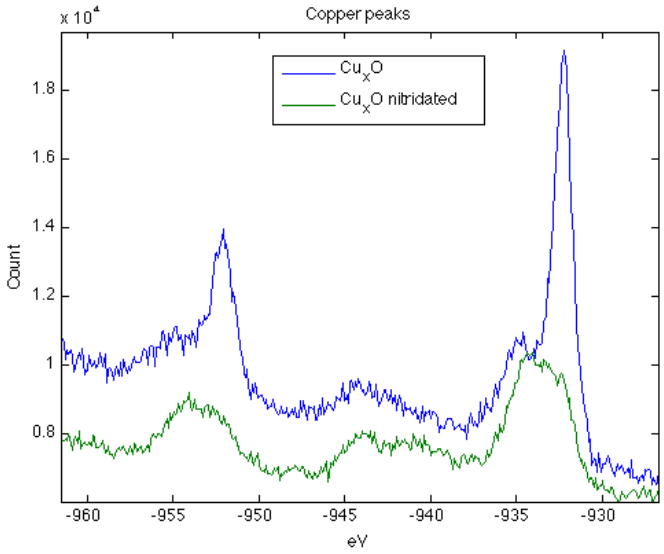

Figure 5.26: Cu 2p XPS spectrum showing a higher binding energy for the nitridated form of Cu_xO.

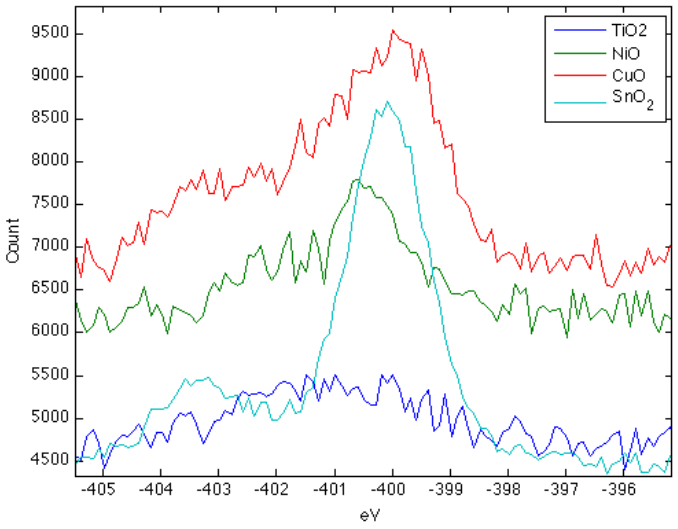

Figure 5.27: Nitrogen 1s XPS spectra associated with the nitridation ofTiO_2, SnO_x, NiO, and Cu_xO depositions.

is 408 eV. in $NaNO_3$ compared to 398.8 eV [190, 228] in NH_3 where the nitrogen has a formal negative charge. Rodriguez, et. al, [8, 229] have carried out an XPS analysis of the interaction of NO_2 with several polycrystalline surfaces, observing a strong peak at 404.5 eV, intermediate to that for absorbed NO (400-401.5 eV [109, 229, 230]) and NO_3, [12, 231] which they tentatively assign to NO_2. They also observe weak features at 396.5 eV and 401

eV, which they assign to N and NO in a metal lattice. The observed features, which we observe are consistent with the N 1s features for NO. They increase in intensity from the TiO_2 treated to the Cu_xO treated interface.

The observed XPS peaks for the Ti 2p region and their change with nitrogen incorporation are quite consistent with an XPS characterization carried out by Gyorgy et.al. [232] These authors have also observed a shift in the Ti 2p binding energy to lower energies as the TiO_2 surface is nitrided, as seen in Figure 5.23. Further, the XPS spectra in Figure 5.23 and 5.27 are consistent with the data obtained by Chen et al. [171] on TiO_xN_y and the earlier results of Saha and Tomkins [227] who have used XPS to characterize the oxidation of a titanium nitride surface.

The observed binding energies for the O 1s XPS spectra are given in Figures 5.28, 5.29, and 5.30. They show significant changes upon nitridation of the metal oxide. The data for TiO_2 are quite interesting verses the typical data that we have observed previously for TiO_2 and its nitridated counterpart TiO_{2-x} N_x. [171][8] The double peak in Figure 28 is, in fact, due to both to SiO_2 (high energy peak at 532.3 eV) and TiO_2 (low energy peak at 530.2 eV) as the signals for these oxides overlap eachother. The data indicate that the nitridated form of both TiO_2 and SiO_2 show a slight increase in binding energy to 532.4 and 530.3 eV respectively.

The SnO_x decorated systems depicted in Figure 29 indicate a significant decrease in binding energy from 532.8 eV to 531.9 eV with nitridation. The NiO decorated interface shows a significant decrease of $\tilde{1}$.8 eV in the O 1s binding energy (Fig. 30) on nitridation and the decrease in binding energy for the Cu_xO decorated interface is even greater ($\tilde{2}$.8 eV). These are important trends and distinctions.

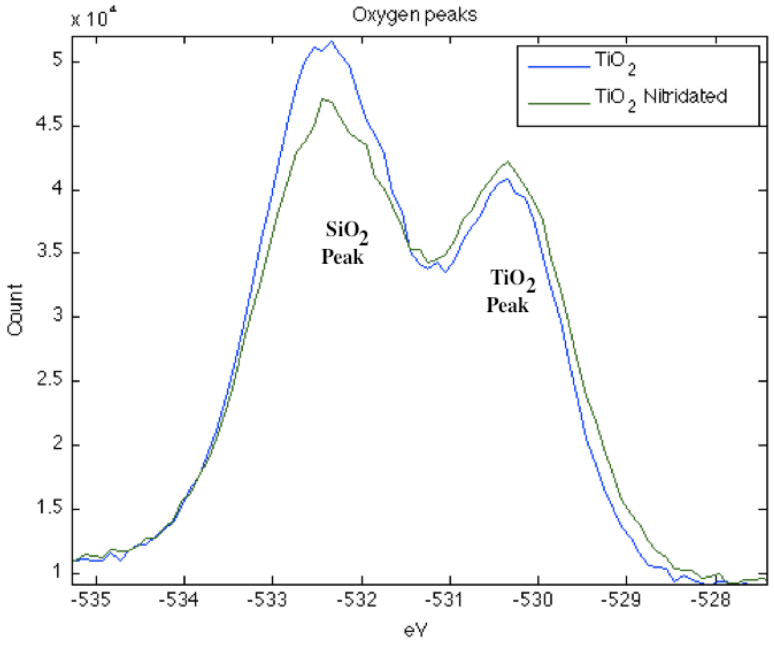

Figure 5.28: Oxygen 1s XPS spectra associated with the nitridation of TiO_2 depositions. Both TiO_2 and SiO_2 peaks are observed and suggest a shift to higher binding energy on nitridation.

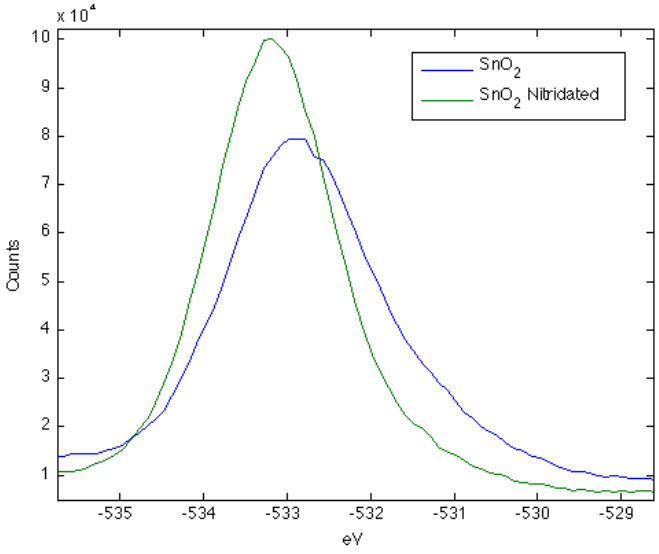

Figure 5.29: Oxygen 1s XPS spectra associated with the nitridation of SnO_2 depositions. The spectra show a notable red shift on nitridation.

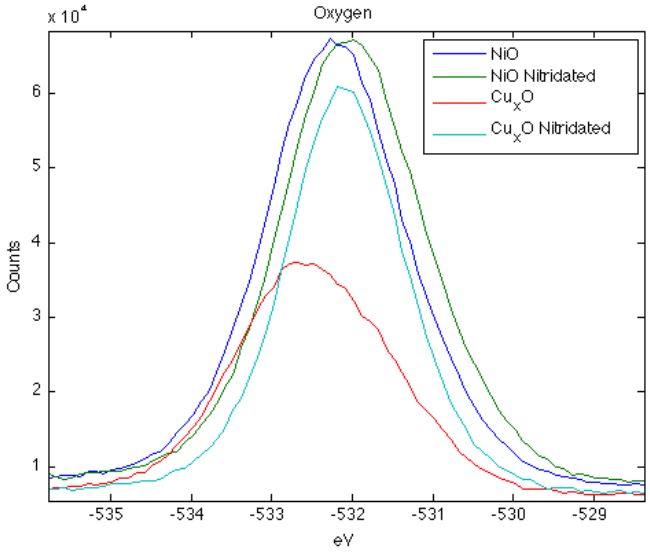

Figure 5.30: Oxygen 1s XPS spectra associated with the nitridation of NiO, and Cu_xO depositions. The data show an increasing and notable shift on nitridation.

5.3 Functionalization with Sulphur Compounds

Now we look at the sulphidation of the nanostructured metal oxides. The sulfidation of the nanostructured metal oxides is facile and represents a means to create sulfur functionalized extrinsic semiconductor interfaces. One possible use for these sulfur functionalized interfaces is in the capture and functionalization of biomolecules [59, 137, 233, 234]. Another possible use for an SR_2 or RSH functionality is to create a viable platform for Li battery operation [235,236]. Here, we employ the organic sulphides for the *in-situ* transformation of the metal oxides to their more basic sulphur treated moieties and the corresponding modification with the thiols to form Brønsted acid sites, in a similar manner to the nitridation.

5.3.1 Results of Sulfidation

The sulfidation of the metal oxides [129] can be used to modify the nanostructure island site Lewis acidity through *in-situ* transformation, interacting with sulfur functionalities(S-$(CH_x)_y$) and their Brønsted acid counterparts(SH-$(CH_x)_y$). Sulfidation with diethyl sulphide are used to introduce a progressively decreasing metal site Lewis acidity ($\tilde{}$increasing basicity) shifting them to the right on Figure 5.31. However, similar *in-situ* treatments with ethane- or butanethiol introduce a progressively increasing acid character ascribed to Brønsted acid SH sites shifting the metal oxysulfides to the left in figure 5.31. The transformation is accomplished in a manner somewhat analogous to that applied to the facile conversion to the oxynitrides following initial studies on the transformation of nanostructured TiO_2 to TiO_{2-x} N_x discused earlier [126, 171].

Figure 32 corresponds to the responses observed when NH_3 contributes electrons to an untreated [137] and ethanethiol treated PS interface. As NH_3 contributes electrons to the treated interface, the conductance of the system increases (resistance decreases).

Figure 5.33 displays the responses observed when NH_3 interacts with an ethanthiol treated TiO_2 deposited PS interface. The interaction increases the conductance for both the etanethiol treated and TiO_2 deposited PS interfaces [137]. Once optimized, the ethanethiol treated surface displays a significant increase in conductance relative to the surface deposited only with titanium dioxide. We will suggest that this results from an increase in the

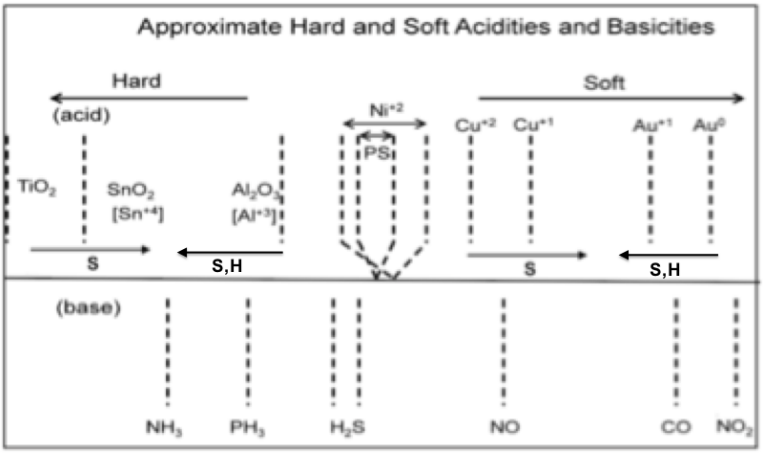

Figure 5.31: Estimated hard and soft acidities and basicities based on resistance change relative to a p- and n-type porous silicon interface. The acidic metal oxides that decorate the semiconductor interface can be modified through *in-situ* sulfidation, decreasing their Lewis acidity. The analytes remain as positioned. A horizontal line is used to separate the metal oxides used to modify the interface (above) and the analytes (below) in the figure.

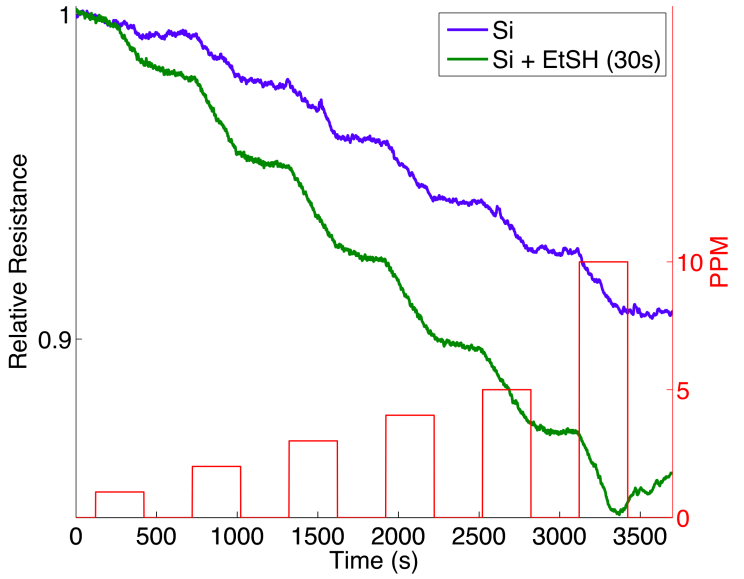

Figure 5.32: Response of ethanethiol treated porous silicon (PS) interface to NH_3 (a) untreated interface exposure and (b) after exposure for 30 seconds (thiol treated interface is acidic after a 30 second exposure). The boxes (red) denote the analyte concentration.

Brønsted acidity of the metal oxide treated interface.

Figure 5.34 displays the observed responses when NH_3 when interacts with an ethanthiol treated tin oxide deposited PS interface. The optimal treatment of ethanethiol on the

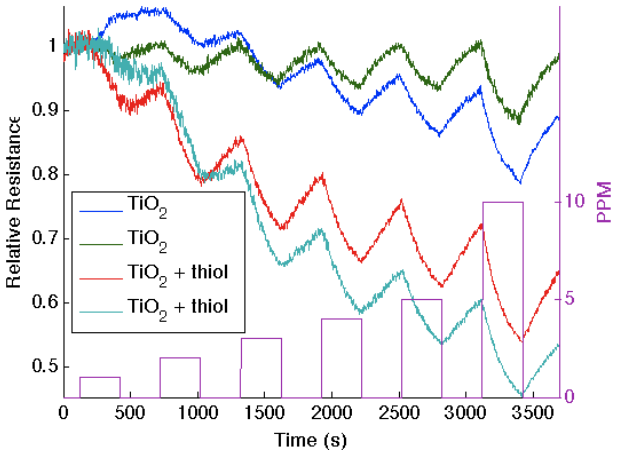

Figure 5.33: Response of ethanethiol treated titanium dioxide nanostructure deposited porous silicon (PS) interface to NH_3 after exposure to thiol for 30 seconds. The sulphidated TiO_2 treated interface is acidic relative to the PS and TiO_2 treated PS acidic sites after a 30 second exposure. The boxes (purple) denote the analyte concentration.

surface displays a significant increase in conductance relative to the surface deposited only with tin oxide. However, Figure 5.34 also demonstrates that at lower thiol exposures, the response of the metal oxide deposited PS interface is quenched. Thus, the precise level of thiol exposure displays an onset for enhancing the acidity of the metal oxide surface that must be carefully assessed.

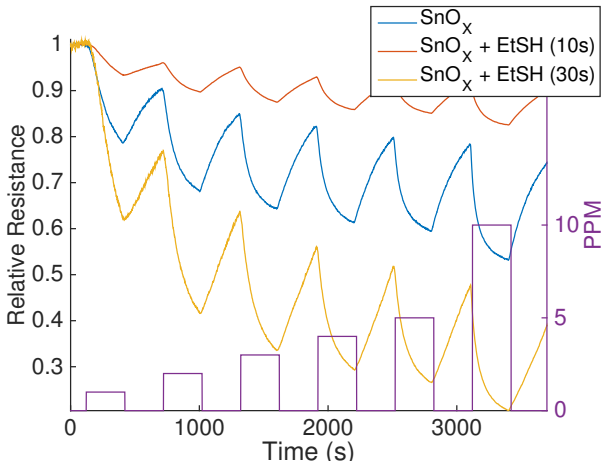

Figure 5.34: Response of ethanethiol treated tin oxide nanostructure deposited porous silicon (PS) interface to NH_3 (a) initial exposure for 10 seconds and (b) after exposure for 30 seconds. The sulphidated SnO_x treated interface is acidic relative to the PS and SnO_x treated PS acidic sites after a 30 second exposure. The boxes (aqua) denote the analyte concentration.

Figure 5.35 illustrates the responses of an ethanthiol treated nickel oxide deposited PS interface with NH_3. With a 30 s exposure to the thiol, the sulfidation increases the conductance change relative to the Ni_xO deposited interface [137]. A similar behavior is observed (Figure 36) for both the ethanthiol and butanethiol treated systems.

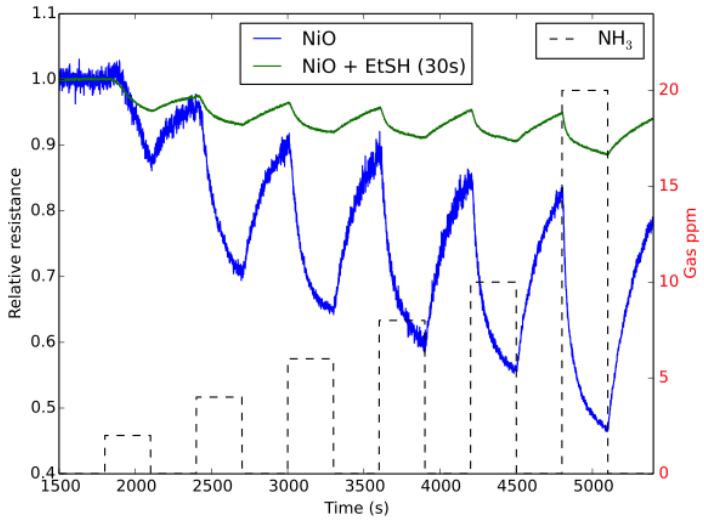

Figure 5.35: Response of ethanethiol treated nickel oxide nanostructure deposited porous silicon (PS) interface to NH_3 (a) exposure for 30 seconds and (b) exposure only to nickel oxide. The sulphidated Ni_xO treated interface is more acidic than the Ni_xO treated PS acidic sites after a 30 second exposure. The boxes (black dashed) denote the analyte concentration.

With each of the treated metal oxide systems, for both the butane- and ethanethiol treated interfaces, the precise level of thiol exposure must be carefully assessed and optimized. With a 30 s exposure the conductance of the thiol treated Ni_xO interface increases substantially. This is likely due to an increase in Brønsted acidity.

Figure 5.38 shows the response of a diethyl sulfide treated titanium oxide deposited PS interface interacting with NH_3. The sulfidation process decreases the ability of the interface to extract electrons from NH_3 and the conductance change for the diethyl sulfide treated, TiO_2 deposited, PS interface decreases. Figure 5.31 suggests that this behavior results as a decreased Lewis acidity on treatment with Et_2S produces a smaller HOMO-LUMO orbital mismatch between TiO_2 and NH_3.

Figure 5.38 corresponds to the responses observed when NH_3 contributes electrons to a

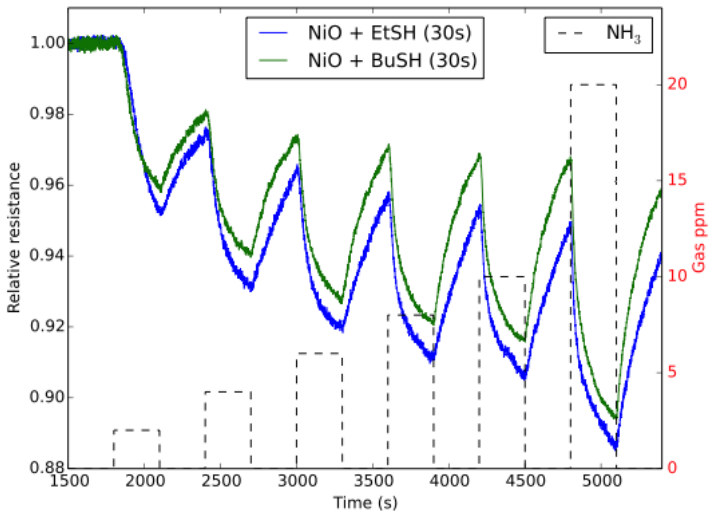

Figure 5.36: Comparison of response to NH_3 of ethanethiol and butanethiol treated Ni_xO nanostructure deposited porous silicon (PS) interfaces for 30 second exposure to the thiols. The sulphidated Ni_xO treated interface is more acidic than the Ni_xO treated PS acidic sites after a 30 second exposure. The boxes (black dashed) denote the analyte concentration.

diethylsulphide treated tin oxide deposited PS interface. The process increases the majority charge carrier concentration (electrons) and the conductance for both the diethyylsulphide treated and tin oxide deposited PS interfaces [137]. After an initial treatment of the tin oxide deposited surface, the diethylsulphide treatment was found to produce a significant increase in conductance relative to the surface deposited only with tin oxide. However, Figure 5.38 also demonstrates that a concomitant heating of the sulfidated surface decreases the conductance relative to the treated metal oxide deposited surface. We will argue that this loss of conductance is due to the removal of interacting water which as it hydrates the sulfide forms Brønsted acid sites.

Figure 5.39 corresponds to the responses observed when NH_3 contributes electrons to a diethylsulphide treated nickel oxide deposited PS interface. The process increases the majority charge carrier concentration (electrons) and the conductance for both the diethyl-sulfide treated and nickel oxide deposited PS interfaces [137]. The initial treatment of the nickel oxide deposited surface with diethylsulfide for ten seconds produces a decrease in conductance relative to the surface deposited only with nickel oxide. However, an increase

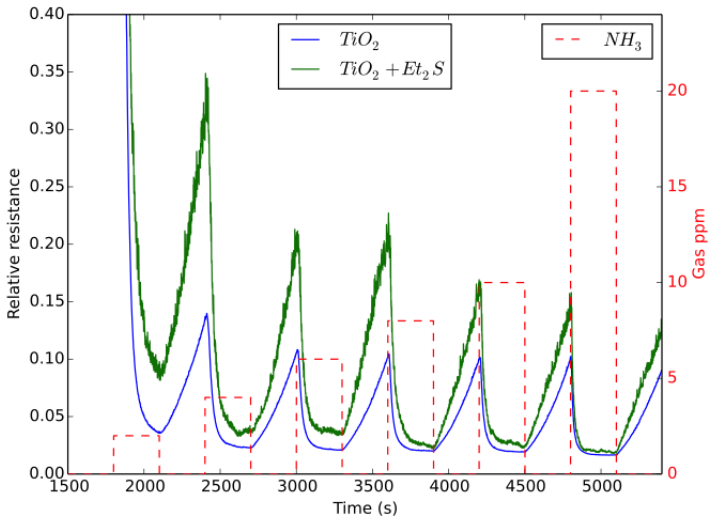

Figure 5.37: Response of diethyl sulfide, Et_2S, treated TiO_2 deposited porous silicon (PS) interface to NH_3. (a) Exposure to TiO_2 treated PS interface (blue). (b) Response of diethyl sulfide treated TiO_2 nanostructure deposited PS interface to NH_3 (green). The Et_2S treated TiO_2 deposited interface is made more basic relative to the PS and TiO_2 treated PS acidic sites. The boxes (red dashed) denote the analyte concentration.

to a 15 second exposure to the diethylsulphide results in an increase in the conductance of the sulfidated surface relative to the treated metal oxide deposited surface. Thus, again the precise level of diethylsulfide exposure must be carefully assessed and optimized.

Figure 5.40 compares the response to NH_3 of a Cu_xO treated PS interface to the Cu_xO + EtSH treated PS interface. The Cu_xO treated interface has a larger change in conductance than the untreated sensor as NH_3 donates electrons and increases majority charge carriers, however the conductance response of the etanethiol treated Cu_xO deposited PS interface decreases relative to that of the Cu_xO decorated PS interface. While the Cu_xO deposited surface has a greater mismatch with NH_3 than the untreated PS interface, the EtSH treatment shifts the Cu_xO +EtSH interface to the hard acid side of Figure 5.31 closer to NH_3, resulting in the sensor response decreasing.

Figure 5.41 correspond to a comparison of the responses for PS, PS decorated with Au_xO, and the Au_xO decorated PS interface treated with ethanethiol. The deposition process increases the majority charge carrier concentration (electrons) for the Au_xO treated interface, however the conductance of the etanethiol treated Au_xO deposited PS interface

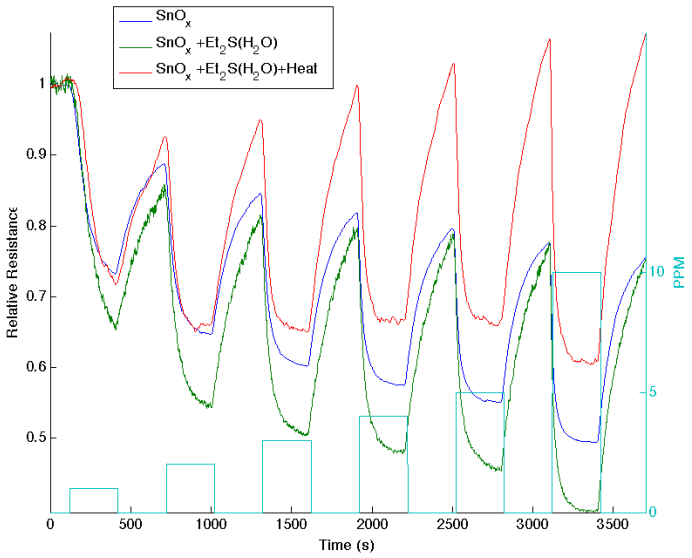

Figure 5.38: Response of diethylsulphide treated tin oxide nanostructure deposited porous silicon (PS) Interface (blue) to NH_3 (a) initial exposure with water present (green) and (b) after heating to remove water (red). The sulphidated SnO_x treated interface is basic relative to the PS and SnO_x treated PS acidic sites but more acidic in the presence of water. The boxes (aqua) denote the analyte concentration.

is found to decrease relative to that of the Au_xO decorated PS. The Au_xO deposited surface presents a greater orbital mismatch than the untreated PS interface with NH_3. This mismatch increases the transfer of electrons to the interface. However, the EtSH treatment moves the Au_xO +EtSH interface to the hard acid side of Figure 5.31 closer to NH_3. The decreased mismatch reduces the amount of electrons transferring to the sensor, lowering the response.

An important comparison is demonstrated in Figure 5.42 where we indicate the response for *p*-type PS decorated with Au_xO, and the Au_xO decorated PS interface subsequently treated with ethanethiol. The interaction process with NH_3 cancels the majority charge carriers and therefore increases the resistance of the *p*-type interface. The Au_xO increases the flow of electrons to the interface, and further decreases the majority charge carrier concentration. This enhancement is due to the larger mismatch between the Au_xO deposited surface and the NH_3 than the untreated PS interface and NH_3. Upon treatment with thiol, the ability of NH_3 to contribute electrons to the *p*-type interface is notably decreansed,

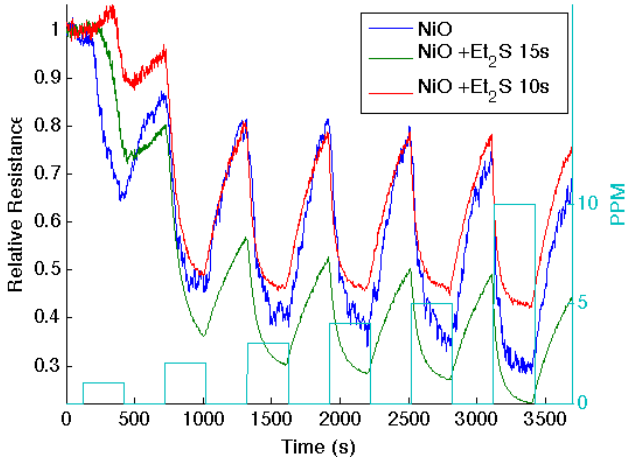

Figure 5.39: Response of diethylsulphide treated nickel oxide nanostructure deposited porous silicon (PS) interface to NH_3 (a) initial response of nickel oxide treated PS, (b) after treatment for 10 seconds with diethylsulphide, and (c) after treatment for 15 seconds with diethylsulphide. The sulphidate Ni_xO treated interface treated for 15 seconds is basic relative to the PS and Ni_xO treated PS. The boxes (aqua) denote the analyte concentration.

demonstrated by a sharp decline in resistance. This decline suggests that the thiol interaction with the Au_xO decorated surface decreases the molecular orbital mismatch with NH_3 causing the decrease in the electron transduction dominated interaction with NH_3.

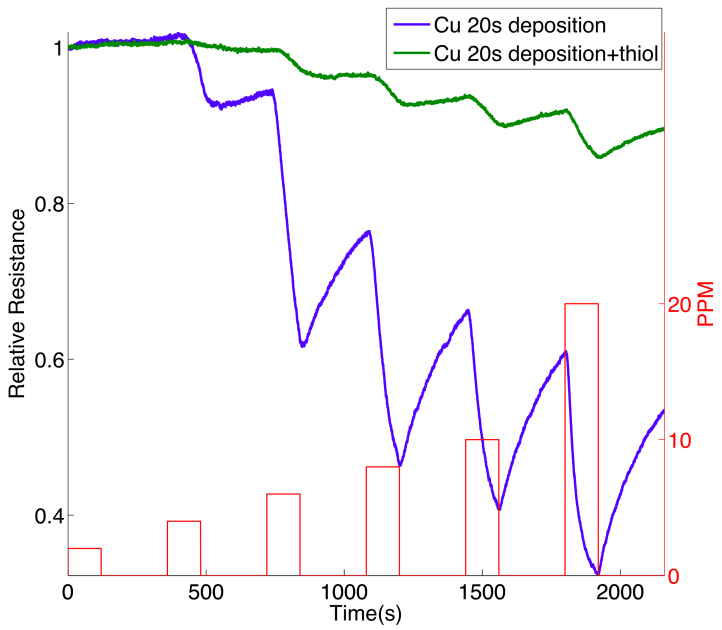

Figure 5.40: Response of ethanethiol treated Cu_x O nanostructure deposited porous silicon (PS) vs. Cu_x O treated PS interface to NH_3 after exposure for 30 seconds. The sulfidated Cu_xO treated interface is more acidic and therefore has a closer orbital matchup with NH_3. Therefore the conductance of the thiol treated interface decreases relative to the Cu_xO treated PS acidic sites. The boxes (red) denote the analyte concentration from 2 to 20 ppm from the beginning of the gas introduction to the end. A rapid response is observed at each concentration.

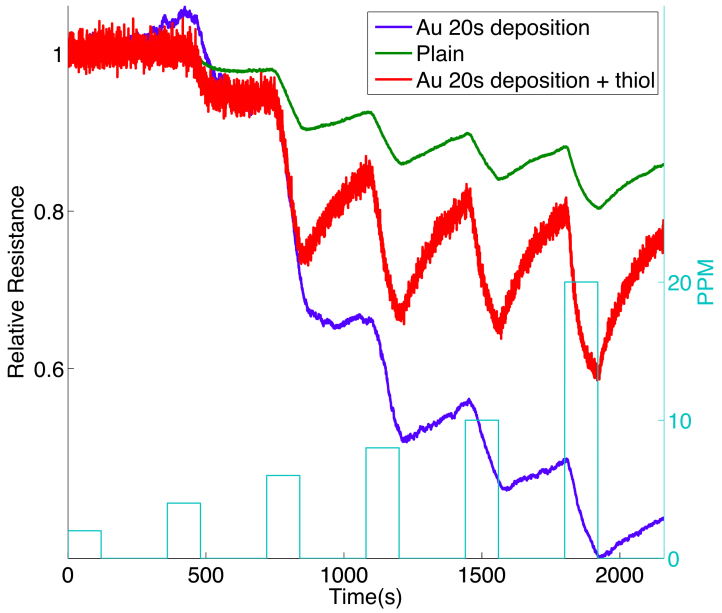

Figure 5.41: Response of Au_xO nanostructure deposited and the sulfidated Au_xO treated porous silicon (PS) interface to NH_3. The Au_xO treated PS interface is acidic relative to the PS interface. Therefore the conductance of the decorated interface increases relative to PS. The sulfidated Au_xO treated interface is more acidic and therefore has a closer orbital matchup with NH_3. Therefore the conductance of the thiol treated interface decrease relative to the Au_xO treated PS acidic sites. The boxes (aqua) denote the analyte concentration from 2 to 20 ppm from the beginning of the gas introduction to the end. A rapid response is observed at each concentration.

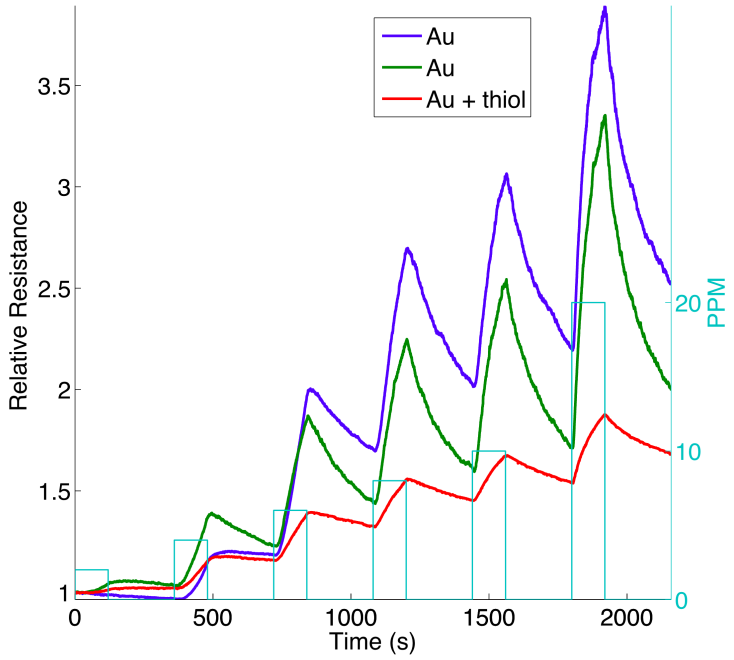

Figure 5.42: Response of ethanethiol treated Au_xO nanostructure deposited p-type porous silicon (PS) vs. an Au_xO treated PS interface to NH_3 after exposure for 30 seconds. The sulfidated Au_xO treated interface is more acidic and therefore has a closer orbital matchup with NH_3. Therefore the transfer of electrons to the thiol treated interface decreases relative to the Au_xO treated PS acidic sites. The boxes (dashed) denote the analyte concentration from 2 to 20 ppm from the beginning of the gas introduction to the end. A rapid response is observed at each concentration.

5.3.2 Sulfur Compound Functionalization Modification to the Response Matrices

The response strength is calculated using the equation shown earlier and placed into a response matrix. The matrix records the increase in signal strength due to the metal oxide nanoparticles relative to the sensor response for the untreated surface. However the data in Table 3 demonstrate that the response matrices for the metal oxides and their sulfur treated counterparts are quite distinct. The importance of this data is that it indicates that the sulfidation process creates additional distinct response matrix elements that can be used to test for a given analyte. The results follow a similar trend seen in the nitridation of the metal oxides.

Table 5.3: Change in the relative conductometric responses of sulfidated metal oxides vs. nanostructured metal oxides to NH_3.

	Disulphide	Thiol
TiO_2	.5	7
SnO_x	.6	6
Ni_xO	2	.1
Cu_xO	- - -	.3
Au_xO	- - -	.6

Table 5.4: Change in the relative conductometric responses of sulfidated metal oxides vs. nanostructured metal oxides to NH_3.

	Disulphide	Thiol
PS functionalized 30 seconds		1.5
TiO_2	2	24
SnO_x	1.5	15
Ni_xO	3	.15
Cu_xO	- - -	.5
Au_xO	- - -	2

5.3.3 X-Ray Photoelectron Spectroscopy (XPS)

XPS profiles for TiO_2, SnO_x, Ni_xO, and Cu_xO and their corresponding sulphur compound functionalized counterparts are show in Figures 5.40- 5.48. Here, we again monitor the

electron binding energy of sites a few nanometers from the decorated interface surfaces. We have examined six areas of the XPS spectrum, the Ti 2p, Sn 3d, Ni 2p, and Cu 2p, regions, the S 2s region near 162 eV, and the O 1s region near 530 eV.

In scanning the Ti 2p regions as depicted in Figure 5.43 we find a slight shift of the Ti binding energy from 458.8 eV, decreasing to 458.6 eV upon treatment with the sulphides and thiols. We observe a shift of approximately 0.2 eV to lower binding energy. The Sn 3d binding energy associated with SnO_x (Figure 5.44) shows a greater shift by $\tilde{0}.3$ eV for the sulphide which increases to $\tilde{0}.4$ eV to lower binding energy for the thiol, both being notably greater than that observed for Ti. The Ni 2p binding energy associated with nanostructured Ni_xO (Figure 5.45) is at $\tilde{8}56.5$ eV and shows a red shift of approximately 0.5eV for treatment with the disulphide. However, the shift increases to $\tilde{+}$ 0.6 eV for the thiol.

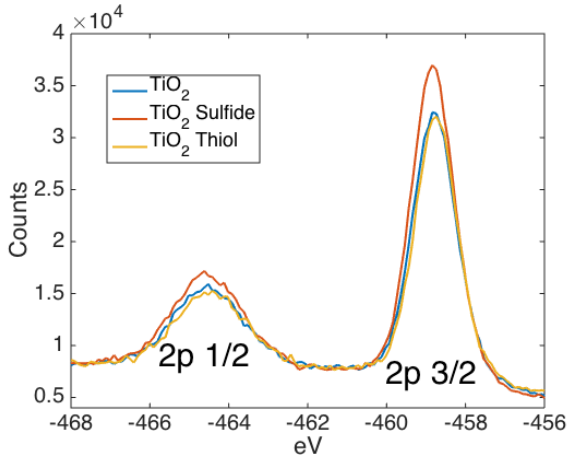

Figure 5.43: Ti 2p XPS spectrum showing a lower binding energy for the sulphur functionalized form of TiO_2.

In contrast to the XPS spectra for TiO_2, SnO_x, and Ni_xO, the Cu 2p peaks for the sulphur functionalized Cu_xO sample show not only a weakening and broadening of the XPS features but also a shift to higher binding energy (Figure 5.46) like the effect seen with nitridation. A similar shift in binding energy is seen in the thiol treated material.

The S 2s XPS features (Figures 5.48-5.49) are notably shifted from those for atomic sulphur. Further, those features associated with the oxygen sites (Figures 5.50 - 5.53) show a clear shift on sulphur compound functionalization as well. The observed binding energies for the O 1s XPS spectra show significant changes upon treatment with the sulphides

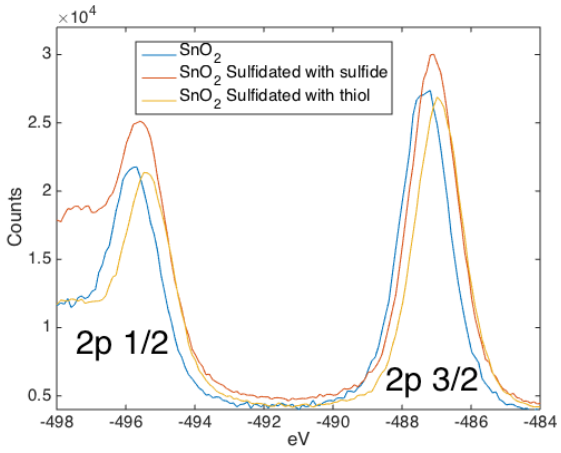

Figure 5.44: Sn 3d XPS spectrum showing a lower binding energy for the sulfur functionalized forms of SnO_x. The shift to lower binding energy after thiol functionalization exceeds that for the sulphide both of which are greater than that for TiO_2.

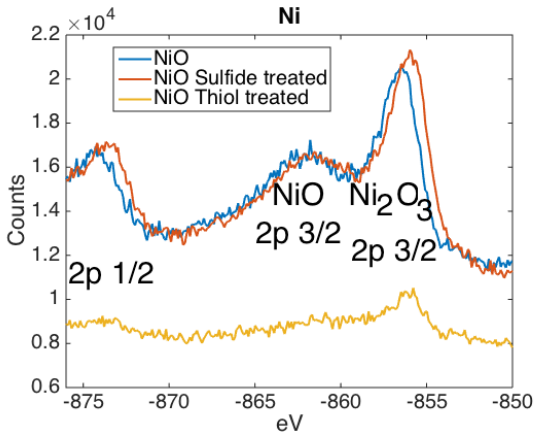

Figure 5.45: Ni 2p XPS spectrum showing a lower binding energy for both the sulphide and thiol functionalized forms of Ni_xO. The shift in binding energy exceeds that for TiO_2 and SnO_2.

and thiols. The data for TiO_2 are quite interesting verses the typical data that we have observed [9]. The double peak in Figure 5.50 is due to both SiO_2 (high energy peak at 532.3 eV) and TiO_2 (low energy peak at 530.2 eV) as the signals for these oxides overlap each other. The data indicate that the sulfidated form of both TiO_2 and SiO_2 show a slight decrease in binding energy to 532.2 and 530.3 eV respectively. While the SnO_x decorated systems depicted in Figure 5.51 indicate a significant decrease in binding energy from 532.4 eV to 532 eV with treatment with the sulphides, they demonstrate a clear increase in binding energy from 532.4 eV to 532.6 eV for treatment with the thiols. By comparison,

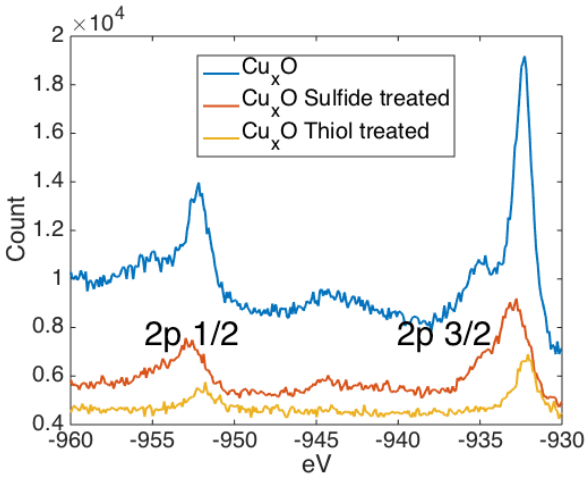

Figure 5.46: Cu 2p XPS spectrum showing a considerable decrease in intensity for the suldide and thiol groups, and a shift to higher binding energy for the sulfide functionalized form of Cu_xO.

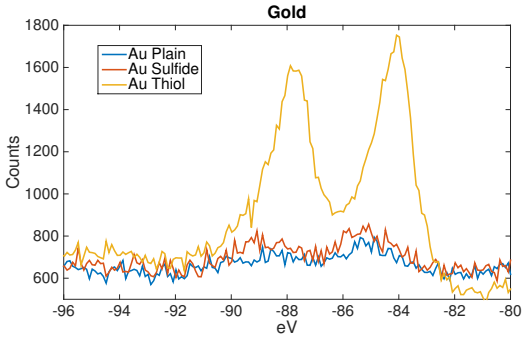

Figure 5.47: Au 4f XPS spectrum showing an increase in the signal for thiol treated gold, suggesting a partial oxidation of the gold, compared to the plain and sulphide treated gold.

the Ni_xO decorated interface, after treatment with the sulphides, shows a notable decrease of ≈4 eV in the O 1s binding energy (Fig. 5.52) and a much smaller red shift on treatment with the thiols. The decrease in binding energy for the sulphide treated Cu_xO (Fig. 5.53) decorated interface is even smaller (-.2 eV). These are clear trends and distinctions.

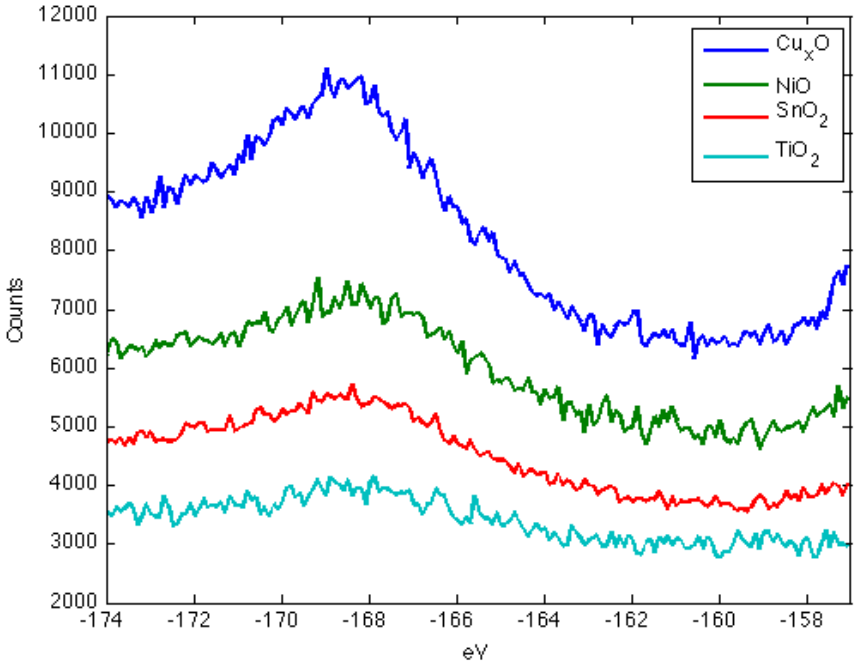

Figure 5.48: Sulfur 2s XPS spectra associated with the sulphur functionalization of TiO_2, SnO_x, Ni_xO, and Cu_xO. The S 2p3/2 peak is shifted to considerably higher binding energy than the typical 2p3/2 feature suggesting a feature due to sulphur bound to a CH_x group or groups.

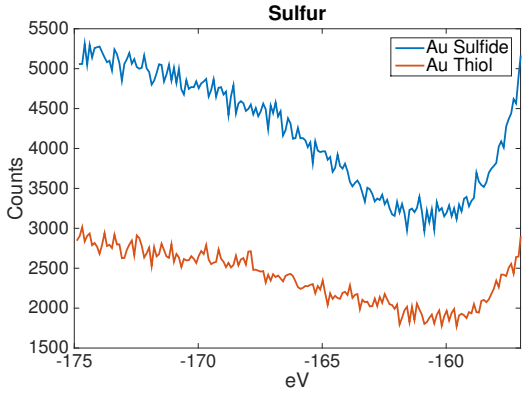

Figure 5.49: Sulfur 2s XPS spectra associated with the sulphur functionalization of Au_xO. The S 2p3/2 group is again shifted to higher energies in agreement with bonded CH_x groups. The peak at 158 eV is a strong SiO_2 peak dominating any other signals including possible thiolate signals.

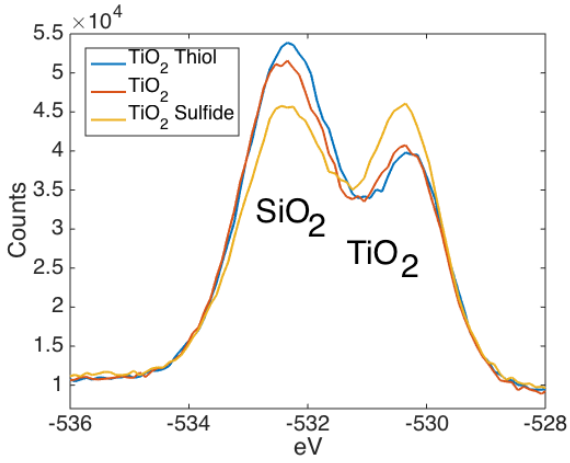

Figure 5.50: Oxygen 1s XPS spectrum associated with the sulphur functionalization of TiO_2 depositions. Both TiO_2 and SiO_2 are observed and suggest a shift to higher binding energy on treatment with the sulphides or thiols.

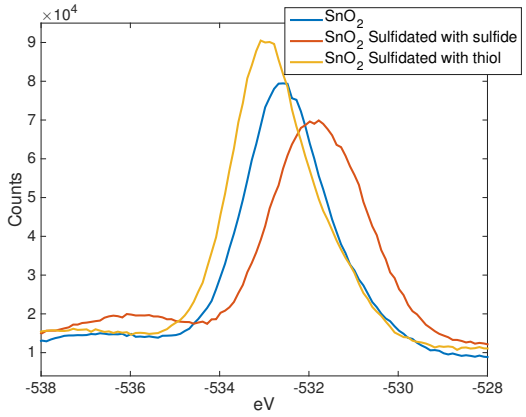

Figure 5.51: Oxygen 1s XPS spectra associated with the sulphur functionalization of SnO_2 depositions. The spectra show a distinct red shift after treatment with the sulphides and, by comparison a clear, albeit smaller blue shift upon treatment with the thiols.

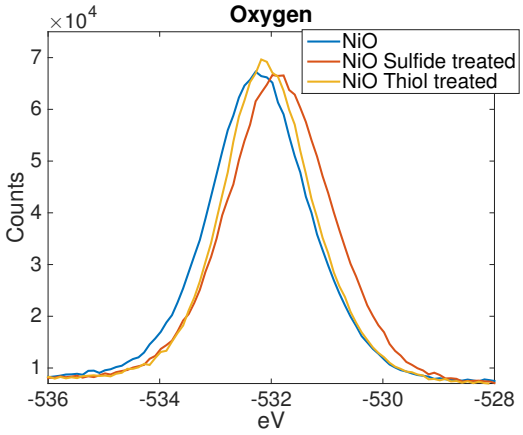

Figure 5.52: Oxygen 1s XPS spectra associated with the sulphur functionalization of Ni_xO depositions. The spectra show a distinct red shift after treatment with the sulphides and a slight red shift upon treatment with the thiols.

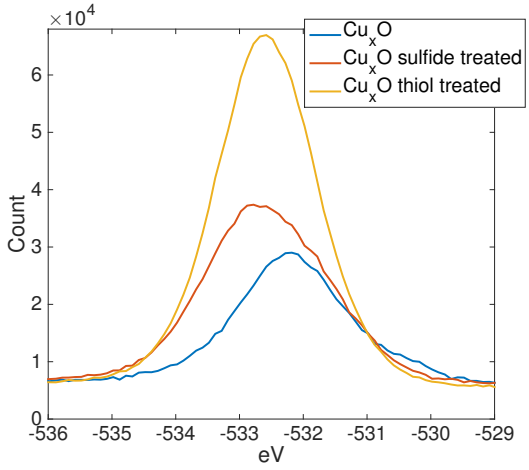

Figure 5.53: Oxygen 1s XPS spectra associated with the thiol and sulphide functionalization of Cu_xO depositions. The spectra, for the disulfides and thiols, show a shift to higher binding energy after treatment.

5.3.4 Discussion

The responses reported in Figures 5.13-22 and 5.32-5.42 can be explained within the framework of the IHSAB principle. The data that we have presented suggests that we can modify the acid/base properties of nanostructured metal oxide (metal centers) and the sensor scale by modifying the metal positive charge through doping *in-situ* with nitrogen or functionalized sulfur groups substituted from appropriate precursors. If nitrogen is used the Lewis acidity of the metal oxides will decrease. Similarly if basic sulfide groups are used, then we lower the Lewis acidity of the metal oxide nanostructures. However if acidic sulfide groups (thiols) are used, the functionalization of S-H with the metal oxides increases the Brønsted acidity.

The IHSAB principle is used to analyze the results. For a TiO_2 nanoparticle site, the Ti, nominally in the +4 oxidation state, when treated with a thiol becomes more acidic (Figure 5.33). This will shift the normal metal acidity toward the hard acid side in the top portion of Figure 5.31. Thus the bonding interaction with the fixed analyte, NH_3, catalogued in the bottom of this figure will decrease and the sensor signal will increase. The thiol removes electron density from the metal through the interaction with oxygen. As a counterpoint when TiO_2 interacts with an amine or a sulfide (Figures 5.5 and 5.37), the functionalized sulfide and amine contributes electrons and lowers the Lewis acidity of the titanium site. This lowering of the acidity increases the bonding interaction with the NH_3, and decreases the physisorption resulting in a decrease in the sensor signal.

Similarly, as the thiol interacts with SnO_x (Figure 5.34) the response again increases. Treatment of the Ni_xO decorated interface (Figure 5.36) with thiol again shifts the acidity of the oxide to the harder acid side of Figure 5.31, however, now this process moves the decorated oxide closer to NH_3 providing for a better HOMO-LUMO orbital matchup and the sensor response decreases as the facility for bonding increases. In contrast, treatment of the decorated SnO_x (Figures 5.19 and 5.38) interface with the amines or sulfides as they contributes electrons, lowering the Lewis acidity of the metal site, leads to a closer matchup of molecular orbitals with NH_3 and a decrease in response. The treatment of the Ni_xO decorated (Figure 5.39) site, as it lowers the Lewis acidity of the metal, shifts the decorated

oxide further from NH_3 leading to a decrease in molecular orbital interaction and an increase in sensor response.

The nitridation of Cu_xO decreases the metal site Lewis acidity (forms more basic sites) and shifts the response of the modified nanostructures further to the soft acid side of Figure 5.12. It is tempting to suggest that the formation of the oxynitride should simply increase the basicity of the nanostructure surface and thus should decrease the response to NH_3. However, this does not occur. The nitridated copper oxide is shifted further to the soft acid side of ammonia in Figure 5.12, dictating a greater HOMO (donor) – LUMO (acceptor) molecular orbital mismatch and an enhanced reversible response to ammonia. The IHSAB principle suggests, counter to intuition, that the response of the *in-situ* treated nitridated copper oxide interface should increase relative to that of Cu_xO, precisely as is observed. In Figure 5.12, NO is positioned directly under the copper oxides. Nitridation shifts the copper oxides to the soft acid side and away from NO, again leading to an increase in molecular orbital mismatch and an increase in the reversible response of the oxynitride to NO.

Finally, the behavior observed for the untreated and nitridated PS interfaces is consistent with the IHSAB principle. Figure 5.12 can be used to demonstrate that the nitridation of the PS interface causes a shift away from NH_3, which leads to an increase in the reversible response to NH_3 and a shift toward NO, which leads to a decrease in the reversible response to NO. These obtained nitridation results suggest that the IHSAB principle can be used as an important distinguishing principle of reversible sensor response as dictated by the dominance of electron transduction over bond formation.

The data in Figures 5.13-22 and 5.30- 5.42 correlates with the XPS data obtained for TiO_2, SnO_2, NiO, and Cu_xO, their oxynitrides, and metal oxide-sulphur moiety. The conductometric data in Figures 5.21 and 5.22 shows demonstrate a significant increase in the signal for the nitridated sample, are consistent with the decrease in signal intensity and the increase in nitrogen binding energy (Fig. 5.26) observed for the copper system. The clear trend in the decrease of the O 1s binding energy from the titanium to copper oxides upon nitridation is consistent with the decrease in the titanium, tin, and nickel site binding energies. However, the data in Figure 5.26 are consistent an increased stability

for the nitrdated copper sites. The copper (Fig. 5.26) and oxygen (Fig. 5.30) data, in concert, would suggest a more significant rearrangement of the nitridated lattice for the copper system.

The sulfur 2s XPS data in Figure 5.47 provide an important result. The data is characteristic of both the sulfides and thiols. The peak response at approximately 168 eV represents a substantial shift from the typical sulfur peak at approximately 162 eV [231]. This shift is attributed to the remnant binding of the CH_x groups to the sulfide and thiol as they interact with the metal oxide decorated interface. This remnant -S-$(CH_x)_y$ may have application to the use of sulfur- carbon moieties in lithium battery configurations as we note the complimentarity of physisorption and chemisorption. A further distinction in these systems is seen in the oxygen peaks described for SnO_x and Ni_xO as the shift in the peak response is less for the thiols than the sulfides. For the Cu_xO, the sulfide doesn't shift the peak; however, the thiol does blue shift the oxygen by 0.2 ev. It seems likely that this results from the Brønsted acid sites present on the thiols.

The XPS spectra obtained in Figures 5.23- 5.30 and 5.43-5.51 are sensitive to 0.1%. The typical time frame for the depositions used to obtain the conductometric data in Figures 5.13-22 and 5.32- 5.39 is under 30 seconds. The XPS data requires that we use deposition times, which are at least 5 minutes. This corresponds approximately to an order of magnitude increase in concentration to obtain signals in the 0.1% range.

The results obtained for conductometric response display a clear quantitative dependence on concentration, however, they are based on semi-quantitative inferences from measuring the conductometric signals from the interactions of molecules interacting with surfaces via donor-acceptor interaction. More detailed physical measurements on the structures of the surfaces and the energetics of these surfaces will provide enhanced understanding. Molecular data needed to address the orbital energy arguments is available in terms of molecular proton affinities, acidities, and ionization potentials but these data are not broadly available for surfaces [163]. While our measurements now provide semi- qualitative data about the doped metal oxide surface sites, further experiments will help to quantify this data.

5.3.5 Conclusions

We have demonstrated the efficacy of fractional nanostructure depositions as a means of obtaining distinct reversible interface responses that show the potential for combination in an array based format. We have considered the conversion of the metal oxides *in-situ* with the amine and organic sulphides. The amines create oxynitrides on the metal oxide nanoparticle surface, while the sulphide interactions form S-$(CH_x)_y$ moieties on the metal oxide nanostructures. The nitrogen and the sulphides are found to lower the Lewis acidity of the metal oxide nanostructures introducing an enhanced basicity to the nanostructure decorated PS interface. In contrast, the thiols are found to enhance the acidity of the metal oxide sites. It is suggested that this results from the S-H bonds and corresponds to an increase in the Brønsted acidity. The behavior of these systems appears to be well represented by the newly developing IHSAB model [74, 137, 226]. It's inverse concept, corresponding to the HSAB model can provide an indication of stronger metal oxide-sulphur moiety interactions. This will be the subject of future studies.

CHAPTER VI

CONCLUSION

In summary, we have examined multiple aspects of the metal oxide nanostructure decorated PS gas sensor interface. We have examined how the analyte gas interactions with the PS can be affected by the doping material of the silicon. We have investigated the analyte gas interaction with the nanostructure decorated PS and with other analyte gases on the surface. And finally, we have functionalized the metal oxide nanostructures and seen how the functionalized nanoparticles can change the gas-sensor interactions. These changes are easily explained by the IHSAB principle.

We looked at creating $p+$-type PS gas sensors, and saw the differences between the $p+$ and the p type sensors. We also examined the effects of using n-type PS sensors. The change from p- to n-type silicon predictably switched the direction of the response for the different analyte gases, since we switched from holes to electrons as the dominant carriers. The unpredicted result of the switch from p to n-type was at higher concentrations of acidic gases such as NO and NO_2 increased the acidity of the surface. If the surface of the sensor became too acidic from the acidic metal oxide nanoparticles and analyte gas, the direction of the electron transduction switched as seen in figures 3.18and 3.19.

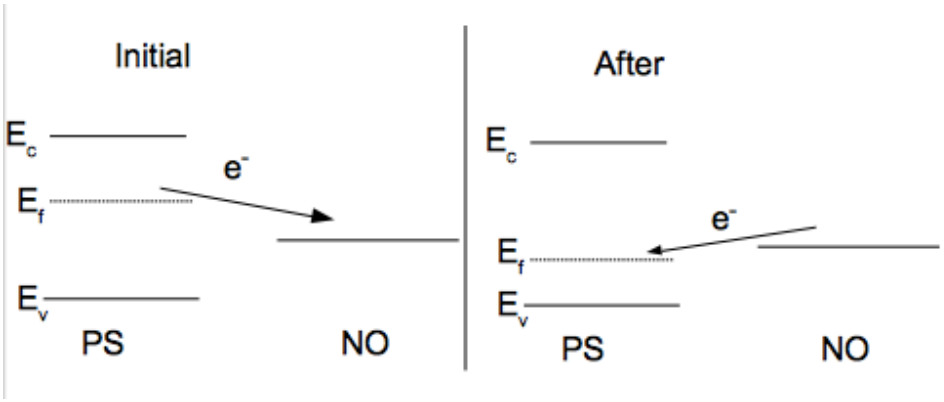

Figure 6.1: Left shows the initial flow of electrons to the analyte gas for the unmodified PS. Right shows the flow after the PS has been modified with acidic metal oxide nanoparticles

We also examined how the sensor saturates at higher analyte concentrations. This saturation of the sensor response in the presence of the metal oxides seems to be caused by the electronic band structure of the silicon saturating, not by the adsorption of the gas. Also, the analyte gas interaction with other analyte gases on the surface was explored. These gas on gas interactions seem to be governed by the IHSAB principle.

Finally we studied the functionalization of metal oxides. The nitrating of the TiO_2 on the sensor surface forms a light sensitive photocatalysis. This photocatalysis is used to create a solar pumped sensor. We also looked at the nitration of other metal oxide nanoparticles. The nitration decreases the Lewis acidity of the nanoparticles. This shift can either reduce or improve the sensor signal to an analyte gas, depending on relative position of the metal oxide and the analyte gas in the IHSAB table. Functionalizing the metal oxide nanoparicles with sulfides or thiols can also change the Lewis acidity of the metal oxides. The sulfide functionalization lowers the acidity of the metal oxides, while the thiol functionalization increases the Lewis acidity.

APPENDIX A

NUMERICAL DIFFUSION SIMULATION CODE

This code simulates the gas diffusing into a 1-D tube using the Fickian equation. It takes in an array of the gas concentration at different times (the input gastime), the diffusion constant divided by l^2 is df and the response1 is how strong the signal of the sensor is to the gas. The code simulates the gas diffusion into the tube then outputs the response

```
    function [response] = sensorm(pastime,response1,df)
%Sensor Modeling
%I will assume that the base resistance is 0
n=10;% number of grid points
dt=0.1;
cc1=zeros(1,n+1);
[ ,tfinal]=size(gastime);
for i=1:tfinal
response(i)=repsonse1*mean(cc1(2:n+1));%adding up all the gas in the tube for the response
cc1(1,1)=gastime(i);


    cc1=gasdefussion1(cc1,df,n,dt);
end
end


    function [ fcon] = gasdefussion1(icon,df,n,dt )
fcon=icon;
ddc=icon(1:n-1)-2*icon(2:n)+icon(3:n+1);
%boundaries are icon 1 =the gas flowing in
```

```
% assume the first derivative at the end is always zero in space
fcon(2:n)=icon(2:n)+dt*df*n2*ddc;
fcon(n+1)=fcon(n);% boundary condition
end
```

APPENDIX B

GAS CONCENTRATION EXTRACTION FROM A SENSOR ARRAY CODE

Takes the sensor data from two sensors (inputed as a1 and b1), the code then outputs when the gases turns on and off and the ppm level of the two gases to a calibration factor. The code requires a noise cutoff for each of the sensors (cutoff1 and cutoff2) and a gas response matrix for the sensors (matrix). This matrix can be modified as needed. An example response matrix is described below.

If the sensor responses goes like this sensor1 = 4*gas2 + gas1

sensor2 = gas2 + 3*gas1

then the response matrix will be

matrix=[1,3;4,1];

Modify the matrix as needed.

```
function (d2gas1,d2gas2)=gasproblem2(a1,b1,cutoff1,cutoff2,matrix)
% function to extract the gas concentration from the response
%adapted from code created by Christian Reitz

%a1 and b1 are the responses from sensor 1 and 2
% cutoff1 and cutoff2 are noise cutoffs needed for the algorithm

l = length(a1);
% inverts the matix and multiples it by the sensor response.
gasMat = inv(matrix)*[a1;b1];
gas1 = gasMat(1,:);
```

```
gas2 = gasMat(2,:);

    %we take the second derivative
%Derrivitives
dgas1 = diff(gas1);
dgas2 = diff(gas2);
d2gas1 = diff(dgas1);
d2gas2 = diff(dgas2);
%this is done to have the response without any bias
s1=cumsum(dgas1);
s2=cumsum(dgas2);

    %Initialize conditional triggers
lookend1 = 0;
lookend2 = 0;

    for i = 1:l-2
%——-First gas————————————
%Examines to find a positive value above the cutoff. If found, looks for a
%negative value with a magnitude larger than the cutoff.
%The cutoff is to get rid of the slight dip in the second derivative.
if d2gas1(i) ¿ cutoff1 && lookend1 == 0
start1 = i;
lookend1 = 1;
elseif d2gas1(i) ¡ -cutoff1 && lookend1 == 1
lookend1 = 0;
max1 = max(d2gas1(start1:i));
d2gas1(start1:i) = max1;
elseif d2gas1(i)¡ cutoff1
```

```
d2gas1(i) = 0;
end
%——-Second gas————————
%Same as first gas
if d2gas2(i) ¿ cutoff2 && lookend2 == 0
start1 = i;
lookend2 = 1;
elseif d2gas2(i) ¡ -cutoff2 && lookend2 == 1
lookend2 = 0;
max1 = max(d2gas2(start1:i));
d2gas2(start1:i) = max1;
elseif d2gas2(i)¡ cutoff2
d2gas2(i) = 0;
end
end
end
```

APPENDIX C

LABVIEW CODE

Front panel

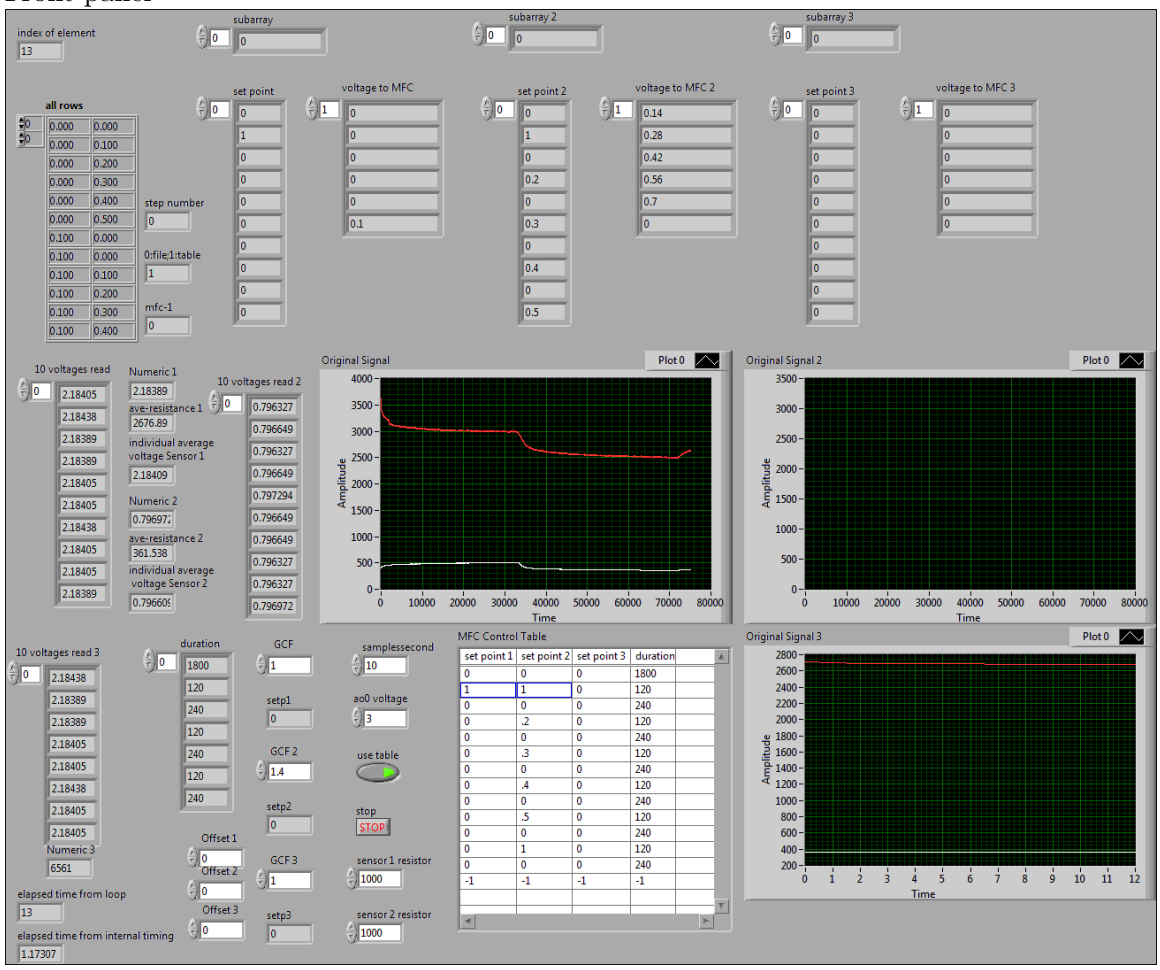

Back end

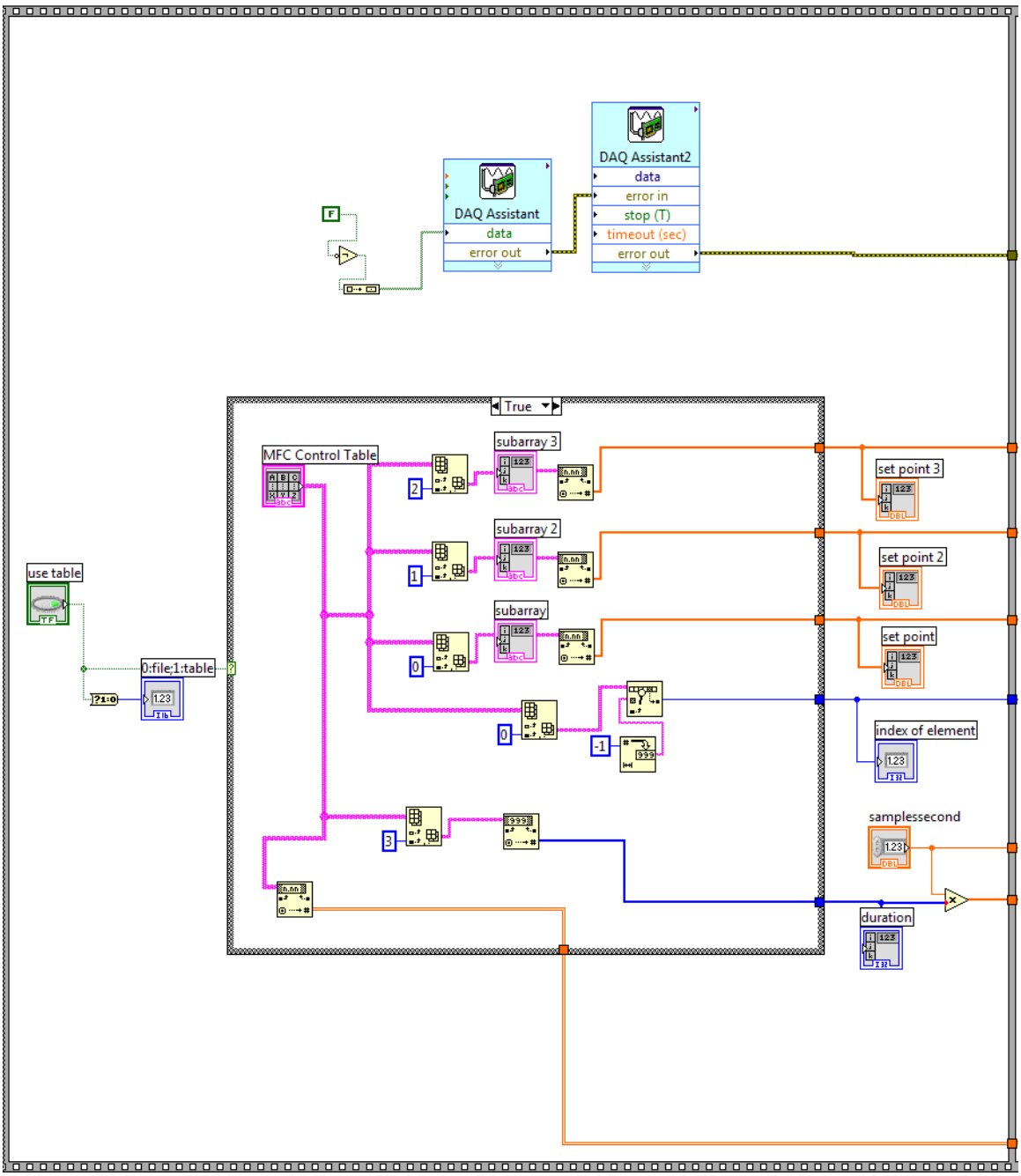
DAQ Assistant2
data
error in
stop (T)
timeout (sec)
error out
DAQ Assistant
data
error out
True
MFC Control Table
subarray 3
subarray 2
subarray
use table
0:file;1:table
set point 3
set point 2
set point
index of element
samplessecond
duration

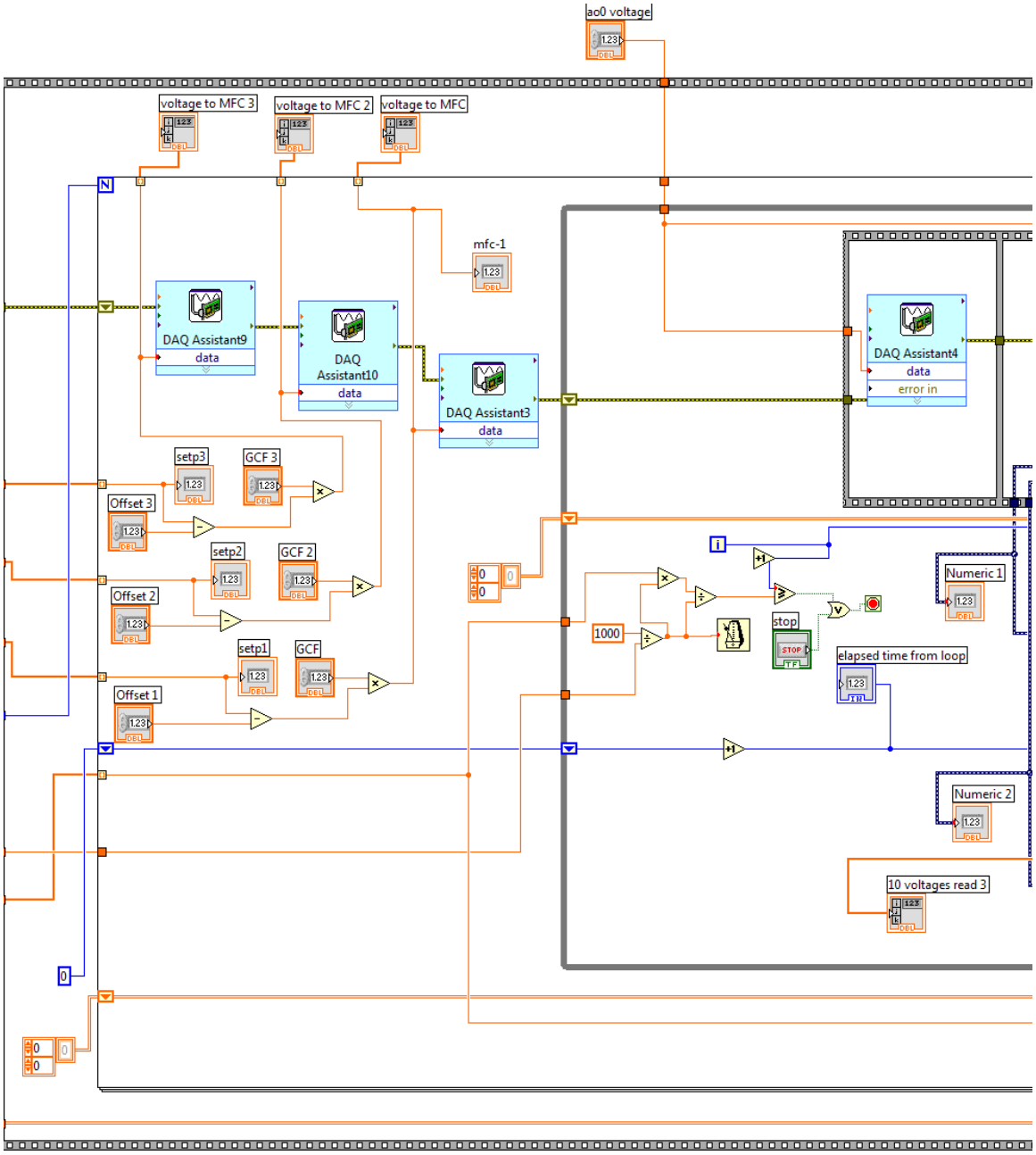
ao0 voltage
voltage to MFC 3
voltage to MFC 2
voltage to MFC
mfc-1
DAQ Assistant9
data
DAQ Assistant10
data
DAQ Assistant3
data
DAQ Assistant4
data
error in
setp3
GCF 3
Offset 3
setp2
GCF 2
Offset 2
setp1
GCF
Offset 1
1000
stop
STOP
elapsed time from loop
Numeric 1
Numeric 2
10 voltages read 3

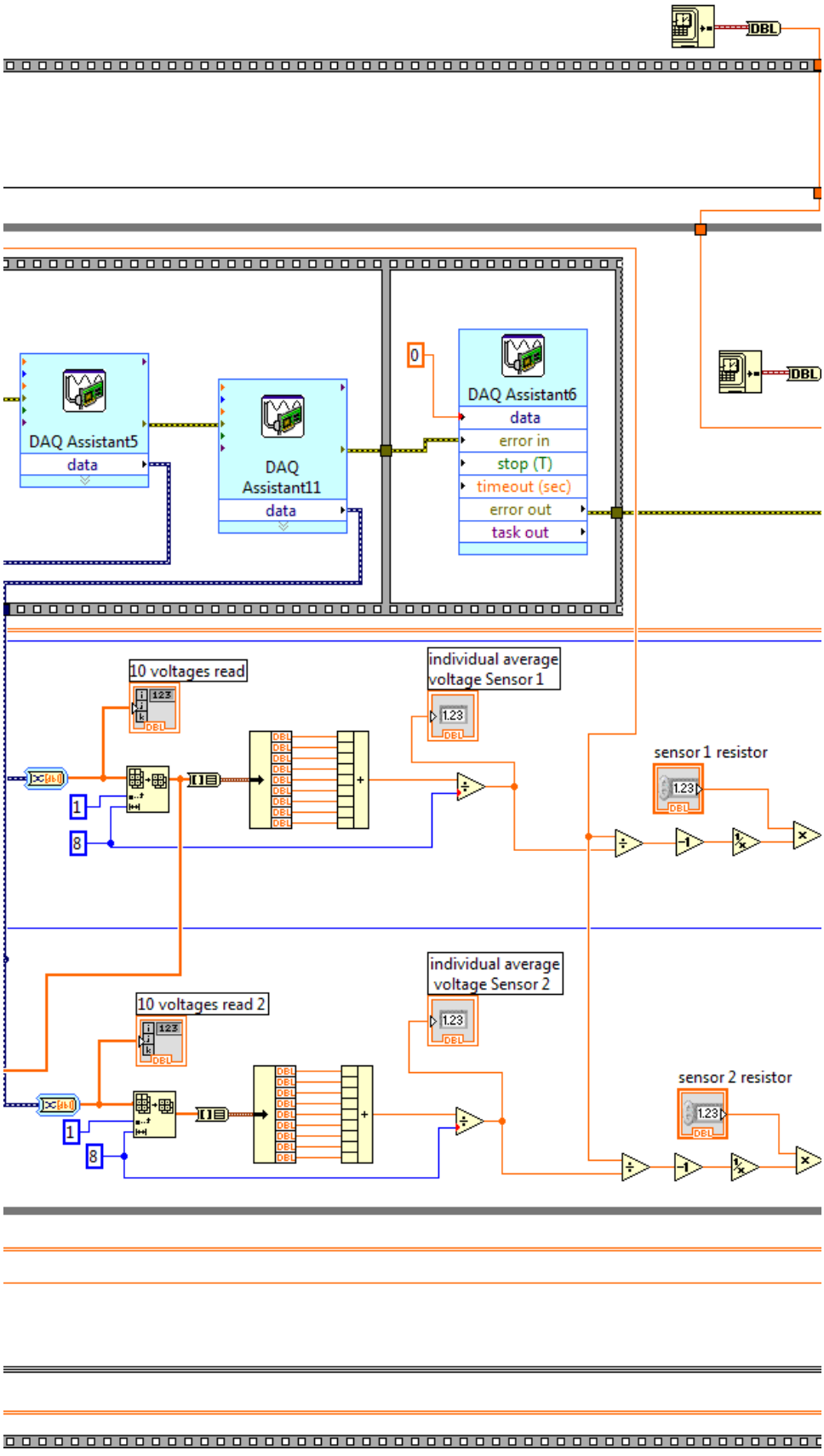
DBL
DAQ Assistant5
data
DAQ
Assistant11
data
0
DAQ Assistant6
data
error in
stop (T)
timeout (sec)
error out
task out
DBL
10 voltages read
individual average
voltage Sensor 1
sensor 1 resistor
1
8
10 voltages read 2
individual average
voltage Sensor 2
sensor 2 resistor
1
8

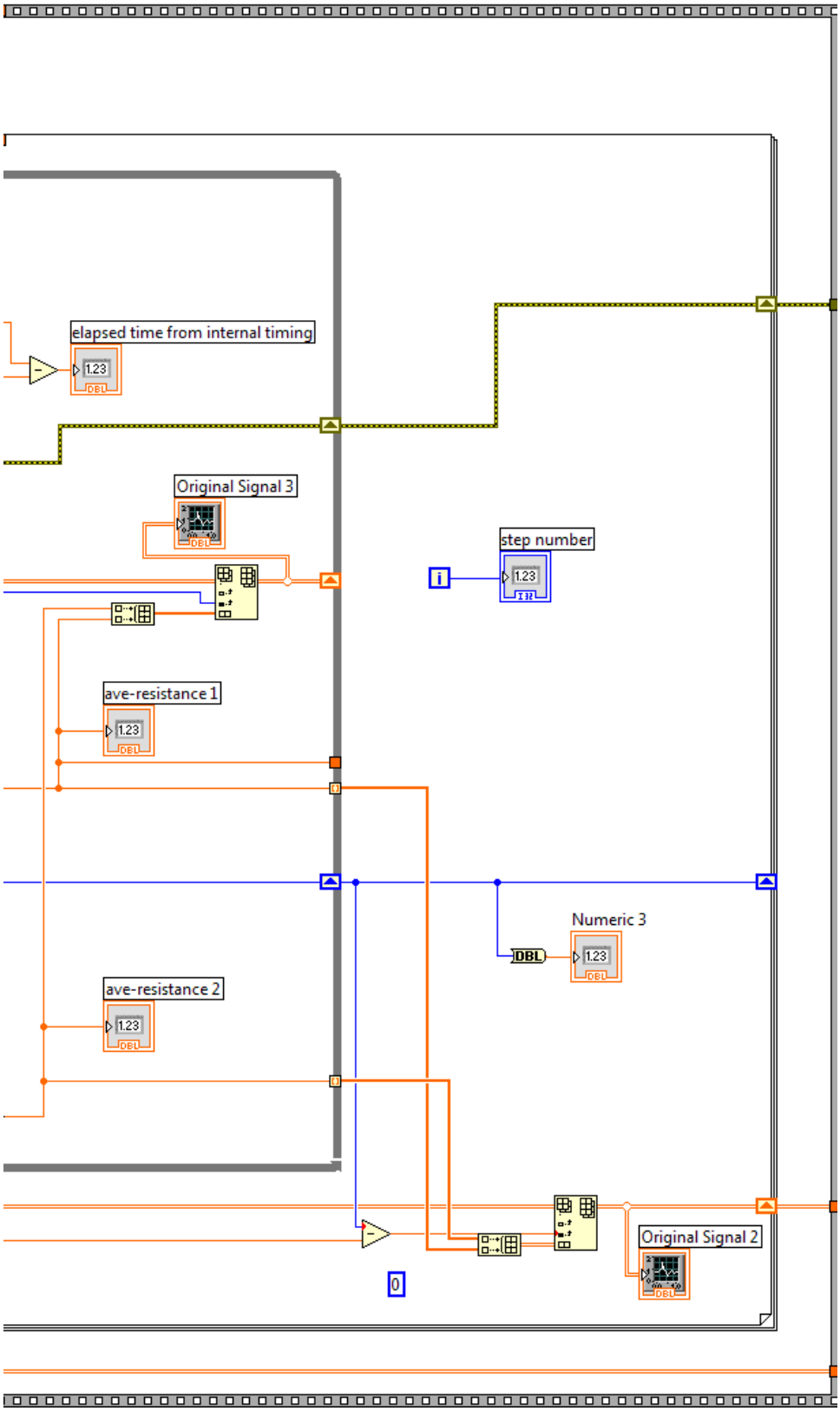
elapsed time from internal timing
Original Signal 3
step number
ave-resistance 1
Numeric 3
ave-resistance 2
Original Signal 2
0

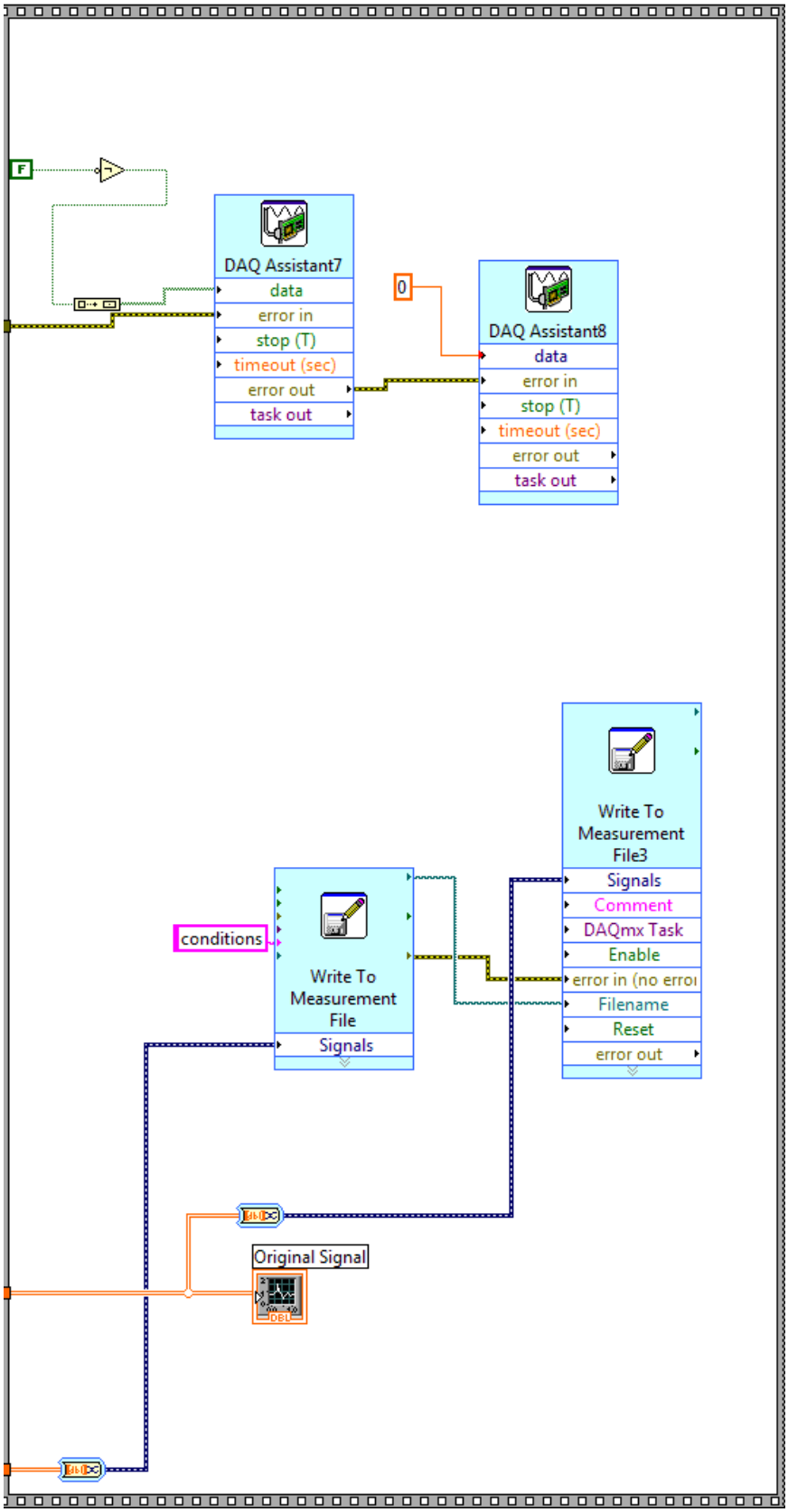
F
DAQ Assistant7
data
error in
stop (T)
timeout (sec)
error out
task out
0
DAQ Assistant8
data
error in
stop (T)
timeout (sec)
error out
task out
Write To Measurement File3
Signals
Comment
DAQmx Task
Enable
error in (no erroi
Filename
Reset
error out
conditions
Write To Measurement File
Signals
Original Signal

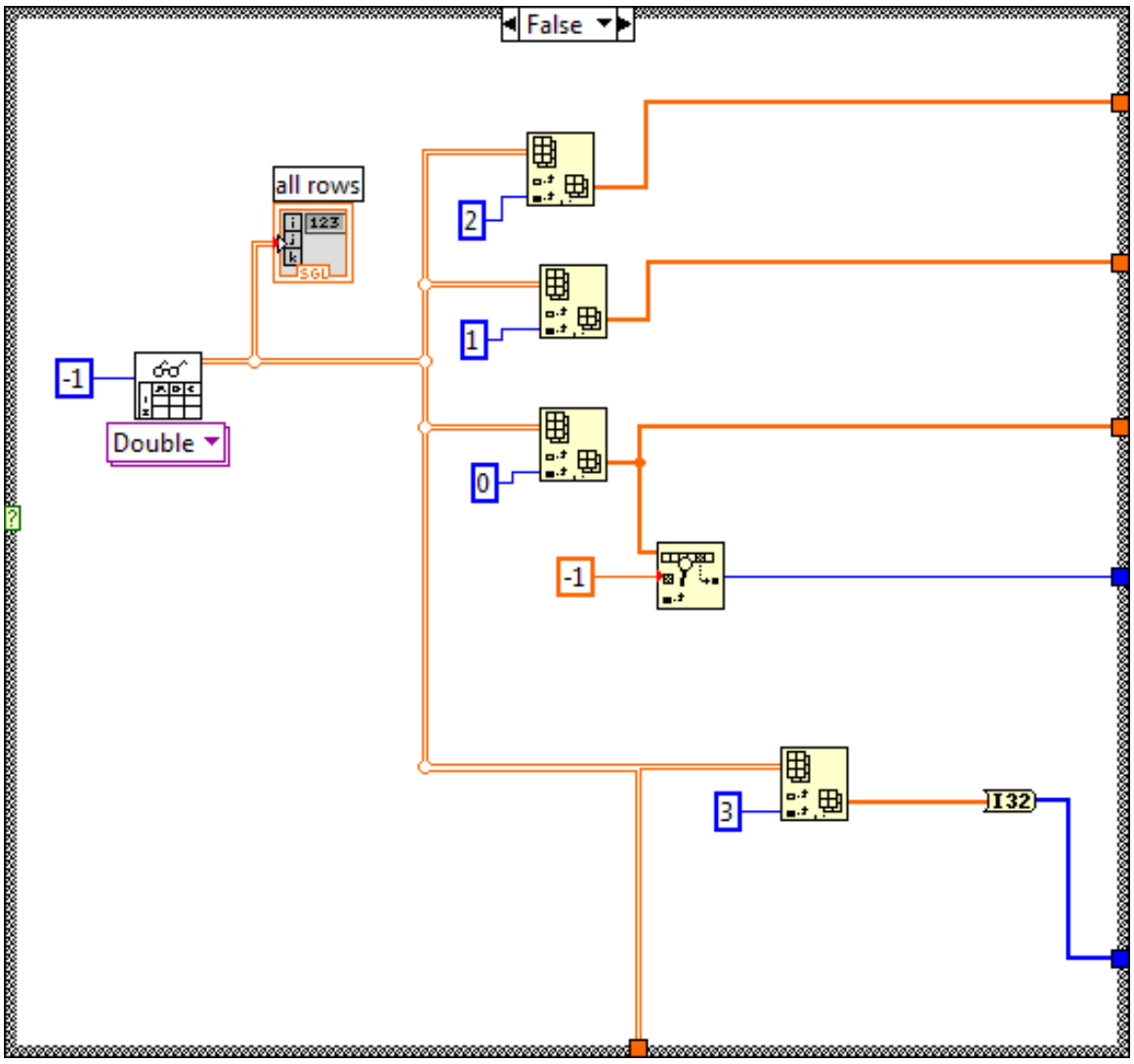
False
all rows
123
SGL
-1
Double
2
1
0
-1
3
I32

REFERENCES

[1] M. E. Franke, T. J. Koplin, and U. Simon, "Metal and metal oxide nanoparticles in chemiresistors: does the nanoscale matter?," *Small* **2**, 36 (2006).

[2] X.-J. Huang and Y.-K. Choi, "Chemical sensors based on nanostructured materials," *Sensors and Actuators B: Chemical* **122**, 659 (2007).

[3] P. Moseley, "Solid state gas sensors," *Measurement Science and Technology* **8**, 223 (1997).

[4] H. Tuller and R. Mlcak, "Advanced Sensor Technology Based on Oxide Thin Film—MEMS Integration," *Journal of Electroceramics* **4**, 415 (2000).

[5] M. Kaur, D. Aswal, and J. Yakhmi, "Chemiresistor gas sensors: materials, mechanisms and fabrication," *Science and Technology of Chemiresistor Gas Sensors," Aswal, DK and Gupta, SK, Eds* , 33 (2007).

[6] T. Seiyama, A. Kato, K. Fujiishi, and M. Nagatani, "A New Detector for Gaseous Components Using Semiconductive Thin Films.," *Analytical Chemistry* **34**, 1502 (1962).

[7] I. Sinclair, *Sensors and transducers* (Newnes, 2000).

[8] J. E. Amoore and E. Hautala, "Odor as an ald to chemical safety: Odor thresholds compared with threshold limit values and volatilities for 214 industrial chemicals in air and water dilution," *Journal of applied toxicology* **3**, 272 (1983).

[9] S. Ozdemir and J. L. Gole, "A phosphine detection matrix using nanostructure modified porous silicon gas sensors," *Sensors and Actuators B: Chemical* **151**, 274 (2010).

[10] S. Ozdemir, T. B. Osburn, and J. L. Gole, "Nanostructure modified gas sensor detection matrix for NO transient conversion of NO to NO_2," *Journal of The Electrochemical Society* **158**, J201 (2011).

[11] A. D'Amico and C. Di Natale, "A contribution on some basic definitions of sensors properties," *IEEE Sensors Journal* **1**, 183 (2001).

[12] V. Bochenkov and G. Sergeev, *Sensitivity, selectivity, and stability of gas-sensitive metal-oxide nanostructures*volume 3 (American Scientific Publishers, 2010), pp. 31–52.

[13] B. Ruhland, T. Becker, and G. Mller, "Gas-kinetic interactions of nitrous oxides with SnO_2 surfaces," *Sensors and Actuators B: Chemical* **50**, 85 (1998).

[14] C. Yu, Q. Hao, S. Saha, L. Shi, X. Kong, and Z. L. Wang, "Integration of metal oxide nanobelts with microsystems for nerve agent detection," *Applied Physics Letters* **86**, 063101 (2005).

[15] G. K. Mor, M. A. Carvalho, O. K. Varghese, M. V. Pishko, and C. A. Grimes, "A room-temperature TiO_2-nanotube hydrogen sensor able to self-clean photoactively from environmental contamination," *Journal of Materials Research* **19**, 628 (2004).

[16] N. Barsan, M. Schweizer-Berberich, and W. Gopel, "Fundamental and practical aspects in the design of nanoscaled SnO_2 gas sensors: a status report," *Fresenius' Journal of Analytical Chemistry* **365**, 287 (1999).

[17] E. Comini, "Metal oxide nano-crystals for gas sensing," *Analytica Chimica Acta* **568**, 28 (2006).

[18] I. Jimenez, J. Arbiol, G. Dezanneau, A. Cornet, and J. Morante, "Crystalline structure, defects and gas sensor response to NO_2 and H_2S of tungsten trioxide nanopowders," *Sensors and Actuators B: Chemical* **93**, 475 (2003).

[19] L. LeGore, R. Lad, S. Moulzolf, J. Vetelino, B. Frederick, and E. Kenik, "Defects and morphology of tungsten trioxide thin films," *Thin Solid Films* **406**, 79 (2002).

[20] S. C. Moulzolf, S. Ding, and R. J. Lad, "Stoichiometry and microstructure effects on tungsten oxide chemiresistive films," *Sensors and Actuators B: Chemical* **77**, 375 (2001).

[21] M. Ponce, C. Aldao, and M. Castro, "Influence of particle size on the conductance of SnO_2 thick films," *Journal of the European Ceramic Society* **23**, 2105 (2003).

[22] S. Rani, S. C. Roy, and M. Bhatnagar, "Effect of Fe doping on the gas sensing properties of nano-crystalline SnO_2 thin films," *Sensors and Actuators B: Chemical* **122**, 204 (2007).

[23] A. Rothschild and Y. Komem, "The effect of grain size on the sensitivity of nanocrystalline metal-oxide gas sensors," *Journal of Applied Physics* **95**, 6374 (2004).

[24] D. H. Yoon and G. M. Choi, "Microstructure and CO gas sensing properties of porous ZnO produced by starch addition," *Sensors and Actuators B: Chemical* **45**, 251 (1997).

[25] S. R. Morrison, "Selectivity in semiconductor gas sensors," *Sensors and Actuators* **12**, 425 (1987).

[26] J. Watson, "The stannic oxide gas sensor," *Sensor Review* **14**, 20 (1994).

[27] N. Yamazoe, K. Shimanoe, D. Aswal, and S. Gupta, *Overview of gas sensor technology* (Nova Science Publishers, Inc.: New York, NY, USA, 2007).

[28] M. J. Madou and S. R. Morrison, *Chemical sensing with solid state devices* (Elsevier, 2012).

[29] Y. Yan, N. Miura, and N. Yamazoe, "Potentiometric sensor using stabilized zirconia for chlorine gas," *Sensors and Actuators B: Chemical* **24**, 287 (1995).

[30] T. Usui, A. Asada, M. Nakazawa, and H. Osanai, "Gas polarographic oxygen sensor using an oxygen/zirconia electrolyte," *Journal of the Electrochemical Society* **136**, 534 (1989).

[31] G. Eranna, B. Joshi, D. Runthala, and R. Gupta, "Oxide materials for development of integrated gas sensors—a comprehensive review," *Critical Reviews in Solid State and Materials Sciences* **29**, 111 (2004).

[32] A. Neubecker, T. Pompl, T. Doll, W. Hansch, and I. Eisele, "Ozone-enhanced molecular beam deposition of nickel oxide (NiO) for sensor applications," *Thin Solid Films* **310**, 19 (1997).

[33] T. Seiyama and S. Kagawa, "Study on a Detector for Gaseous Components Using Semiconductive Thin Films.," *Analytical Chemistry* **38**, 1069 (1966).

[34] G. Jernigan and G. Somorjai, "Carbon monoxide oxidation over three different oxidation states of copper: metallic copper, copper (I) oxide, and copper (II) oxide-a surface science and kinetic study," *Journal of Catalysis* **147**, 567 (1994).

[35] A. Chowdhuri, V. Gupta, K. Sreenivas, R. Kumar, S. Mozumdar, and P. Patanjali, "Response speed of SnO 2-based H 2 S gas sensors with CuO nanoparticles," *Applied Physics Letters* **84**, 1180 (2004).

[36] Y. Nakamura, H. Zhuang, A. Kishimoto, O. Okada, and H. Yanagida, "Enhanced CO and CO 2 gas sensitivity of the CuO/ZnO heterocontact made by quenched CuO ceramics," *Journal of the Electrochemical Society* **145**, 632 (1998).

[37] D. H. Yoon, J. H. Yu, and G. M. Choi, "CO gas sensing properties of ZnO–CuO composite," *Sensors and Actuators B: Chemical* **46**, 15 (1998).

[38] R. Nahar and V. Khanna, "A study of capacitance and resistance characteristics of an Al2O3 humidity sensor," *International Journal of Electronics Theoretical and Experimental* **52**, 557 (1982).

[39] E. Comini, G. Faglia, G. Sberveglieri, Z. Pan, and Z. L. Wang, "Stable and highly sensitive gas sensors based on semiconducting oxide nanobelts," *Applied Physics Letters* **81**, 1869 (2002).

[40] I.-D. Kim, A. Rothschild, B. H. Lee, D. Y. Kim, S. M. Jo, and H. L. Tuller, "Ultrasensitive chemiresistors based on electrospun TiO_2 nanofibers," *Nano Letters* **6**, 2009 (2006).

[41] C. Rusu and J. Yates, "Photochemistry of NO chemisorbed on TiO_2 (110) and TiO_2 powders," *The Journal of Physical Chemistry B* **104**, 1729 (2000).

[42] M. Ferroni, V. Guidi, G. Martinelli, G. Faglia, P. Nelli, and G. Sberveglieri, "Characterization of a nanosized TiO_2 gas sensor," *Nanostructured materials* **7**, 709 (1996).

[43] B. Karunagaran, P. Uthirakumar, S. Chung, S. Velumani, and E.-K. Suh, "TiO 2 thin film gas sensor for monitoring ammonia," *Materials Characterization* **58**, 680 (2007).

[44] A. Kolmakov, Y. Zhang, G. Cheng, and M. Moskovits, "Detection of CO and O2 using tin oxide nanowire sensors," *Advanced Materials* **15**, 997 (2003).

[45] K. Jain, R. Pant, and S. Lakshmikumar, "Effect of Ni doping on thick film SnO_2 gas sensor," *Sensors and Actuators B: Chemical* **113**, 823 (2006).

[46] P. Esser and W. Gpel, ""Physical" adsorption on single crystal zinc oxide," *Surface Science* **97**, 309 (1980).

[47] P. T. Moseley and B. Tofield, *Solid-state gas sensors* (A. Hilger, 1987).

[48] C. Wang, L. Yin, L. Zhang, D. Xiang, and R. Gao, "Metal oxide gas sensors: sensitivity and influencing factors," *Sensors* **10**, 2088 (2010).

[49] Z. Huang, N. Geyer, P. Werner, J. De Boor, and U. Gsele, "Metal-Assisted Chemical Etching of Silicon: A Review," *Advanced materials* **23**, 285 (2011).

[50] R. Smith and S. Collins, "Porous silicon formation mechanisms," *Journal of Applied Physics* **71**, R1 (1992).

[51] S. Ozdemir, *Formation, characterization, and flow dynamics of nanostructure modified sensitive and selective gas sensors based on porous silicon*, Thesis Georgia Institute of Technology 2011.

[52] H. Kim, B. Han, J. Choo, and J. Cho, "Three-dimensional porous silicon particles for use in high-performance lithium secondary batteries," *Angewandte Chemie* **120**, 10305 (2008).

[53] M. Brunet and P. Kleimann, "High-Density 3-D Capacitors for Power Systems On-Chip: Evaluation of a Technology Based on Silicon Submicrometer Pore Arrays Formed by Electrochemical Etching," *Power Electronics, IEEE Transactions on* **28**, 4440 (2013).

[54] A. Benilov, M. Cabrera, V. Skryshevsky, and J.-R. Martin, "Porous silicon localization for implementation in matrix biosensors," *Materials Science and Engineering: B* **139**, 221 (2007).

[55] G. D. Francia, V. L. Ferrara, S. Manzo, and S. Chiavarini, "Towards a label-free optical porous silicon DNA sensor," *Biosensors and Bioelectronics* **21**, 661 (2005).

[56] S. P. Low, N. H. Voelcker, L. T. Canham, and K. A. Williams, "The biocompatibility of porous silicon in tissues of the eye," *Biomaterials* **30**, 2873 (2009).

[57] J.-H. Park, L. Gu, G. Von Maltzahn, E. Ruoslahti, S. N. Bhatia, and M. J. Sailor, "Biodegradable luminescent porous silicon nanoparticles for in vivo applications," *Nature Materials* **8**, 331 (2009).

[58] A. K. Shalek *et al.*, "Vertical silicon nanowires as a universal platform for delivering biomolecules into living cells," *Proceedings of the National Academy of Sciences* **107**, 1870 (2010).

[59] A. M. Rossi, L. Wang, V. Reipa, and T. E. Murphy, "Porous silicon biosensor for detection of viruses," *Biosensors and Bioelectronics* **23**, 741 (2007).

[60] T. Matsumoto, M. Daimon, H. Mimura, Y. Kanemitsu, and N. Koshida, "Optically induced absorption in porous silicon and its application to logic gates," *Journal of the Electrochemical Society* **142**, 3528 (1995).

[61] O. Bisi, S. Ossicini, and L. Pavesi, "Porous silicon: a quantum sponge structure for silicon based optoelectronics," *Surface Science Reports* **38**, 1 (2000).

[62] A. Cullis, L. T. Canham, and P. Calcott, "The structural and luminescence properties of porous silicon," *Journal of Applied Physics* **82**, 909 (1997).

[63] M. M. Das, M. Ray, N. R. Bandyopadhyay, and S. M. Hossain, "Estimation of oxide related electron trap energy of porous silicon nanostructures," *Materials Chemistry and Physics* **119**, 524 (2010).

[64] J. L. Gole, F. P. Dudel, D. Grantier, and D. A. Dixon, "Origin of porous silicon photoluminescence: Evidence for a surface bound oxyhydride-like emitter," *Physical Review B* **56**, 2137 (1997).

[65] J. L. Gole, E. Veje, R. Egeberg, A. Ferreira da Silva, I. Pepe, and D. A. Dixon, "Optical analysis of the light emission from porous silicon: A hybrid polyatom surface-coupled fluorophor," *The Journal of Physical Chemistry B* **110**, 2064 (2006).

[66] S. E. Lewis, J. R. DeBoer, J. L. Gole, and P. J. Hesketh, "Sensitive, selective, and analytical improvements to a porous silicon gas sensor," *Sensors and Actuators B: Chemical* **110**, 54 (2005).

[67] S. Ozdemir and J. L. Gole, "The potential of porous silicon gas sensors," *Current Opinion in Solid State and Materials Science* **11**, 92 (2007).

[68] C. Burda, Y. Lou, X. Chen, A. C. Samia, J. Stout, and J. L. Gole, "Enhanced nitrogen doping in TiO_2 nanoparticles," *Nano letters* **3**, 1049 (2003).

[69] J. L. Gole, S. M. Prokes, J. D. Stout, O. J. Glembocki, and R. Yang, "Unique properties of selectively formed zirconia nanostructures," *Advanced Materials* **18**, 664 (2006).

[70] S. Prokes, W. Carlos, L. Seals, S. Lewis, and J. L. Gole, "Formation of ferromagnetic Ni/SiO_2 nanospheres," *Materials Letters* **54**, 85 (2002).

[71] C. Baratto, G. Faglia, E. Comini, G. Sberveglieri, A. Taroni, V. La Ferrara, L. Quercia, and G. Di Francia, "A novel porous silicon sensor for detection of sub-ppm NO_2 concentrations," *Sensors and Actuators B: Chemical* **77**, 62 (2001).

[72] L. Boarino, C. Baratto, F. Geobaldo, G. Amato, E. Comini, A. Rossi, G. Faglia, G. Lerondel, and G. Sberveglieri, "NO_2 monitoring at room temperature by a porous silicon gas sensor," *Materials Science and Engineering: B* **69**, 210 (2000).

[73] S. Chakane, A. Gokarna, and S. Bhoraskar, "Metallophthalocyanine coated porous silicon gas sensor selective to NO_2," *Sensors and Actuators B: Chemical* **92**, 1 (2003).

[74] J. L. Gole and S. Ozdemir, "Nanostructure-Directed Physisorption vs Chemisorption at Semiconductor Interfaces: The Inverse of the HSAB Concept," *ChemPhysChem* **11**, 2573 (2010).

[75] C. Hui-Qing, H. Ming, Z. Jing, and W. Wei-Dan, "The light-enhanced NO_2 sensing properties of porous silicon gas sensors at room temperature," *Chinese Physics B* **21**, 058201 (2012).

[76] C. Xu, M. Li, X. Zhang, K.-N. Tu, and Y. Xie, "Theoretical studies of displacement deposition of nickel into porous silicon with ultrahigh aspect ratio," *Electrochimica acta* **52**, 3901 (2007).

[77] C. Xu, X. Zhang, K.-N. Tu, and Y. Xie, "Nickel displacement deposition of porous silicon with ultrahigh aspect ratio," *Journal of the Electrochemical Society* **154**, D170 (2007).

[78] A. Foucaran, F. Pascal-Delannoy, A. Giani, A. Sackda, P. Combette, and A. Boyer, "Porous silicon layers used for gas sensor applications," *Thin Solid Films* **297**, 317 (1997).

[79] I. Schechter, M. Ben-Chorin, and A. Kux, "Gas sensing properties of porous silicon," *Analytical Chemistry* **67**, 3727 (1995).

[80] N. S. Subramanian, R. V. Sabaapathy, P. Vickraman, G. V. Kumar, R. Sriram, and B. Santhi, "Investigations on Pd: SnO_2/porous silicon structures for sensing LPG and NO_2 gas," *Ionics* **13**, 323 (2007).

[81] F. Rahimi *et al.*, "Characterization of porous poly-silicon impregnated with Pd as a hydrogen sensor," *Journal of Physics D: Applied Physics* **38**, 36 (2005).

[82] F. Rahimi *et al.*, "Characterization of Pd nanoparticle dispersed over porous silicon as a hydrogen sensor," *Journal of Physics D: Applied Physics* **40**, 7201 (2007).

[83] V. Arakelyan, V. Galstyan, K. Martirosyan, G. Shahnazaryan, V. Aroutiounian, and P. Soukiassian, "Hydrogen sensitive gas sensor based on porous silicon/$TiO_{2\text{-}X}$ structure," *Physica E: Low-dimensional Systems and Nanostructures* **38**, 219 (2007), Proceedings of the E-MRS 2006 Symposium C: Silicon Nanocrystals for Electronic and Sensing Applications.

[84] M. Galova, "M. Schlesinger, M. Paunovic (eds) Modern electroplating, 4th edn.," *Journal of Solid State Electrochemistry* **6**, 357 (2002).

[85] M. Paunovic and M. Schlesinger, *Fundamentals of Electrochemical Deposition*The ECS Series of Texts and Monographs (Wiley, 2006).

[86] G. L. Weller and S. J. Pratt, "Measuring phosphine: how sensors work," 2003.

[87] J. Zeng, M. Hu, W. Wang, H. Chen, and Y. Qin, "NO_2-sensing properties of porous WO $_3$ gas sensor based on anodized sputtered tungsten thin film," *Sensors and Actuators B: Chemical* **161**, 447 (2012).

[88] M. Bjorkqvist, J. Paski, J. Salonen, and V.-P. Lehto, "Studies on hysteresis reduction in thermally carbonized porous silicon humidity sensor," *Sensors Journal, IEEE* **6**, 542 (2006).

[89] M. Bjrkqvist, J. Salonen, E. Laine, and L. Niinist, "Comparison of stabilizing treatments on porous silicon for sensor applications," *Physica Status Solidi (a)* **197**, 374 (2003).

[90] M. Bjrkqvist, J. Salonen, J. Paski, and E. Laine, "Characterization of thermally carbonized porous silicon humidity sensor," *Sensors and Actuators A: Physical* **112**, 244 (2004).

[91] A. Foucaran, B. Sorli, M. Garcia, F. Pascal-Delannoy, A. Giani, and A. Boyer, "Porous silicon layer coupled with thermoelectric cooler: a humidity sensor," *Sensors and Actuators A: Physical* **79**, 189 (2000).

[92] J. L. Gole and S. E. Lewis, *Porous Silicon–Sensors and Future Applications* (Elsevier: London, 2007).

[93] Z. Rittersma, A. Splinter, A. Bodecker, and W. Benecke, "A novel surface-micromachined capacitive porous silicon humidity sensor," *Sensors and Actuators B: Chemical* **68**, 210 (2000).

[94] S. Zangooie, R. Bjorklund, and H. Arwin, "Vapor sensitivity of thin porous silicon layers," *Sensors and Actuators B: Chemical* **43**, 168 (1997).

[95] B. H. King, A. M. Ruminski, J. L. Snyder, and M. J. Sailor, "Optical-Fiber-Mounted Porous Silicon Photonic Crystals for Sensing Organic Vapor Breakthrough in Activated Carbon," *Advanced Materials* **19**, 4530 (2007).

[96] T. Karacali, U. C. Hasar, I. Y. Ozbek, E. A. Oral, and H. Efeoglu, "Novel design of porous silicon based sensor for reliable and feasible chemical gas vapor detection," *Journal of Lightwave Technology* **31**, 295 (2013).

[97] F. Besenbacher and J. K. Nrskov, "Oxygen chemisorption on metal surfaces: General trends for Cu, Ni and Ag," *Progress in Surface Science* **44**, 5 (1993).

[98] E. G. Derouane, "Zeolites as solid solvents," *Journal of Molecular Catalysis A: Chemical* **134**, 29 (1998).

[99] K. K. Kolasinski, *Surface science: foundations of catalysis and nanoscience* (John Wiley & Sons, 2012).

[100] M. Bgner and T. Doll, *Introduction to the Electroadsorptive Effect and its Applications* (Springer, 2003), pp. 1–39.

[101] Z. Zhang and J. T. Yates, "Band Bending in Semiconductors: Chemical and Physical Consequences at Surfaces and Interfaces," *Chemical Reviews* **112**, 5520 (2012).

[102] C. R. Barrett, W. D. Nix, and A. S. Tetelman, *The principles of engineering materials* (Prentice-Hall Englewood Cliffs, NJ, 1973).

[103] N. Barsan and U. Weimar, "Conduction model of metal oxide gas sensors," *Journal of Electroceramics* **7**, 143 (2001).

[104] P. Grndler, *Chemical sensors: an introduction for scientists and engineers* (Springer, 2007).

[105] D. Simon and J. McQuarrie, *Physical Chemistry: A Molecular Approach* (University Science Books: Sausalito, CA, 1997).

[106] K. J. Albert, N. S. Lewis, C. L. Schauer, G. A. Sotzing, S. E. Stitzel, T. P. Vaid, and D. R. Walt, "Cross-reactive chemical sensor arrays," *Chemical Reviews* **100**, 2595 (2000).

[107] F. Rock, N. Barsan, and U. Weimar, "Electronic nose: current status and future trends," *Chemical Reviews* **108**, 705 (2008).

[108] J. W. Gardner and P. N. Bartlett, "A brief history of electronic noses," *Sensors and Actuators B: Chemical* **18**, 210 (1994).

[109] C. Di Natale, A. Macagnano, E. Martinelli, R. Paolesse, G. D'Arcangelo, C. Roscioni, A. Finazzi-Agro, and A. D'Amico, "Lung cancer identification by the analysis of breath by means of an array of non-selective gas sensors," *Biosensors and Bioelectronics* **18**, 1209 (2003).

[110] T. G. Dietterich, "Approximate statistical tests for comparing supervised classification learning algorithms," *Neural computation* **10**, 1895 (1998).

[111] M. A. Figueiredo and A. K. Jain, "Unsupervised learning of finite mixture models," *Pattern Analysis and Machine Intelligence, IEEE Transactions on* **24**, 381 (2002).

[112] H. Yoo and R. Pimmely, "Short term load forecasting using a self-supervised adaptive neural network," *Power Systems, IEEE Transactions on* **14**, 779 (1999).

[113] R. A. Johnson, D. W. Wichern, and P. Education, *Applied multivariate statistical analysis*volume 4 (Prentice hall Englewood Cliffs, NJ, 1992).

[114] W. J. Krzanowski, *Principles of multivariate analysis* (Clarendon, 2000).

[115] D. C. Montgomery, E. A. Peck, and G. G. Vining, *Introduction to linear regression analysis*volume 821 (John Wiley & Sons, 2012).

[116] K. S. Narendra and S. Mukhopadhyay, "Adaptive control of nonlinear multivariable systems using neural networks," in *Decision and Control, Proceedings of the 32nd IEEE Conference on* pp. 3066–3071 IEEE 1993.

[117] H. Frigui and R. Krishnapuram, "Clustering by competitive agglomeration," *Pattern recognition* **30**, 1109 (1997).

[118] R. Xu and D. Wunsch, "Survey of clustering algorithms," *Neural Networks, IEEE Transactions on* **16**, 645 (2005).

[119] S. Wan, S. M. Wong, and P. Prusinkiewicz, "An algorithm for multidimensional data clustering," *ACM Transactions on Mathematical Software (TOMS)* **14**, 153 (1988).

[120] J. W. Gardner and P. N. Bartlett, *Electronic noses: principles and applications*volume 233 (Oxford University Press New York, 1999).

[121] M. Schweizer-Berberich, J. Zheng, U. Weimar, W. Gpel, N. Barsan, E. Pentia, and A. Tomescu, "The effect of Pt and Pd surface doping on the response of nanocrystalline tin dioxide gas sensors to CO," *Sensors and Actuators B: Chemical* **31**, 71 (1996).

[122] T. Morikawa, R. Asahi, T. Ohwaki, K. Aoki, and Y. Taga, "Band-gap narrowing of titanium dioxide by nitrogen doping," *Japanese Journal of Applied Physics* **40**, L561 (2001).

[123] O. Diwald, T. L. Thompson, E. G. Goralski, S. D. Walck, and J. T. Yates, "The effect of nitrogen ion implantation on the photoactivity of TiO_2 rutile single crystals," *The Journal of Physical Chemistry B* **108**, 52 (2004).

[124] H. Irie, Y. Watanabe, and K. Hashimoto, "Nitrogen-concentration dependence on photocatalytic activity of TiO_{2-x} N_x powders," *The Journal of Physical Chemistry B* **107**, 5483 (2003).

[125] X. Chen and S. S. Mao, "Titanium dioxide nanomaterials: synthesis, properties, modifications, and applications," *Chemical Reviews* **107**, 2891 (2007).

[126] J. L. Gole, J. D. Stout, C. Burda, Y. Lou, and X. Chen, "Highly Efficient Formation of Visible Light Tunable TiO_{2-x} N_x Photocatalysts and Their Transformation at the Nanoscale," *The Journal of Physical chemistry B* **108**, 1230 (2004).

[127] X. Tang and D. Li, "Sulfur-doped highly ordered TiO_2 nanotubular arrays with visible light response," *The Journal of Physical Chemistry C* **112**, 5405 (2008).

[128] J. C. Yu, W. Ho, J. Yu, H. Yip, P. K. Wong, and J. Zhao, "Efficient visible-light-induced photocatalytic disinfection on sulfur-doped nanocrystalline titania," *Environmental Science & Technology* **39**, 1175 (2005).

[129] W. I. Laminack and J. L. Gole, "Nanostructure-directed chemical sensing: The IHSAB principle and the effect of nitrogen and sulfur functionalization on metal oxide decorated interface response," *Nanomaterials* **3**, 469 (2013).

[130] S. Y. Bae, H. W. Seo, and J. Park, "Vertically aligned sulfur-doped ZnO nanowires synthesized via chemical vapor deposition," *The Journal of Physical Chemistry B* **108**, 5206 (2004).

[131] C. Chartier, S. Bastide, and C. Levy-Clement, "Metal-assisted chemical etching of silicon in HF-H_2 O_2," *Electrochimica Acta* **53**, 5509 (2008).

[132] V. Lehmann and U. Gsele, "Porous silicon formation: A quantum wire effect," *Applied Physics Letters* **58**, 856 (1991).

[133] E. K. Propst and P. A. Kohl, "The electrochemical oxidation of silicon and formation of porous silicon in acetonitrile," *Journal of The Electrochemical Society* **141**, 1006 (1994).

[134] M. M. Rieger and P. A. Kohl, "Mechanism of (111) Silicon Etching in HFAcetonitrile," *Journal of the Electrochemical Society* **142**, 1490 (1995).

[135] S. Lust and C. Lvy-Clment, "Chemical limitations of macropore formation on medium-doped p-type silicon," *Journal of The Electrochemical Society* **149**, C338 (2002).

[136] C. LvyClment, A. Lagoubi, and M. Tomkiewicz, "Morphology of Porous nType Silicon Obtained by Photoelectrochemical Etching I. Correlations with Material and Etching Parameters," *Journal of The Electrochemical Society* **141**, 958 (1994).

[137] J. L. Gole, E. C. Goude, and W. Laminack, "Nanostructure-Driven Analyte–Interface Electron Transduction: A General Approach to Sensor and Microreactor Design," *ChemPhysChem* **13**, 549 (2012).

[138] S. E. Lewis, "The creation of a viable porous silicon gas sensor," (2006).

[139] D. Meyerhofer, "Characteristics of resist films produced by spinning," *Journal of Applied Physics* **49**, 3993 (1978).

[140] W. Laminack, N. Pouse, and J. Gole, "Dynamic Interaction of NO2 with a Nanostructure Modified Porous Silicon Matrix: Acidity, Sensor Response, and the Competition for Donor Level Electrons," *ECS Journal of Solid State Science and Technology* **1**, Q25 (2012).

[141] J. L. Gole and S. E. Lewis, "Nanostructure and morphology modified porous silicon sensors," in *Integrated Optoelectronic Devices* pp. 573–583 International Society for Optics and Photonics 2005.

[142] L. Seals, J. L. Gole, L. A. Tse, and P. J. Hesketh, "Rapid, reversible, sensitive porous silicon gas sensor," *Journal of Applied Physics* **91**, 2519 (2002).

[143] J. L. Gole, J. Corno, S. Ozdemir, S. Prokes, and H. Shin, "Active microfiltered sensor interfaces, photocatalytic reactors, and microbatteries using combined micro/nanoporous interfaces," *Physica Status Solidi (c)* **6**, 1773 (2009).

[144] J. L. Gole, S. Lewis, and S. Lee, "Nanostructures and porous silicon: activity at interfaces in sensors and photocatalytic reactors," *Physica Status Solidi (a)* **204**, 1417 (2007).

[145] S. Ozdemir and J. L. Gole, "Porous silicon gas sensors for room temperature detection of ammonia and phosphine," *ECS Transactions* **16**, 379 (2008).

[146] R. G. Parr and R. G. Pearson, "Absolute hardness: companion parameter to absolute electronegativity," *Journal of the American Chemical Society* **105**, 7512 (1983).

[147] R. G. Pearson, "Hard and soft acids and bases," *Journal of the American Chemical Society* **85**, 3533 (1963).

[148] R. G. Pearson, "Absolute electronegativity and hardness: application to inorganic chemistry," *Inorganic Chemistry* **27**, 734 (1988).

[149] R. G. Pearson, "Chemical hardness," (1997).

[150] R. G. Pearson, "Chemical hardness and density functional theory," *JOURNAL OF CHEMICAL SCIENCES-BANGALORE-* **117**, 369 (2005).

[151] M. H. Cohen and A. Wasserman, "On the foundations of chemical reactivity theory," *The Journal of Physical Chemistry A* **111**, 2229 (2007).

[152] P. Geerlings, F. De Proft, and W. Langenaeker, "Conceptual density functional theory," *Chemical Reviews* **103**, 1793 (2003).

[153] R. G. Parr, R. A. Donnelly, M. Levy, and W. E. Palke, "Electronegativity: the density functional viewpoint," *The Journal of Chemical Physics* **68**, 3801 (1978).

[154] R. G. Parr and W. Yang, *Density-functional theory of atoms and molecules*volume 16 (Oxford university press, 1989).

[155] W. Yang, R. G. Parr, and R. Pucci, "Electron density, Kohn Sham frontier orbitals, and Fukui functions," *The Journal of Chemical Physics* **81**, 2862 (1984).

[156] C.-G. Zhan, J. A. Nichols, and D. A. Dixon, "Ionization potential, electron affinity, electronegativity, hardness, and electron excitation energy: molecular properties from density functional theory orbital energies," *The Journal of Physical Chemistry A* **107**, 4184 (2003).

[157] K. Fukui, T. Yonezawa, and H. Shingu, "A molecular orbital theory of reactivity in aromatic hydrocarbons," *The Journal of Chemical Physics* **20**, 722 (1952).

[158] W. Yang and R. G. Parr, "Hardness, softness, and the fukui function in the electronic theory of metals and catalysis," *Proceedings of the National Academy of Sciences* **82**, 6723 (1985).

[159] W. Price, "The far ultraviolet absorption spectra and ionization potentials of H2O and H2S," *The Journal of Chemical Physics* **4**, 147 (1936).

[160] J. Beauchamp and S. Buttrill Jr, "Proton Affinities of H2S and H2O," *The Journal of Chemical Physics* **48**, 1783 (1968).

[161] T.-H. Wang, J. L. Gole, M. G. White, C. Watkins, S. C. Street, Z. Fang, and D. A. Dixon, "The surprising oxidation state of fumed silica and the nature of water binding to silicon oxides and hydroxides," *Chemical Physics Letters* **501**, 159 (2011).

[162] P. Politzer, "A relationship between the charge capacity and the hardness of neutral atoms and groups," *The Journal of Chemical Physics* **86**, 1072 (1987).

[163] C. LvyClment, "Macroporous Microstructures including Silicon," *Encyclopedia of Electrochemistry* (2002).

[164] H. Li, J. Xu, Y. Zhu, X. Chen, and Q. Xiang, "Enhanced gas sensing by assembling Pd nanoparticles onto the surface of SnO_2 nanowires," *Talanta* **82**, 458 (2010).

[165] S. S. Kim, J. Y. Park, S.-W. Choi, H. S. Kim, H. G. Na, J. C. Yang, and H. W. Kim, "Significant enhancement of the sensing characteristics of In2O3 nanowires by functionalization with Pt nanoparticles," *Nanotechnology* **21**, 415502 (2010).

[166] A. Kolmakov, D. Klenov, Y. Lilach, S. Stemmer, and M. Moskovits, "Enhanced gas sensing by individual SnO2 nanowires and nanobelts functionalized with Pd catalyst particles," *Nano Letters* **5**, 667 (2005).

[167] M. T. Bowers, "Gas phase ion chemistry," (1979).

[168] C. H. DePuy, V. M. Bierbaum, and R. Damrauer, "Relative gas-phase acidities of the alkanes," *Journal of the American Chemical Society* **106**, 4051 (1984).

[169] C. E. Moore, "Ionization potentials and ionization limits derived from the analyses of optical spectra," (1970).

[170] M. N. Rudden and J. Wilson, *Elements of solid state physics* (Wiley, 1993).

[171] X. Chen, Y. Lou, A. C. Samia, C. Burda, and J. L. Gole, "Formation of Oxynitride as the Photocatalytic Enhancing Site in NitrogenDoped Titania Nanocatalysts: Comparison to a Commercial Nanopowder," *Advanced Functional Materials* **15**, 41 (2005).

[172] K. M. Ervin, J. Ho, and W. C. Lineberger, "Ultraviolet photoelectron spectrum of nitrite anion," *The Journal of Physical Chemistry* **92**, 5405 (1988).

[173] D. J. Grant, M. H. Matus, K. D. Anderson, D. M. Camaioni, S. R. Neufeldt, C. F. Lane, and D. A. Dixon, "Thermochemistry for the dehydrogenation of methyl-substituted ammonia borane compounds," *The Journal of Physical Chemistry A* **113**, 6121 (2009).

[174] M. J. Travers, D. C. Cowles, and G. B. Ellison, "Reinvestigation of the electron affinities of O_2 and NO," *Chemical Physics Letters* **164**, 449 (1989).

[175] L. Pancheri, C. Oton, Z. Gaburro, G. Soncini, and L. Pavesi, "Very sensitive porous silicon NO_2 sensor," *Sensors and Actuators B: Chemical* **89**, 237 (2003).

[176] G. Sberveglieri, S. Groppelli, and P. Nelli, "Highly sensitive and selective NO_x x and NO_2 sensor based on Cd-doped SnO_2 thin films," *Sensors and Actuators B: Chemical* **4**, 457 (1991).

[177] G. Williams and G. S. Coles, "NO_x response of tin dioxide based gas sensors," *Sensors and Actuators B: Chemical* **16**, 349 (1993).

[178] W. Miekisch, J. K. Schubert, and G. F. Noeldge-Schomburg, "Diagnostic potential of breath analysisfocus on volatile organic compounds," *Clinica Chimica Acta* **347**, 25 (2004).

[179] P. P. Rosias, E. Dompeling, H. J. Hendriks, J. W. Heijnens, R. A. Donckerwolcke, and Q. Jobsis, "Exhaled breath condensate in children: pearls and pitfalls," *Pediatric allergy and immunology* **15**, 4 (2004).

[180] J. W. Grate, B. M. Wise, and M. H. Abraham, "Method for unknown vapor characterization and classification using a multivariate sorption detector. Initial derivation and modeling based on polymer-coated acoustic wave sensor arrays and linear solvation energy relationships," *Analytical Chemistry* **71**, 4544 (1999).

[181] R. Haggerty and S. M. Gorelick, "Multiplerate mass transfer for modeling diffusion and surface reactions in media with porescale heterogeneity," *Water Resources Research* **31**, 2383 (1995).

[182] T. W. Weber and R. K. Chakravorti, "Pore and solid diffusion models for fixedbed adsorbers," *AIChE Journal* **20**, 228 (1974).

[183] J. Crank, "The mathematics of diffusion," (1975).

[184] E. N. Fuller, P. D. Schettler, and J. C. Giddings, "New method for prediction of binary gas-phase diffusion coefficients," *Industrial & Engineering Chemistry* **58**, 18 (1966).

[185] J. Gole and W. Laminack, "A Variable Response Phosphine Sensing Matrix Based on Nanostructure Treated *p*, *p+*, and *n*-type Porous Silicon Interfaces," *Sensors Journal, IEEE* **14**, 2731 (2014).

[186] J. D. Hamilton, *Time series analysis*volume 2 (Princeton university press Princeton, 1994).

[187] A. V. Neimark, P. I. Ravikovitch, and A. Vishnyakov, "Adsorption hysteresis in nanopores," *Physical Review E* **62**, R1493 (2000).

[188] L. Sarkisov and P. Monson, "Modeling of adsorption and desorption in pores of simple geometry using molecular dynamics," *Langmuir* **17**, 7600 (2001).

[189] J. Rouquerol, F. Rouquerol, P. Llewellyn, G. Maurin, and K. S. Sing, *Adsorption by powders and porous solids: principles, methodology and applications* (Academic press, 2013).

[190] J. Appel, "Freundlich's adsorption isotherm," *Surface Science* **39**, 237 (1973).

[191] K. Foo and B. Hameed, "Insights into the modeling of adsorption isotherm systems," *Chemical Engineering Journal* **156**, 2 (2010).

[192] I. Langmuir, "THE CONSTITUTION AND FUNDAMENTAL PROPERTIES OF SOLIDS AND LIQUIDS. PART I. SOLIDS," *Journal of the American Chemical Society* **38**, 2221 (1916).

[193] H. Freundlich, "Over the adsorption in solution," *J. Phys. Chem* **57**, 385 (1906).

[194] M. Dubinin and L. Radushkevich, "Equation of the characteristic curve of activated charcoal," *Chem. Zentr* **1**, 875 (1947).

[195] M. Temkin and V. Pyzhev, "Kinetics of ammonia synthesis on promoted iron catalysts," *Acta Physiochim. URSS* **12**, 217 (1940).

[196] A. V. Hill, "The possible effects of the aggregation of the molecules of haemoglobin on its dissociation curves," *J Physiol (Lond)* **40**, 4 (1910).

[197] O. Redlich and D. L. Peterson, "A useful adsorption isotherm," *Journal of Physical Chemistry* **63**, 1024 (1959).

[198] R. Sips, "Combined form of Langmuir and Freundlich equations," *J. Chem. Phys* **16**, 490 (1948).

[199] J. Toth, "State equations of the solid-gas interface layers," *Acta Chim Acad Sci Hungar* **69**, 311 (1971).

[200] S. Brunauer, P. H. Emmett, and E. Teller, "Adsorption of gases in multimolecular layers," *Journal of the American Chemical Society* **60**, 309 (1938).

[201] T. L. Hill, "Theory of physical adsorption," *Adv. Catal* **4**, 1 (1952).

[202] W. McMillan and E. Teller, "The assumptions of the BET theory," *The Journal of Physical Chemistry* **55**, 17 (1951).

[203] R. D. Harter, "Curve-fit errors in Langmuir adsorption maxima," *Soil Science Society of America Journal* **48**, 749 (1984).

[204] J. W. Grate and B. M. Wise, "A method for chemometric classification of unknown vapors from the responses of an array of volume-transducing sensors," *Analytical chemistry* **73**, 2239 (2001).

[205] J. N. Butler and R. S. Brokaw, "Thermal conductivity of gas mixtures in chemical equilibrium," *The Journal of Chemical Physics* **26**, 1636 (1957).

[206] E. Mason and S. Saxena, "Approximate formula for the thermal conductivity of gas mixtures," *Physics of Fluids (1958-1988)* **1**, 361 (1958).

[207] V. Y. Timoshenko, T. Dittrich, V. Lysenko, M. Lisachenko, and F. Koch, "Free charge carriers in mesoporous silicon," *Physical review B* **64**, 085314 (2001).

[208] C. Peng, K. D. Hirschman, and P. M. Fauchet, "Carrier transport in porous silicon light emitting devices," *Journal of Applied Physics* **80**, 295 (1996).

[209] T. Burr, A. Seraphin, E. Werwa, and K. Kolenbrander, "Carrier transport in thin films of silicon nanoparticles," *Physical Review B* **56**, 4818 (1997).

[210] M. Ben-Chorin, F. Möller, and F. Koch, "Band alignment and carrier injection at the porous-silicon–crystalline-silicon interface," *Journal of applied physics* **77**, 4482 (1995).

[211] M. Ben-Chorin, A. Kux, and I. Schechter, "Adsorbate effects on photoluminescence and electrical conductivity of porous silicon," *Applied physics letters* **64**, 481 (1994).

[212] E. Lebedev, E. Smorgonskaya, and G. Polisski, "Drift mobility of excess carriers in porous silicon," *Physical Review B* **57**, 14607 (1998).

[213] P. Jurs, G. Bakken, and H. McClelland, "Computational methods for the analysis of chemical sensor array data from volatile analytes," *Chemical Reviews* **100**, 2649 (2000).

[214] R. Saferstein, "Criminalistics: An introduction to forensic science," (2004).

[215] R. Astala, S. M. Auerbach, and P. Monson, "Density functional theory study of silica zeolite structures: Stabilities and mechanical properties of SOD, LTA, CHA, MOR, and MFI," *The Journal of Physical Chemistry B* **108**, 9208 (2004).

[216] F. Dogan, K. D. Hammond, G. A. Tompsett, H. Huo, W. C. Conner Jr, S. M. Auerbach, and C. P. Grey, "Searching for microporous, strongly basic catalysts: Experimental and calculated 29Si NMR spectra of heavily nitrogen-doped Y zeolites," *Journal of the American Chemical Society* **131**, 11062 (2009).

[217] D. Lesthaeghe, V. Van Speybroeck, and M. Waroquier, "Efficient use of bifunctional acid-base properties for alkylammonium formation in amine-substituted zeolites," *Journal of the American Chemical Society* **126**, 9162 (2004).

[218] D. Lesthaeghe, V. Van Speybroeck, G. B. Marin, and M. Waroquier, "DFT investigation of alkoxide vs alkylammonium formation in amine-substituted zeolites," *The Journal of Physical Chemistry B* **109**, 7952 (2005).

[219] J. L. Gole, S. M. Prokes, O. Glembocki, J. Wang, X. Qiu, and C. Burda, "Study of concentration-dependent cobalt ion doping of TiO 2 and TiO 2 x N x at the nanoscale," *Nanoscale* **2**, 1134 (2010).

[220] S. M. Prokes, J. L. Gole, X. Chen, C. Burda, and W. E. Carlos, "Defect Related Optical Behavior in Surface Modified TiO_2 Nanostructures," *Advanced Functional Materials* **15**, 161 (2005).

[221] C. E. Webb and J. D. Jones, *Handbook of Laser Technology and Applications: Laser design and laser systems*volume 2 (CRC Press, 2004).

[222] O. Diwald, T. L. Thompson, T. Zubkov, E. G. Goralski, S. D. Walck, and J. T. Yates, "Photochemical activity of nitrogen-doped rutile TiO_2 (110) in visible light," *The Journal of Physical chemistry B* **108**, 6004 (2004).

[223] G. R. Torres, T. Lindgren, J. Lu, C.-G. Granqvist, and S.-E. Lindquist, "Photoelectrochemical study of nitrogen-doped titanium dioxide for water oxidation," *The Journal of Physical Chemistry B* **108**, 5995 (2004).

[224] J. L. Gole and W. Laminack, "Nanostructure-directed chemical sensing: The IHSAB principle and the dynamics of acid/base-interface interaction," *Beilstein Journal of Nanotechnology* **4**, 20 (2013).

[225] P. A. Kottke, A. G. Fedorov, and J. L. Gole, *Multiscale Mass Transport in Porous Silicon Gas Sensors* (Springer, 2009), pp. 139–168.

[226] J. Gole, W. Laminack, and G. Korotcenkov, "General approach to design and modeling of nanostructure modified semiconductor and nanowire interfaces for sensor and microreactor applications," *Chemical Sensors: Simulation and Modeling* **3**, 85 (2012).

[227] N. C. Saha and H. G. Tompkins, "Titanium nitride oxidation chemistry: an xray photoelectron spectroscopy study," *Journal of Applied Physics* **72**, 3072 (1992).

[228] S. W. Sharpe, T. J. Johnson, R. L. Sams, P. M. Chu, G. C. Rhoderick, and P. A. Johnson, "Gas-phase databases for quantitative infrared spectroscopy," *Applied spectroscopy* **58**, 1452 (2004).

[229] T. Jirsak, J. Dvorak, and J. A. Rodriguez, "Adsorption of NO2 on Rh (111) and Pd/Rh (111): photoemission studies," *Surface science* **436**, L683 (1999).

[230] L. A. DeLouise and N. Winograd, "Adsorption and desorption of NO from Rh 111 and Rh 331 surfaces," *Surface Science* **159**, 199 (1985).

[231] C. Wagner, W. Riggs, L. Davis, J. Moulder, and G. Muilenberg, "Handbook of X-ray Photoelectron SpectroscopyPerkin-Elmer," *Eden Prairie, MN* **188** (1979).

[232] E. Gyrgy, A. Perez del Pino, P. Serra, and J. Morenza, "Depth profiling characterisation of the surface layer obtained by pulsed Nd: YAG laser irradiation of titanium in nitrogen," *Surface and Coatings Technology* **173**, 265 (2003).

[233] J. L. Lawrie, Y. Jiao, and S. M. Weiss, "Size-dependent infiltration and optical detection of nucleic acids in nanoscale pores," *Nanotechnology, IEEE Transactions on* **9**, 596 (2010).

[234] G. Rong and S. M. Weiss, "Biomolecule size-dependent sensitivity of porous silicon sensors," *Physica Status Solidi (a)* **206**, 1365 (2009).

[235] C. Liang, N. J. Dudney, and J. Y. Howe, "Hierarchically structured sulfur/carbon nanocomposite material for high-energy lithium battery," *Chemistry of Materials* **21**, 4724 (2009).

[236] H. Wang, Y. Yang, Y. Liang, J. T. Robinson, Y. Li, A. Jackson, Y. Cui, and H. Dai, "Graphene-wrapped sulfur particles as a rechargeable lithiumsulfur battery cathode material with high capacity and cycling stability," *Nano Letters* **11**, 2644 (2011).

VITA

William Laminack was born in the U.S.A. and got his Bachelor's of Science in Physics from the Physics Department at the Georgia Institute of Technology in 2008. He got his non-thesis Master's in science from the Physics Department at the Georgia Institute of Technology in 2010. He has worked on his PhD degree, with a focus on porous silicon gas sensors in the School of Physics at the Georgia Institute of Technology until April 2015. He plans to work in industry.